CRANFIELD UNIVERSITY

CRANFIELD UNIVERSITY LIBRARY

CHRISTOPHER JAMES ROACH

DEVELOPMENT OF POROUS CERAMIC AIR BEARINGS

SCHOOL OF INDUSTRIAL AND MANUFACTURING SCIENCE

Ph.D. THESIS

CRANFIELD UNIVERSITY

SCHOOL OF INDUSTRIAL AND MANUFACTURING SCIENCE

Ph.D. THESIS

Academic Year 2000 - 2001

CHRISTOPHER JAMES ROACH

Development of Porous Ceramic Air Bearings

Supervisors: D. J. Stephenson

J. Corbett

February 2001

This thesis is submitted in complete fulfilment of the requirements for the degree of Doctor of Philosophy

Abstract

Porous air bearings enjoy some important advantages over conventional air bearing types such as increased load carrying capacity, higher stiffness and improved damping. However, these types of bearings have yet to find widespread acceptance due to problems with obtaining materials with consistent permeability, instability issues relating to the volume of gas trapped at the bearing surface in the pores, and manufacturing the bearing without altering the permeability.

Using a series of fine grades of alumina powder to minimise surface pore volume it has been demonstrated that it is possible to consistently and reproducibly manufacture porous bearings by injection moulding and slip casting. The relationship between powder size, processing conditions, porosity, mechanical properties and fluid flow characteristics were experimentally determined. The temperature of processing and the green density were found to be the controlling parameters in the resulting fluid flow properties for a given powder size.

Test bearings were produced from the range of processing conditions investigated. It was found that the fine powder size bearings were stable over the entire range of test conditions irrespective of their initial manufacturing route. The most important consideration for the bearing performance was the quality of manufacture. The bearings were found to be sensitive to the flatness of their working surface and quality of fit in their test holder.

The bearings were compared with published theories for load capacity and stiffness. A reasonable agreement was found with load carrying capacity once a correction for surface roughness was incorporated. Stiffness predictions provided a useful tool for the analysis and prediction of properties such as

optimum values of permeability for a given geometry, if certain allowances are made.

Acknowledgements

The author would like to thank the following people for all of their help and advice during the period of this degree.

In the main these were my supervisors, Professors John "Oops, I broke another one!" Corbett and David "It would be nice if..." Stephenson, whose guidance during the early stages of the programme was invaluable, and without whose suggestions writing this thesis would have been a lot faster.

I am grateful for all the technical support that I received during the research, particularly that from Andrew "Your job is next in the queue, honest!" Baldwin, John "You're not putting that in my HIP!" Hedge, Peter "They broke the mould" Logan and Andrew "Delirious" Dyer.

Thanks are also due to the EPSRC, Landis Lund, Cranfield Precision, T&N, TENMAT, Dynamic Ceramic, and International Metrology Systems for their financial support.

Finally, he would like to thank Patrick Kwan, the researcher who carried out the previous investigation into porous ceramic bearing development at Cranfield University, for leaving such a clear and unambiguous thesis as a record of his work.

Chris Roach

February 2001

To Clare

Table of Contents

1 Introduction 1

1.1 Background 1

1.2 Gas Bearings 3

1.2.1 Aims of Present Work 1

2 Historical Development of Bearing Systems 7

2.1 Materials 8

2.2 Introduction to Fluid Film Bearings 11

2.3 Hydrostatic Bearings 11

2.4 Water Hydrostatic Bearings 13

2.5 Air Bearings 14

2.5.1 Problems with Instability 18

2.5.2 Types of Air Bearings 19

2.5.3 Porous Air Bearings 23

2.5.4 Porosity and Permeability 24

2.5.5 Graphite Air Bearings 27

2.5.6 Sintered Bronze Bearings 30

2.5.7 Porous Ceramic Bearings 32

2.6 Theoretical Analysis 33

2.6.1 Flow Through Porous Media 33

2.6.2 Porous Air Bearing Theory 35

2.7 Experimental Comparisons 38

2.8 Slip Flow 39

2.9 Mechanical Properties 41

2.10 Manufacturing Routes 43

2.10.1 Slip Casting 43

2.10.2 Injection Moulding 47

2.10.3 Sintering 49

2.10.3.1 Sintering Aids 52

2.10.4 HIP 53
3 Experimental Procedure 55
3.1 Materials Processing 55
3.1.1 Powder Preparation 57
3.1.2 Vibratory packing 58
3.1.3 Higher Pressure Sintering By Capsule Free HIPing 60
3.1.4 Slip Casting 60
3.1.5 Injection Moulding 65
3.1.6 Solvent Debinding 75
3.1.7 Sintering 76
3.1.8 Powder Size Classification 78
3.1.9 Combination Route Bearings 78
3.1.10 Silicon Nitride Bearing Preparation 79
3.2 Mechanical Properties 80
3.2.1 Density Measurements 81
3.3 Experimental Rigs 84
3.3.1 Permeability Rig 85
3.3.1.1 Measurement Procedure - Permeability 91
3.3.1.2 Measurement Procedure – Bubble Pore Test and Extended Bubble Pore Test 93
3.3.2 Stiffness Rig 97
3.4 Microscopy 100
3.5 Other Equipment 101
3.5.1 Surface Profilometry 101
3.5.2 Grinding 102
3.5.3 Moduli Measurement 103
4 Results and Discussion 107
4.1 Permeability and Open Porosity 107
4.2 Processing Conditions and Open Porosity 111
4.2.1 Alumina Bearings 111
4.2.2 Silicon Nitride Bearings 114

4.2.3 Dip in Slip 117
4.3 Mechanical Properties 119
4.4 Permeability Ratio 125
4.5 Bearing Performance 127
4.5.1 Comparison of Bearing Performance Data 130
4.5.1.1 Load Carrying Capacity 130
4.5.1.2 Bearing Stiffness 142
4.5.1.3 Slip Cast and Injection Moulding Comparison 156
4.5.1.4 Comparison with Commercially Available Porous Bearing 158
5 Summary of Development Methodology 164
6 Conclusions 166
7 Suggestions For Further Work 168
7.1 Improvements To Machining Process 168
7.2 Improvements To Stiffness Test Procedure 170
7.3 Pore Size Distribution Measurement 170
7.4 Dynamic Performance Testing 171
7.5 Improvements To Current Manufacturing Routes 171
7.6 Other Manufacturing Routes 172
References 173

List of Figures

Figure 1 Principles of aerostatic air bearing operation..... 15
Figure 2. Different types of compensation, A) orifice, B) capillary, C) porous plug, D) inherent..... 17
Figure 3 General types of air bearings, A) cylindrical journals with annular thrust bearings, B) conical journal bearings, C) Yates bearing, D) hemispherical journals (from [27]) 19
Figure 4. Types of thrust bearings, A) rectangular with single feed hole, B) circular with single feed hole, C) rectangular with multiple feed holes, D) circular with multiple feed holes and grooves 20
Figure 5 Tilting pad air bearing (from [28]) 21
Figure 6 Flexible membrane air bearing (from [30]) 22
Figure 7 Porous air bearing 23
Figure 8 Graphite bearing (from [39]) 28
Figure 9 Example of a spindle using porous graphite bearings (from [41]) 30
Figure 10 Tangential velocity slip flow 40
Figure 11 Free body diagram of loading on circular thrust bearing 41
Figure 12 Worst case loading on circular thrust bearing 42
Figure 13 Injection moulding process schematic (from [92]) 48
Figure 14 Stages of sintering (from [95]) 50
Figure 15 Slip casting moulds 63
Figure 16 Rotational slip casting mould 64
Figure 17 Porous ceramic journal bearing produced by rotational slip casting. 65
Figure 18 Dassett injection moulding machine 66
Figure 19 Twin screw extruder 69
Figure 20 Mould for thrust bearings 71
Figure 21 Green and sintered thrust bearings 72
Figure 22 Green machined thrust bearings 73
Figure 23 Journal bearing mould 74
Figure 24 Green and sintered journal bearing 74

Figure 25 Heptane debinding rig 75
Figure 26 "Smearing" on the surface of a silicon nitride bearing 79
Figure 27 Cutting edge of diamond tool used against silicon nitride bearings (Courtesy Paulo Beltrão) 80
Figure 28 Permeability rig 86
Figure 29 Edge loss compensation (from [117]) 88
Figure 30 Zero error correction 92
Figure 31 Permeability measurement plot 93
Figure 32 0.5µm pore diameter comparison 95
Figure 33 Stiffness rig 97
Figure 34 Schematic of stiffness rig, (from [100]) 98
Figure 35 The Tetraform grinding machine 103
Figure 36 Viscous permeability related to open porosity 107
Figure 37 Inertial permeability related to open porosity 108
Figure 38 Open porosity as a function of processing temperature 112
Figure 39 Densification as a function of temperature 114
Figure 40 Open porosity as a function of pressing conditions 115
Figure 41 Variation in E with powder size distribution and pressing conditions 116
Figure 42 Variation of Youngs' Modulus with open porosity for Si_3N_4 117
Figure 43 DIS penetration micrograph 118
Figure 44 Modulus data for each bearing type 119
Figure 45 Youngs' Modulus as a function of density 120
Figure 46 Torsional Modulus as a function of density 121
Figure 47 Poissons ratio as a function of density 122
Figure 48 Permeability ratio 127
Figure 49 Bearing gap as a function of load 128
Figure 50 Pressure distribution under well machined bearing 129
Figure 51 Pressure distribution under poorly machined bearing 130
Figure 52 Surface profile of well-machined bearing in the direction of grinding 132

Figure 53 Surface profile of well-machined bearing perpendicular to grinding direction 133
Figure 54 Surface profile of poorly machined bearing in the direction of grinding 133
Figure 55 Surface profile of poorly machined bearing perpendicular to grinding direction 134
Figure 56 Metallic pick-up on surface of bearing 134
Figure 57 Surface form of better bearing in grinding direction 135
Figure 58 Surface form of better bearing perpendicular to grinding direction 136
Figure 59 Surface form of poorer bearing in grinding direction 136
Figure 60 Surface form of poorer bearing perpendicular to grinding direction 137
Figure 61 Normalised load as a function of bearing number 138
Figure 62 Deflection as a function of load for "average" bearing 140
Figure 63 Extended bearing response to increasing load 141
Figure 64 Bearing holder 143
Figure 65 Bearing holder out of roundness 146
Figure 66 Roundness profile for a bearing that performed well 147
Figure 67 Roundness profile for a bearing that performed poorly 147
Figure 68 Stiffness data from every stiffness test at a gap of 2.5µm 148
Figure 69 Best stiffness data at a gap of 2.5µm 149
Figure 70 Best stiffness data at a gap of 5µm 149
Figure 71 Best stiffness data at a gap of 7.5µm 150
Figure 72 Best stiffness data at a gap of 10µm 150
Figure 73 Theoretical optimum bearing stiffness, (from [72]) 152
Figure 74 Experimental optimum bearing stiffness at a 2.5µm gap 152
Figure 75 Experimental optimum bearing stiffness at a 5µm gap 153
Figure 76 Experimental optimum bearing stiffness at a 7.5µm gap 153
Figure 77 Experimental optimum bearing stiffness at a 10µm gap 154
Figure 78 Deflection as a function of load for injection moulded and slip cast bearings 156

Figure 79 Pressure profiles measured for injection moulded and slip cast bearings 157
Figure 80 Deflection as a function of normalised load for injection moulded and slip cast bearings 157
Figure 81 Deflection as a function of load for commercial 1.5″ diameter bearing, (from [140]) 159
Figure 82 Deflection as a function of load for commercial 2″ diameter bearing, (from [140]) 159
Figure 83 Re-plotted data from New Way 161
Figure 84 Overview of processing methodology 164
Figure 85 Talysurf measurement across conventionally ground bearing surface 169
Figure 86 Talysurf measurement of Tetraform ground surface 169

Nomenclature

Symbol	Meaning	Units
A_A	Constant	
A	Area of inner tube	m^2
A_m	Mutual collision cross section	m^2
A_p	Area of porous sample	m^2
E	Young's Modulus	Pa
Ea	Activation energy	kJ/mol
G	Torsional modulus	Pa
K	Dimensionless specific stiffness	
P	Pressure	Pa
P_1	Gas pressure upstream of sample, absolute	Pa
P_2	Gas pressure downstream of sample, absolute	Pa
P_{ref}	Gas pressure to which the measured flow	
	rate refers, absolute	Pa
Δp	Pressure drop across porous sample	Pa
Q	Volumetric flow of gas	m^3
Q_{mean}	Volume flow rate at mean pressure across	
	porous specimen	m^3
R	Universal gas constant	
R_a	Arithmetic mean deviation of the profile	m
R_p	Maximum profile peak height	m
R_t	Distance between highest peak and lowest valley	m
T	Temperature	°K
Vs	Volume of sample	m^3
$d_{pore\ max}$	Largest circular capillary equivalent	
	pore diameter	m
e	Thickness of sample	m
g	Acceleration due to gravity	m/s^2

h_w	Head of water	m
k_a	Rate coefficient	1/s
k_n	Knudsen number	
m_1	Dry mass of specimen	kg
m_2	Fully impregnated mass of specimen	kg
m_3	Mass of weighing pan in air	kg
m_4	Mass of weighing pan in water	kg
m_5	Mass of porous specimen and pan in water	kg
n	Number of gas molecules per unit volume	$1/m^3$
p	Bearing working pressure	Pa
P_a	Atmospheric pressure	Pa
P_g	Gap pressure	Pa
P_s	Supply pressure	Pa
r_p	Radius of porous pad	m
z_g	Bearing gap	m
z_p	Thickness of sample	m
Φ_e	Coefficient of equivalent permeability	m^2
Φ_v	Coefficient of viscous permeability	m^2
Φ_i	Coefficient of inertial permeability	m
Λ	Non-dimensionalised bearing number	
X	Non-dimensionalised bearing parameter	
μ	Micro	1E-6
γ	Surface tension	N/m
γ_w	Surface tension of water	N/m
η	Viscosity of air	Pas
λ	Mean free path of gas molecule	m
ν	Poisson's ratio	
ρ	Density of air at atmospheric pressure	kg/m^3
ρ_{mean}	Mean density of air in bearing during permeability test	kg/m^3

ρ_w	Density of deionised water	kg/m^3
Γ_{ss}	Surface energy of a solid-solid interface	J/m^2
Γ_{sv}	Surface energy of a solid-vapour interface	J/m^2
ζ	Porosity	
ζ_c	Closed porosity	
ζ_{cr}	Critical porosity at which the elastic moduli approaches zero	
ζ_o	Open porosity	
ζ_t	Total porosity	

1 Introduction

1.1 Background

The theory and proper understanding of bearings is of fundamental importance in the design of any system that contains rotating or moving parts. Virtually every mechanical man-made device contains rotating elements, from the wheel on a supermarket trolley to the shaft of a truck's turbo charger, and in every case the selection of the correct materials and careful design are required to ensure the component meets its design life.

The choice of bearing system is ever increasing, with new innovations constantly appearing and already established ones being improved upon. As the choice of candidate materials increases and the level of understanding of the bearing mechanisms improve, the range of systems available to the designer is also widened.

Currently bearing techniques can be divided into two broad categories; contact and non-contact. Examples of contacting bearings are rolling element bearings, such as ball and roller bearings commonly used for supporting rotating axles or driveshafts. These are available in a wide variety of sizes, materials, and are suitable for a great number of applications. They have enjoyed several centuries of development, and while they remain the mainstay of the bearing world, and indeed will remain so for some considerable time, they do posses certain limitations that constrain their function in certain applications.

Despite the use of modern production techniques it is still very difficult to produce a rolling element bearing that is perfectly smooth. Problems arise due to slight errors in the roundness of rollers, or changes in the curvature of ball bearings. Likewise, the tracks that they run in will always carry some error in

their curvature. The result being that these imperfections in roundness, which can cause vibration and imbalance, are carried over to the shaft that they are supporting. For applications that require a great deal of precision, such errors can constrain the usefulness of the machine.

There is also a physical limit to which such a bearing can be made to rotate. The faster the bearing rotates the greater speed that the elements move over the surface of the cage. This naturally increases wear, limiting their useful life. As the elements and cages are of appreciable mass, they are also subject to centrifugal forces during operation. As the centrifugal force is proportional to the rotating mass it can be seen that rotational speeds will be limited. With a general requirement of lubrication, an additional constraint is applied. Many high precision uses for bearings require clean operation, which is compromised through contamination from grease and oil.

Non-contact bearings on the other hand, as the name suggests, are bearings in which no physical contact is made between the bearing surfaces. Magnetic and fluid film bearings are examples of this. These are a relatively new technology, with the bulk of the development having taken place within the last sixty years. Due to their unique mode of operation, non-contact bearings have successfully carved an important, and expanding, niche in the market.

Non-contact bearings offer certain advantages over conventional rolling element type bearings due to their nature. This makes them the ideal solution to certain problems that would otherwise be prohibitively expensive, if at all possible, to overcome. Due to their non-contacting nature, surface irregularities tend to be evened out, leading to lower vibrations and errors in precision applications. Damping performance is improved. For gas and magnetic bearings, true cleanroom capability can be achieved due to the total absence of a lubricant. In addition, no wear takes place, thus giving effectively an infinite

life. With gas and magnetic bearings, rotational speeds can also be increased due to their very low friction, and low rotating mass.

1.2 Gas Bearings

Gas bearings are a particular subset of fluid film bearings, and consist of a further two categories; aerostatic and aerodynamic. The latter depend on the relative motion of the bearing surfaces to locally increase the pressure through aerodynamic lift in the bearing gap, in order to separate the surfaces and provide a gas lubricating film. The former utilises an external power source to compress the gas that provides the lift in the gap. These are not exclusive sets, as aerostatic bearings may also have profiles machined into the surface that aim to provide aerodynamic effects, creating hybrid bearings with the goal of improving the bearing performance.

Air bearings posses several advantages that make them particularly attractive to designers of precision and high-speed systems. As the demand for increasing accuracy in both manufacture and measurement continues, externally pressurised bearings offer the following advantages:

- Zero starting friction and very low running friction due to the low viscosity of air
- Absence of wear as the bearing is of a non-contacting nature
- Minimum heat generation regardless of speed of operation
- The surface averaging effect resulting from their non contact nature can help reduce the need for high precision in their manufacture and, also for thrust bearings, compensates for small errors in the flatness of the counterface upon which they act
- As the viscosity of air alters only slightly with temperature, their performance is only marginally affected by changes in the ambient environment

- In a well designed and manufactured system they offer freedom from vibration that can occur in conventional rolling element bearings
- Due to the low viscosity of air, it is possible to run at very high speeds
- They lend themselves ideally to applications where cleanliness is vital, due to the lack of contamination from the lubricant

These advantages have led to the use of air bearings in applications as diverse as from high speed drilling spindles to co-ordinate measuring machines, and from gyroscopes to high precision diamond turning and grinding machines [1, 2, 3, 4]. Their properties cannot be overstated, the precision now available and advances that have occurred due to their availability impact greatly upon everyday life.

However, air bearings do posses certain limitations. Examples of this are due to their relatively low stiffness and load carrying capacity. In addition, due to the operating fluid being a compressible gas, it is possible for them to experience a self-exciting vibration called air hammer, which can be sufficiently damaging as to destroy the bearing.

It is with these limitations in mind that the concept of porous bearings was conceived. Many of the limitations of conventional air bearings could be overcome, or sufficiently improved upon, by the utilisation of a porous pad instead of the discreet orifices which supply the compressed gas that the traditional air bearings require. As the gas is now supplied more evenly across the surface of the bearing, the load carrying capacity, stiffness, and stability all benefit. This concept also brought in new problems, mainly how to overcome manufacturing problems and produce consistent bearings.

It is due to these advantages described above, and a desire to overcome the current operational limitations, that this research is aimed. The specific aim of this research programme is to establish manufacturing routes that will enable

the consistent production of porous ceramic bearings that exhibit uniform performance. The performance and potential of these bearings will be highlighted by comparisons with published theories on bearing performance, complimented by a series of physical tests.

1.2.1 Aims of Present Work

Porous bearings have been successfully demonstrated in many applications and the previous work in the field of porous ceramic bearings has shown significant advantages in performance through the correct selection of materials and processing conditions [5]. However, in common with its more conventional porous cousins, it fails in one important respect, that of simplicity of construction.

Owing to the complicated nature of the manufacturing process required for the two layered porous ceramic air bearing, it was considered necessary to investigate simpler, more reliable, and more cost effective, routes of fabrication. Slip casting, injection moulding, and a hybrid two-layer technique were identified as potential candidates. A test programme was devised that involved the production of test bearings by each of these methods. Their mechanical, fluid flow and bearing performance properties were quantified and compared to published performance theories and data.

To this end, the main objectives of this current research programme are:

- Produce porous ceramic bearings by slip casting, injection moulding, and two layer techniques consisting of a variety of powder sizes.

- Determine fluid flow characteristics, particularly the permeability of different bearings produced by different routes.

- Evaluate bearing performance in terms of load carrying capacity and stiffness

- Compare the performance of the bearings manufactured by the different routes
- Determine the optimum processing route and conditions for bearing performance.

- Compare actual bearing performance with published bearing performance theory.

As this work follows from the foundations laid by previous research at Cranfield University (reference 5), a brief resume of this work is included in Appendix H.

2 Historical Development of Bearing Systems

Bearings have been around as long as man has had the need to transport items that were otherwise difficult to move by hand. Starting from the earliest recorded civilisations, great loads have been successfully moved, often hundreds of miles from their points of origin, to their final resting-place. A classic example within the UK is Stonehenge, an ancient structure comprising great stone monoliths, whose sarsens weigh up to 26 tons. Originally quarried from the Prescelly Mountains in Pembrokeshire in approximately 2500-2600BC, they were laid to rest in Salisbury Plain some 100 miles away. The pyramids in Egypt and various countries in South America are others, with stone blocks used to form massive tombs and temples, again often carried some distance to be used.

Typically the early bearing system for moving these loads consisted of a simple roller arrangement; large smooth logs were placed under the load allowing relatively easy movement of the blocks. This system, although useful, was basically flawed. As the load moved forwards, it did so faster than the rollers, necessitating their removal from behind the load and subsequent placing at the front again. From this the next stage was to attach the roller to the object to be moved by constructing a solid axle from the roller and mounting a table over the top, simplifying the movement. However, this type of arrangement tends to suffer from erratic movement over rough ground and a change to large diameter rollers at the ends of a separate axle likely followed. Finally, wheels fixed to a stationary axle were developed; a method that has proved so successful that it is still used widely today [6].

The earliest recording of large diameter discs fitted to an axle is attributed to the Egyptian Fifth Dynasty, approximately 3000 B. C., upon which a scaling ladder was mounted. Reference is also made to chariot wheels in the Old Testament, when the Israelites crossed the Red Sea, and remains of such wheels were

uncovered when the tomb of Tutankhamen was excavated in 1922. Further development of bearing systems and their applications are recorded into the start of the first millennium from various sources around the eastern Mediterranean countries. The trail then goes cold until the Middle Ages when Leonardo da Vinci turned his attention to a study of rolling friction [6]

The first publication on rolling friction was by the French physicist, Coulomb. Although better known for his work in the field of electricity, he never the less found time to enunciate a series of laws relating to the friction of dry surfaces moving relative to each other at low speeds and pressures [7]. His laws were universally accepted and built upon by many researchers, including Reynolds, and several others in the then new and emerging field of railway wheels [8, 9, 10]. It was not until the work by Dupuit that errors in his postulations were noticed, but at first disbelieved [11]. It was only when Dupuit repeated his findings on his detractors' equipment that he was finally taken seriously. A comprehensive set of rolling friction reviews can be found by Hersey *et al* [12, 13, 14, 15]. Since that time development of bearing systems has increased exponentially, not only in their type, material choice, complexity, but also the number of applications.

2.1 Materials

From the earliest days it has been apparent that some materials were preferable to others for bearing applications. At first the development was limited by the availability of different types of materials, and for a long time after, by the understanding of the material properties.

Initially, use was made of what was available locally, with wood being almost universally available. This led to the development of various rollers and wheel systems, as mentioned previously, and it was some time before the use of different materials and improved designs appeared.

After wooden rollers, stone seems to have been the next development. Vitruvius Pollio in circa 100 B. C. wrote of the use of cylindrical stone blocks with iron pins fitted to their ends, held in a wooden frame with bearings for the pins, being used to transport the large pillars that form part of the temple of Artemis. The first recorded use of a thrust bearing utilising spherical bearings dates from circa A. D. 12-41, when a system was developed that used bronze balls rotating in a track between two wooden plates, likely for the display of ornamental statues. The use of cast iron was not recorded until 1520, when it is thought that cast iron balls were placed under large artillery pieces to facilitate their ease of movement. In Gibraltar troughs were laid on each side of the road into which cannon balls were placed, allowing large pieces of ordnance to be moved [6].

During use, the surface of a rolling element bearing is subjected to stresses of great intensity, causing compression, tension, flexure, sliding and local heating. In order to allow the bearing industry to develop, improved materials with more desirable mechanical properties were developed. A big step forward occurred in the early years of the 1900's, with the advent of case hardened steels.

Case hardening steels are hypoeutectiod with a structure comprising of small areas of pearlite and large ferrite crystals. Due to their carbon deficiency, they are not capable of being hardened directly, and require carburisation during heating to allow the formation of a eutectiod or hypereutectiod zone. This is achieved by heating in close proximity to a carbonaceous material; carbon is absorbed into the surface of the steel, and a hard and wear resistant eutectiod or hypereutectiod region is formed.

However, this process is difficult to control accurately, and has many pitfalls. Firstly, slag inclusions are not confined to the core, and the bond between the slag inclusions and the hardened skin is usually weak, allowing it to be

relatively easily removed. The resulting hole soon grows as the edges of the hole weaken and crumble, leading to the destruction of the bearing.

The main parameters controlling the carburisation process are the nature and condition of the carburising material, the temperature and chemical composition of the steel, as well as the time spent at temperature. Also, the carburising material can contain impurities that form agglomerates on the surface of the steel, thus locally preventing the absorption of carbon and causing soft spots. Depending on the conditions used to form the case hardened structure, a sudden change in microstructure between the hypoeutectic skin and the eutectic core leads to a plane of weakness. Finally, excess carbon causes cementite to form preferentially along the grain boundaries, leading to crack nucleation sites. As can be seen, case hardening steels are somewhat of a capricious material. In order to overcome these disadvantages, various chrome steels have been developed. These contain about 1.0% carbon and around 1.5% chromium, and can be heat-treated directly. With the use of high quality ingredients and good process control these steels proved extremely useful.

However, these steels are still vulnerable to the effects of corrosion from moisture and other corrosive environments. Initially hard bronze was used, but with a hardness no higher than 200 Brinell the bearings were required to be excessively large to cope with the loads. Bearing manufacturers turned their attention to stainless steels, and despite initial disappointment in their performance, after considerable development they are now readily available in such grades as AISI 440C [6, 16, 17, 18]. There now exist a great number of different types of rolling element bearings along with a concurrent amount of applications.

2.2 Introduction to Fluid Film Bearings

The fundamentals of fluid film bearings can be traced to three men who within a few years of each other, discovered and formulated the mechanism of hydrodynamic lubrication and laid its foundation as a branch of engineering science.

These were the Russian Petrov, and two Britons, Tower and Reynolds. These three men perceived the process of lubrication as being due not to the mechanical interaction between the bearing surfaces, but to the dynamics of the film separating them. This fundamental aspect of hydrodynamic lubrication led to the establishment of theoretical and experimental foundations within three brief years.

Petrov postulated two important concepts with regard to hydrodynamic lubrication. Firstly, that the viscosity of the fluid is the important property when determining friction, and not density, and secondly, that friction in a bearing is the result of shearing of the fluid, and not the interaction of the two surfaces [19].

2.3 Hydrostatic Bearings

The potential of new developments in bearing technology have not always been immediately recognised. The work on hydrostatic lubrication by Beauchamp Tower in 1885 that led to the fundamental work on the subject by Osborne Reynolds the following year was met with some derision from certain quarters, as the following extract from *The Engineer* illustrates.

"I anticipated that Mr. Towers researches would have had some practical value; but as far as I can see they might just as well never been undertaken.

action is converted to heat. This heating of the working fluid is the major limitation to the application of oil hydrostatic bearings.

This heat source has several unfortunate consequences, the heating causes thermal expansion of the machine, the energy that goes into heating the oil is wasted, and finally the excess heat in the oil then requires removal.

Thermal growth effects the accuracy of the machine, the heat from the shearing action taking place in the oil as it passes through the bearing, is conducted through the structure, causing it to distort. For very high and ultra precision applications these distortions can lead to appreciable errors on the work piece, which require complicated control and measurement techniques to overcome.

In addition, this heat energy represents a loss in the system in terms of energy, as it performs no useful work. Larger pumps are then required to provide enough energy so that when these losses are taken into account there is still sufficient energy to power the machine effectively. These larger pumps in turn require more energy to operate, thus making the operation of the machine more expensive, as well as adding to the capital required to purchase the machine initially. If the heating effect is sufficiently large, chillers must be added into the system to cool the oil before it is pumped around again. Once again the energy requirements and capital outlay of the machine increase.

The faster that the bearing has to operate, the greater this heating effect as the faster the oil is sheared. It can be seen therefore, that there exists a limit beyond which oil hydrostatic bearings cannot realistically be used.

2.4 Water Hydrostatic Bearings

One potential solution to the limitations imposed by the use of oil as the working medium is to switch to water. Water, like oil, can be considered

incompressible under normal working pressures and temperatures, but because it possesses a much lower viscosity than that of a typical hydraulic oil, it produces much less heat when sheared through a hydrostatic bearing. Another major advantage is that it also possesses a greater specific heat capacity, which means that it requires a greater amount of heat energy to raise the temperature relative to that of oil. Thus it is simple to see that a system capable of greater speeds with lower energy requirements should be possible. Another positive aspect is that water is environmentally much safer than oil in the event of leakage, a seeming inevitability with hydraulic machinery. These advantages have led to much research work into the use of water as a working fluid. Work at Cranfield University has demonstrated the application of water in grinding machines, and much progress has been made in the characterisation of porous ceramic bearing systems utilising water as the working fluid [22].

A series of experimental journal bearings of 50mm internal diameter by 50mm long have been investigated for use in high-speed precision grinding machines for automotive applications. A highly instrumented test rig was specifically developed for their investigation and the research resulted in a bearing with greater stiffness, higher operating speed, and lower energy consumption than a conventional oil hydrostatic bearing. The optimum processing conditions were established for the correct permeability using a capsule free HIP method, which was also demonstrated as being consistent.

2.5 Air Bearings

As mentioned in section 1.1, air bearings fall into two broad categories, aerostatic and aerodynamic. The fundamental difference between these two types of gas bearings is due to the nature of the pressurised gas in the bearing gap. Aerodynamic bearings utilise lift generated from their relative motion over a counterface, and for this reason they are also known as self-acting bearings. The pressure is generated by viscous shearing of the lubricant as gas is dragged

into the bearing gap between converging faces. The aerostatic bearings use pressurised gas supplied from an external source, such as from a compressor. It is fed to the bearing gap via a fine hole, or series of holes in the bearing face, and lift is produced from the resulting pressure in the gap acting on the bearing face. In addition, there have been attempts to marry the advantages of these two types in the creation of hybrid bearings. A smaller third set is also worth mentioning for completeness, that of squeeze film bearings. These operate by vibratory oscillations of either the bearing face or the counterface, caused for example by piezo-electric devices. The resulting pressure variations in the gap cause lift to be generated.

Thus it can be seen that air bearings posses several desirable properties that make them suited to applications where high-speed operation or high precision are requirements.

The principles of operation of an aerostatic bearing can be explained with the aid of figure 1.

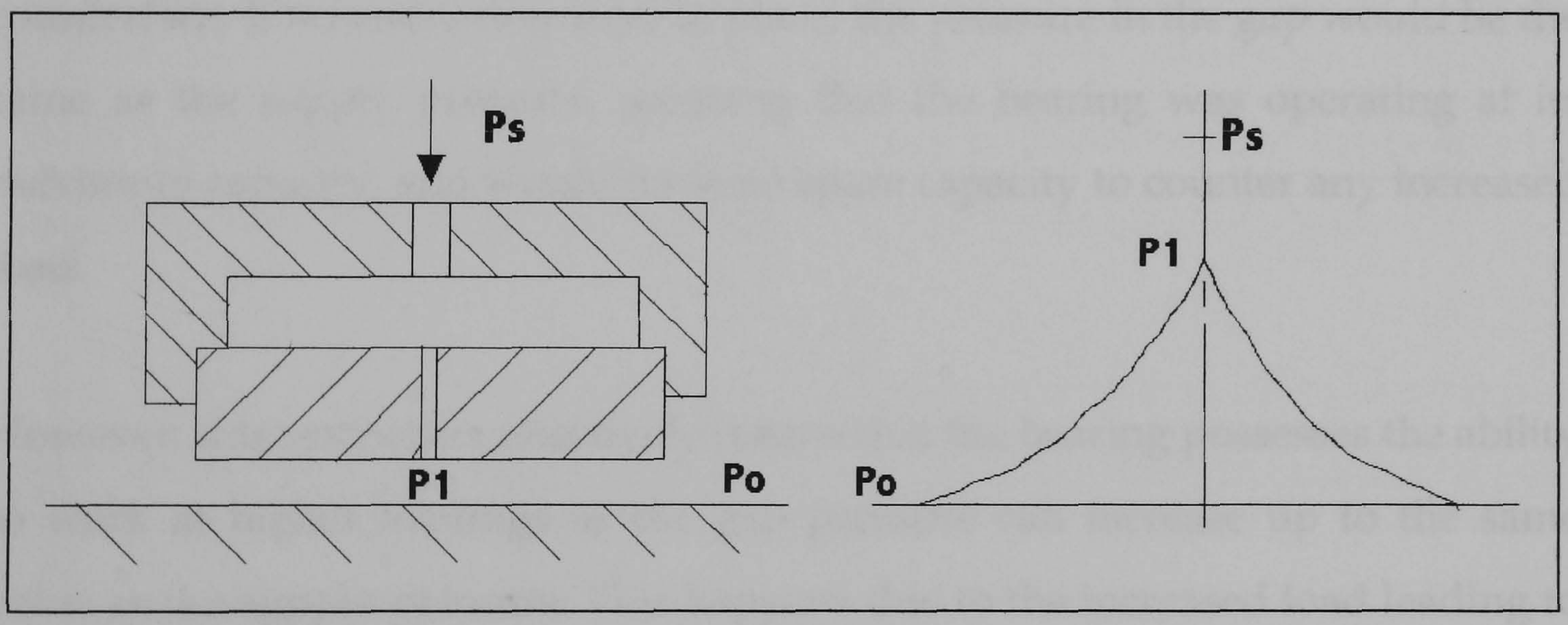

Figure 1 Principles of aerostatic air bearing operation.

Figure 1 above illustrates the principle components of a circular conventional aerostatic bearing with a central supply orifice. The main parts are; the bearing itself, which provides the final path through which the gas must pass in order to enter the bearing gap, and also the face that the resultant force acts on to

provide thrust, and the bearing holder which serves two functions. Firstly, it serves to seal the bearing in a gas tight surround so that the pressurised supply gas must pass through the bearing, and secondly it provides the mechanical linkage to the machine to which the bearing is attached.

The corresponding pressure distribution under the bearing is also illustrated. Here we see that gas is supplied at a pressure P_s, and is reduced to pressure P1 directly under the orifice in the bearing face. This pressure trails off towards the edge of the bearing to atmospheric pressure Po. It is the net result of this pressure acting on the bearing face area that produces the lifting force.

As can be seen from the above simple illustration, the pressure in the bearing gap below the central feed hole is lower than the gas supply pressure. This is due to a restriction being placed in the gas path to restrict the flow of gas through the bearing. This simple technique allows the bearing to respond to external loads without touching the bearing counterface surface. Should the load on the bearing be increased, the bearing would tend to sink towards the counterface. If no restriction were in place, the pressure in the gap would be the same as the supply pressure, meaning that the bearing was operating at its maximum capacity, and would have no spare capacity to counter any increased load.

However, this restriction effectively means that the bearing possesses the ability to work at higher loadings as the gap pressure can increase up to the same value as the supply pressure. This happens due to the increased load leading to a reduction in the bearing gap, which in turn makes it more difficult for the gas to escape through the bearing and out of the bearing gap. This reduces the flow rate, and hence increases the pressure.

Compensation describes the technique the bearing uses to regulate the flow of gas between the pressurised air supply and the film under the bearing. There

are four basic types of compensation, orifice, capillary, porous plug, and inherently compensated bearings. These are illustrated in figure 2 below.

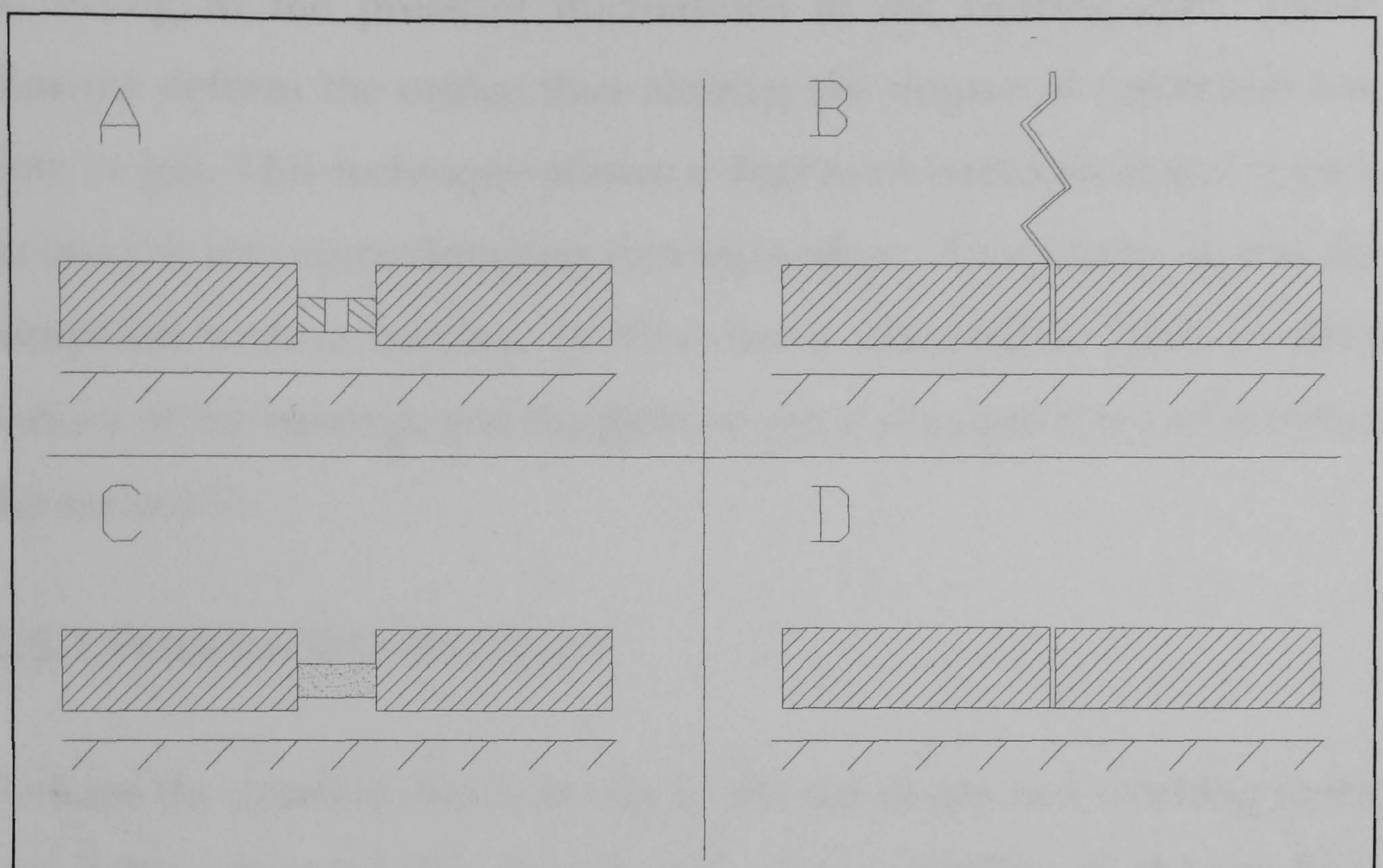

Figure 2. Different types of compensation, A) orifice, B) capillary, C) porous plug, D) inherent

The first three types of compensation infer that the restriction is placed between the bearing and the gas supply source. Inherently compensated bearings restrict the flow of gas at the surface of the bearing, and have the advantage of being, in general terms, the most stable of the four types [23]. However, the load carrying capacity of these bearings are below that available from other designs.

The stability of capillary compensated bearings is the lowest of the four types, while porous plug and orifice bearings tend to be somewhere in between [23].

Pocketed compensation can give greater stiffness than inherently compensated bearings, by a factor of up to 1.5. However, the process of inserting the restrictor into the bearing can distort the size and shape of the orifice, leading to inconsistent performance from nominally identical bearings [24]. This increase in stiffness can be attributed to the fact that the throat area is independent of the local bearing gap [25].

A further development in compensation is the use of a compliant orifice. In this case the orifice itself is made from a flexible material which changes shape according to the pressure fluctuations in the bearing film. These pressure changes deform the orifice thus altering the degree of restriction and thus the flow of gas. This technique allows a degree of feedback in the system, and can be used to introduce damping into the system. A variation on this theme is the compliant surface bearing. In this case a deformable layer is placed on the surface of the bearing, and the flow of gas is changed due to the deformation of the surface [23].

2.5.1 Problems with Instability

Perhaps the greatest disadvantage in the use of gas as a working lubricant is the possibility of instability due to the compressibility of the medium. Careful design of the bearing system is required, along with a good knowledge of the working conditions that the bearing must endure, to take into account the normal loading and any transient conditions that would otherwise lead to failure of the bearing.

When a change occurs in the bearing gap, such as when the load carried by the bearing is altered, gas must either enter the gap or leave from it in order to maintain equilibrium. As the bearing gap has an appreciable volume, this process takes a finite amount of time, and lags behind the load. Depending on the nature of the load change, frequency, magnitude, etc., this lag can set up a self-exciting oscillation that can cause the bearing to strike the counterface if allowed to continue unchecked.

Although designed for non-contact operation, it is conceivable that under certain extreme conditions, touchdown may occur. In this case, and in the case of stop/start operation with aerodynamic bearings, a degree of wear resistance is useful. Research into improving the sliding wear resistance of alumina includes such techniques as heat-treatment, neutron irradiation, gold plating,

and coating the surface of the alumina by a chemical vapour deposition technique, as well as machining techniques.

Rowe [26] made a comprehensive investigation into these parameters, and the effect of the sliding wear resistance of alumina against both ruby and sapphire counterfaces. He concluded that neutron irradiation at $5x10^{17}$ nvt and vapour deposition of aluminium oxide onto the surface of the alumina both served to increase the wear resistance under a range of loads and sliding times. Further, it was revealed that many factors simultaneously effect the wear properties of the alumina, and it is control of all of the properties of the material, porosity, grain size, hardness, and the machining techniques, that contribute to the behaviour of the bearing with regard to attritive wear. Further work on contact between journal bearings and shafts at high speed has shown alumina to be beneficial to wear resistance [27]. It seems therefore that the designer must take into account not only the operating conditions, but also the processing of the materials, if the bearing is to be successful.

2.5.2 Types of Air Bearings

In common with the wide variety of hydrostatic bearings mentioned earlier, there exists a number of diverse types and applications of air bearings. A selection are shown in figure 3.

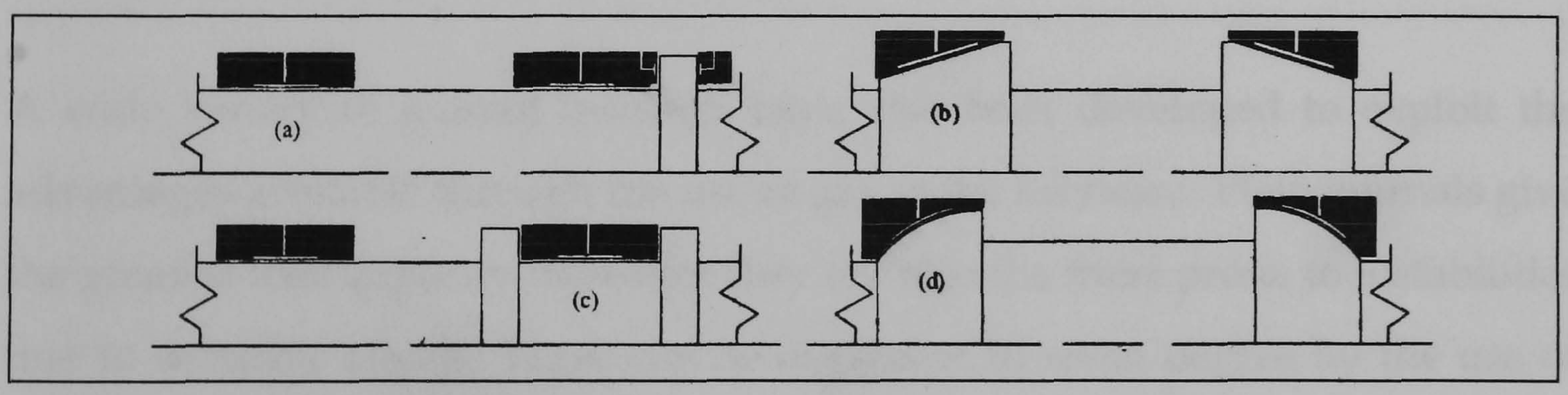

Figure 3 General types of air bearings, A) cylindrical journals with annular thrust bearings, B) conical journal bearings, C) Yates bearing, D) hemispherical journals (from [28])

The simplest is the thrust bearing. This type provides thrust solely, and can be externally pressurised, self-acting, or hybrid of the two and they are normally of circular or rectangular plan, see figure 4. In the case of external pressurisation, gas is fed to the surface via holes through the bearing. The simplest bearing has a single feed hole in the centre of the bearing, though bearings with multiple air entrances, slots, and grooves are common. Care must be taken when including features such as slots and pockets to ensure that the volume of these does not exceed 1/40th of the volume of the bearing gap to ensure stable vibration free performance.

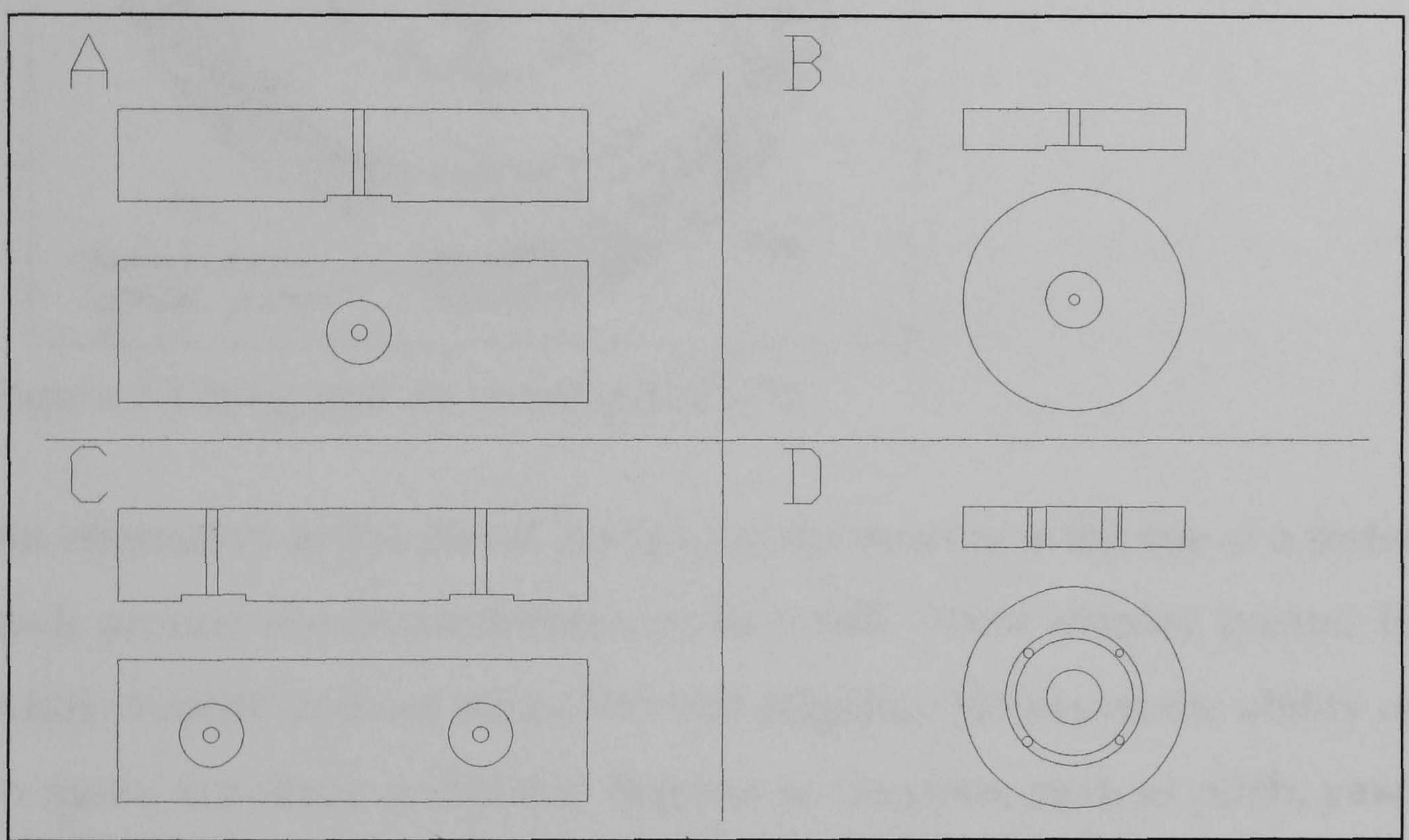

Figure 4. Types of thrust bearings, A) rectangular with single feed hole, B) circular with single feed hole, C) rectangular with multiple feed holes, D) circular with multiple feed holes and grooves

A wide variety of journal bearings have also been developed to exploit the advantages available through the use of gas as the lubricant. Plain journals give the greatest load capacity, however they are also the most prone to instabilities due to dynamic effects. These can be overcome to some degree by the use of modifications to the surface, either of the bearing or the shaft. Axial grooves were first investigated to provide a sink for pressure accumulation during rotation which leads to self-exited whirl. These increase the film damping effects of the gas leading to increased stability, and in addition act as a location

for any deposit of debris that otherwise could built up and clog the bearing film.

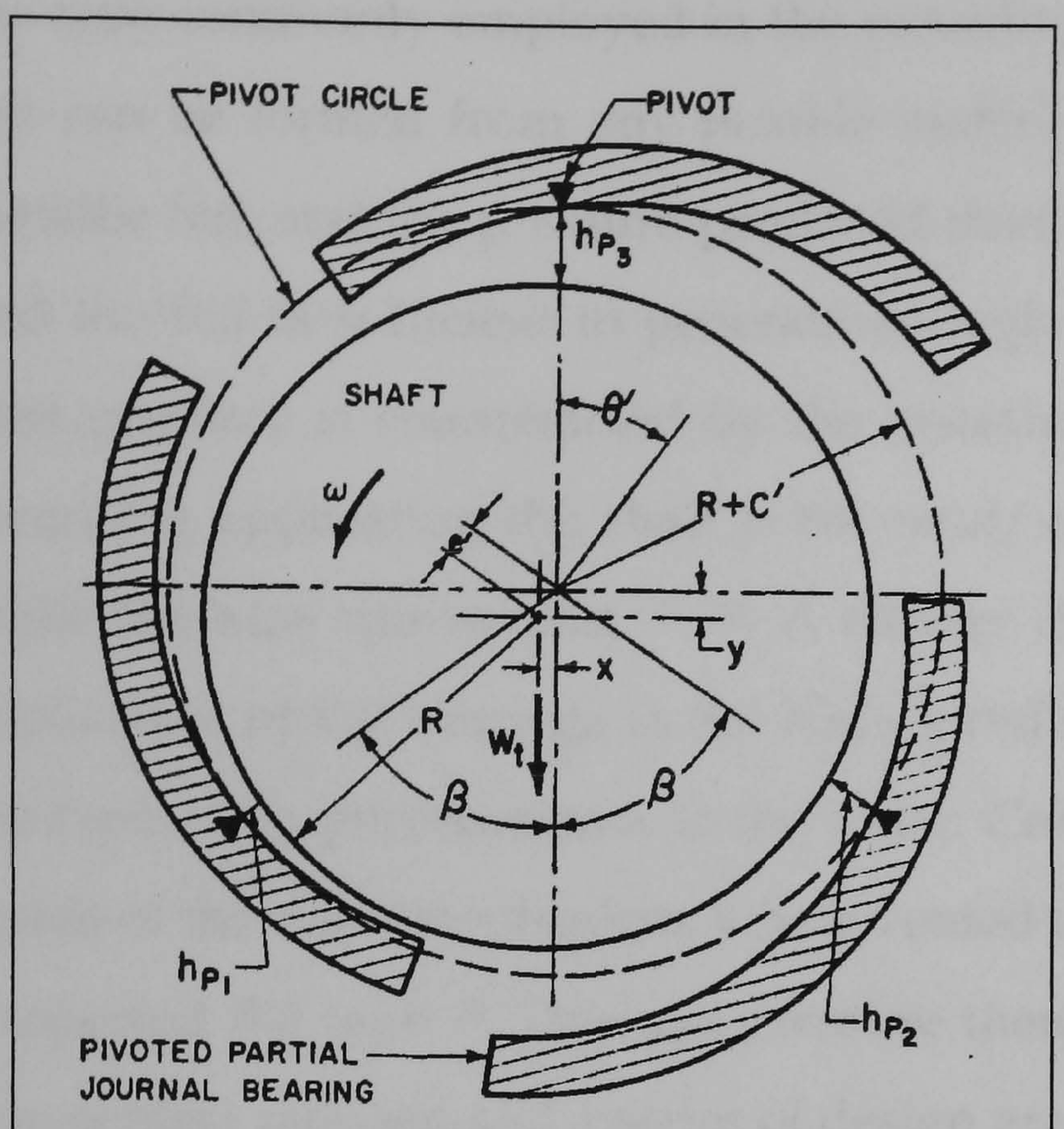

Figure 5 Tilting pad air bearing (from [29])

An alternative to the use of a solid journal bearing is the use of a series of tilting pads around the circumference of the shaft. These display greater high speed whirl stability and are inherently self-aligning. However, the ability of the pads to move introduce additional degrees of freedom, such as pitch, yaw, and roll, which complicate the analysis and design of the bearing system. Nevertheless, a great number of high speed bearing were developed for a variety of applications from cryogenic pumps to high temperature gas circulators in nuclear plants [29]

Hybrid bearings combine the advantages found in externally pressurised and self-acting bearings. These bearings are externally pressurised, but also benefit from aerodynamic effects during rotation that arise from careful design of aerodynamic features either on the shaft or the bearing. These bearings posses the ability to stop without touchdown, as well as improved stability during high-speed operation [23].

Foil bearings are another alternative journal type. These are, as the name suggests, formed by the use of a strip of foil upon which the shaft bears. This is the type commonly employed in the recording of magnetic media on tape. The foil can be formed from any flexible material, such as a plastic strip or thin metallic foil, and the pressure produced during the relative motion of the shaft and the foil is sufficient to generate enough lift to separate the two surfaces. This pressure is counteracted by the resulting tension in the foil. In the tape recording application the shaft is the read/write head, and is held stationary while the tape moves past [23, 29]. A further development of this idea was the application of foil bearings in the high-speed idlers that support the passage of the tape using porous media as the roller. Compressed gas was supplied to the inside of the roller mechanism, which vented through the walls of the roller and supported the tape [30]. This gas pressure then supported the passing tape in a non-contact manner, and a series of design graphs were produced.

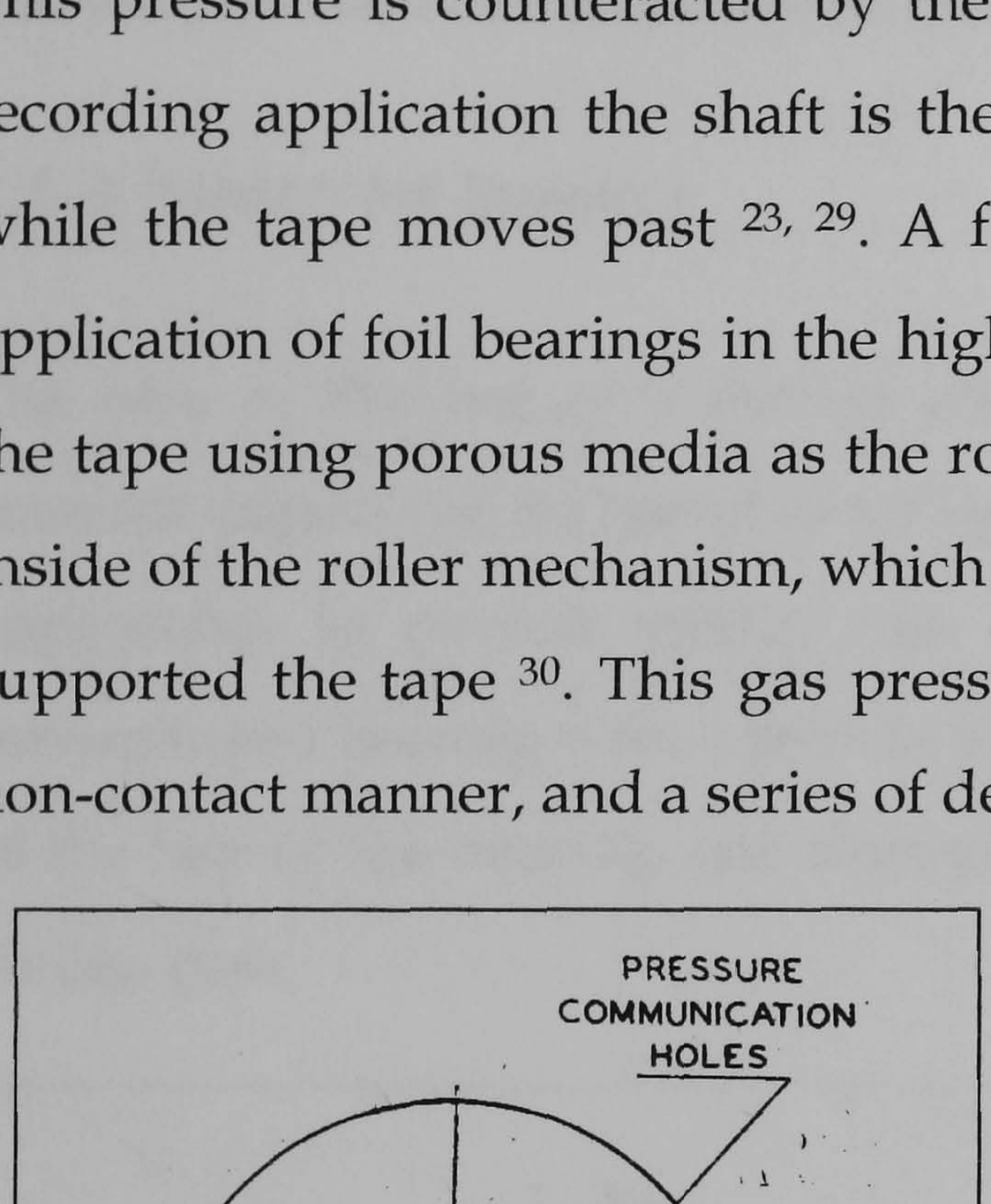

Figure 6 Flexible membrane air bearing (from [31])

Other concepts have also been considered, For example the use of a flexible membrane underneath the bearing pad of aerostatic thrust bearing was investigated by Levy *et al*, as illustrated in figure 6 [31]. Essentially the principle of operation is as follows; air is supplied to the bearing through a central orifice,

and inflates the membrane by means of four pressure communication holes in the underside of the skirt. As the pressure under the bearing increases, lift is created and the bearing rises to an equilibrium position. Air escapes under the membrane in the gap between the skirt and the reaction surface. This leads to a bearing that possesses good load carrying capacity, and an ability to operate over undulating surfaces. This reduces the need for precision in its manufacture and the precision of the counterface, leading to a reduction in cost.

2.5.3 Porous Air Bearings

The idea of the use of a porous medium to provide restriction is not new, research papers can be found as far back as the mid 1960's [32, 33, 34]. There are two approaches to porous media, one is to simply replace the restrictor in a conventional bearing with a porous plug, the second to use the porous material as the face of the bearing, and thus greatly increase the area through which the air can pass.

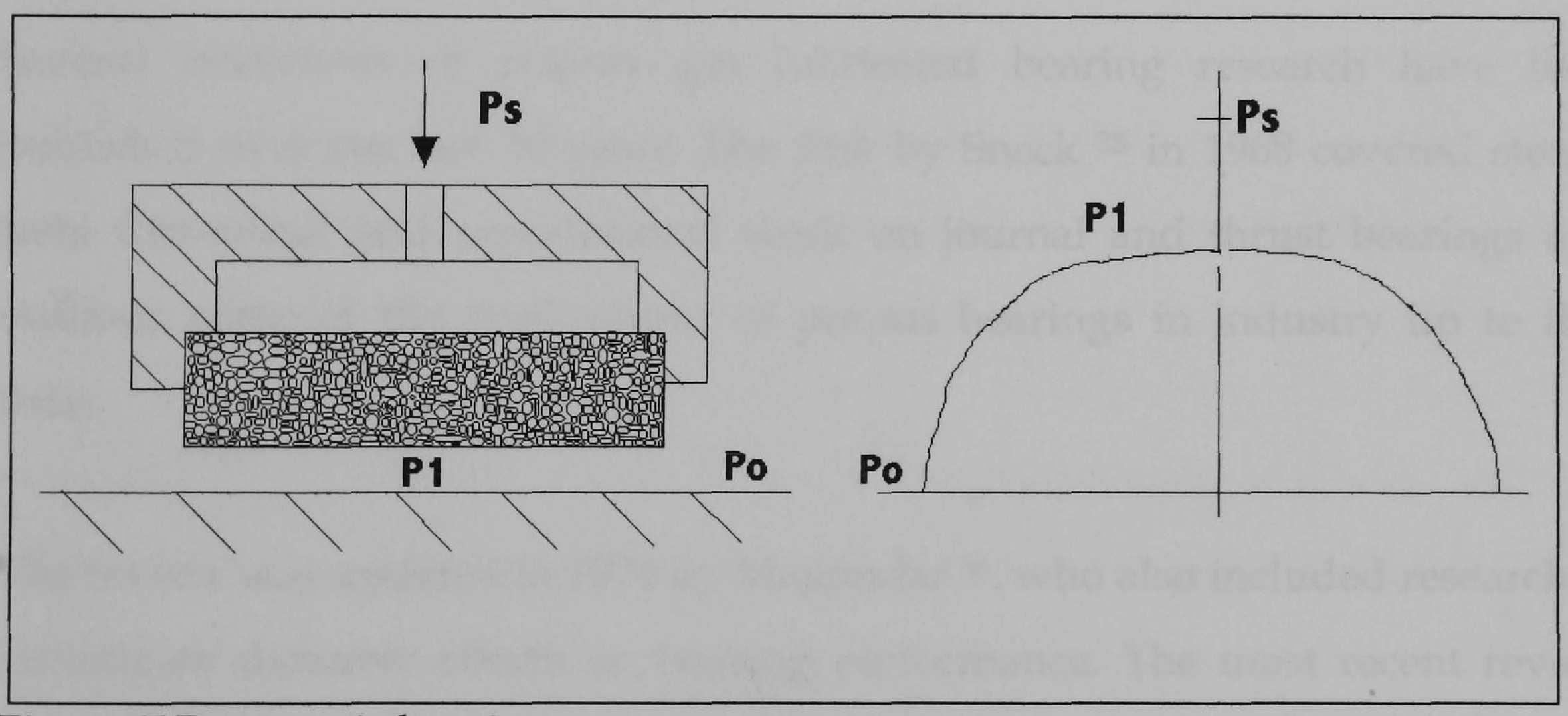

Figure 7 Porous air bearing

As the former type is basically a modification of the conventional aerostatic bearing described previously, no further mention will be made of it here. The latter, however, warrants further attention. This type promises several important advantages over the conventional, and the successful production has been a quest that many researchers have attempted over the years. This is the type illustrated in figure 7. This is basically the same as seen in figure 1

previously, although now the supply gas is able to enter the gap across the entire face of the bearing. This modifies the pressure profile to be more like a parabola.

The main reasons for the development of a porous bearing can be summarised as follows:

- Simplicity of construction
- Improved load capacity and stiffness
- Superior damping and dynamic characteristics
- Improved stability

However, the translation of these aims into reality has proved to be a goal that has so far proved difficult to researchers and manufacturers alike, as will be outlined in the following sections.

Several overviews of porous gas lubricated bearing research have been published over the last 30 years. The first by Sneck [35] in 1968 covered steady state theoretical and experimental work on journal and thrust bearings and outlined some of the applications of porous bearings in industry up to that time.

The review was updated in 1974 by Majumdar [36], who also included research to investigate dynamic effects on bearing performance. The most recent review was completed by Kwan in 1998 [37]. This review brought the subject up to date and incorporated references to several studies on non-Darcian flow through porous media.

2.5.4 Porosity and Permeability

The structure of a porous material is by definition, not fully dense. However, it is necessary to differentiate between open and closed porosity. It is possible that

a body of a material not be fully dense but still be impermeable to the passage of a fluid. This is due to closed porosity, which is porosity that is not fully interconnected, and so is unable to provide passage for the fluid. Porosity of this kind is of no use in a porous bearing, and successful manufacture must seek to limit this type of structure.

Conversely, open porosity is fully interconnected through the body of a porous medium. It is often idealised as being formed by continuous channels or capillaries through the material having a constant cross section and cylindrical symmetry, and capable of letting fluid pass through.

Holdsworth classifies a further three types of porosity: loop channels, which do not contribute to the steady state flow properties, semi-open or blind pores, which have the same limitation as for loop channels, and pocket or ink bottle pores where the entrance is narrow and leads to a larger closed pore [38].

Porosity is then defined as the ratio of pore or void volume to the bulk volume of the consolidated material. No account is taken of the type of porosity in this figure, as all types are included in its calculation, and it is therefore a unique measure of the porous material.

Several different techniques exist to determine the porosity of a body, and the final value may well include more than one measurement technique. The simplest is to measure the geometry and to weigh the sample. Then, dividing the mass by the volume to determine the density, a comparison may be made with the value for a fully dense body.

The porous structure that is open to the outer surface is measurable by fluid density measurements, the total pore volume from crystallographic data from X-ray measurements, and the bulk pore volume by liquid displacement techniques. For fine pored open materials, the use of gaseous pikanometry may

be useful. The adsorption of helium is commonly used in the determination of porosity with a very high degree of accuracy, but its use requires some skill in order to achieve a high level of reproducibility.

Mercury is a commonly used liquid for pikanometry applications. It is applicable for a wide range of pore sizes, though does suffer two drawbacks, hysteresis and incomplete removal from the test sample after investigation.

The material may also be cross-sectioned and analysed via microscopy. Any resulting micrographs may be used in conjunction with an image analysis system to obtain data on the porosity of the sample, as well as other data on the pore geometry, and distribution.

It is seldom the case that all of the pores in a body are of equal geometry, except in the most idealised of systems. Owing to the presence of the differing types of porosity, as mentioned above, along with the range of different pore sizes possible in a body, a real porous structure may contain a great number of different pore shapes and sizes. This variety in the size and shape of pores in a body gives rise for the need to classify the pore size distribution.

The pore size distribution is difficult to express with any degree of absoluteness, due to the value given depending solely on the model chosen to represent the system. Several different methods exist to obtain this distribution. The first, and most simple, is the bubble test method.

The porous material is impregnated with a fluid, and a slowly increasing ramp pressure is applied from one side. This continues until bubbling occurs on the low-pressure side, and the pressure at which this happens can be related to the diameter of the pore at which it occurs through the relationship

$$d_{pore\max} = \frac{4.\gamma}{P_1 + \rho_w . g . h_w} \qquad \text{Equation 1}$$

Where $d_{poremax}$ is the diameter of the largest through pore, which occurs at pressure P_1, and with a fluid of surface tension γ [39].

This method may also be extended slightly to give a qualitative assessment of the pore size distribution by continuing to increase the supply pressure. As the pressure is further increased, more and more pores are cleared of liquid, and a greater number of bubbling points can be seen. It can be observed by eye if a great number of pores bubble simultaneously, indicating a tight pore size distribution, or if a great pressure difference exists between the first and subsequent pores becoming cleared, indicating a wider pore size distribution [5].

The maximum surface pore size can also be calculated through the use of the above equation. If the supply pressure is slowly reduced following the extended bubble pore test described immediately above, we approach a point where there is now only one source of bubbling on the low-pressure side of the porous material. At the point where this collapses due to the surface tension, the maximum pore size may be calculated. This is usually larger than the through pore size, as determined by the bubble pore test. The pores within the sample, although they might be of smaller diameter, no longer have any effect as they are now largely cleared of water.

2.5.5 Graphite Air Bearings

The most successful and widespread application of porous air bearings is through the use of porous graphite. This material is easily machined and fairly cheap. It is also readily available to bearing manufacturers in a variety of different grades. Another important advantage is that in the event of an accidental touchdown during operation, no damage is observed as the graphite is worn away in the form of a lubricating carbon dust. However, the downside of this is that air-bearing production using porous graphite is highly labour intensive and any contamination due to carbon dusting is unacceptable in applications where clean room capabilities are required, such as in

semiconductor manufacture. An illustration of a graphite air bearing is shown in figure 8.

The greatest disadvantage with the use of porous graphite is that no two pieces of graphite are the same. This means that each bearing must be checked during manufacture, and where necessary, modifications made. The structure of each piece is unique, and may vary considerably from one place to another, which effects the flow properties of the gas, and hence the overall performance of the air bearing.

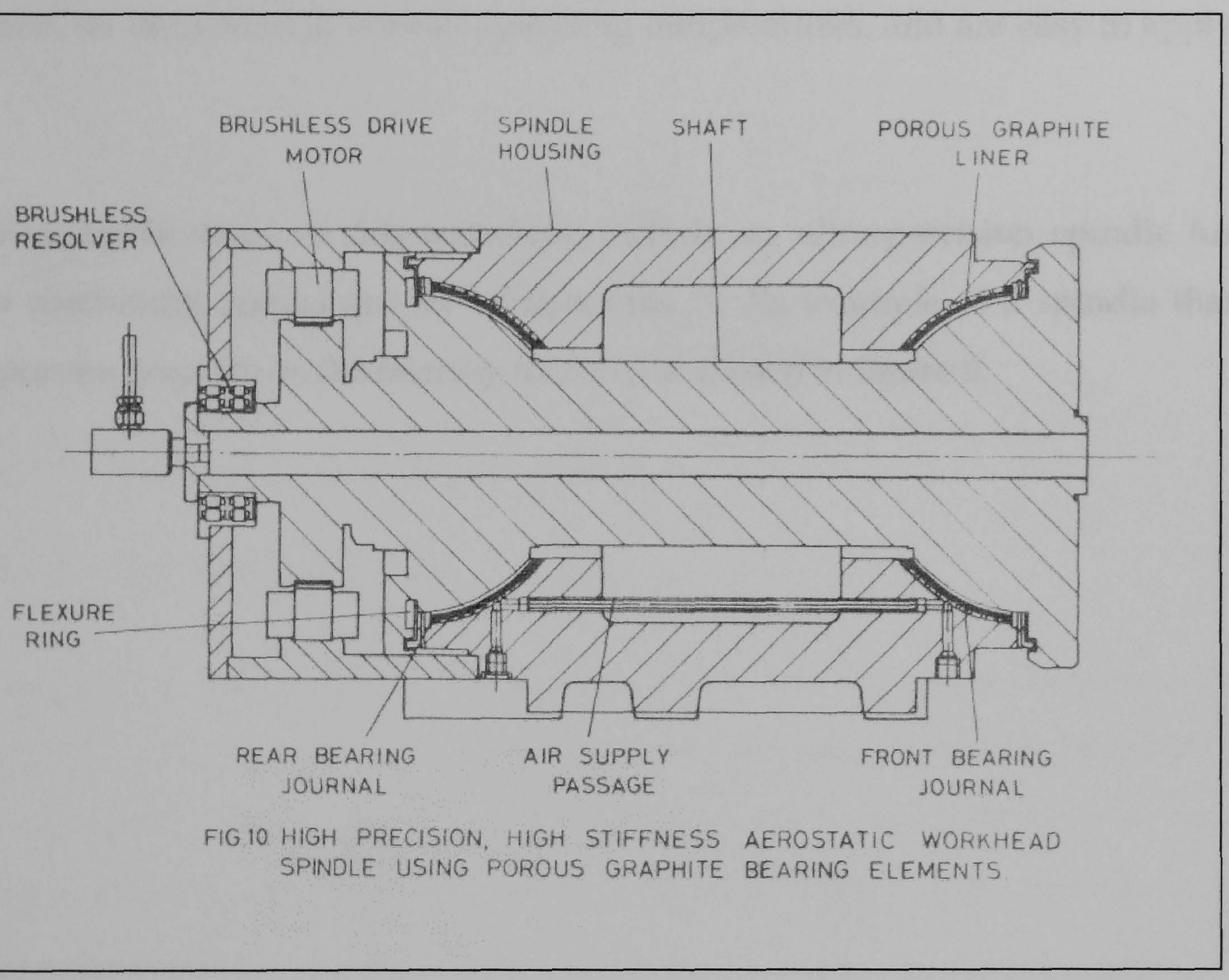

FIG.10 HIGH PRECISION, HIGH STIFFNESS AEROSTATIC WORKHEAD SPINDLE USING POROUS GRAPHITE BEARING ELEMENTS

Figure 8 Graphite bearing (from [40])

The procedure to ensure that the bearing is able to supply gas at an equal pressure across its entire working surface is somewhat of a time consuming process. The graphite is firstly machined and bonded to a backing substrate, usually steel, to provide a means of sealing the bearing so the supply air will have to pass through the bearing. The working surface of the bearing is then lapped to a conformable geometry relative to the surface upon which it will act.

The bearing is then pressurised and a pressure gauge placed on a small section on the working area of the bearing. It is then moved across the surface, and any differences noted. The ideal pressure drop through the graphite material needs to have been calculated previously, and the surface of the bearing modified accordingly. This is done by selectively blocking the pores of the surface, and thus restricting the flow of gas through the bearing where necessary.

Several soluble materials have been used for this application, such as shellac, or an acrylic lacquer dissolved in methylene chloride, as they bond well to the graphite, do not soften at normal operating temperatures, and are easy to apply [41].

Previous applications of this technique include an ultra-precision spindle for micro machining optical quality components [40]. An example of a spindle that uses porous graphite as the bearing material is shown in figure 9.

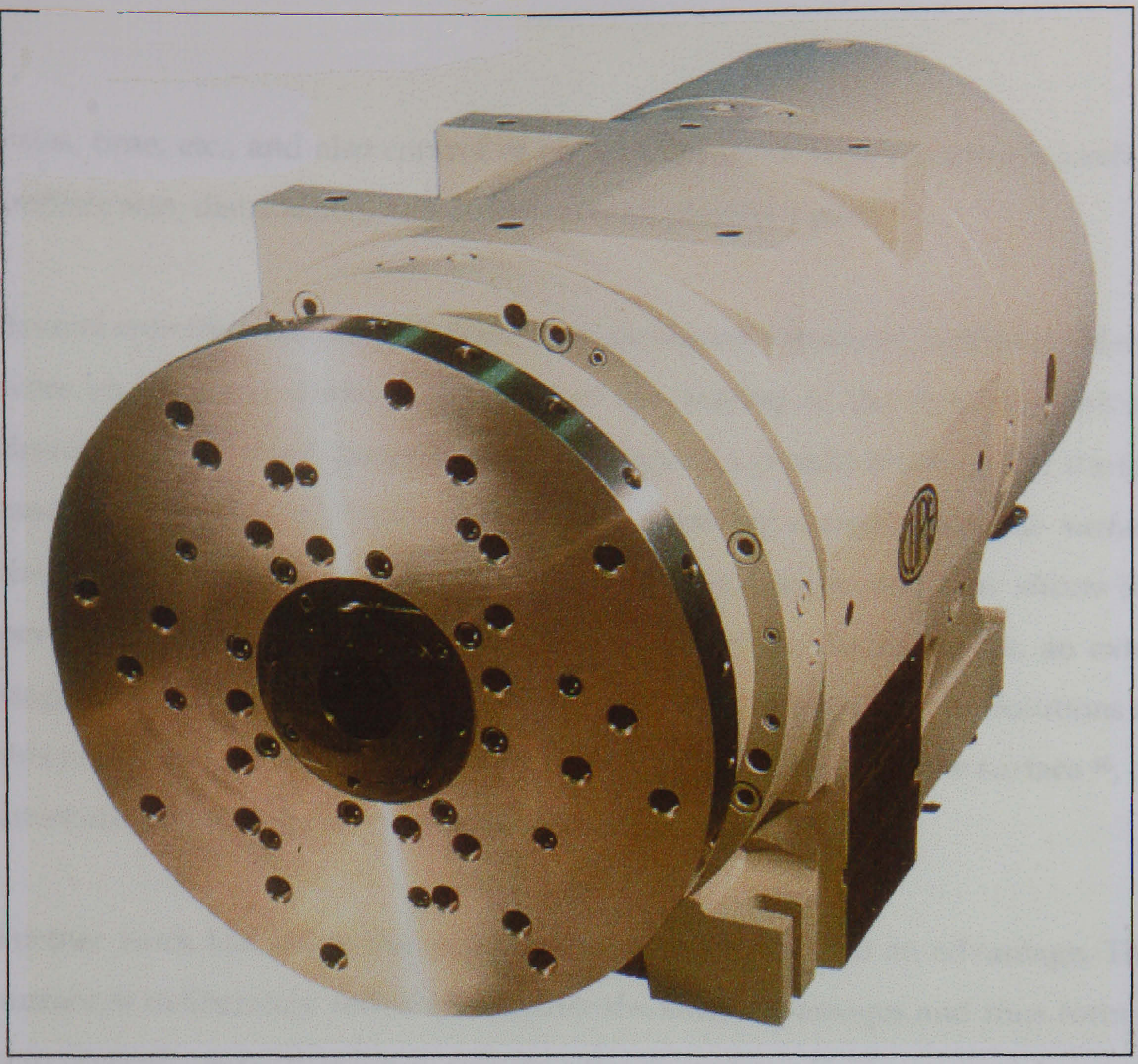

Figure 9 Example of a spindle using porous graphite bearings (from [42])

2.5.6 Sintered Bronze Bearings

This is another approach that has received much attention over the years, and in common with the graphite bearing described above, suffers from limitations. The idea behind its construction is to loosely sinter bronze powder to form a porous solid with sufficient mechanical strength to support the in service loads that it should see.

Although simple enough in concept, the route to a successful bearing via the sintered bronze path is somewhat flawed in practice. Firstly, there exists the problem of being able to reproduce the sintered structure of the bronze body. This requires careful control of sintering parameters such as temperature, ramp

rates, time, etc., and also control of the powder itself, with parameters such as particle size, distribution, and aspect ratio all playing a part. [43]

Several experimental bearings have been produced. However, further problems were encountered during machining of the bearing to the final dimensions. Bronze is quite a soft material that machines in a ductile manner, and during machining it tends to "smear" [44, 45]. This smearing compromises the surface finish of the bearing, tending to cover the exposed pores, and thus affects the permeability. As the permeability is no longer of the desired value, an extra stage must be included to open up the porous structure once again. Solutions to this problem have been put forward, including laser drilling of the surface [46], or alternatively etching the smeared surface away [23].

Further work has led to this smearing effect being used to an advantage. The surface is deliberately rolled to constrict the surface passages and thus form a thin pressure-restricting layer, reducing the flow of gas [47]. This approach can be useful in overcoming instability of the air bearing, as the surface void volume is reduced.

A major restriction in the use of bronze is due to its low stiffness. Under load and over time (particularly at elevated temperature), the material creeps quite readily, thus the geometrical tolerances are lost [48, 49].

Cusano and Phelen investigated porous bronze bearings using oil previously impregnated and replenished at 10psi [49]. Their findings showed that oil lubricated porous bearings run at higher eccentricity ratios than solid journal bearings. They also noted a considerable heating effect due to the shearing of the oil used to provide the lubrication. This heating effect increased with increasing load and speed, though it was found that the coefficient of friction dropped to a minimum with increasing load and speed, before rising again. The cause of the increase in friction was attributed to pore closure on the surface of

the porous bronze due to warpage, thus pointing to one of the main disadvantages in the use of a ductile material for porous bearing applications, that of plastic deformation under load.

Mori and Yabe have attempted to account for this phenomenon with an investigation into the use of a porous bronze journal bearing with surface loading effect [50]. They proposed a theoretical analysis to account for the surface loading, and undertook a series of experiments that gave good agreement with the predicted data.

Overall, it can be seen that there already exist several types of porous air bearing. What can also be seen is that they all suffer from various disadvantages, in particular it can be seen from the above that none of the existing bearings have successfully addressed what is perhaps the greatest potential advantage of all, that of simplicity of construction.

2.5.7 Porous Ceramic Bearings

Porous ceramic bearings potentially solve the shortcomings of other material systems for the fabrication of porous bearings. The main failings of the historically most popular materials, brass and graphite, have been outlined above. These were lack of reproducibility of permeability, difficulties in maintaining the measured permeability during bearing manufacture, and changes in bearing geometry over time.

Firstly, the permeability of porous ceramics can be controlled with a good degree of precision. Provided powders of a similar size and size distribution are packed and sintered in a reproducible manner, it is highly likely that the resulting material will be consistent with any other made by the same method.

Secondly, as ceramics are of a brittle nature, surface grinding does not smear the material over the remaining pores, but rather tends to remove the ceramic

as a fine dust. This means that the pores are not effected by the machining operation, and so permeability remains unaffected.

Finally, owing to the high stiffness and temperature stability of engineering ceramics, creep due to constant loading and/or elevated temperatures is not a factor.

These are the advantages that designers have sought to exploit through the use of ceramic as the porous material in porous gas bearings.

2.6 Theoretical Analysis

2.6.1 Flow Through Porous Media

The basis of flow through porous media lies with Darcy [51], and with very few exceptions [52, 53], forms the fundamental assumption of every published analysis. Many researchers have analysed fluid flow through porous materials subsequently, using a variety of different media materials and conditions [54, 55, 56, 57, 58, 59]. This states that in the case of incompressible flow, the volume flow rate is directly proportional to the pressure difference across a porous material.

$$Q = \Phi_v . \frac{A_p}{z_p . \eta} . \Delta P \qquad \text{Equation 2}$$

When considering compressible flow, the relationship becomes

$$Q = \Phi_v . \frac{A_p}{z_p . \eta} . \frac{p_1^2 - p_2^2}{2 . p_{ref}} \qquad \text{Equation 3}$$

Which can also be expressed as

$$Q_{mean} = \Phi_v . \frac{A_p}{z_p . \eta} . \Delta P \qquad \text{Equation 4}$$

By referring the volume flow rate to the mean pressure drop across the porous medium.

Another important consideration for the flow of gas through permeable materials is the inertia effect. As a gas particle passes through a porous medium, it is subjected to a tortuous path of twists and turns, expansions and contractions, as it passes through a continuous set of interconnected pores. These varying forces acting on the gas as it passes through the medium cause momentum to be lost and regained in accordance with local fluid velocity, and in effect cause a loss to the system whose effect is to reduce the effective flow.

The most widely accepted model for this phenomenon is the Forchheimer model [60]

$$\frac{p_1^2 - p_2^2}{2.p_{ref}} = \frac{z_p.\eta.(Q/A_p)}{\Phi_v} + \frac{z_p.\rho.(Q/A_p)^2}{\Phi_i} \qquad \text{Equation 5}$$

Whether this relationship is universally valid has been the subject of some work [61, 62] and as discussed below, at a certain flow rate the effects of inertia can be ignored with little effect on accuracy. It was further suggested that for porous air bearings this regime, where inertial terms are insignificant, applies [63, 64].

Other researchers have attempted to correlate the permeability of porous materials with their physical attributes. Porosity was related to permeability firstly by Robinson [65], then by Cliffel [66]. Robinson used tungsten powders of 12 to 420μm with a porosity range of 0.095 to 0.36 whereas Cliffel used sintered nickel with a powder size range of 5 to 30μm and porosity from 0.15 to 0.85. Both used the same power law model to describe the relationship, but differed in the resulting exponentials. German [67] repeated the work for stainless steel particles of size range 59 to 715 microns, and porosity values of 0.25 to 0.56.

Again, using the same power law model slightly different exponentials were found.

Smith [68] used the specific surface area of the porous structure instead of the powder size to relate to permeability. His data was then used by German [67] in his model that resulted in quite different coefficients. This data is tabulated below in table 1.

The data shown below varies considerably from researcher to researcher. Given that several techniques were used to determine the powder size, and that different materials have different particle aspect ratios, it is of no surprise that the constants for permeabilities are different, even across sets of material data that at first glance appear to be reasonably close to one another.

Table 1 Relationships between permeability, porosity, and powder size

Reference	Equation	k	a	b
Robinson [65]	$\Phi = k.\zeta^a.d_w^b$	--	4.38	2.18
Cliffel [66]	$\Phi = k.\zeta^a.d_w^b$	--	1.871	1.871
German [67]	$\Phi = k.\zeta^a.d_w^b$	4.6E-11	6.8	0.73
German [67](data from Smith [68])	$\Phi = k.\zeta^a.d_w^b$	4.8E-13	4.8	1.3
Smith [68]	$\Phi = k.\zeta^a.s_v^b$	190	2.42	-2.42

2.6.2 Porous Air Bearing Theory

Porous air bearing investigations begin with Sheinberg and Shuster [69], who, in 1960 reported on a thrust bearing in a grinding spindle which utilised a porous graphite restrictor. Load capacity, pressure distribution under the bearing, and gas consumption analyses were carried out. This analysis also introduced the concept of a bearing parameter χ, which was later modified [70] and became known as the bearing number Λ.

This bearing number term Λ, is a non-dimensional design variable which takes into account permeability, radius, thickness, and bearing gap. It is a useful method of taking in all the important variables in porous bearing design into one simple equation. There are several variations on the definition that have evolved, as will be seen subsequently.

Mori *et al* [33] treated the problem somewhat differently. Instead of the porous material being represented by an array of uniaxially and uniformly distributed fine capillaries as did Sheinberg and Shuster, the porous medium was considered as equivalent to an additional fluid film. This accounted for the two-dimensional flow, and importantly, introduced the concept of an equivalent clearance.

Gargulio and Gilmour [70] produced an analysis of porous thrust bearings using a finite difference approach. The equations so derived were used to predict the load carrying capacity and gas consumption of bearings of various geometries, assuming compressible, isothermal, laminar flow. These were then compared to experimentally obtained data, which pointed to the need to use an equivalent gap in order to compensate for the surface roughness effects. Permeability anisotropy was also investigated, leading to the conclusion that a reduction in the gas consumption without any deleterious effect on the load capacity was possible by reducing the radial permeability.

Correction for surface roughness was also a feature of the analysis carried out by Andrisano and Maggiore [71]. This numerical analysis featured a lumped parameter approach, and included the effects of bearing tilt. Experimental work was also carried out to determine load capacity and gas consumption. The surface roughness correction was predicted to require values lying between R_a and R_p.

From these models the next evolution in the analysis was with regard to the velocity slip at the porous bearing surface. Whereas the previously mentioned researchers treated it as a solid surface, i.e., no slip flow was present, Ishizawa and Hori [72] developed a theory that allowed for slip flow to occur.

Several authors then developed this idea further, and corrections to the original definition of the bearing number were proposed. Murti included terms for the bearing number after analysis for compressibility of the gas medium but no slip flow [73], and shortly after for slip flow based on the analysis of Beavers [80], but assuming incompressible flow [74]. These corrections gave better agreement to the experimental data presented by Gargulio and Gilmour [70].

Perturbation methods were used by Jones *et al* [75] to correct for slip flow and compressibility. Load carrying capacity predictions tied in well with that found experimentally with Gargulio and Gilmour [70], but the predicted values of gas consumption did not.

Slip flow was later updated by investigations by Verma [76] and Singh [77], the later using a full slip criterion for the basis of the analysis, unlike Murti [74] who used a simplified approach.

Complex 3D flow models require a large computing capability for the solution of the governing equations. Modified Reynolds equations deduced from Darcy's equation have been attempted in this way.

In an effort to reduce processing time, a simplified 1D model of a porous circular thrust pad was analysed by Tian [78]. Using a finite element analysis approach, it was found that the resulting computational time was around 30% for the time required of the classical 3D approach. The resulting model gave good agreement with experimental work, though was not precise at large values of radius/height and small values of film thickness.

2.7 Experimental Comparisons

Several authors have attempted to compare physical porous air bearings with predictive theories of their performance. One of the earlier thrust bearing works was by Scheinberg and Schuster [69], who considered the case of a non-rotating circular thrust bearing with and without a central hole for a shaft. Whilst no data is given for the performance of such a bearing, they do say that the bearing performs in a highly stable manner.

The paper by Gargulio and Gilmour [70] several years later was a major milestone in the understanding and prediction of the performance of porous air bearings, as mentioned earlier. Mass flow rate of gas and load carrying capacity were experimentally and theoretically determined and compared. The concept of an equivalent clearance for the bearing gap in order to compensate for the surface roughness of the bearing was also introduced.

More recently work by Kwan [5] on two non-rotating porous ceramic circular thrust bearings investigated the relationship between process parameters and porosity, the relationship between porosity, particle size and the resulting fluid flow and mechanical properties from experimental data. Processing temperature was found to be the most important variable affecting the reproducibility of permeability of the porous material.

Prototype bearings were manufactured and tested, one a single layer single 7μm powder particle size bearing, and the other a two-layer bearing. This bearing consisted of a coarse 23μm substrate to provide the mechanical strength and a fine 0.5μm pressure-restricting layer on the surface. The 23μm portion was formed by HIPing, and ground to shape, the 0.5μm layer was slip cast, then ground, and the two layers were subsequently hot pressed together using a tape cast layer to provide the interface.

The single layer bearing was found to be unstable over a wide operating range, whilst the double layer bearing was perfectly stable. This was found to be due to the much lower gas volume at the surface of the bearing for the sample with the fine pressure-restricting layer. It was found necessary to introduce an equivalent gap due to velocity slip for the analysis of both bearings. The slip coefficient varied considerably from that predicted by Beavers [80] and the value of the equivalent gap was experimentally deduced. The static load carrying capacity was investigated for both bearings and with the incorporation of the above mentioned equivalent clearance performed in line with published theories.

2.8 Slip Flow

There exist two cases of potential slip flow in relation to porous air bearings. Both have received attention in relation to this application, and where appropriate, corrections to existing theories have been postulated.

The first case where slip flow is thought to occur is when a gas passes through a narrow passage of similar dimension to the molecular mean free path of the gas. This is referred to as molecular velocity slip flow. In reality this phenomenon is of little concern to the porous bearing designer.

Taking the molecular free path of a gas molecule as:

$$\lambda = \frac{1}{\sqrt{2}.n.A_m} \qquad \text{Equation 6}$$

and taking the onset of slip flow as when the Knudsen number, $k_n > 0.01$, where k_n is defined by:

$$k_n = \lambda / z_g \qquad \text{Equation 7}$$

The mean free path of air at atmospheric conditions as defined by the International Civil Aviation Organisation is 6.6317E-8 m [79]. As the gas pressure increases, this number decreases. At 2.5 bar gauge pressure it reduces to approximately 2.6E-8 m. If we take a bearing operating at this pressure at a gap of 10 microns, the resulting Knudsen number is 2.6E-3, indicating that slip flow should not be significant.

The second slip flow consideration is best explained with reference to the following figure, figure 10.

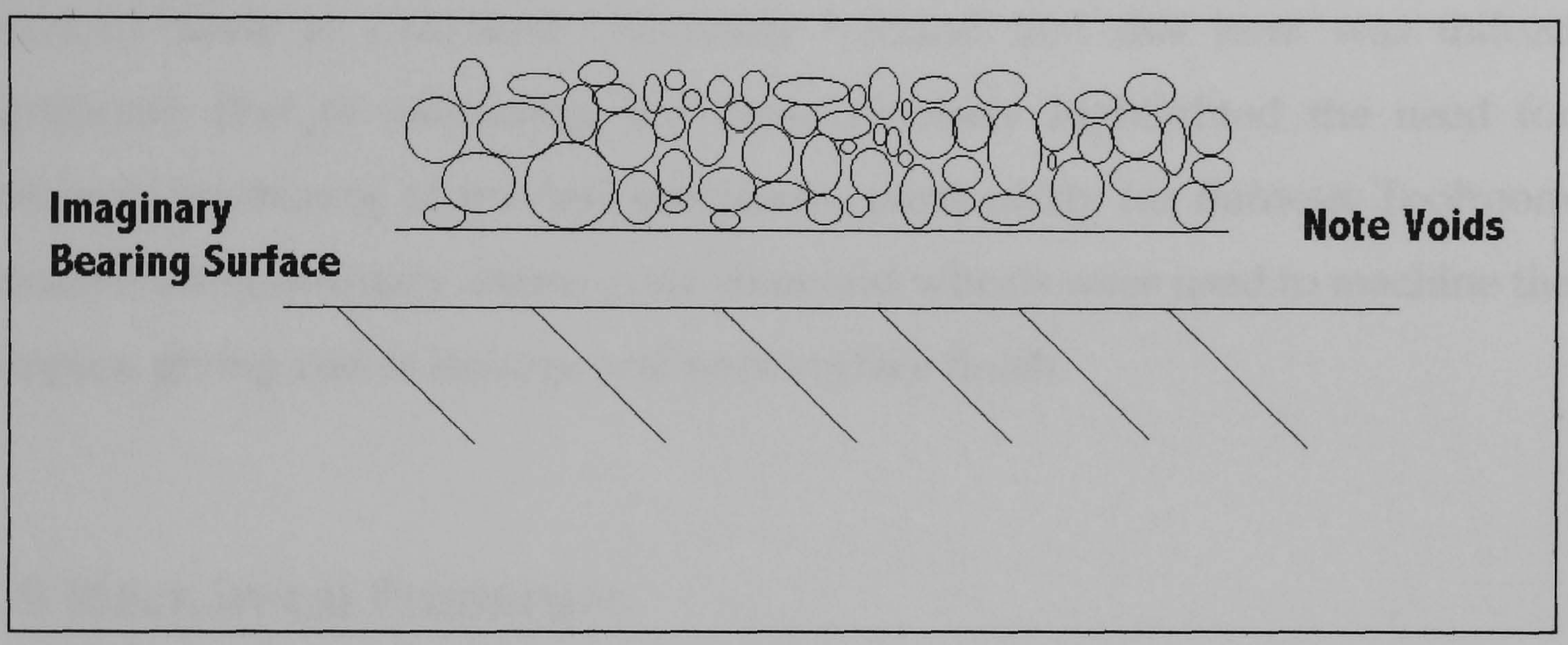

Figure 10 Tangential velocity slip flow

The aim of this figure is to illustrate the fact that porous materials do not have a solid boundary, but are bounded by a series of interconnected pores and particles. The solid line drawn above is an imaginary boundary touching the outermost peaks of the porous material. What should be noticed is the large void volume behind this line, which are gas filled.

If it were assumed that this porous material was part of a bearing, gas would flow through the bearing into the gap, and exit to either side. To ensure continuity, the velocity of this exiting gas at the imaginary boundary must be the same as the velocity of the gas immediately inside this line. This gives rise to a phenomenon known as tangential velocity slip [80].

It is thought that this type of slip is independent of Reynolds number and the flow velocity, though pore size seems to effect it directly [80]. This concept has been further investigated by various authors, who have confirmed its validity [81, 82, 83].

The overall effect of this phenomenon is to increase the flow of gas in the bearing as the resistance to flow is effectively reduced. This means that the bearing behaves as if it were operating at a larger bearing gap. This can be compensated for by a roughness term that increases the effective gap.

Previous work at Cranfield University [5] found that this term was indeed significant, though measuring the value precisely highlighted the need for precision machining of the test specimens, particularly for flatness. Toolroom grinders using ordinary coarse grain diamond wheels were used to machine the samples, giving rise to leakage and poor surface finish.

2.9 Mechanical Properties

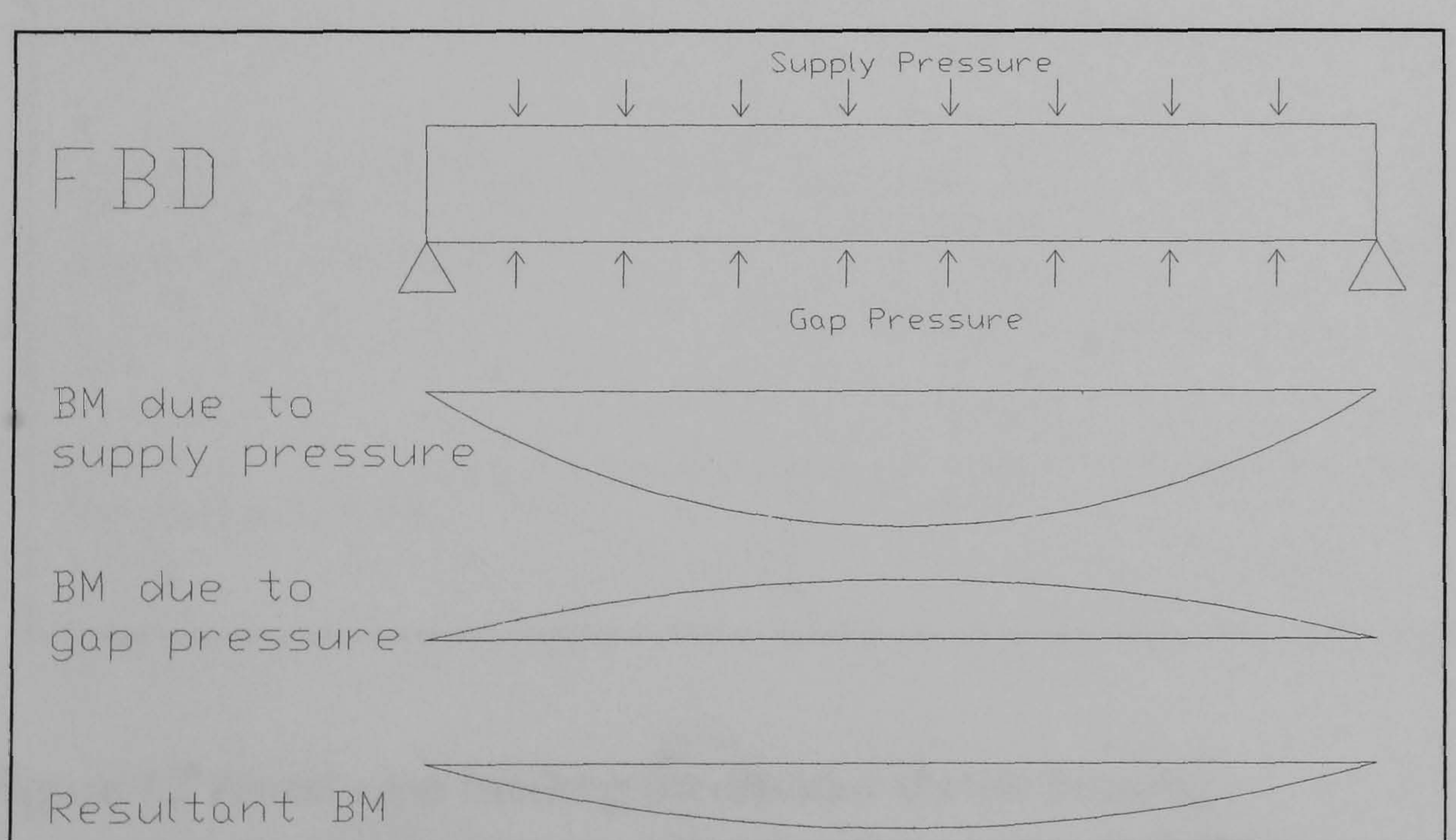

Figure 11 Free body diagram of loading on circular thrust bearing

As with any mechanical device, certain goals need to be set with regard to a set of minimum mechanical properties. The bearing under consideration is held in

a solid backing plate, the purpose of which is to supply the bearing with the compressed gas at the supply pressure that it requires to operate. On the exhaust side of the bearing it sees the gap pressure, and the resultant load that the bearing must withstand is the difference between these two. A free body diagram summarising the loading is illustrated in figure 11.

However, it is prudent to a assume worst case scenario and to design for survivability under those conditions. This would represent the situation under which the bearing finds itself with full supply pressure but no supporting gap pressure, such as if lifted away from the counterface during operation. In this situation the bearing structure must support the full bending moment due to the supply pressure with no counteracting moment from the gap pressure. In this case the bearing must withstand the loading illustrated in the FBD in figure 12.

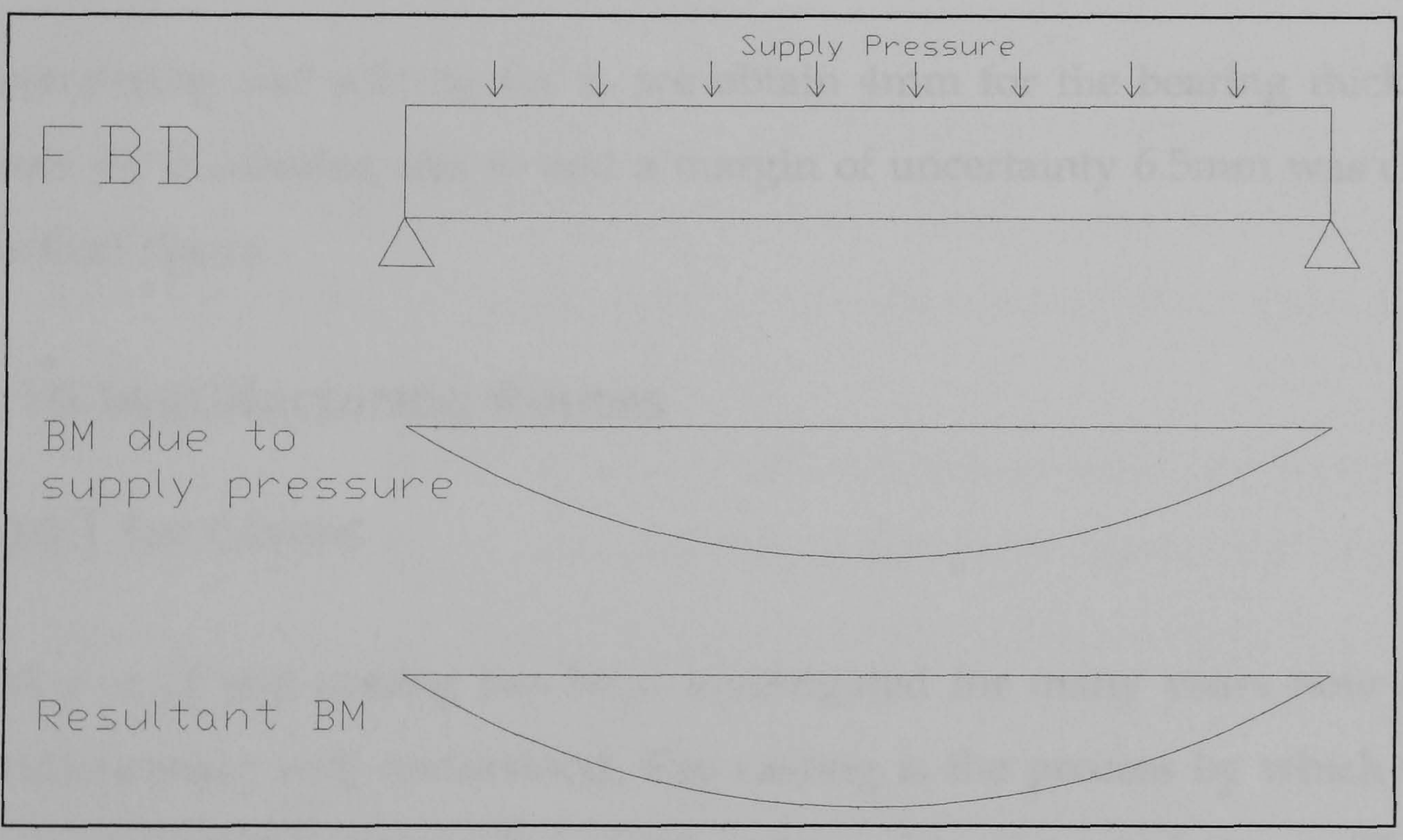

Figure 12 Worst case loading on circular thrust bearing

The ideal properties of a typical bearing would have to meet several design criteria. Firstly looking at the mechanical strength required we can come up with a figure as follows; assume the bearing approximates to a simply supported disc with the supports at the perimeter, and limit the elastic

deformation to approximately 1μm. We have from Roark's Formulas for Stress and Strain [84]:-

$$\delta_c = 0.07 \frac{\Delta P . r_p^4}{E . z_p^3} 12(1-\upsilon^2) \qquad \text{Equation 8}$$

where δ_c = Deflection, 1μm

ΔP = Pressure drop across the bearing, approximately 0.17 Mpa

r_p = Radius of the pad, 20mm

E = Young's Modulus of Elasticity where $E = E_o(1-\zeta_\tau)^{2.14}$ [134], E_o is the Modulus for alumina, 410GPa, and ζ_t is the total open porosity, typically 0.35, giving E = 160GPa.

z_p = Thickness of the bearing, to be calculated

ν = Poisson's Ratio, approximately 0.15 from present work

Rearranging and solving for z_p we obtain 4mm for the bearing thickness. To allow for machining and to add a margin of uncertainty 6.5mm was chosen as the final figure.

2.10 Manufacturing Routes

2.10.1 Slip Casting

The area of slip casting has been investigated for many years now and it is fundamentally well understood. Slip casting is the process by which virtually every household ceramic is formed and consists of several stages. The first is the preparation of the slip. In this stage the ceramic, or clay in the case of household ceramic items, is added to water to form a stable colloid of dispersed particles. This is then cast into a porous plaster of paris mould that removes the water from the slip by capillary action, leaving a "green" component with sufficient strength to be handled. The mould is then split open and the green

component is removed and fired, giving it the necessary strength for the purpose it is intended.

However, for the majority of engineering ceramics this is not quite such a simple exercise. The problem lies in the surface chemistry of the ceramic. When added to water the ceramic powder particles tend to flocculate together instead of forming a consistent colloidal suspension. This results in sedimentation of the slip, poor flow characteristics during pouring, and inconsistent density from point to point within the green. At best this results in a green with varying density and mechanical properties, but more often can lead to large flaws which translate into cracks in the final component.

These effects are due to short-range interparticle forces termed the Van der Waals forces. Once in water the particles can gain surface charges through preferential absorption of ions, dissociation of surface groups, isomorphic substitution or the adsorption of polyelectrolytes. A good example of isomorphic substitution occurs when clay is added to water, there is a cation exchange in the lattice; Si_4^+ is replaced by Al_3^+, leading to surface adsorption of +ve ions. Na^+ passes freely into solution leaving a negatively charged particle [85].

Engineering ceramics tend to adsorb polyelectrolytes and their surface charge varies with the pH of the solution into which they are placed. The pH is a measure of the relative acidity/alkalinity of an aqueous solution. It is defined as the negative log of the aqueous concentration of hydrogen ions [86]. At high pH they become positively charged, and negatively charged at low pH. At some intermediate point the process will balance and the surface will be neutral. This point is termed the isoelectric point.

The isoelectric point of alumina has been measured by potentiometric titration to be at a pH of 9.06 [87]. This has been shown to change slightly with

temperature, the value of 9.06 refers to 30°C, and reduces by 0.7 pH when the temperature is increased to 90°C [87].

At a point far from the isoelectric point the ceramic particles will have like surface charges but their repulsion is not simply due to this effect, but is aided by an electrical double layer that surrounds the particles. For a stable suspension there exists an equal and opposite charge in the solution to the charge on the particles, so giving an overall charge of zero. Brownian motion of the ions in solution due to thermal effects prevents these ions from settling on the particles and instead they form a diffuse cloud of ions around the ceramic particles. It is this diffuse layer that repels other double layer charged ceramic particles and prevents them from coming into contact.

An alternative approach is that of steric hindrance. Here the idea is to prevent particles from coming into contact due to a physical barrier. A polymer chain is utilised to hold the particles apart by attaching one end to the ceramic while the other remains free in the solution. This system is dependant upon finding a polymer which can adhere well to the ceramic, and ideally is hydrophobic with a low tendency to react with other polymer chains.

A further development of this idea is to charge the chains thus adding electrostatic repulsion to the steric hindrance, reducing the likelihood of flocculation. One disadvantage of the system of using a physical barrier is that at some stage the polymer must be removed, as any remaining polymer may have deleterious effects on the mechanical properties of the ceramic.

Previous work in the area of electrostatic stabilisation confirms the ability of alumina powder to be successfully suspended in an aqueous solution using a pH controlled approach [88]. Using a pH of 3 it was found that 0.5μ powders could be suspended although subsequent rheological examination revealed a slightly higher than ideal viscosity for slip casting. The addition of citric acid

greatly improved the slip, reducing the viscosity by two orders of magnitude, leading to much improved pour characteristics. Repeat tests over a period of two weeks revealed that the addition of the citric acid also promoted greater stability over time, as the slip showed very limited tendency to flocculate. This also reduced the likelihood of trapped air in the resultant green. The reasons for this improved performance were thought to be due to a short-range steric hindrance effect in addition to the surface charge imparted onto the powders.

Investigations of other media for the purpose of suspending alumina have also been investigated. Wang *et al* [89] successfully dispersed alumina powders in ethanol using a pH-controlled approach. The behaviour of alumina powder in ethanol, a polar non-aqueous solvent, is slightly different to that in water. It was found that at low pH the powder develops a positive charge through adsorption of protons onto the surface and at high pH the surface becomes negative through adsorption of hydroxyls. The resulting isoelectric point was moved to a pH of 7.1 in the ethanol. It was also found that a stable suspension of the 0.22μm powders could be achieved over a range of pH.

Other ceramic systems have also come in for investigation by the use of slip casting. The rheology of silicon nitride systems using non-aqueous systems have been investigated and characterised. Using Decalin as the nonpolar solvent and Hypermer KD-3 as a polymeric dispersant it was found that stable solutions with solid loadings up to 50% could be achieved [90]. Using aqueous silicon carbide slips of 37vol% of various viscosity's in the range 58 to 180 mPas it was found that only the fully defloculated slip was stable when cast, the others caused the local void volume to increase as a function of the cake thickness [91].

In order to shorten the processing times involved with slip casting alumina suspensions, the use of microwave energy was investigated as a means of increasing the casting rate. It was found that using a slip prepared with 72wt%

alumina and hydrochloric acid and nitric acids as dispersing agents, the casting rate did increase. It was postulated that the flow of water through the mould was enhanced, and an increase in the solubility of the ions responsible for coagulation of the alumina particles took place [92].

2.10.2 Injection Moulding

Injection moulding has become commonplace amongst the plastics and rubber moulding industries. In essence it is a process where a material is injected into a mould under pressure, allowed to harden, then removed. It is a process that allows the rapid and repeatable fabrication of high complexity, and lends itself to high volume production.

In its simplest form, plastic injection moulding involves heating a thermoplastic to a temperature at which flow is possible, forcing the plastic into a shaped cavity, and cooling it [93].

In order to increase the component strength, it is possible to incorporate a filler into the polymeric mix. This technique can be used to tailor specific strength, thermal, magnetic, or electrical properties of a component.

Taking this technique further, by maximising the volume of filler into the moulding and extracting the polymer after the moulding process has taken place, we can create an intricate piece in the same manner as mentioned previously, but out of a material that would not otherwise lend itself to moulding. In our case this allows the moulding of ceramic components.

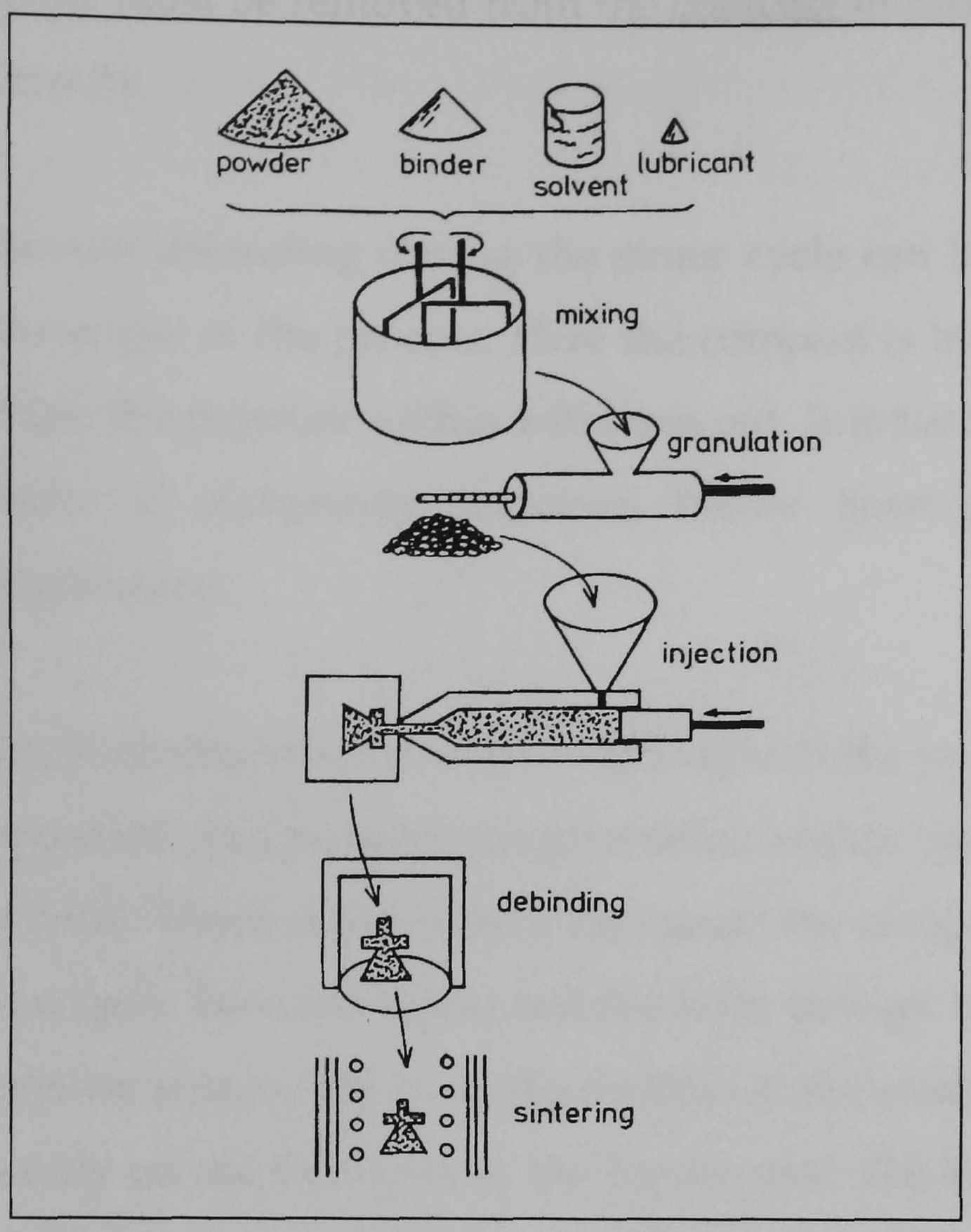

Figure 13 Injection moulding process schematic (from [93])

It has been demonstrated that this method can be applicable to ceramics, with examples as early as the 1920's [94]. The main steps involved in the production of a ceramic by injection moulding are as illustrated in figure 13 above. These are selection and preparation of the powder, mixing the powder with a suitable binder system, the production of homogeneous granulated feed stock, the moulding process itself, then debinding and sintering to achieve the desired density and mechanical properties.

The principle component of a binder is usually a thermoplastic chosen for its viscosity, stability, compatibility with the other moulding components, mechanical strength, long shelf life, ease of removal, low cost, and flow characteristics at moulding temperature. Other systems have been used, such as water or other substances such as starches [95]. Once moulded and cooled, the

binder must be removed from the compact in order to allow the piece to sinter correctly.

Thermal debinding during the sinter cycle can be a useful way of combining two stages of the process. Here the compact is heated slowly to a temperature where the polymer within will burn out. It is held at this temperature until the binder is completely removed, before heating again to the final sinter temperature.

This is an important process to get right. If the heating rate is too high, thermal expansion, and possibly gas generation within the body, can cause the compact to burst. Heating too slowly can cause the compact to slump, as the polymer once again becomes liquid and the body droops. It is also a slow process, as the polymer is removed from the surface of the compact, debinding time depends heavily on the thickness of the component. Thicker pieces are also more prone to gas entrapment due to the difficulty in venting any moisture trapped within the structure of the green body.

One solution to this problem is to use a two-part binder system. If an inorganic substance such as wax were blended with the binder polymer, and was removed before thermal debinding, a continuous network of open pores would be left. This allows the venting of any trapped gasses, and reduces the chances of component failure. This wax removal can be accomplished by the use of a solvent in a hot bath. The disadvantage of this method is that an extra step is introduced, increasing the process time and adding extra cost.

2.10.3 Sintering

Sintering is the process by which granular materials such as ceramic powders can be consolidated into a useful shape. The term refers to the pore shape change, pore shrinkage, and grain growth which particles in contact undergo during heating. The driving force for sintering is a decrease in the surface free

energy of powdered compacts, by replacing solid-vapour interfaces (of surface energy Γ_{sv}) with solid-solid (Γ_{ss}) interfaces, where $\Gamma_{ss} < \Gamma_{sv}$. Thermodynamically, sintering is an irreversible process in which a free energy decrease is brought about by a decrease of surface area.

In the case of non-silicate ceramics such as alumina, this is a solid state process, with the predominant densification mechanism through solid state diffusion.

The process can be broken down into three distinct phases as shown in figure 14. A stage of sintering may be described as an interval of geometric change in which the pore shape is totally defined, or an interval of time during which the pore shape remains constant in shape while decreasing in size.

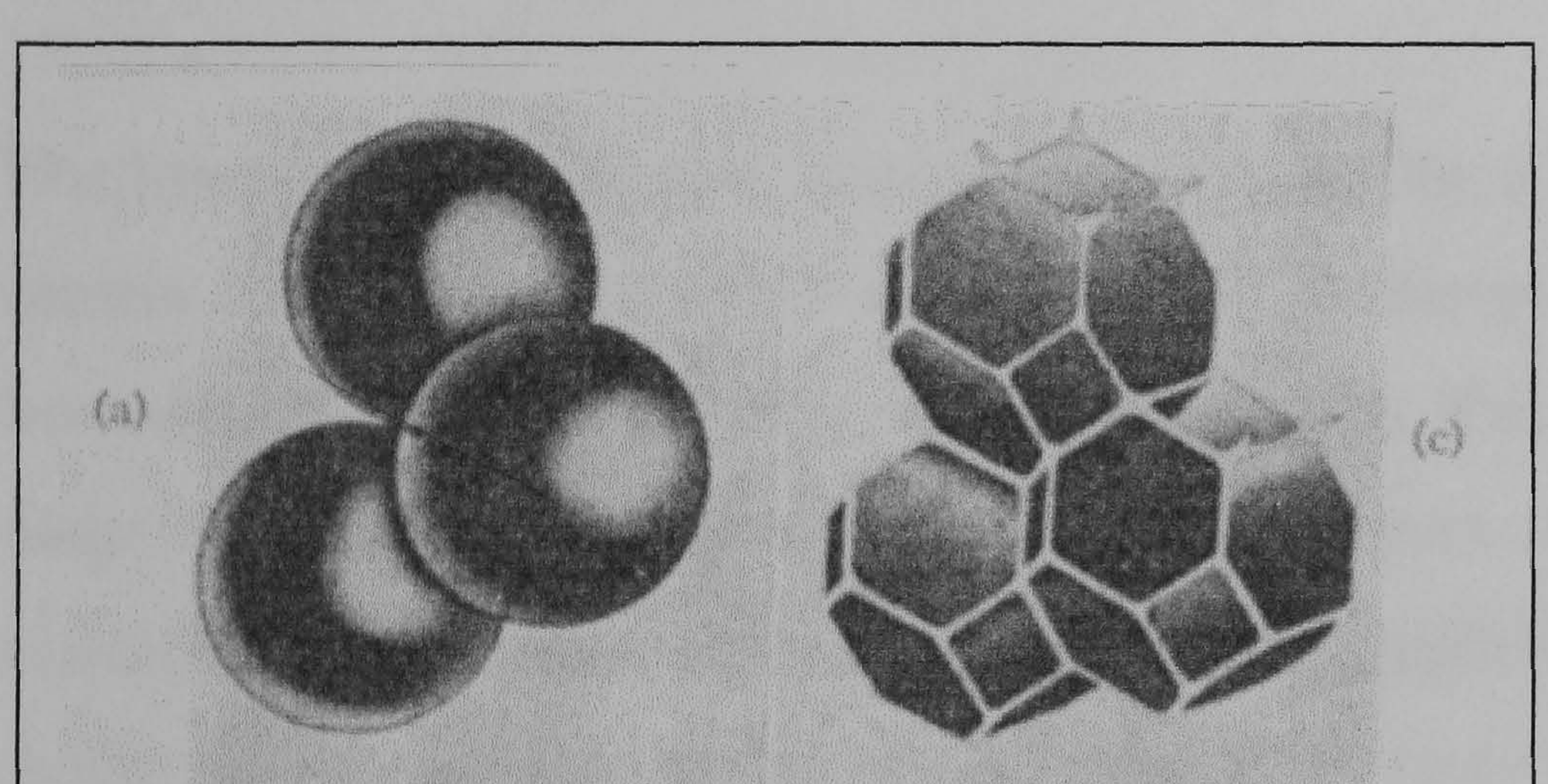

Figure 14 Stages of sintering (from [96])

The first stage is commonly referred to as neck growth. In this stage the interparticle contact area is increased from zero to ≈ 0.2 of the cross sectional area of the particle. This is shown by the transition from figure 14a to b. Accompanying this change is an increase in relative density, nominally from 0.5

to 0.6 for a normal compact [96]. This starts at local contact points which fuse together along with a smoothing of the free surface of the particles. These contact points grow into necks with concave curvature, in contrast to the convex curvature of the particles.

Grain growth is inhibited during this stage of sintering due to the acute angle of the particle to particle contact. This means that the solid-vapour surfaces diverge, and any grain growth would require the boundary to move away from the minimum energy position and increase in area and energy. Once the neck growth increases and becomes blunted, this restriction is reduced, and grain growth becomes possible. The point at which this occurs marks the end of the initial stage of sintering [97].

The intermediate sintering stage is characterised by a pore and grain boundary matrix consisting of dihedral angles formed on the pore surface with the grain boundaries. This equilibrium state is dictated by the surface tension [97, 98]. This stage is represented by figure 14c. The compact at this stage possesses a continuous open network of pores bounded by grain boundaries. The shrinkage in the intermediate stage can result in densities up to 95%. However, shrinkage does not necessarily take place during this stage of sintering. If the only material transport mechanism originates on the surface of the particles, as surface diffusion, the compact will not shrink. In such a case a change in the shape and size of the pores is and particles is observed and is commonly defined as grain growth, or coarsening. This depletes the system of energy and effectively stops the densification of the compact, even if other mass transport mechanisms become operational. At best, due to the reduction in the driving force for sintering, the intermediate stage is stunted.

The final stage of sintering takes the body to full density. This is shown by figure 14d. Here we see the energetically favoured geometry of closed small pores occupying the corners of the grain. Allowed to continue, the pores will

disappear completely, and sintering will be complete [96]. The final stage of sintering begins at around 93-95% of full density when porosity becomes isolated. The complete elimination of pores can only happen when all the pores are connected to short diffusion paths along grain boundaries. This is of course only possible is the pores follow the movement of the grain boundaries, and are not trapped within the grains themselves.

In the final stage of sintering small pores attached to grain boundaries move quickly to collapse together and thus reduce the surface energy. Along with pores, grain boundary movement is accelerated, leading eventually to discontinuous grain grow when pores no longer pin the grain boundaries. This leads to rapidly moving grain boundaries that consume small grains. This leads to the situation where some grain appear with many highly curved sides, thus further accelerating the process, leaving behind closed porosity that is trapped within large grains. Lattice diffusion becomes the dominant mechanism in removing these pores, which is slow due to the long diffusion paths, and is further hindered by the gas trapped in the pores.

2.10.3.1 Sintering Aids

The addition of sintering aids to either increase or reduce sintering rates has been looked at in some detail. For a typical air bearing application it is of interest to maintain an open porous structure and so doping the ceramic with a material that will hinder densification is potentially advantageous. It has been found that yttria doped submicrometer grain α alumina displays such characteristics [99]. Using a range of 0 to 1500 ppm yttria it was shown that during densification yttria initially retarded the sintering rate by raising the apparent activation energy while in an atomic state and below the saturation point at the grain boundaries. During the peak rate densification the yttrium segregates to the grain boundaries and increases the rate of densification. Once past the peak rate the yttrium once again acts to slow the rate of densification by the formation of yttrium rich precipitates along the grain boundary.

Another study by Fang *et al* [100] looked into the effects of both yttrium and lanthanum on the sintering of alumina. Using 1000 ppm yttrium and lanthanum decreased the final stage densification rate by factors of 11 and 21 respectively. The reason for this was postulated as being that these large elements strongly diffuse to the grain boundaries in alumina and restrict the movement of ions along the grain boundary. This leads to a decrease in the grain boundary diffusivity and a corresponding drop in the densification rate. It was also discovered that the addition of these elements led to a reduction in the grain size for a given density of alumina.

2.10.4 HIP

HIPing is a process normally used in the fabrication of various ceramic and metallic materials in order to produce a final component with high theoretical density. It combines the effects of heat and pressure to reduce the residual porosity often left by sintering alone. There are two normal approaches to HIPing, canned and containerless. As the name suggests, in canned HIPing the material to be consolidated is placed in a can and sealed before being entered into the HIP. The can then acts as a gas tight skin around the material and the heat and pressure deform the can, pressing the material together, leading to a high finished density. The can is then machined off, leaving the material available for further processing. This process is suited to produce high-density materials from porous substances, for example powders, which otherwise would allow the pressure to infiltrate the porous structure and not aid densification.

Containerless HIPing is generally used to densify materials that are close to their final density and contain no interconnected porosity. Here the use of an extra gas tight skin is not required as the material is non-porous and so it will deform under the action of the increased pressure.

In the case of producing ceramic bearings with predictable porosity and permeability it has been found that the influence of pressure is useful in preventing the material from fully sintering [5]. Ceramic powder is vibration packed into graphite moulds and inserted into the HIP. As the graphite is porous it offers no resistance to the pressure and so the ceramic is not forced to consolidate in the same manner as in canned HIPing. What happens in this case is that the gas infiltrates the open powder structure and helps prevent it from becoming densified, thus preserving the open structure necessary for effective gas flow in bearing applications.

3 Experimental Procedure

3.1 Materials Processing

Several material processing routes were investigated in the course of this research. As the aim was to produce a successful porous ceramic bearing with all of the inherent advantages of the concept, but with the added advantage of simplicity of construction, it was decided that more than one approach be adopted in order to evaluate changes in processing route on bearing performance.

The manufacturing processes must be capable of reproducible bearing manufacture, meaning that for a given set of processing parameters, bearing performance must not vary significantly. This covers a range of parameters, from the uniformity of porosity, density, mechanical properties, to the pressure distribution under a finished bearing and its stiffness.

As cost is of significant importance in manufacturing, the processes investigated were chosen either for their high volume capability, as in the case for injection moulding, or low set-up costs, as for slip casting. The exception was the HIPing route, this was tried as a bridge between previous successful research carried out at Cranfield University [5] and the present research project.

Several different alumina powder sizes were chosen for investigation. These were 0.5µm, 1µm, 4µm, 7µm and 23µm. As the aim of the injection moulding and slip casting processes were to produce a bearing consisting of a single layer of ceramic, and it has been noted previously that the volume of gas trapped at the surface of a bearing is important [69, 5], smaller powders (0.5 to 4µm) were chosen for these processes.

This was due to gas trapped at the surface of the bearing in the voids having an important impact on the stability of the bearing. If these voids are too large it can take an appreciable time for them to fill and to empty in response to a change in the load that the bearing sees. This can lead to a self-exciting situation known as air hammer, where the vibration can be severe enough to cause the bearing to strike the opposing face, causing damage. The obvious way around this is to minimise the void volume at the surface, and through the use of small powder particles it was hoped to achieve this.

The 7μm powder was used to determine where the stability cut off lay. Previous work had shown that a bearing made from 7μm powder was partially stable, so it was intended to explore this further [5]. The 23μm powder was used to provide the mechanical backbone to an experimental two layer bearing. This idea was used in previous research[5]. The difference this time was that instead of having a fine powder size pressure-restricting layer attached by hot pressing, the second layer would be formed in situ. It was hoped to achieve this by using a dip in slip approach (DIS). The method was to firstly consolidate the coarse 23μm powder in a HIP, then dip it in a slip prepared from 0.5μm powder, thus making a second layer.

These powders were used from the same batches of powder supplied for the initial investigations [5, 101, 102, 104]. Details of powder size characterisation can be found in section 3.1.8.

Table 2 shows an overview of the different temperatures, powder sizes and whether the samples were sintered in an air atmosphere furnace or whether the HIP was used. The left column shows the powder size and the route, where VIB means that the sample was vibratory packed, IM means that the sample was injection moulded, and SC means that the sample was slip cast. The darker section to the left-hand side of the table designates those samples formed by conventional sintering in a air atmosphere furnace, whilst the lighter right hand

side designates those that were consolidated in the HIP. Further details of each process can be found in the appropriate section.

The points were selected to obtain useful data for the processes and powder sizes investigated. Varying the temperature for a given powder size and processing route allowed the effects of temperature on parameters such as density, permeability, bearing stiffness, etc., to be determined. Varying the powder size and processing route for a given set of sintering conditions allowed the effects of the altering the powder size and processing route to be compared directly.

Table 2 Densification map

	Temperature														
Size	1100	1150	1200	1250	1300	1350	1400	1450	1500	1550	1600	1650	1700	1750	1800
23 VIB											■	■	■	■	■
7 VIB					■	■	■	■	■	■	■				
4 IM					■	■	■								
4 SC						■	■	■	■						
1 IM	■	■	■	■	■	■									
1 SC		■	■	■	■	■									
0.5 IM 55%	■	■	■	■	■	■									
0.5 IM 50%	■	■	■	■	■										
0.5 SC	■	■	■	■	■	■									

3.1.1 Powder Preparation

Before processing began, all powders used were firstly dried for 24 hours in a vacuum oven at 110°C, and were furnace cooled under vacuum. Alumina is naturally hydrophilic, loose powder can contain 2.3 to 17% by weight of water on its surface [103, 104], so it was considered necessary to remove excess moisture.

Any extra moisture could have a negative affect on the processing route. For example, it was found that moisture from undried alumina was liberated in the form of steam during injection moulding, leaving voids in the body of the moulding piece [105]. Damp powders are also more inclined to clump together, reducing the effectiveness of vibratory packing. For the slip casting process surface chemistry of the alumina is all-important, and any water introduced by the alumina could contain impurities that may affect this technique [106]. As the powder used had been stored in an unheated out building for some time prior to use, it was suspected that atmospheric moisture may contain trace compounds that potentially could go into solution in the slip and affect the reproducibility of the process.

3.1.2 VIBRATORY PACKING

Owing to the very high temperatures required to sinter the larger particles to a condition where they possessed sufficient mechanical properties to allow them to be tested, it was necessary to resort to the use of a HIP. This was due to no atmospheric furnaces being available that had the required temperature range to allow sintering to take place. As sintering is driven by a desire to reduce the free surface of a compact, larger particles with a greater volume to surface area ratio require a larger energy input to sinter. Hence the need for higher temperatures.

This situation applied to the 23 and 7μm powders, which required processing at temperatures higher than the 1500°C air atmosphere furnaces otherwise used.

The powder was first packed into porous graphite moulds whose purpose was to give the required geometry to the alumina bearing, and allow the inert gas to penetrate the mould and act directly on the ceramic. This gas, argon, was normally introduced into the heating chamber to provide the high pressures required in a normal HIP run. It is necessarily inert, as the HIP uses graphite

heating elements, and so any oxidising atmosphere would lead to the loss of these elements.

The internal faces of these moulds were first sprayed with a boron nitride solution and allowed to dry completely. This fine layer acted as a mould lubricant and eased the removal of the ceramic disk at the end of the HIPing cycle. Graphite was chosen for the material of the moulds as it was essential to use a porous material that would survive the high temperatures.

These moulds were of circular plan, and of internal dimensions diameter 53mm and height 8mm. A lid was also used, to prevent spillage during gas purging of the HIP. The purging of the heating chamber was of a rapid nature, with argon being pumped through to displace the air. Any loose powders would become entrained in the gas flow and be forced out of the chamber, and so a lid was necessary to prevent this.

To allow proper filling of the moulds in a consistent manner, a vibratory packing technique was used. This is known to be effective for packing of larger powders, and leads to a highly uniform packing density [107]. For the 23µm powder used here, it has been shown that packing density achievable was 0.54 with a standard deviation of less than 0.01 [5].

The mould was filled with powder and placed on the vibratory table, a Vibratechniques K16/FFT300 pneumatic ball vibrator. The frequency of vibration was controlled by air pressure supplied to the ball vibrator, and was set at 200Hz. This frequency was determined previously [5] as being effective for reproducible packing density, and was measured by a Thurlby Thander PFM 1300 frequency counter. All samples were vibrated for 5 minutes, and a load of approximately 0.2MPa was applied intermittently to the lid of the mould to encourage the powder to settle.

As the dimensions of the mould and the amount of powder added were known, the final height of the lid was measured so the internal volume was known. This gave a measure of the green density of the sample.

3.1.3 Higher Pressure Sintering By Capsule Free HIPing

It was decided that containerless HIPing should be used (see section 1.10.4), thus allowing gas to enter the porous structure. This has been demonstrated as being beneficial to maintaining an open porous structure [5]. To allow a better comparison to the materials sintered in a more conventional manner, the HIP was used at a low gas pressure, approximately 2 bar gauge.

The heating rate was standardised at 5°C/minute, with the HIPing temperature from 1600°C to 1800°C for the 23µm alumina powder, and 1300°C to 1600°C for the 7µm alumina powder. In all cases the sustain time at temperature was 1 hour, with a 10°C/minute cooling rate. The pressure was added before the heating ramp begun, and was kept as constant as possible during the cycle. Once the furnace was cool (below 100°C), gas pressure was released.

3.1.4 Slip Casting

The process of slip casting of ceramics has been used for a great number of years to shape all manner of components. The casting of clays to make pots for example has been known to have been in existence for at least 10,000 years. At its simplest, the powder is added to water where it disperses uniformly to form a slip. This is then cast into a porous mould where the water is removed by capillary action to leave a fragile facsimile of the cavity into which it was poured. Once fired to give the item some useful strength, the product is ready for use.

This process is slightly more complicated for engineering ceramics. As mentioned previously in section 2.10.1, once added to water these tend not to

form even slips, but instead the powders tend to flocculate together. This is due to the chemistry of the interaction between the powder and the liquid. The surface of the powder tends to become charged due to the presence of attractive Van der Walls forces.

Whilst these Van der Walls forces are largely determined by the particular ceramic in a particular solvent, repulsive forces can be modified over a wide range by the addition of organic and inorganic matter. For engineering ceramics, control of the slip is usually through the formation of repulsive double layer forces around the particles. These can be created by three methods.

The first is through protonation or deprotonation of the surface hydroxyl groups (-OH) by changing the pH of the solution, thus giving a surface charge. The second is due to adjustment of the ionic strength of the solution, and the third is due to the addition of specific adsorbing organic or inorganic oligo- or polyelectrolytes. By adsorption on the particle surface, these additives can cause a change in the surface charge resulting in a change in the double layer repulsion [108].

What was attempted was a combination of alteration of the surface charge through changing the pH of the solution, and the addition of citric acid to act as a dispersant. The point at which the net charge is zero is termed the point of zero charge (pzc), or the isoelectric point. Taking the isoelectric point of alumina at room temperature to be approximately 9.06 [87] we can modify the pH of a solution to produce an environment where alumina will stay in suspension [108]. Using a pH of 3, slip formed by adding 0.5 weight % citric acid to distilled water and balancing the pH with potassium hydroxide results in a very stable slip in which 150g of alumina has been successfully suspended in 90ml of slip, as determined by leaving the slip over a period of two weeks before casting . Once the predried powder is added to the readied liquid the resulting mixture is ball milled for 12 hours, initially using a Pascall 9VS mill, then owing to

mechanical failure, a Turbula figure of eight shaker. The powder and slip liquid were placed in a plastic jar with a 150g alumina ball load for 12 hours, to ensure any agglomerations are properly broken down and the surface chemistry of the alumina particles was suitably modified.

The slip is then cast into the bearing moulds and allowed to dry for 48 hours at room temperature before removal and storage in a desiccated environment. Attempts to shorten this time by earlier removal and increasing the temperature to drive off the water faster resulted in cracked samples.

This proved successful for 0.5, 1, and 4μm powder sizes. Trials with 7μm and greater powder sizes found an unacceptably poor stability, with sedimentation of the ceramic powder becoming visible within several minutes after ball milling. It was found that 23μm powder was not stable at all after ball milling.

As the quality of ceramics produced by wet processing depends strongly on the state of the suspension, slip viscosity was highlighted as a potentially important measurement. This would allow good comparison between different slip compositions. Attempts to measure the viscosity with a Contraves Rheomat 115 viscometer did not prove successful. This was due to the very low viscosity of the slip, close to that of water, and the unavailability of a couette head. This viscosity proved to be below the range that the machine could resolve, and so this investigation was abandoned.

Instead, the stability of the slip was checked empirically by leaving the slip in a glass container for 24 hours and visually examining for sedimentation. It was found that the 0.5μm powder proved exceptionally stable, the 1μm almost as good, with the 4μm powder showing some sedimentation. Therefore in the interest of reproducibility all slip was poured into moulds within a few minutes of ball milling ending.

The moulds used for casting the slip into were commercially supplied through a mould making and design consultant [109]. These were made to the specifications as detailed in Appendix G. Figure 15 below shows a three-part

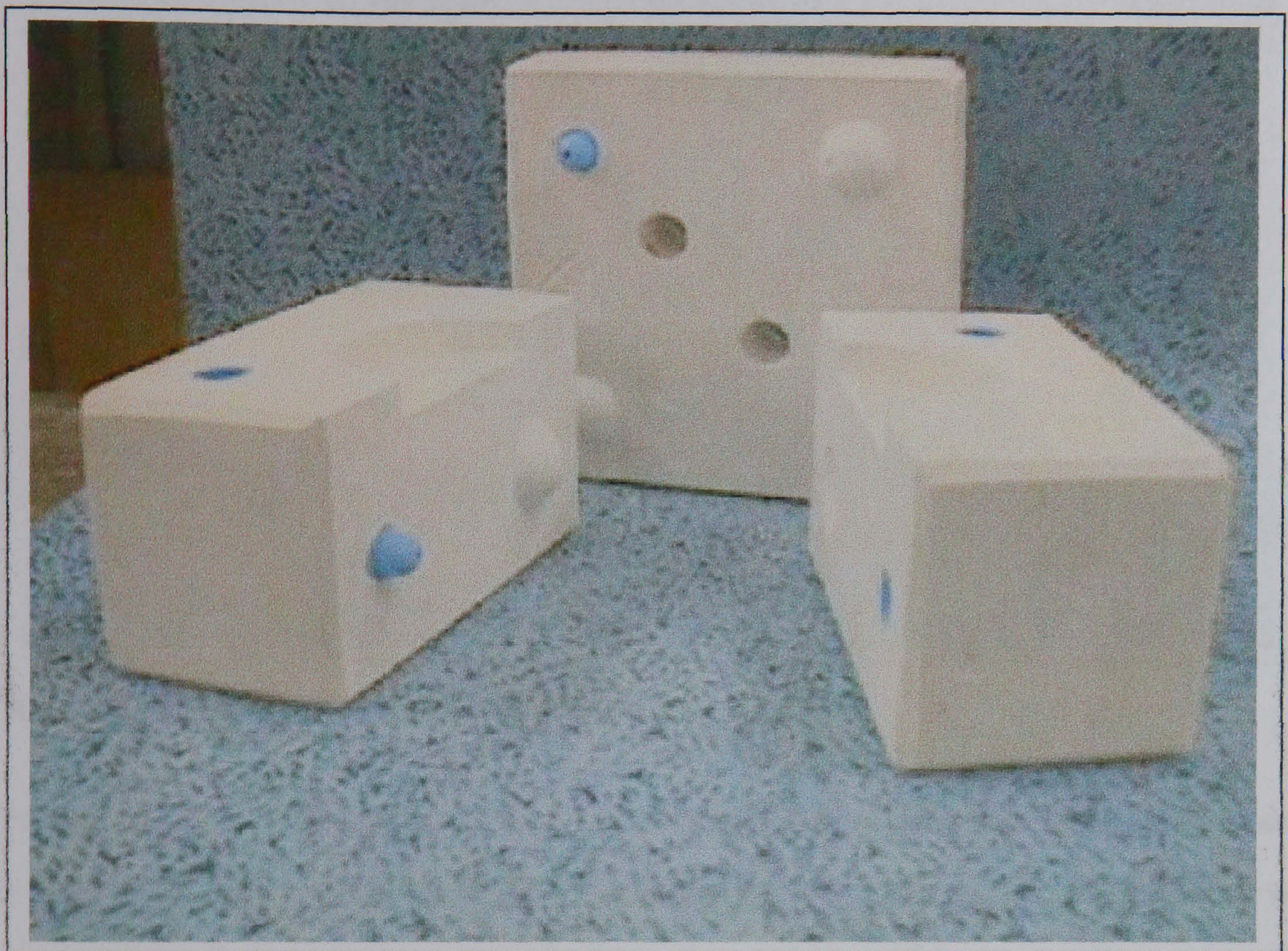

mould used in the course of this research.

Figure 15 Slip casting moulds

In addition to slip casting the circular thrust bearings in this conventional manner, an attempt was made to manufacture journal bearings through slip casting. A requirement for a large diameter porous journal bearing was highlighted by one of the sponsors of the programme, and slip casting was evaluated as a possible method of manufacture.

Owing to the problem of obtaining a mould geometry suitable for a journal bearing by conventional slip casting, an alternative method was devised. This took the form of rotational slip casting. In this technique a split cylinder of plaster of paris filled with slip and bounded by solid aluminium ends was

continually rotated for 24 hours at 200 rpm until all of the slip fluid was taken up by the mould material. This mould is shown in figure 16 below.

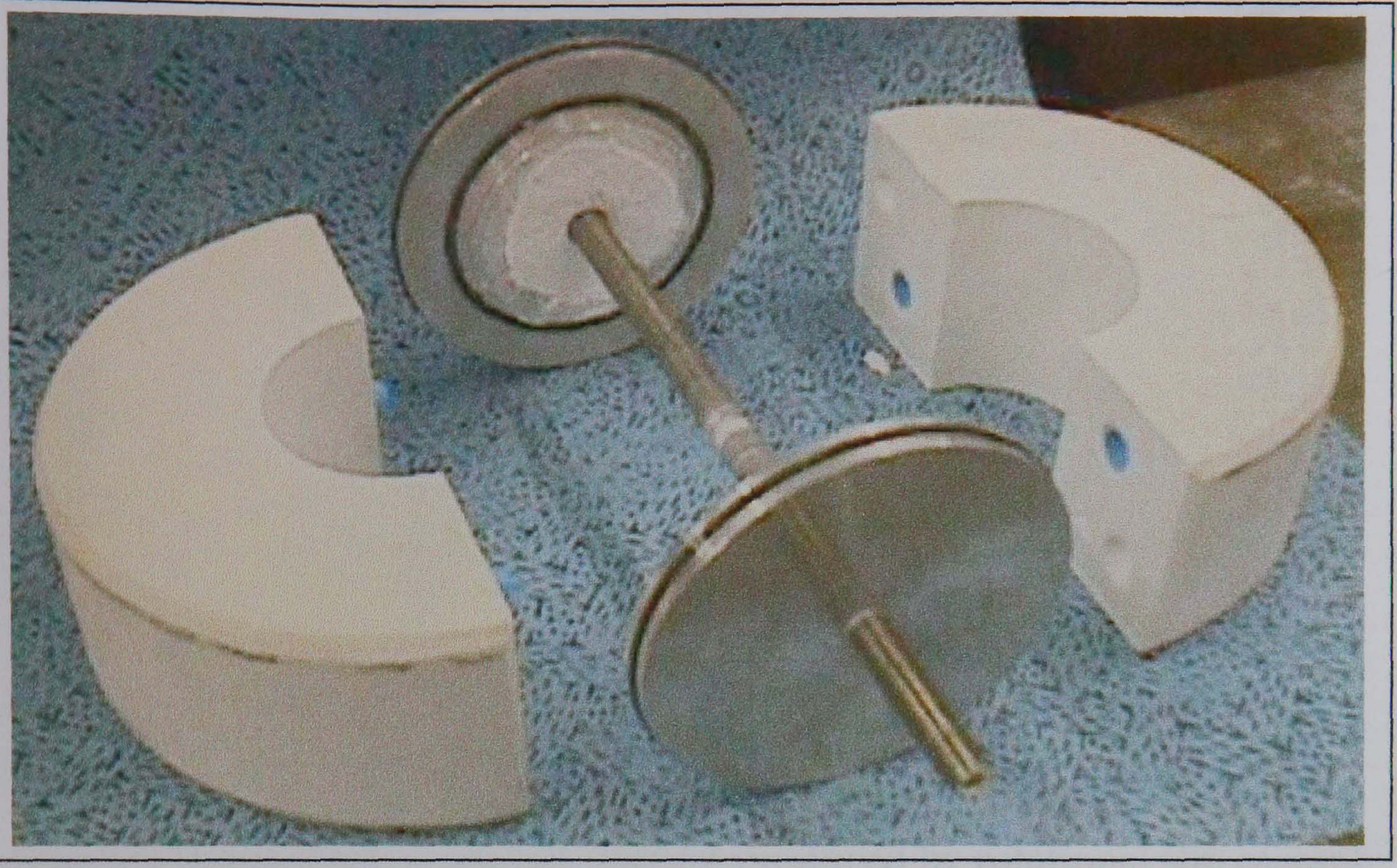

Figure 16 Rotational slip casting mould

Owing to the peripheral interest of this bearing geometry to the main research objectives, a thorough investigation was not carried out, and so the process was never optimised. However, it did show that it is possible to produce a bearing of journal type geometry, as illustrated in figure 17.

Figure 17 Porous ceramic journal bearing produced by rotational slip casting

This figure shows a bearing produced by rotational slip casting, and though not perfect, indicates that with further work this could be a possible method of manufacture. What is shown is a complete journal and a fractured piece from another slip cast journal. This fractured piece shows an interesting characteristic of slip casting. Midway through the thickness of the section, a line can be seen. This line marks the point where the rate at which the removal of water from the slip is no longer controlled by the capillary action of the mould, but instead by the powder deposited on the mould wall that the water must first pass through.

This set of trials used 0.5µm powder with a load of 300g of alumina powder ball milled for 24 hours in a solution of 200ml of slip liquid.

3.1.5 Injection Moulding

Injection moulding trials of the porous ceramic bearings were undertaken on a Dassett 30-tonne co-injection moulding machine, shown in figure 18 below.

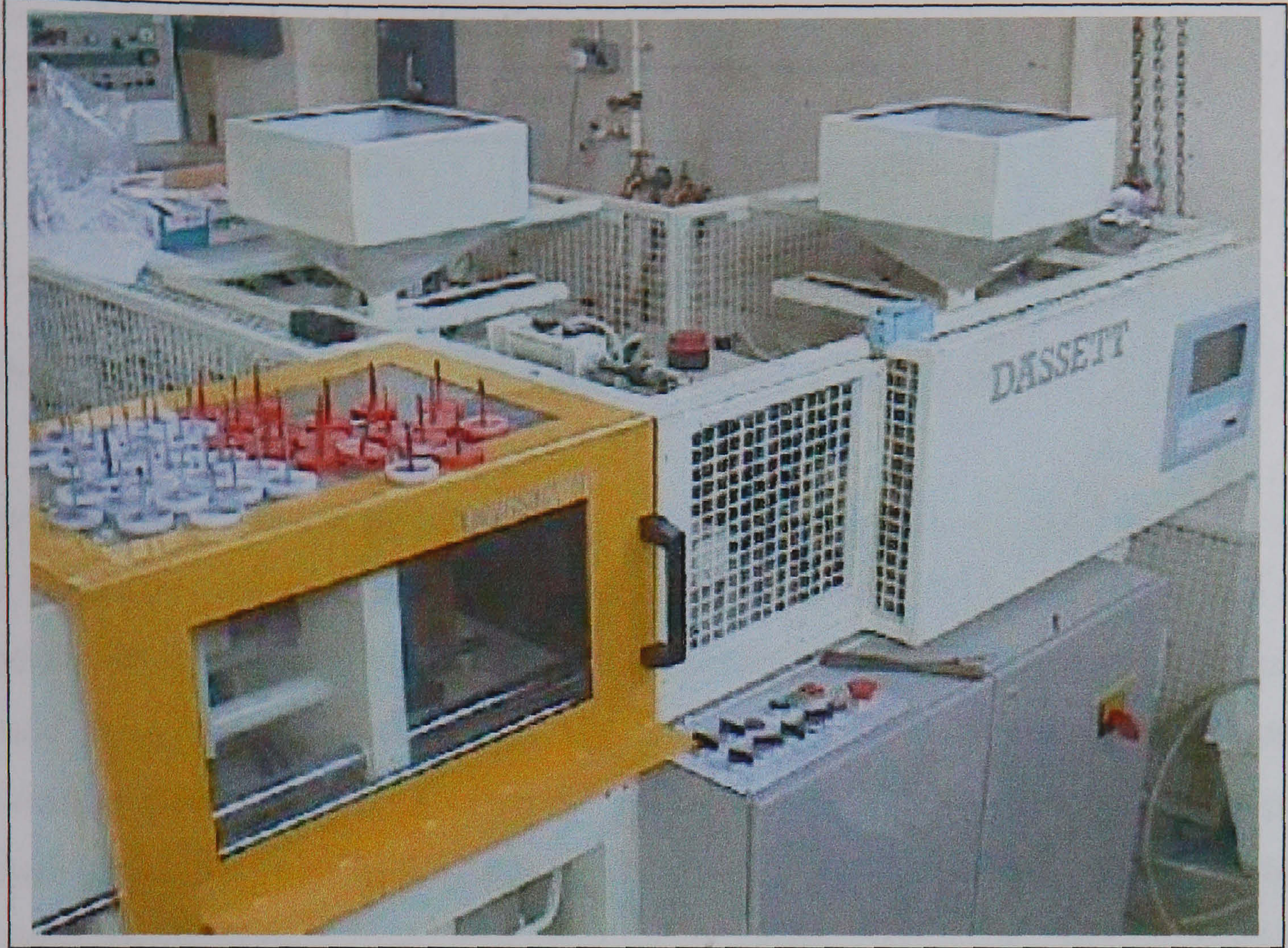

Figure 18 Dassett injection moulding machine

This machine has two separate injection moulding barrels mounted at 90° to one another for the purpose of co-injection into the same mould. This allows two separate materials to be introduced into a mould cavity at different times, giving the possibility of manufacturing a component with a core of one material and a skin of another. This concept has been demonstrated to work with both ceramics and metals [105]. However, for the purposes of the current research, only one barrel was utilised.

As smaller powder sizes had been previously identified as being better suited to porous ceramic bearings [5], injection moulding trials concentrated on 0.5 to 4μm powder sizes. Based on previous research, the powder volume fractions used for the feedstock were as follows:

Table 3 Feedstock volume fractions

Powder Size	0.5µm		1µm	4µm
Volume Fraction	50%	55%	50%	60%

The majority of the work carried out was on the 0.5µm powder systems.

Before moulding was possible it was necessary to mix the ceramic powder with a binder system, in a process known as compounding. The ingredients of the binder system are chosen to provide a workable viscosity to the mixture so it may be easily injected into a mould at the correct temperature. Another consideration related to the choice of ingredients is their removal from the part once moulding has taken place. As a two stage debind was planned, wax formed a significant volume fraction of the blend. The constitution of the blend used is shown in the following tables [105]:

Table 4 For 50% alumina by volume

Material	Weight %
Alumina	80.82
Polypropylene	11.48
Paraffin Wax	6.11
Carnauba Wax	1.33
Stearic Acid	0.29

Table 5 For 55% alumina by volume

Material	Weight %
Alumina	84.18
Polypropylene	9.44
Paraffin Wax	3.04
Carnauba Wax	1.10
Stearic Acid	0.24

Table 6 For 60% alumina by volume

Material	Weight %
Alumina	90.94
Polypropylene	5.41
Paraffin Wax	2.88
Carnauba Wax	0.63
Stearic Acid	0.14

All of the values in the above tables are quoted in terms of weight % instead of volume % to ease repetition of the system.

Polypropylene is a semicrystalline polymer, which in common with other semicrystalline polymers, becomes a viscous liquid when melted. This material provides the bulk of the binder system and is incorporated to allow the blend to be more easily moulded. Paraffin wax is incorporated as the main constituent to be removed during the solvent debind. The carnauba wax is added to help bind solvents and oils present in the polypropylene from sweating out during moulding. Stearic acid fulfils two roles. Firstly it acts as a plasticiser to the polypropylene, and secondly it serves as a surfactant and helps keep the ceramic powder uniformly dispersed [111].

The ingredients for the binder system blend were firstly ground into a powder form to ensure a more even mixing. This was done by cooling the waxes and polymers with liquid nitrogen to below their glass transition temperature to make them very brittle, and grinding in a household coffee bean grinder.

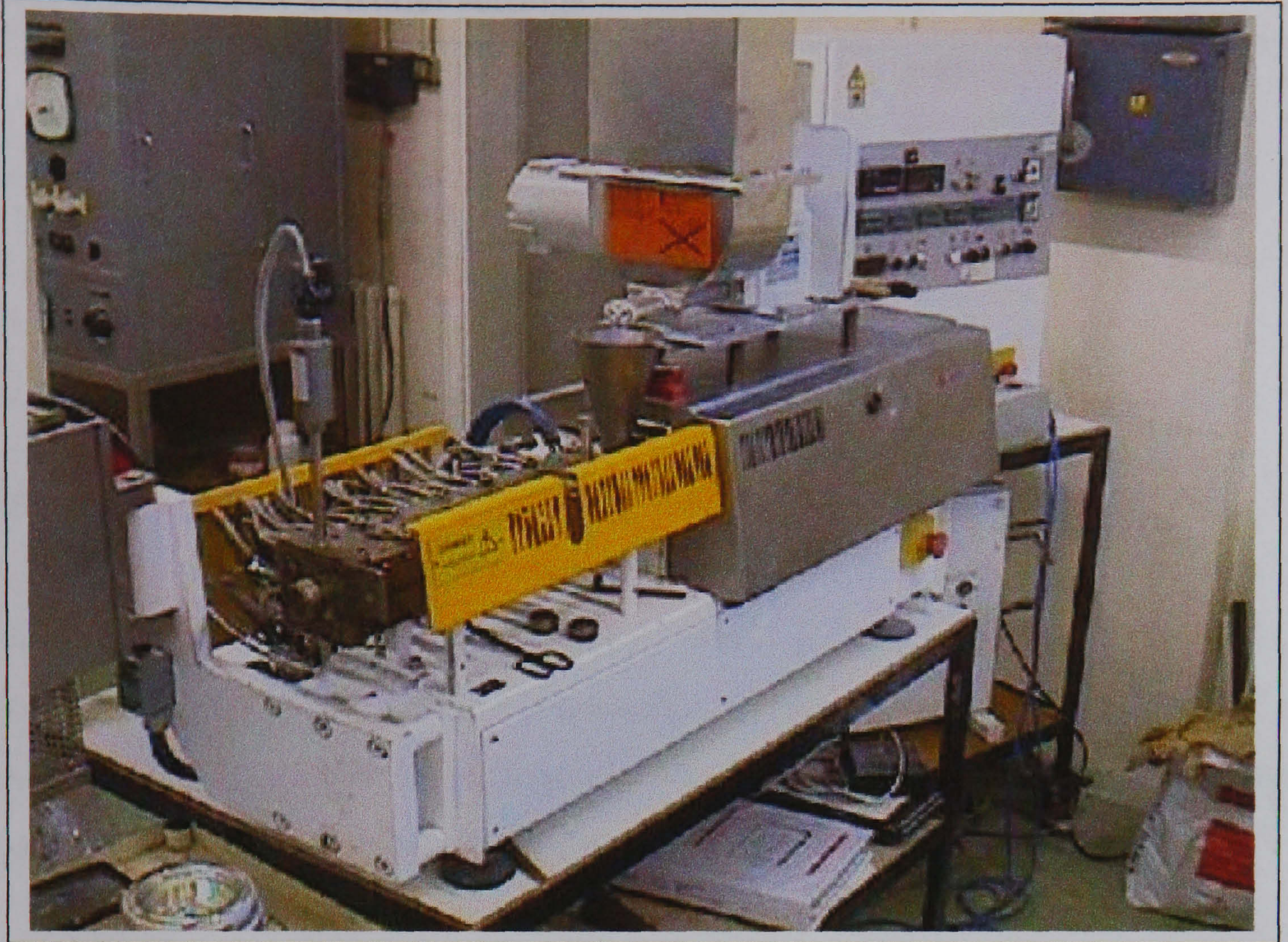

Figure 19 Twin screw extruder

The initial mixing was done manually in clear plastic bags. This meant that it was possible to visually see the uniformity of the mix, as the different colours of the components became blended together. This also avoided the problem of the waxy constituents becoming adhered to the sides of the mixing container and not being incorporated into the blend, as was found when using the Turbula TC5 figure of eight mixer.

Once the blend was mixed to a satisfactory level, it was further processed in an APV MPF19 twin screw extruder, shown in figure 19. The purpose of this stage was to produce a more homogeneous feedstock by exposing the blend of powders to conditions above the melting point of all of the binder components and use the shearing action of the twin co-rotating screws to create a uniform combination of alumina, polymers, and waxes. Typical settings for this machine are shown in the following table:

Table 7 Twin screw extruder settings

Parameter	Setting
Barrel Pressure	220 Bar
Barrel Temperature	240°C
Screw Speed	300 rpm
Torque	20%

These settings were as used previously, and found to be suitable for the blend of materials used here [5, 105]. The resulting extrudate was allowed to cool before being pelletised to provide the correct type of feedstock for the injection-moulding machine. Some of this feedstock was always used to purge the barrel before moulding began to ensure that the risk of contamination from other materials that may have been used in the machine was minimised.

The conditions that the injection-moulding machine was run at are tabulated in Appendix B. These are shown for the 55% alumina blend, but did not vary greatly from blend to blend. These conditions were arrived at by starting with those used successful previously [105] and modifying the various parameters to optimise the conditions for each specific material. For this the experience of the injection moulding machine operator was invaluable in recognising the various moulding faults and knowing the correct parameters to adjust in order to overcome them.

The design of the mould used for the thrust bearings was based on theory for the injection moulding of polymers. Although ceramic injection moulding has been used for many years now, it was surprisingly difficult to obtain mould design data and guidelines specifically for the moulding of ceramics. Instead, existing tried and tested design parameters were used from design handbooks, albeit is slightly modified form to account for the presence of a ceramic phase [110, 111, 112, 113, 114, 115]. The resulting mould was manufactured from the drawing in Appendix G, and is shown mounted in the Dassett machine in figure 20 below.

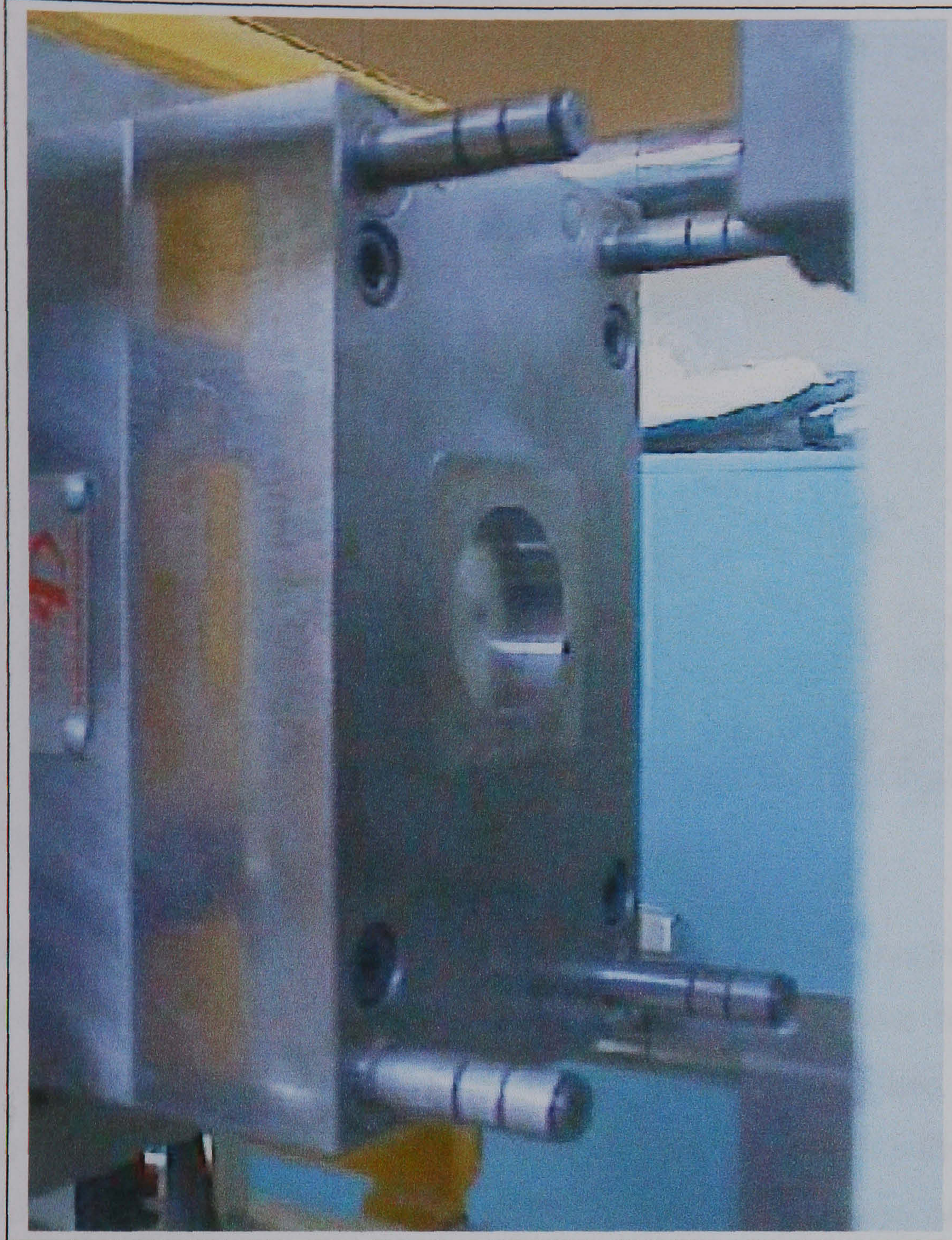

Figure 20 Mould for thrust bearings

This gave a mould of internal dimensions of diameter 55mm by 10mm deep. It was of some initial concern that the thickness of the green bearing would be too great as problems had been encountered in thermal debinding 4mm thick specimens previously [5]. However, this was successfully overcome, as mentioned in the section on sintering.

Shown below in figure 21 are a selection of green as-moulded bearings and full sintered and ground bearings.

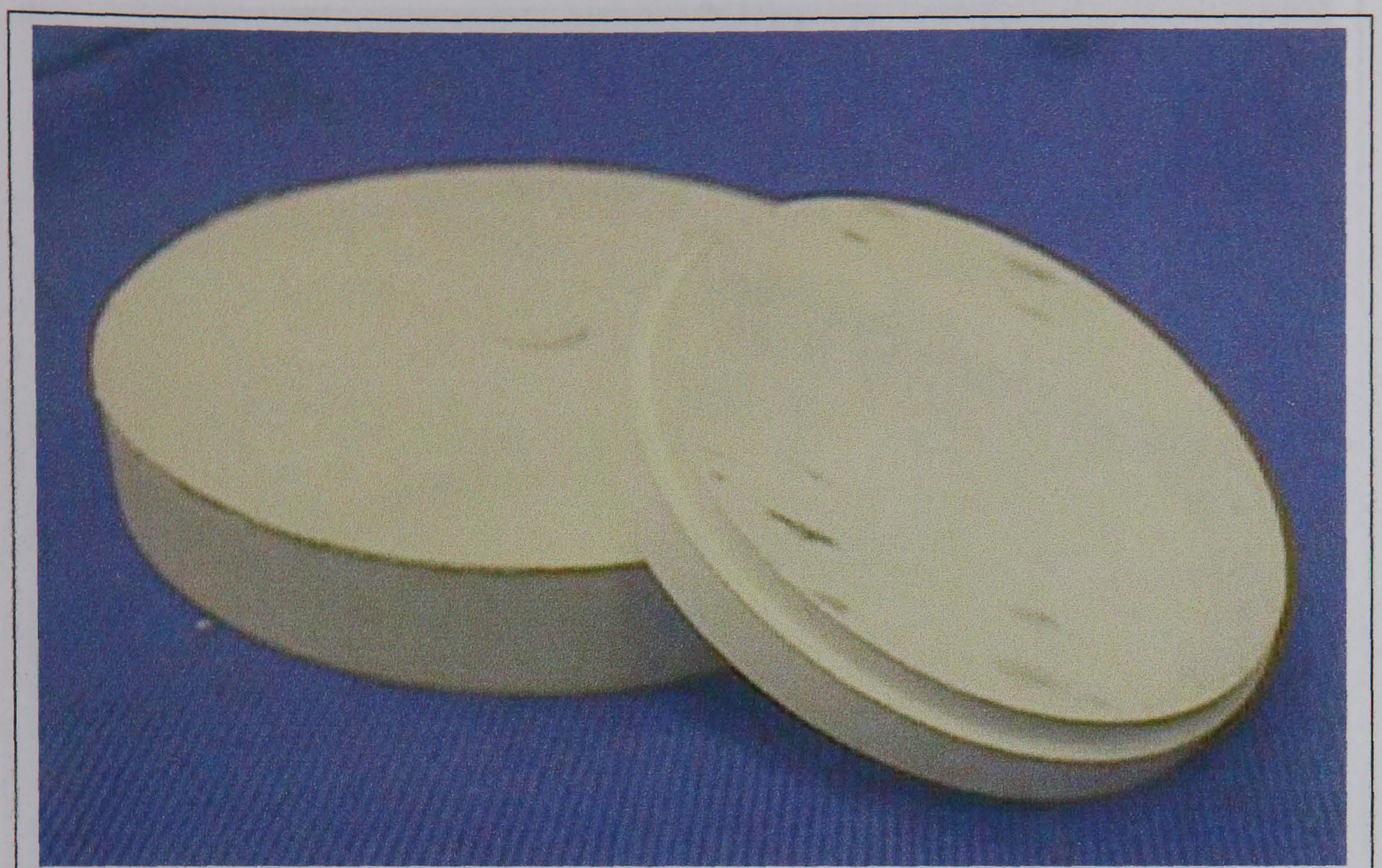

Figure 21 Green and sintered thrust bearings

Several green thrust bearings were conventionally machined to introduce features which it was hoped would accurately survive the debinding and sintering processes. Green machining is obviously less demanding than grinding a sintered ceramic piece as the body is much softer and less brittle. Also the range of machining tools for the incorporation of features into the bearing is greater, once sintered the bearing was limited to cylindrical and horizontal grinding whereas green machining could include drilling, lathe operations, sawing, etc. The purpose of this test was to check that if any detailed features were required would it be possible to machine them in before sintering. The resulting bearings can be seen in figure 22 below.

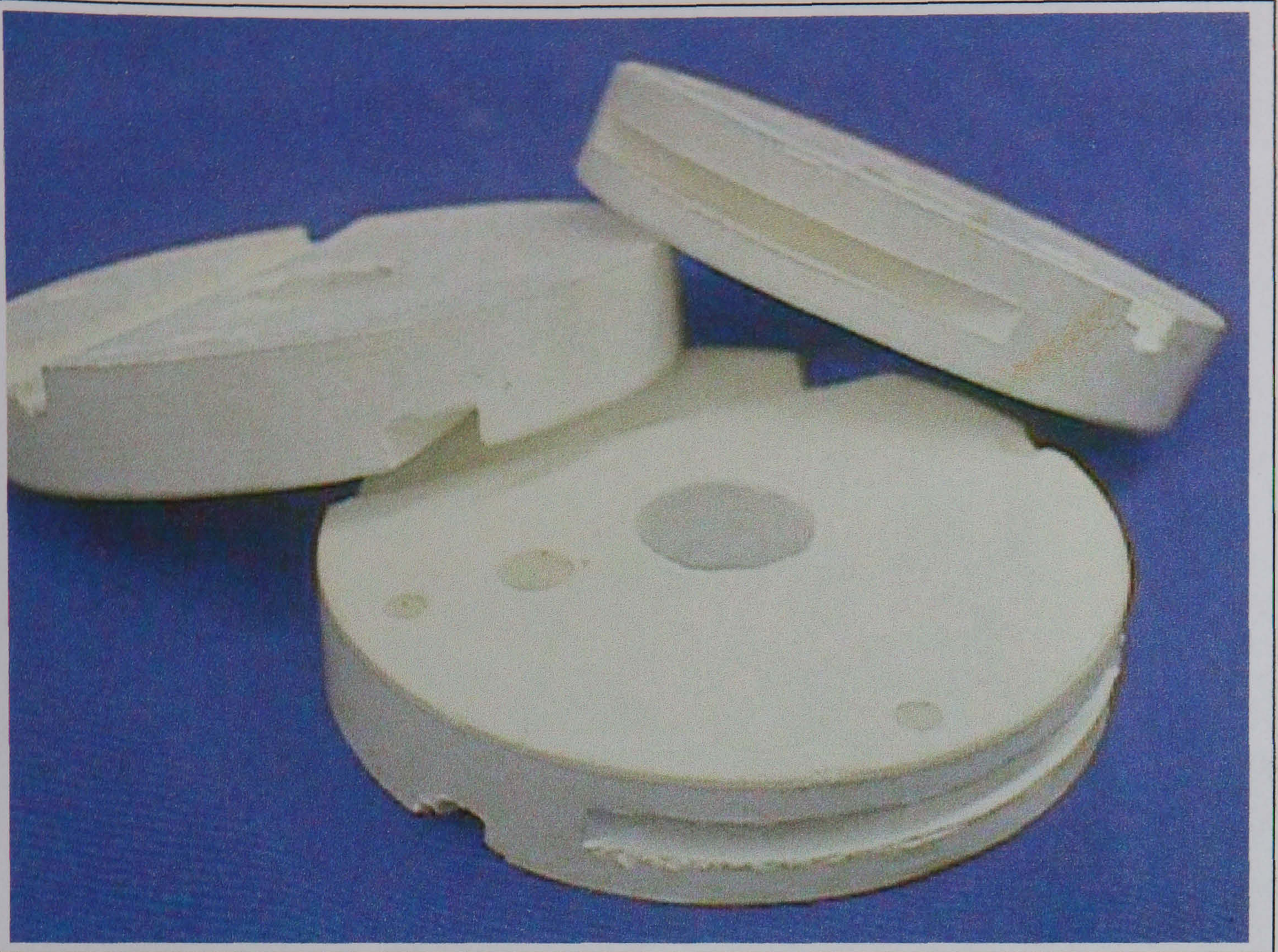

Figure 22 Green machined thrust bearings

The slots were introduced with a bandsaw, whilst the holes were machined out using a pedestal drill. As this was a small test, no attempt was made to optimise the cutting conditions, meaning that the edges were often chipped during machining. All of the features survived, illustrating the robustness of the debinding and sintering process.

Around this time interest from a sponsor led to the development of a slightly more complicated mould for a small journal bearing. As the thrust bearing mould proved so successful it was of interest to demonstrate the versatility of the technique to other geometries. This led to the development of the mould shown in Appendix G, and in figure 23 below.

Figure 23 Journal bearing mould

The resulting journal bearings are shown in figure 24 below. What is shown are a selection of green as moulded bearings, and fully sintered bearings that were finish ground.

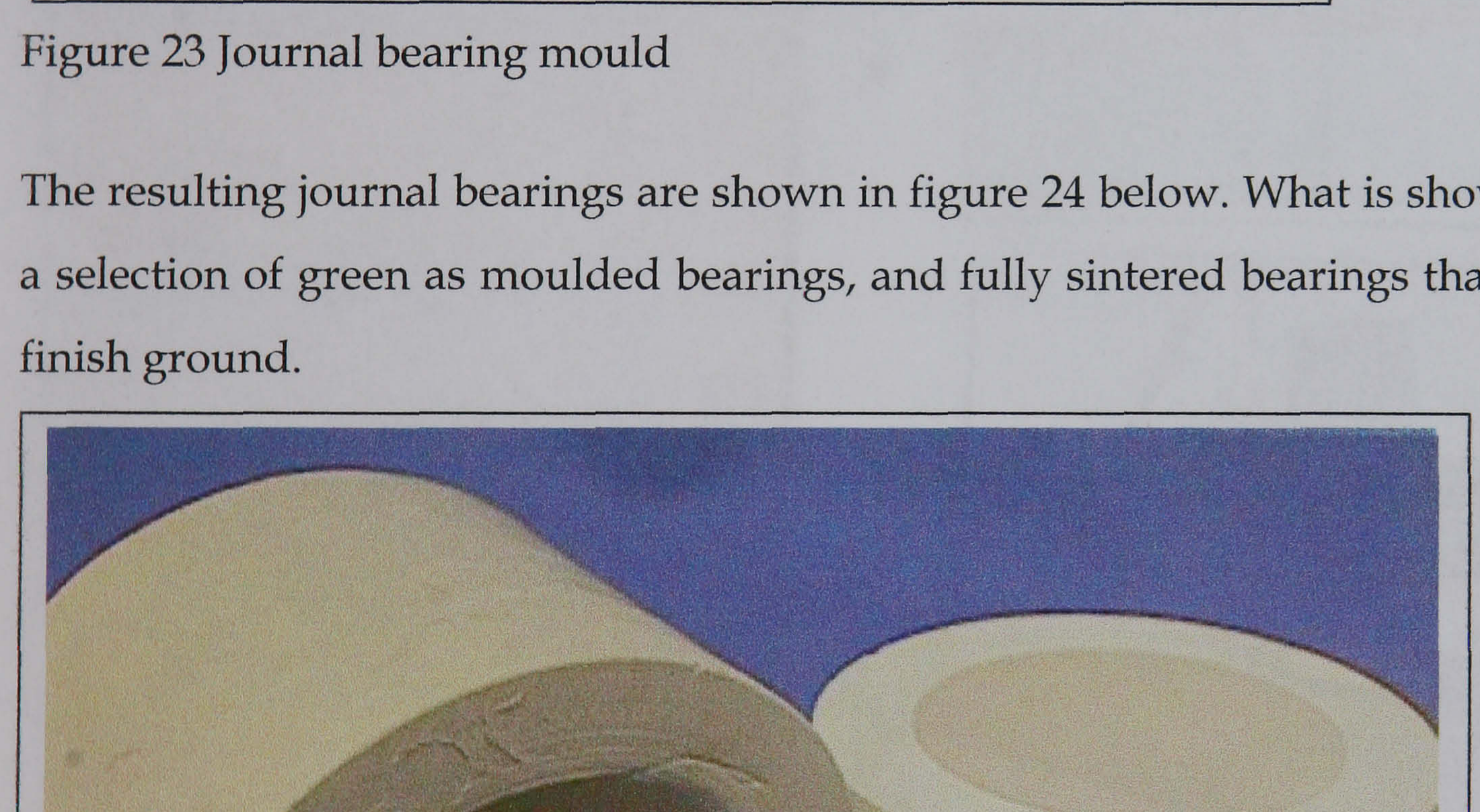

Figure 24 Green and sintered journal bearing

3.1.6 Solvent Debinding

After moulding, it was necessary to remove the wax component of the binder blend in order to open a porous network within the green body. The aim of this system of channels was to ease the escape of the remaining polymeric component during thermal debinding.

The wax was removed through use of a solvent system, which dissolved the wax and left the polymer unaffected. Heptane was found to have suitable solvent properties and so was used. In order to increase the solubility of the wax in the heptane, the heptane was heated. After some revision, the final debinding rig was as illustrated in figure 25 below.

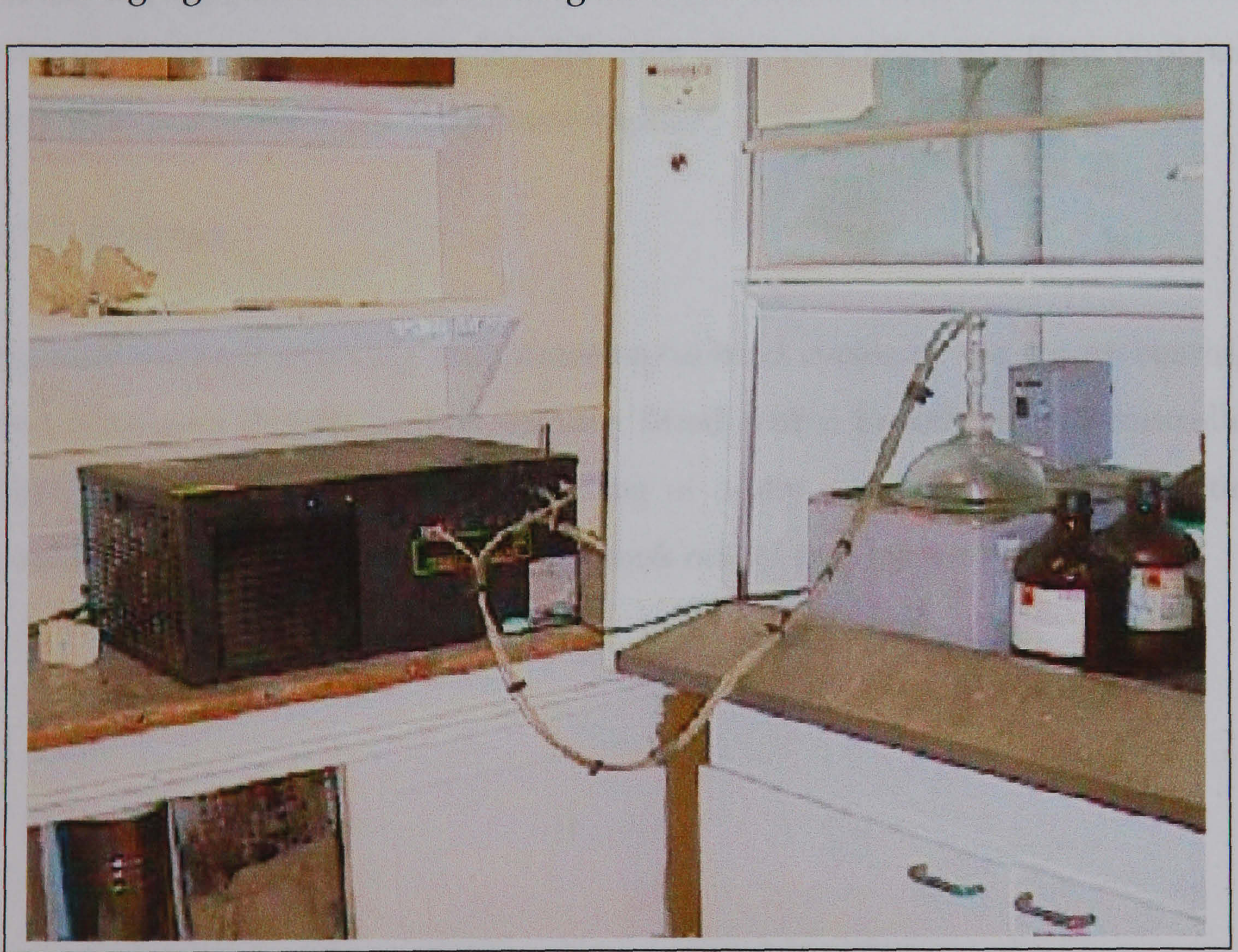

Figure 25 Heptane debinding rig

The main debinding container body was a large glass desiccator which was placed in a heated Grant water bath, model Y22, set at 90°C. A condensing column was fitted to the upper lid, through which refrigerated water was pumped, thus cooling the heptane vapour and condensing it out preventing it

from escaping and allowing it to be recycled. The cooling water was provided by a Whitlenge HC 20 EF chiller, which circulated cold water via a closed loop cooling circuit. To prevent excessive evaporation of the heating bath water, plastic spheres were liberally spread over the exposed water surface.

The samples were placed on a low wire tray towards the base of the desiccator. This was to ensure that once the heptane became saturated and the excess wax began to come out of solution it sank below the samples and did not cover them again. Heptane was added until the samples were completely covered, a smear of silicone grease was applied to the lid to ensure a good leak proof seal, and the cycle was begun. The debinding process typically took 24 hours, with a charge of heptane proving effective for around 36 hours before becoming saturated and requiring changing. All debinding took place in a fume cupboard to minimise the risk from the solvent vapour.

3.1.7 Sintering

All conventional sintering and sintering/debind cycles of the thrust bearings took place in a Pyrotherm box furnace, fitted with a Eurotherm 818 controller. Depending on whether it was sintering of a slip cast sample or an injection moulded sample, the sintering profile took one of two routes:

Table 8 Sintering parameters

Route	Sinter Slip cast	Sinter Injection Moulding
Primary Heating Ramp	5°C/Min	1°C/Min
Hold Temperature	N/A	100°C
Hold Time	N/A	3 Hours
Secondary Heating Ramp	N/A	1°C/Min
Hold Temperature	N/A	200°C
Hold Time	N/A	1 Hour
Tertiary Heating Ramp	N/A	5°C/Min
Target Temperature	1100 to 1400°C	1100 to 1400°C
Cooling Rate	5°C/Min	5°C/Min

The demonstration injection moulded journal bearings that were manufactured were sintered with the same temperature profile as for the thrust bearings above. The trial large diameter journal bearings were sintered to 1300°C using the ramp rates as for the other slip cast samples detailed above.

Care had to be exercised with the injection moulded samples, as the temperature profile tended to suffer from considerable overshoot when started. This had disastrous consequences for the samples being sintered. Either the sample would slump, thus losing its shape, or else if the initial heating rate was sufficiently high the sample would burst open. This appeared to be due to gas entrapment within the green body. When heated quickly vapours liberated could not escape fast enough, and pressures built up to the point where the mechanical properties of the green body were exceeded. The solution to this was to take control of the furnace momentarily just after the cycle was started with the manual override option, and reduce the power output level to just a few percent of maximum. Once automatic control was restored the controller operated without any further problems.

3.1.8 Powder Size Classification

The range of powder sizes investigated here paralleled those previously used for porous ceramic air bearing investigations. The actual powder batches used were the same as supplied previously [116], and at that time particle size measurements were made. This work was undertaken on a Micrometrics 5100 Sedigraph machine. Details of the procedure can be found elsewhere, and so is not repeated here [5]. Any reference to powder size contained within this research programme refers to the nominal powder size as specified by the manufacturers.

3.1.9 Combination Route Bearings

Another potential technique that was investigated in the quest to find a robust and simple manufacturing route for porous ceramic air bearings was the combination route, or dip in slip (DIS) bearings. The idea was based on the two-layer approach successfully demonstrated previously, but without the manufacturing complexity and cost associated with that approach [5].

This involved the manufacture of a coarse powder size load bearing section, and the addition of a thin pressure-restricting layer. The 23µm substrates manufactured by vibratory packing into graphite moulds and HIPing were used as the basis for these bearings. It was then intended that one face of such a substrate be placed to a set depth in a slip of 0.5µm alumina, prepared in accordance to that specified earlier, for a set time. It was hoped that capillary action would take the slip into the porous 23µm body where it would dry out once removed from the slip, and deposit the fine powder to form the pressure restricting layer once sintered.

Due to the low number of samples tested and change in parameters, it is impossible to draw any pertinent information regarding the change in character

of samples tested and change in parameters, it is impossible to draw any pertinent information regarding the change in character of the bearing from the data presented here. Owing to greater interest in slip casting and injection moulding, and time restrictions, this method was never fully investigated.

3.1.10 Silicon Nitride Bearing Preparation

An initial permeability test on the silicon nitride bearings supplied by a sponsoring company revealed much lower and more variable than expected values of permeability. An investigation on the SEM revealed a surface that appeared smeared in a ductile manner. These were ground as specified in section 3.5.2. A sample micrograph is shown in figure 26.

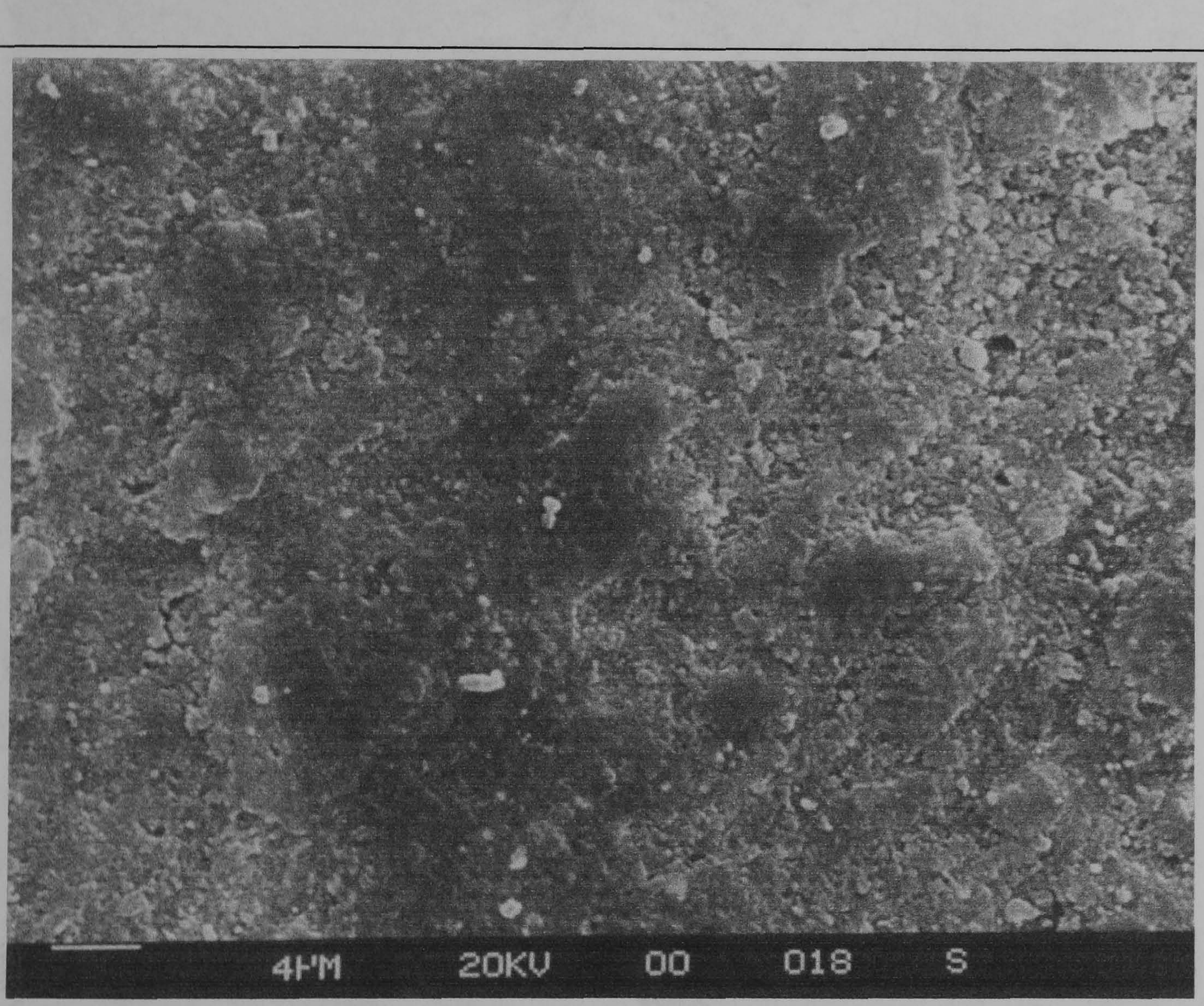

Figure 26 "Smearing" on the surface of a silicon nitride bearing

Additional work was undertaken on these bearings to clean the surfaces to improve the flow of gas. This was done on a CUPE single point diamond precision turning lathe. The resulting finish was then much cleaner, and an

improvement in the permeability test values was noticed. The diamond tool tip is shown in figure 27, indicating that the smearing seen in the micrograph was

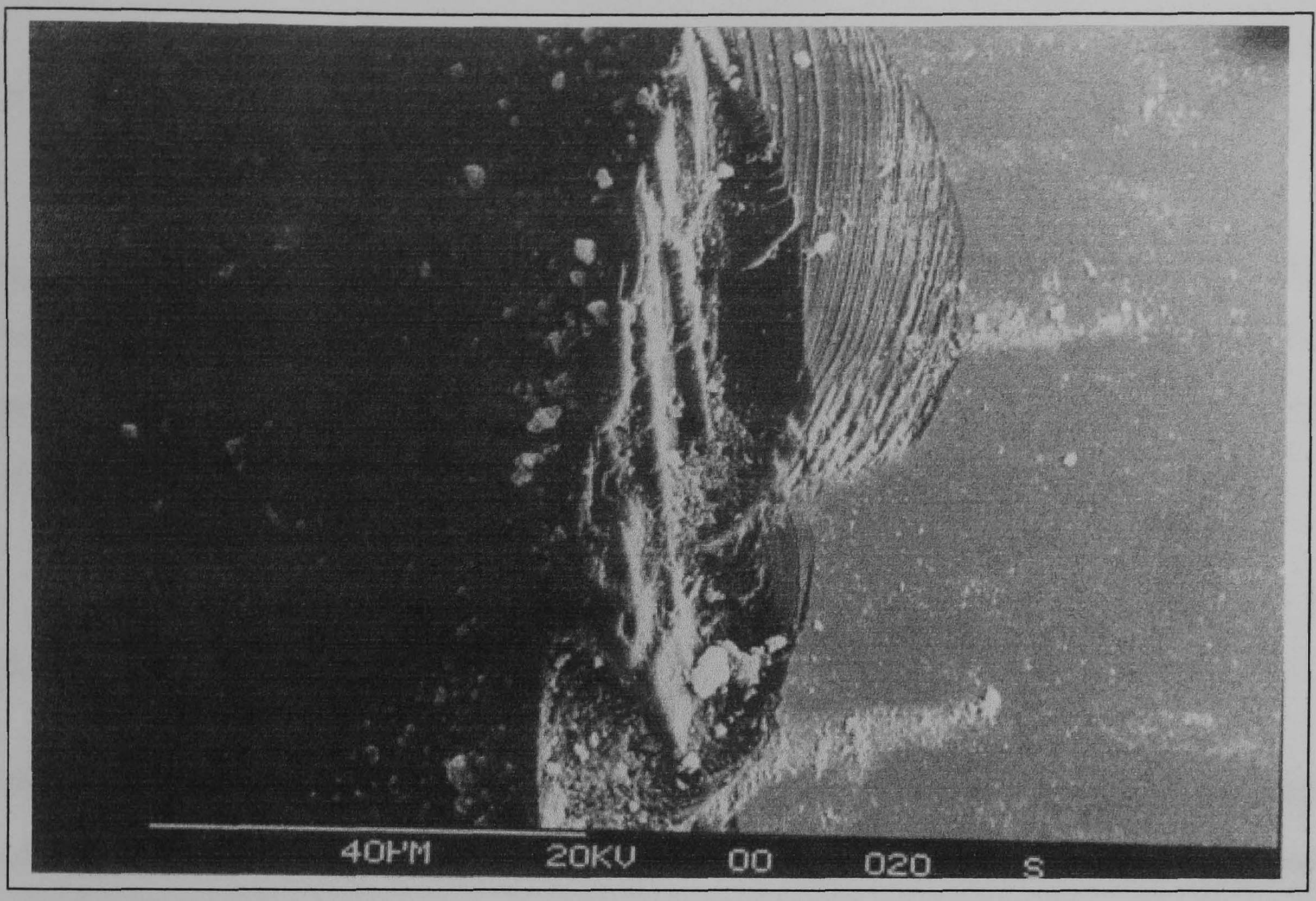

certainly not ductile.

Figure 27 Cutting edge of diamond tool used against silicon nitride bearings (Courtesy Paulo Beltrăo)

3.2 Mechanical Properties

The structural requirements for the bearing were briefly mentioned earlier. The maximum deflection permitted under working load was to be 10% of the working bearing gap. Using equation 8 given earlier and rearranging for E, the modulus, we obtain:-

$$E = 0.07 \frac{\Delta P . r_p^4}{\delta_c . z_p^3} 12(1-\upsilon^2)$$

Equation 9

$$= 100\, GPa$$

The working stress that the bearing sees is also an important parameter, and can be calculated from the following simple equation [84]:-

$$\sigma = \frac{3pr_p^2(3+\upsilon)}{8z_p^2}$$ Equation 10

giving a working stress of 6.6MPa. A target of 35MPa was chosen for the bearings to allow a good margin for any uncertainties. Previous work with porous alumina indicates that it is possible to comfortably exceed the working stress even when a high volume fraction of porosity is present [5].

3.2.1 Density Measurements

The density measurement techniques employed here were a modified version of ISO 2738: 1987, and density calculated from the measured volume and mass of the samples.

This calculation can be shown from the two following equations, the first calculates the volume of the sample;

$$V_s = \frac{m_1 + m_4 - m_5}{\rho_w}$$ Equation 11

And the second calculates the open porosity;

$$\zeta_0 = \frac{m_1 + m_4 - m_5}{\rho_w . V_s}.100$$ Equation 12

The modified version of ISO 2738: 1987 was developed at Cranfield University specifically to address shortcomings in the standard with respect to porous alumina bearings [5]. Two changes resulted, firstly the choice of oil for impregnation was rejected in favour of deionised water, and secondly, the vacuum degassing of the sample and impregnation of liquid procedure was changed.

Alumina has a natural affinity for water, which aids wetting of the surfaces during the density measurement process. Oil, the recommended fluid, is difficult to remove completely from the pores, and is not required in this case for corrosion resistance as it may be for metals. Other low surface tension liquids such as toluene and xylene that aid the surface wetting are flammable and have health risks related to their use. This effectively precludes their use.

The changes to the vacuum degassing stage were found necessary due to incomplete impregnation of the samples, leading to incorrect density measurements. The standard advocates placing the sample in the measurement liquid and drawing a vacuum until no further bubbling is observed. Owing to the fine pore size of the smaller powder size bearings and the resulting high surface tension within these pores, not all the air escaped.

The solution was to vacuum degas the sample and liquid together until no further bubbling was seen, then let the degassed bearing enter the liquid. The surface tension effect could then be ignored, leading to full penetration of the pores upon repressurisation to atmospheric pressure.

The sample was first weighed after thorough drying to give m_1, before impregnation with the liquid to determine the porosity by Archimedes principle.

The vacuum evacuation time was set at a minimum of 15 minutes, longer if required. Once fully impregnated the sample was removed from the liquid and the excess water was wiped off. The sample was then weighed on a previously calibrated Sartorius Type 1712 electronic balance giving m_2. m_3 and m_4 are the weight of the weigh scale pan upon which the sample was placed, as measured in air and water respectively. The sample was then placed on the weigh scale pan and reweighed fully immersed in deionised water, which gave m_5.

This modified procedure proved reliable and reproducible for repeat density measurements carried out on the same sample. It was also more accurate than the standard.

A quicker, though slightly less accurate method of determining the density of the porous samples, was by calculating the bulk volume by measuring the geometry, and weighing the sample dry. This error was later found to be within 3%.

The sample was first ground to a regular geometry such as a disk, and the dimensions measured with a Mityotoyo digital vernier caliper, Absolute Digimatic model. The dimensions, such as diameter or height, were measured in five separate locations, and an average was taken. The samples were again weighed on a Sartorius Type 1712 electronic balance, capable of resolving down to 1µg.

Knowing the volume of the sample, and the mass, the density was calculated by dividing the latter by the former. This method was compared to the previously described water impregnation technique, and was found to be within a few percent of the figure quoted by that method. Owing to the large number of samples tested, this became the preferred method of determining density due to the time saving potential. As a check, samples were occasionally measured by

use of the water impregnation technique, but no significant errors were ever found.

Table 9 Comparison of water impregnation with geometrical density measurements for 0.5µm alumina

	Measured ρ	% Difference	Measured ρ	% Difference	Measured ρ	% Difference
Water Method	2.612g/cm^3	N/A	2.066g/cm^3	N/A	2.528g/cm^3	N/A
Geometric-al Method	2.517 g/cm^3	3.77%	2.109 g/cm^3	2.05%	2.655 g/cm^3	4.77%

Table 9 gives a brief comparison of the measurements taken by both the water impregnation technique and that based on the geometry. As can be seen these are very close. Indeed it was the geometrical method that was used previously to check the validity of the modification to the water impregnation technique used here [5]. Closed porosity was found to small enough to be neglected, of the order of less than 1%. This was as expected, as closed porosity does not tend to become prevalent until the latter stages of sintering once the density reaches somewhere of the order of 90%. As the maximum density investigated here was in the region of 75%, closed porosity was insignificant.

3.3 Experimental Rigs

Two experiment rigs were developed specifically for use for porous air bearing research. These were the permeability rig and the stiffness rig. Although both of these rigs existed previously, it was necessary to completely rebuild them, developing new software for their control and data acquisition, adding new instrumentation, and addressing some of the shortcomings of the original design.

3.3.1 Permeability Rig

The main function of the permeability rig was the measurement of permeability in accordance with BS 5600 [117]. This standard lays out a methodology that allows the determination of the fluid permeability of a permeable material in which the porosity is continuous or interconnecting. The tests are carried out in such a manner as to allow the determination of permeability in terms of viscous and inertial coefficients.

The principle of operation for this test is to measure the pressure drop and volumetric flow rate across a permeable material, using a fluid of known viscosity and density.

This rig is shown in figure 28 below.

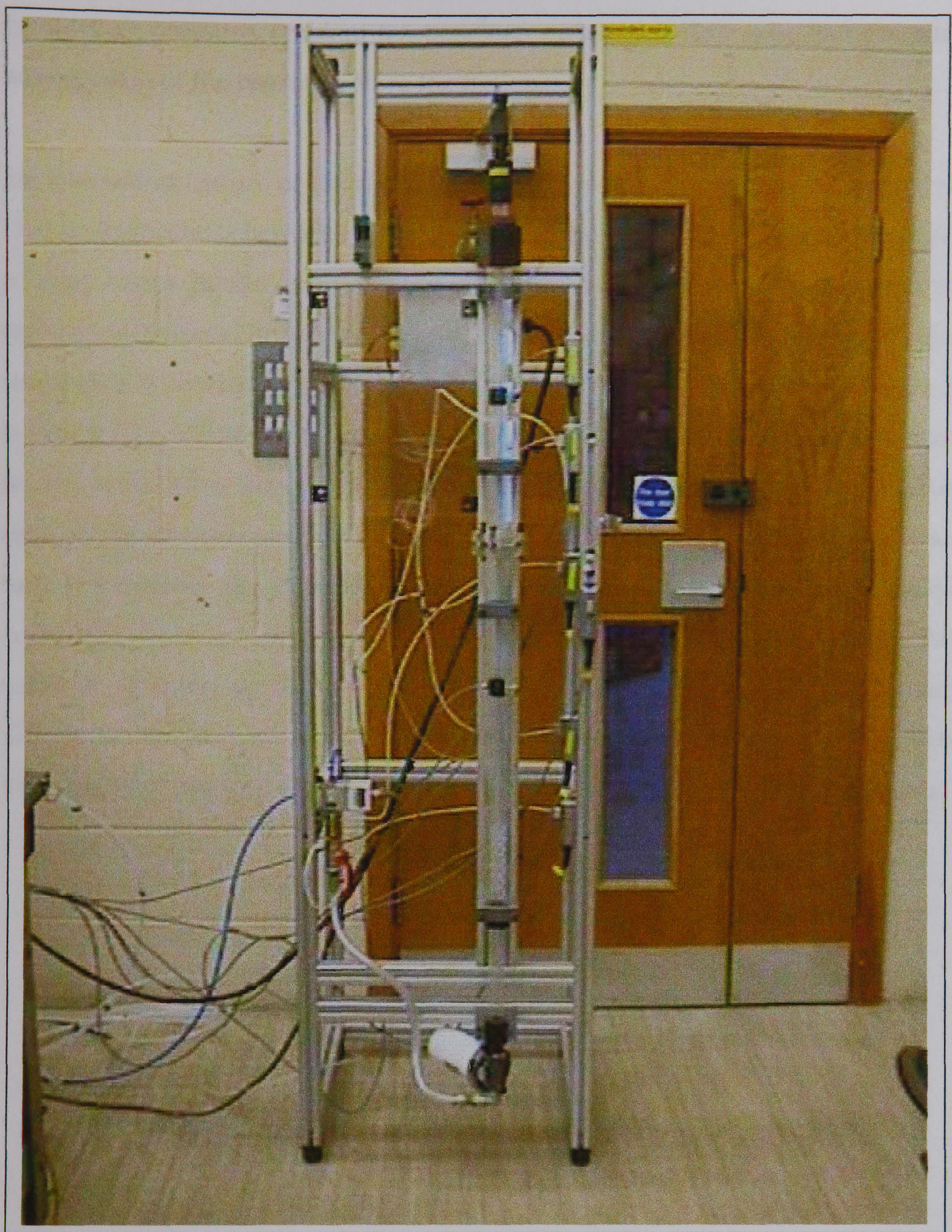

Figure 28 Permeability rig

Figure 28 shows the rig ready for permeability testing. Compressed air is fed to the rig via the computer controlled pneumatic regulator at the base of the rig, the air passes through the bearing in the centre, and is ejected at the top. The pressure drop across the bearing is recorded, along with gas temperature,

ambient air pressure, ambient temperature, volumetric flow rate, and pressure downstream of the bearing before the flowmeter.

An interesting feature of the rig design is the two concentric tube arrangement. This is illustrated schematically in figure 29. This simple detail allows the effect of edge losses in the sample being measured to be ignored. As the sintered ceramic is permeable in every direction, not only perpendicular to the flat surfaces, it is inevitable that some of the high pressure gas supplied to the high pressure face will move sideways to escape to atmosphere. The air that is used for the volumetric flow rate measurements is collected at the exit to the inner tube on the downstream low-pressure side of the rig. The purpose of the outer tube is to balance the pressure in this downstream section by use of a pressure equalising valve situated between the exit of this tube and atmosphere. This valve is adjusted so that as the supply pressure is increased any pressure difference between the inner and outer tubes can be cancelled, so the flow through the flowmeter is in fact a true reading, and not affected by edge losses.

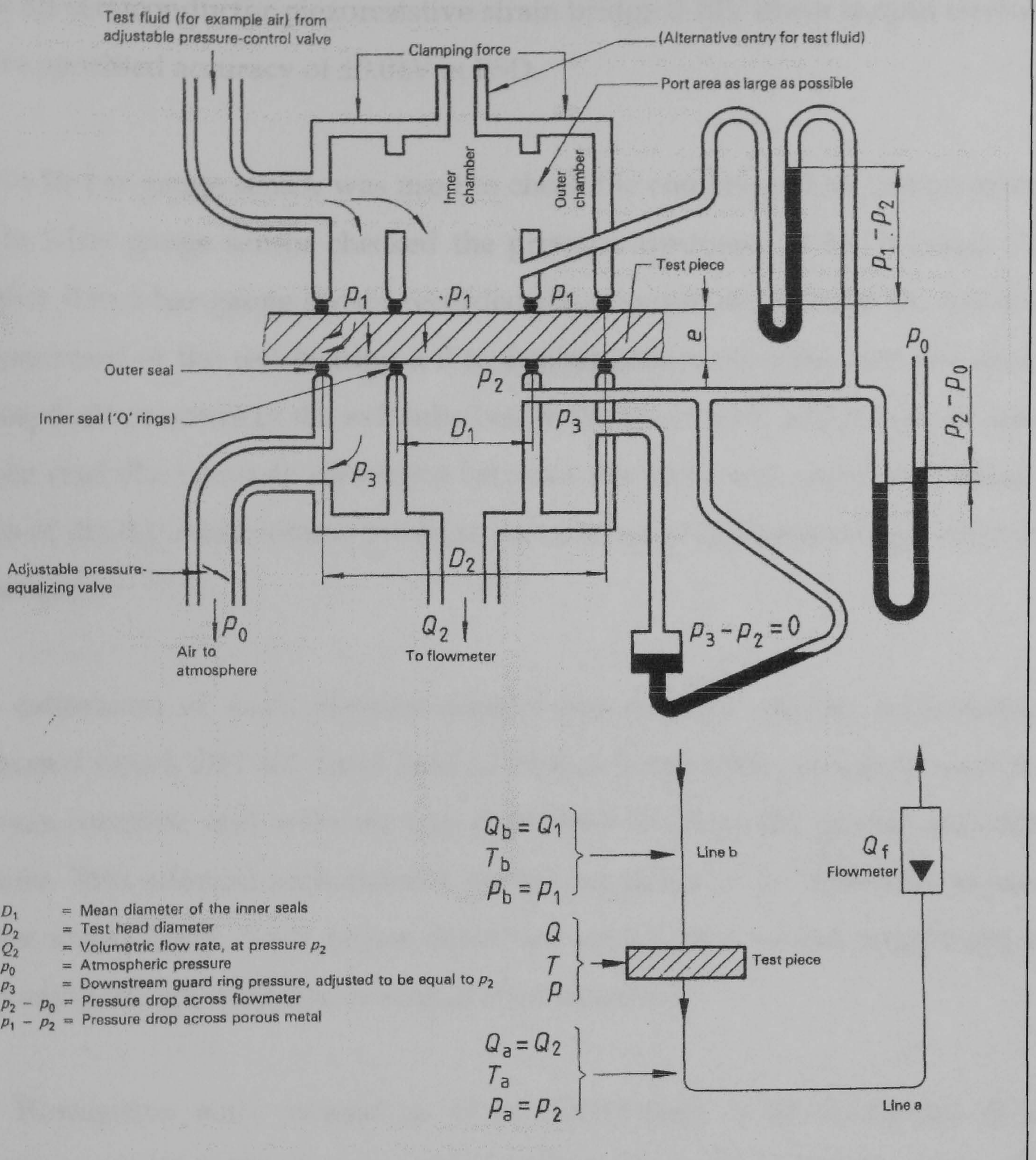

Figure 1 — Guard ring test head

Figure 29 Edge loss compensation (from [117])

The instruments used to record data during testing were all calibrated to ensure accuracy in the experimental results. These instruments consisted of a collection of pressure gauges and flowmeters. All the pressure gauges were Sensortechnics [118] differential pressure gauges, and the flowmeters were Honeywell [119] air and gas mass flow sensors.

In total five pressure gauges were used whose range covered 5 mbar to 10-bar gauge. These were a combination of 144, 144LP, and 103LP series sensors. These

were all semiconductor piezoresistive strain bridge 0-10V linear output devices, with a specified accuracy of ±0.01V at FSD.

A 0 to 10-bar gauge sensor was used to check the compressed air line pressure, a 0 to 5-bar gauge sensor checked the pressure upstream of the bearing, and another 0 to 5-bar gauge sensor recorded the pressure drop across the bearing. Downstream of the test bearing a 0 to 5 mbar sensor recorded any rise above atmospheric pressure in the exit tube before the flowmeter, and a final ±5 mbar sensor read the pressure difference between the inner and outer downstream tubes of the rig. Atmospheric pressure was manually recorded using a mercury barometer.

The calibration of each pressure sensor was checked against a previously calibrated Druck DPI 601 hand held calibrator device. This was done once the rig was complete and software was developed to allow the control and data capture. This allowed each channel on the computer to be calibrated to each sensor individually. Each sensor contained rotary pots for the adjustment of span and gain, allowing fine-tuning of their accuracy.

The flowmeters were ranged as 0 to 0.2l/minute, 0 to 1l/minute, 0 to 5l/minute, and 0 to 20l/minute sensors. These sensors were based on hot wire annenometry principles, with two Wheatstone bridges. The first provides closed loop heater control that is kept at a constant temperature above the ambient gas flow, while the other contains the sensing elements. The larger flow rate sensors gave a linear 1 to 5V output proportional to the measured flow, but the two smaller gave a highly non-linear response.

As these sensors had not been used for more than a year and the original calibration had been carried out using nitrogen rather than air, it was considered prudent to check their calibration. This was undertaken using a bell prover. This device acts as a very large store of air that can be considered to be

isothermal. The temperature and pressure inside the prover is recorded during the test. The air can be discharged at a variety of rates to suit the flowmeter being tested.

A known volume of air is allowed to escape the prover at a constant rate in a known time, thus giving a volumetric flow rate. All readings were over a minimum of 20 minutes to negate any errors introduced due to starting and stopping the test.

It was found that the 0 to 0.2l/minute sensor could be adequately described by a 2nd order polynomial expression and the 0 to 1l/minute sensor by a 3rd order polynomial. Both the 0 to 5 and 0 to 20l/minute sensors were found to have highly linear responses. The resulting calibration graphs can be found in Appendix F.

The output from the thermocouples used were calibrated by immersing them in boiling and iced water.

The compressed air was supplied via a SMC Series ITV2000 electro-pneumatic regulator [120]. This was software controlled with the output of 0 to 5 bar proportional to a 0 to 10V input. The linearity of this device was specified as ±1% or less at full span. After every pressure change several seconds were allowed to pass before recording data in order to allow the device to achieve steady state conditions.

All data capture and rig control was taken care of by specifically designed software run on a Dell 486SX personal computer. The software chosen was LabView 4.1, which allowed a comprehensive programme suite to be built without having to first learn a command line programming language. A full overview of the software developed and operating procedures can be found in

Appendix C to E. The software also re-zeroed all of the sensors before each test was initiated in order to negate any sensor drift that may have taken place.

A 16-channel National Instruments AT-MIO-16D data acquisition card provided the interface to the PC. This was set up in a single ended non-referenced format, to allow full use of all of the channels. A custom power supply box and rig interface box were constructed to supply the various sensors and controllers with the correct supply voltage, and to sort the return signals to allow them to be fed to the correct channel on the data acquisition card.

The permeability rig was designed in such a way that it was capable of more than purely permeability testing. With a small amount of alteration it could also be used for the bubble test, a simple test to determine the largest through pore size, the extended bubble test, which allows the largest surface pore size to be determined, and gives a qualitative assessment of the uniformity of pore size across the bearing surface.

3.3.1.1 Measurement Procedure - Permeability

Once the sample was secured in the rig and the software initiated the test was begun. The appropriate flowmeter was installed on the rig, and pressure was introduced to the lower section of the test rig. All tests were initiated at an opening pressure of 0.75 bar, and continued until the flowmeter approached its maximum calibrated value, or the pressure in the tube reached 5 bar. In the case where a flowmeter did not have the required range to run to 5 bar, a check was made with the next largest meter.

In every case the final flow rate exceeded the initial by a minimum factor of 10, and 18 readings were taken at equal pressure increments. The software automatically calculated a mean value of the data to be recorded at every point in order to eliminate any transient results. Unfortunately the data acquisition system did not prove to be completely inert from electrical noise generated

from other equipment in use in the laboratory despite extensive grounding and shielding, and so each data point recorded was taken as the average of 100 consecutive samples. This was in addition to waiting several seconds between each pressure increase for the flow to achieve steady state conditions. The volume flow, pressure, temperature, density and viscosity of the air were corrected to the mean conditions in the test piece from standard tables [121] in accordance with BS 5600.

The data resulting from this test are then plotted in terms of;

$$y = \frac{\Delta p . A}{e . Q . \eta}$$ Equation 13

$$x = \frac{Q . \rho}{A . \eta}$$ Equation 14

Linear curve fitting by a least-squares method was applied to the resulting graph, and the intercept with the y-axis and the slope of the line are calculated. The value of the intercept gives the reciprocal of the viscous permeability, and the value of the slope of the line gives the reciprocal of the inertial permeability.

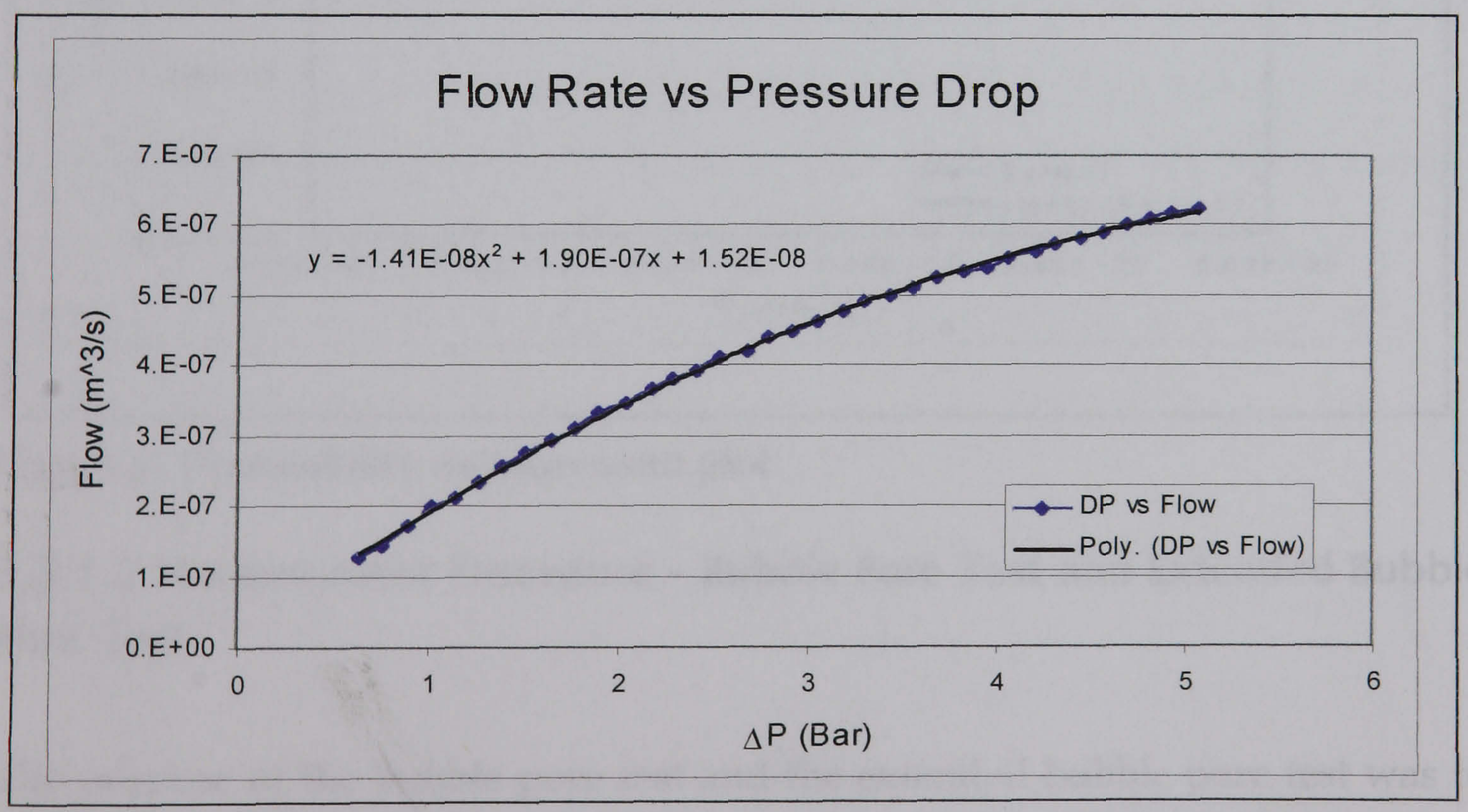

Figure 30 Zero error correction

As was found previously [5], zero errors played a significant part in the accuracy of the test, and so before the data were converted to the format required by the

standard, the recorded flow was plotted against pressure drop. Curve fitting was used to estimate a zero error in the flow that was then either added to or subtracted from the measured value as appropriate.

This was done by obtaining a best-fit line from the data and calculating where it crosses the pressure axis. The value at which this occurred was taken as the zero error. These appear to be due to the poor resolution of the flowmeters at the lower end of their calibration. Figure 30 illustrates a second order polynomial curve which has been fitted to the data to provide a beast fit line. The equation of this line is shown on the figure, and is then used to calculate the zero flow error by setting the x values to zero. Figure 31 gives an example of the graph resulting from the analysis according to BS 5600: Part 3: Section 3.6.

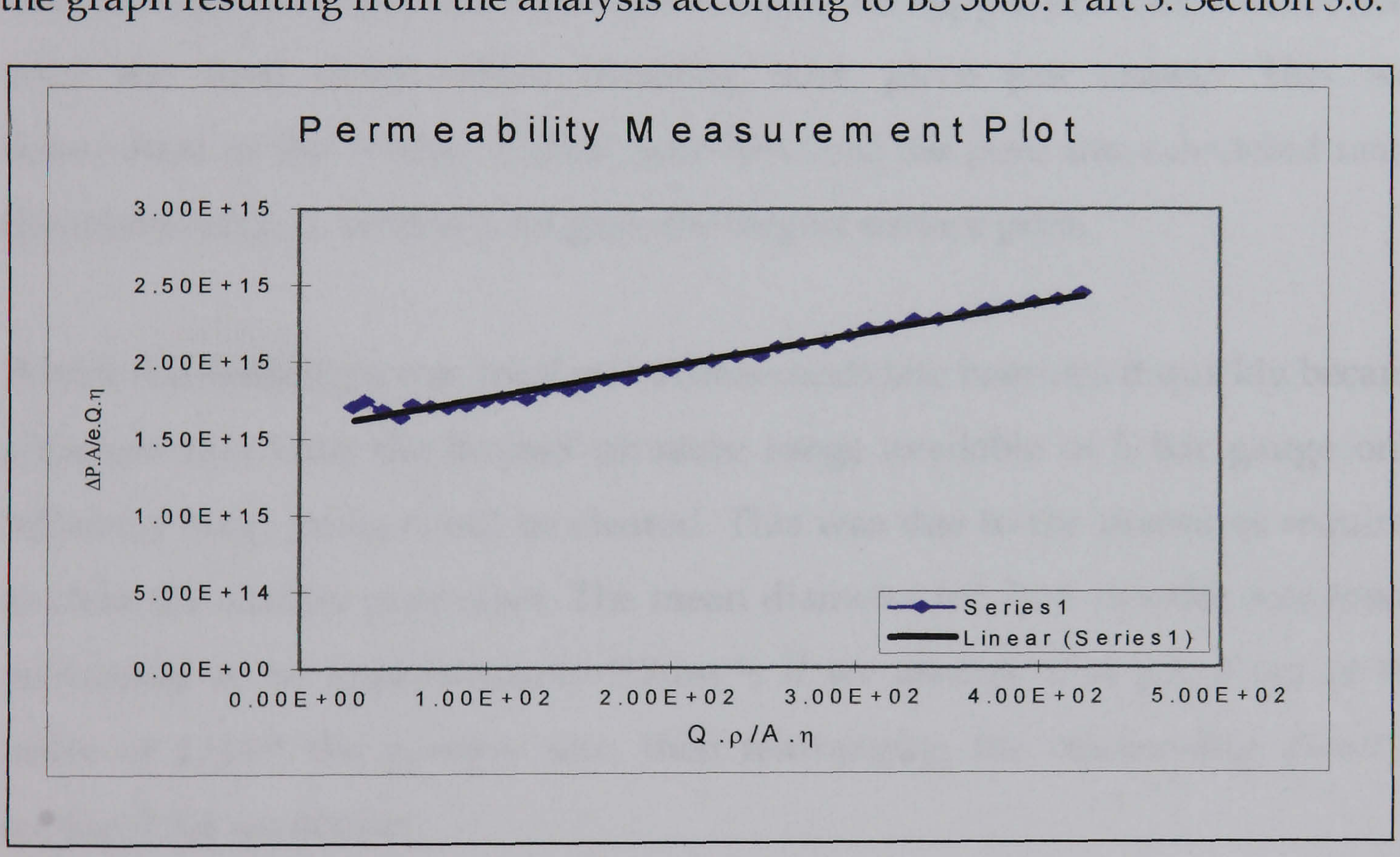

Figure 31 Permeability measurement plot

3.3.1.2 Measurement Procedure – Bubble Pore Test and Extended Bubble Pore Test

The purpose of the bubble pore test and the extended bubble pore test was to estimate the size of the pores within, and on, the surface of the samples. It also provided a qualitative appreciation of the spatial variation of the pore sizes across the surfaces. This test is in accordance to ISO 4003 [39]. The permeability

rig was altered to accommodate this test by removing the mid tube in the low pressure section, and appropriate software was written to control the rig.

The procedure was to impregnate fully the sample with deionised water and apply a pressure ramp of between 0 and 50mbar per second to one side. A known head of water was placed on the low-pressure side, and the pressure at which the first bubble appeared was recorded. The largest through pore was then calculated in accordance with the relationship described in section 2.5.4.

A visual indication of the spatial distribution was possible by continuing to increase the pressure in the supply tube, and pausing the ramp where desired. Once bubbling was general across the surface, the supply pressure was reduced until the final point where bubbling took place just ceased. This was determined as the reverse bubble pore test, and the pore size calculated using the relationship in section 2.5.4 gave the largest surface pore.

Whilst this technique was tried on various candidate bearings it quickly became apparent that with the limited pressure range available of 5 bar gauge only relatively large pores could be cleared. This was due to the pressures required to clear the smaller pore sizes. The mean diameter for 7µm powder was found previously to be approximately 0.7µm [5]. If we assume that pores are of the order of 1/10th the powder size, then rearranging the relationship given in section 2.5.4 we obtain:

$$P_1 = \frac{4.\gamma_w}{d_p} + \rho_w.g.h_w \qquad \text{Equation 15}$$

If we were to investigate a 0.5µm powder whose mean pore size was also 1/10th the powder size, or 0.05µm, the resulting pressure required to clear that pore would be over 58 bar.

Given the constraints on equipment this was obviously not possible. For this reason no further development work was carried out on the bubble pore tests, nor on the dynamic water expulsion test [122, 123, 124, 125, 126], This test has in the past proved valuable for determination of the distribution of pore size within porous bodies [127]

It soon became clear that 4µm alumina powder was the largest powder size that operated in a stable manner as a bearing, and therefore this technique became redundant. Instead another method had to be used assess the pore size distribution.

The university intended to purchase a mercury porosimeter, and advantage was taken of the opportunity to trial equipment from the two competing companies. These were Micromeritics and Quantachrome with their Penetrometer and Poremaster respectively.

A single 0.5µm bearing was sectioned and half was sent to each company for analysis. The resulting data regarding pore diameter is summarised in figure 32 below.

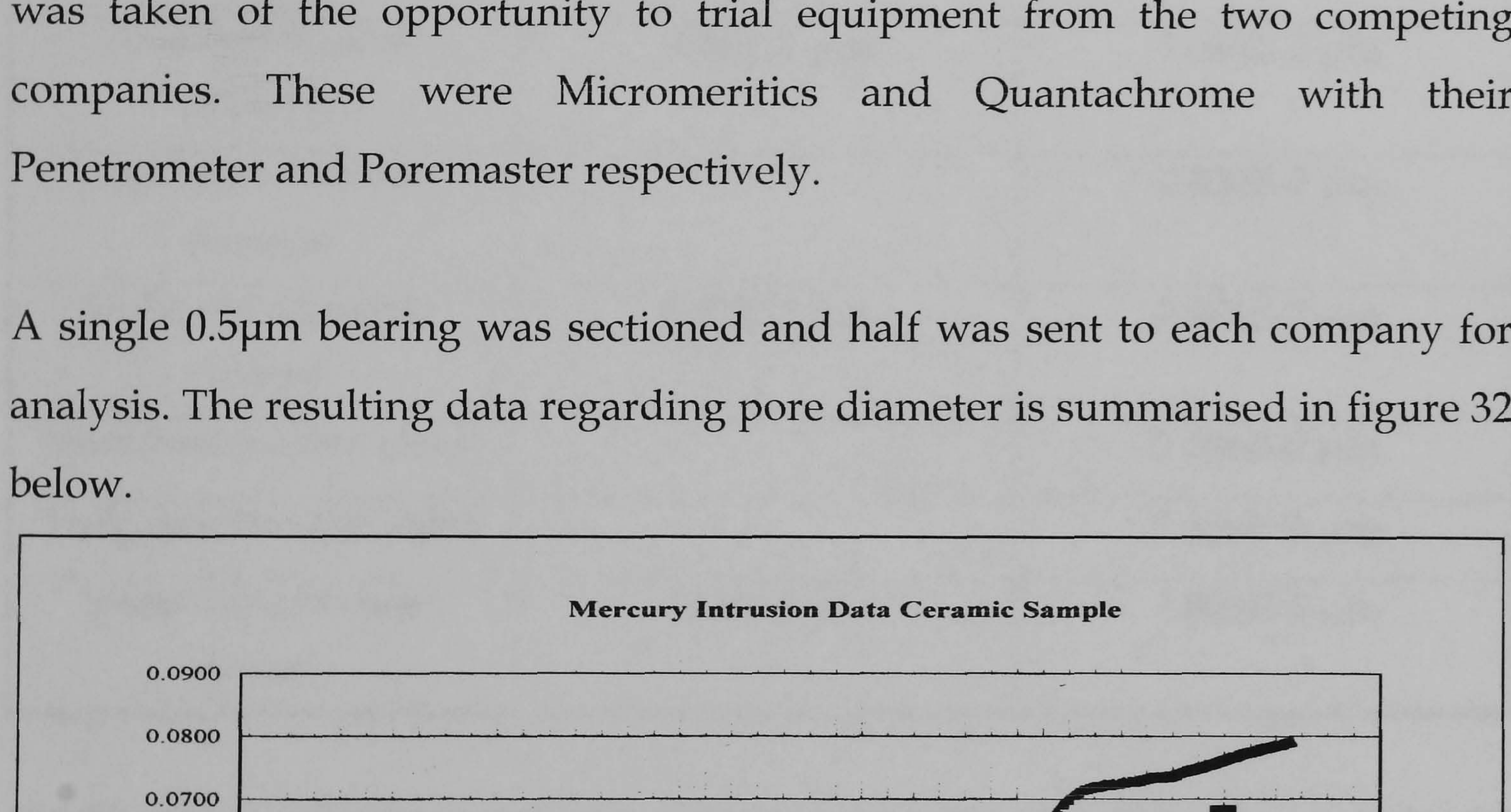

Figure 32 0.5µm pore diameter comparison

What is obvious from this graph is that both sets of equipment are in broad agreement as to the pore size distribution. The relevant data provided from these analyses is tabulated below.

Table 10 Mercury porisimitry comparison

Data Range	Micromeritics	Quantachrome
Pressure Range	0.62 – 59938.23 PISA	0.883 – 29747.932 PSIA
Pore Diameter Range	290.0823 – 0.003µm	202.678986 - 0.006017µm
Bulk Density	3.0358 g/ml	-
Skeletal Density	3.9957 g/mL	-
Pore Surface Area	8.297 m^2/g	7.7771m^2/g
Porosity	24.0236%	-
Mean Pore Diameter (Volume)	3.81E-2 µm	3.506E-2 µm
Mode Pore Diameter (Volume)	-	7.400E-3 µm
Median Pore Diameter (Volume)	6.82E-2 µm	7.571E-2 µm
Mean Pore Diameter (Area)	-	3.506E-2 µm
Mode Pore Diameter (Area)	-	7.400E-3 µm
Median Pore Diameter (Area)	4.18E-2 µm	7.802E-3 µm

All the data in the above table is as reported by the two manufacturers. As the work was done by the manufacturers independently, no further details were available regarding the accuracy, precision, or reproducibility of the machines used.

Unfortunately, it was only possible to measure one sample. This technique for pore size distribution is obviously limited in the current application as the sample is non-returnable due to the problem of incomplete mercury removal from the pores. However, from the above data we can see that the mean pore

size can be taken as approximately 3.5E-2µm. If we were to repeat the calculation earlier to determine the pressure at which the bubble pore test would clear the largest pore, we find that we would require a massive 84.4 bar.

By means of comparison, the density of the above 0.5µm powder size sample as measured by geometry alone was 2.945g/cm^3, an error of 3%.

3.3.2 Stiffness Rig

The purpose of the stiffness rig was to accurately measure the bearing performance under steady state conditions. Figure 33 below shows the actual rig, and figure 34 illustrates the main features.

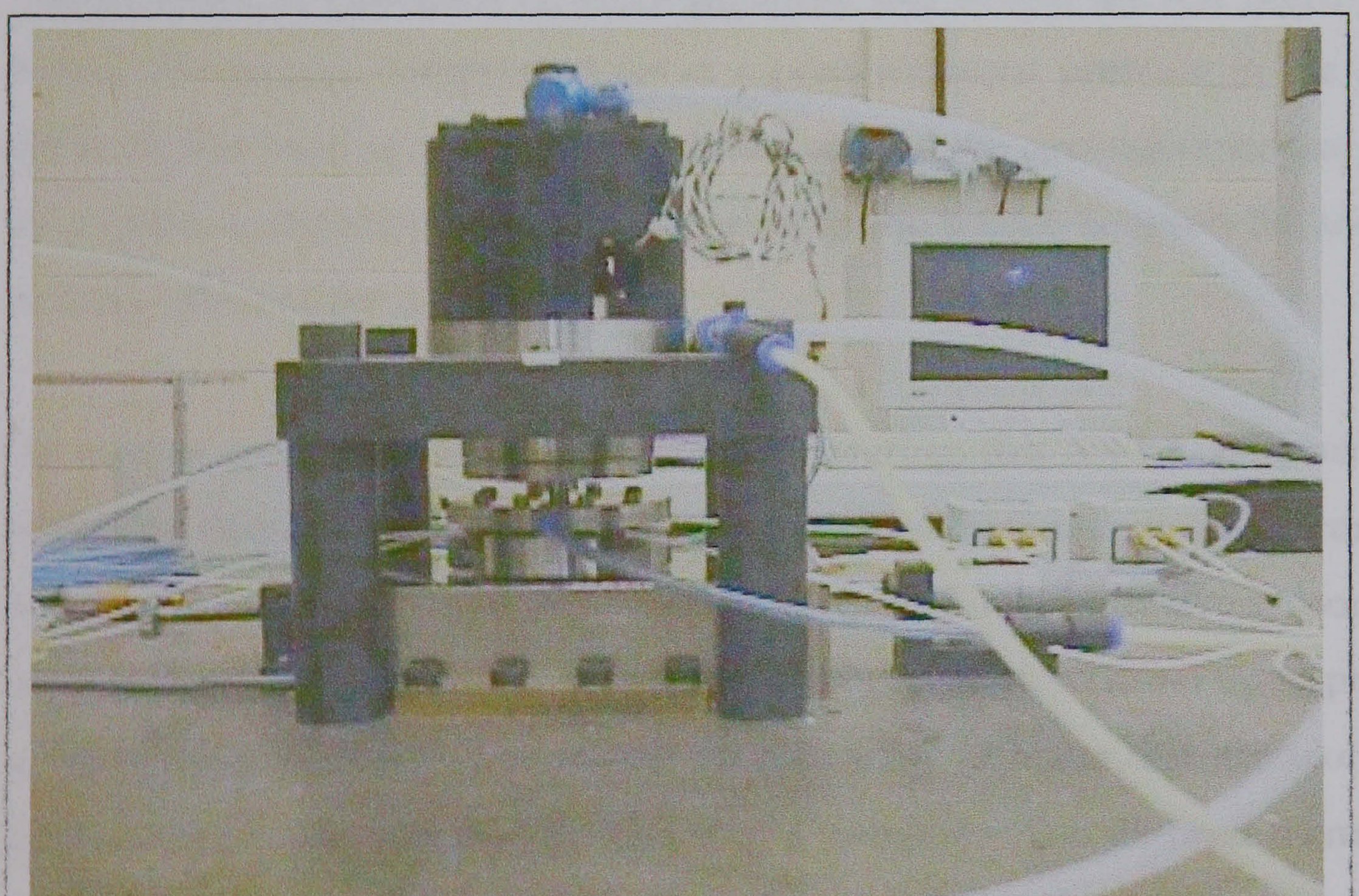

Figure 33 Stiffness rig

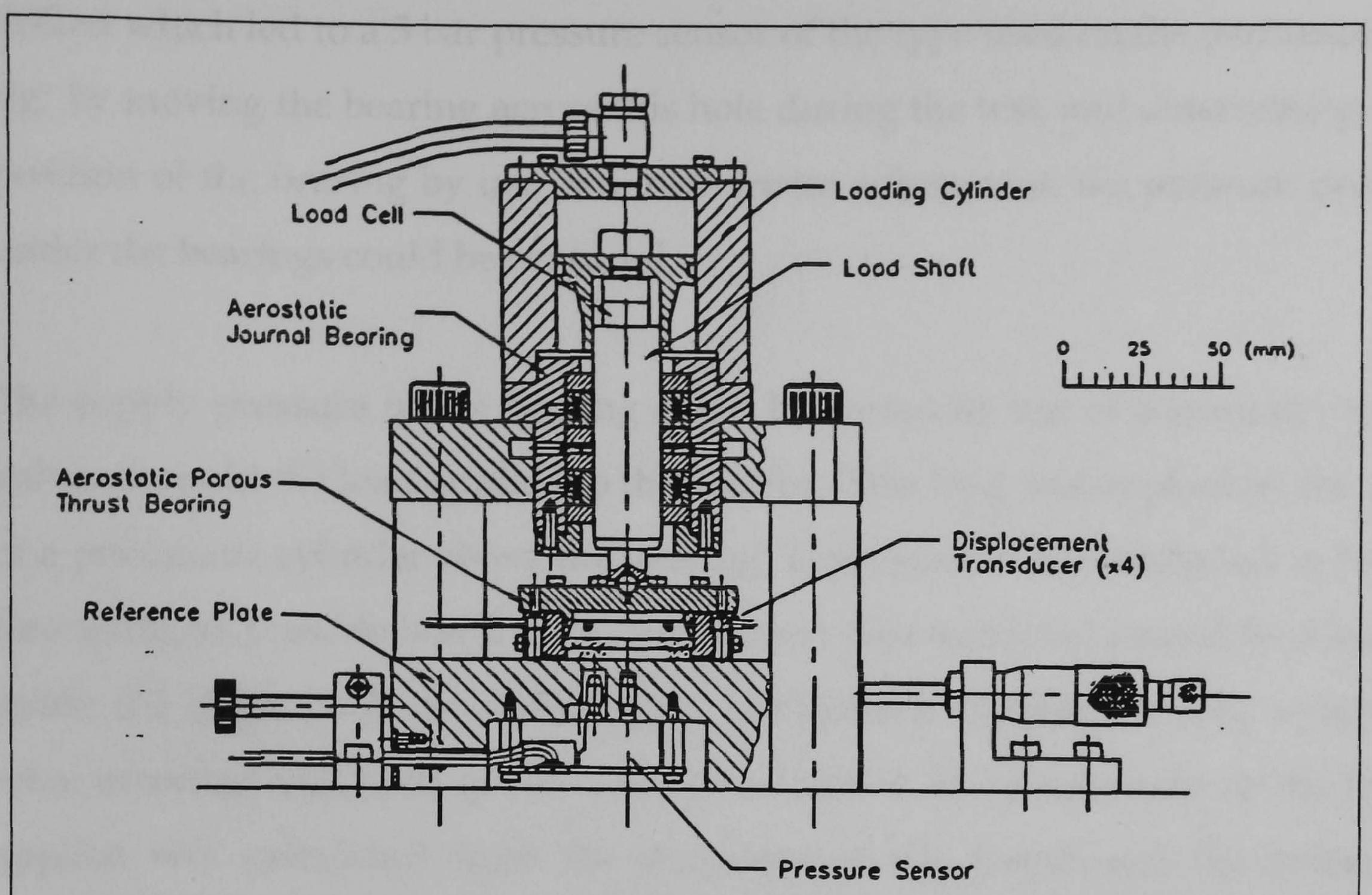

Figure 34 Schematic of stiffness rig, (from [5])

The principle of operation of this equipment was to seal the test bearing in a holder and supply compressed air at a predetermined pressure to the cavity above it. The bearing had a step machined around the circumference that acted as a location shoulder to trap the bearing in the holder between the top and bottom halves of the holder.

As well as providing the air supply to the bearing, this holder contained four inductive displacement sensors around the outer circumference to record the bearing gap and tilt. These were Kaman SMU-9200-15N inductive sensors that were calibrated against a 316 stainless steel target. They were set up to provide a 50µm range with a 100µm offset with a linearity of better than 0.5% of span. Their position was adjusted by means of a fine screw that allowed them to be set individually in order to take into account any height difference between bearings.

The counterface was a large block of 316 stainless steel, lapped to better than 1µm over 50mm. In the centre of the counterface block a fine capillary hole was

drilled which led to a 5 bar pressure sensor of the type used on the permeability rig. By moving the bearing across this hole during the test, and determining the position of the bearing by use of a micrometer adjustment, the pressure profile under the bearings could be captured.

The supply pressure to the bearing could be varied by use of a manual rotary valve, as could the load applied to the bearing. This load was applied by the use of a pneumatic cylinder above the bearing. This cylinder was designed to be as free acting as possible and used a double entry slot-restricted journal bearing to guide the shaft. Both the pressures to the bearing supply and load cylinder were recorded via 5 bar gauge sensors as before. The magnitude of the load applied was calculated from the geometry of the piston and the pressure supplied, with an allowance for the dead weight of the system. A load cell was incorporated but not used, as it was found to be out of calibration and suffered greatly from drift.

Varying the load through the use of pressure in a pneumatic cylinder meant that no changes in the mass of the system took place. This was specifically to avoid any instability that may be caused by the dead weight of the bearing [128]. Where the shaft contacted the bearing holder roof, a ball end made contact into the centre of the holder. This pin jointed approach ensured no moments could be transferred from the shaft to the bearing.

The same PC and data acquisition system that was used for the permeability rig was used. Further software was developed for this test that allowed real-time display of various bearing parameters such as each inductive sensor gap, the mean gap, supply pressure, and bearing load, as well as alarms to warn of touchdown. The position of the bearing relative to the pressure tapping in the counterface was entered manually, and all data could be saved to disk. In common with the permeability data acquisition, all data was first smoothed to

remove spurious spikes that could give erroneous measurements in a similar manner.

Although extremely accurate, the Kaman inductive sensors were found to drift considerably over time. To counter this effect, the software re-zeroed the sensors between tests.

Two sets of tests were undertaken for each bearing. Firstly, the load from the load cylinder was incrementally increased from zero until the bearing just touched the counterface. The load on the bearing and the resulting bearing gap were recorded. This was done with three different supply pressures, 5 bar, 4 bar, and 3 bar, and allowed the calculation of the bearing stiffness under various supply conditions. The details for this calculation are to be found in the Results and Discussion chapter under the Bearing Stiffness section.

The other test was the pressure profile test. Set bearing gaps were imposed on the bearing and it was traversed across the pressure sensor. The bearing supply pressure was kept constant at 5 bar for these tests. The gaps were chosen to be 2.5µm, 5µm, 7.5µm, and 10µm, as well as one allowing the bearing to float freely with only the dead weight of the holder and load shaft acting.

3.4 Microscopy

All electron microscopy was carried out on an ABT 55 electron microscope fitted with a conventional film camera. The macro photography used a Sony MVC-FD5 digital camera.

3.5 Other Equipment

3.5.1 Surface Profilometry

Surface profilometry was undertaken using a Talysurf 10 and a Talysurf 120L, while the roundness profiles used a Talyrond. These devices, though different in application, operate in a similar manner. Both depend on a stylus traversing the surface to record the profile. The output from the stylus is amplified and fed to a chart recorder. The gain on the amplifier is user adjustable, allowing the level of detail to be varied.

The Talyrond gives a graphical output that allows an estimate of out of roundness to be calculated. It also gives a visual indication of the smoothness of the surface that it measures.

The Talysurf 10 can calculate a value for R_a as well as outputting a graphical indication of the surface. R_a is a measure of the surface, and is defined as the arithmetic mean of the absolute values of the profile departures within the measuring length [129]. There are many other terms that can be used to define a surface, however R_a is all that this particular model would report.

As the surface is porous, a low value of R_a will never be seen as the stylus will always fall into holes as it traverses the surface. What this technique was particularly good at was highlighting the difference between grinding methods. All bearings were conventionally ground, but several were additionally reground with a Tetraform grinding machine (see next section). This machine was capable of obtaining much flatter surfaces than the conventional one, and so in effect all that were left were valleys as the peaks had been removed.

The Talysurf 120L was used only infrequently as it required a trained operator to be present, who was not always available.

3.5.2 Grinding

All conventional table grinding of the flat parallel surfaces on the bearings was done using a Elbe Werke surface grinder. The wheel was a D76 50 BR4A, and the speed was 2700rpm. All of the cylindrical grinding was undertaken on a Jones and Shipman universal grinding machine.

Some additional grinding of the bearing surfaces was undertaken using a Tetraform grinding machine. This machine was designed as a three-axis vertical spindle cup wheel grinder, with maximum stiffness in mind. It has an unusual geometry for a grinding machine, based around the shape of a tetrahedral structure which can be seen in figure 35.

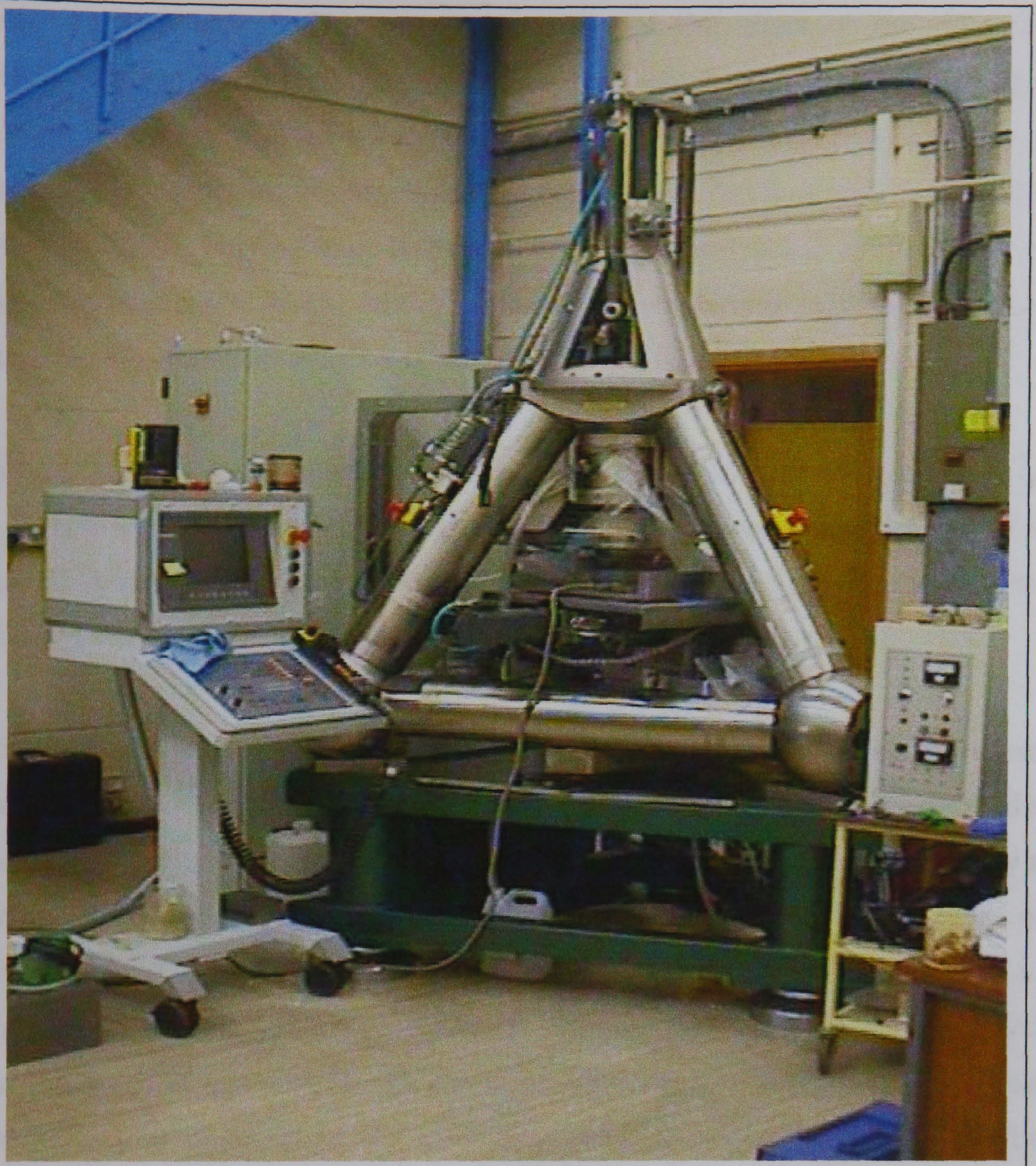

Figure 35 The Tetraform grinding machine

Grinding work with this machine has led to previously unattainable levels of surface finish through a grinding process. Despite being at an early stage of development, it proved that it would be an extremely useful tool for the finishing cuts on the bearing surface.

3.5.3 Moduli Measurement

All testing of the elastic, torsional moduli, as well as Poisson's ratio, was carried out in a non-destructive manner. This allowed the properties of every potential

bearing to measured. This gave a measure of the effect of the different processing routes, sintering temperatures, etc., which is of interest to as any significant deviation from the desired bearing properties can lead to excessive bearing pad deflection, or even failure of the bearing. Previous work had used a concentric ring compression test to evaluate the mechanical properties in a destructive manner. As the aim of this research programme was to generate as large a data set as possible, it was preferred to not resort to this approach.

Instead, a Lemmings Grindosonic Mk5 was used. This device when attached to a computer running EMOD version 9.15 software, allowed the calculation of E and G moduli, as well as Poisson's ratio, starting from the object's physical characteristics (dimensions and mass) and its natural frequency.

The principle of operation of this device was based on frequency measurement of the disks in two modes of vibration [130]. The disk was set to vibrate in the flexural and torsional modes, and the vibrational frequency was measured by a small contacting pickup placed at the diameter of the sample. The readings of the measured frequencies were subject to certain limits, the ratio of flexural to torsional frequency had to be within 1.35 to 1.9, and the calculations were based on the work of Glandus [131]. This data, along with data relating to the mass, thickness and diameter of the sample allowed the software to calculate the values of moduli and Poisson's ratio. The major advantage of this method was that every bearing could be tested at an early stage of the manufacturing process, giving a large range of data. The non-destructive testing enabled the candidate bearings to double as both mechanical test pieces, as well as later on as real test bearings. This increased the amount of data that was available from a set number of bearings.

The testing was undertaken before the bearing was ground to its finished dimensions. In order for this approach to work the bearing had to be in the form of a regular shaped disk. After sintering the samples were ground to the

finished thickness, (6.5mm), but the cylindrical grinding was only to give a smooth, nominally round, outer edge. The geometry was measured using a digital vernier calliper, as mentioned previously, and this data, along with the mass as weighed on a Sartorious balance was entered into the computer.

The disks were then placed on a thin X shaped foam support, designed to allow the disk to vibrate in the desired modes. The pickup from the Lemmings machine was placed against the side of the disk, and the top of the sample was struck lightly with a small hammer. Depending on where the sample was struck it was possible to obtain different modes of vibration. The frequency of this vibration was displayed on the Lemmings machine, and once consistent readings were obtained, the data was entered into the computer.

The computer then calculated the corresponding values of flexural and torsional moduli, along with a value for Poisson's ratio.

As this method depended upon the pickup receiving the frequency of the vibration that travelled across the surfaces of the sample, it was highly sensitive to surface flaws. Any imperfection such as an area of large porosity meant that it was difficult to obtain consistent meaningful data for the frequency of vibration. Any surface cracks made this method useless. The torsional mode of vibration was particularly susceptible to erroneous random readings due to this. However, once some experience was built up with several different samples, it was possible for the user to obtain a feel for the correct values. By carefully selecting the point to be tapped and setting up the supports with precision, an obvious pattern could be spotted amongst the data reported by the Lemmings device.

4 Results and Discussion

4.1 Permeability and Open Porosity

The manner in which permeability varies with open porosity is shown in figures 36 and 37. Figure 36 shows the relationship between viscous permeability and open porosity, while figure 37 shows the relationship between inertial permeability and open porosity. These two graphs are plotted using a log/log scale, resulting in linear relationships.

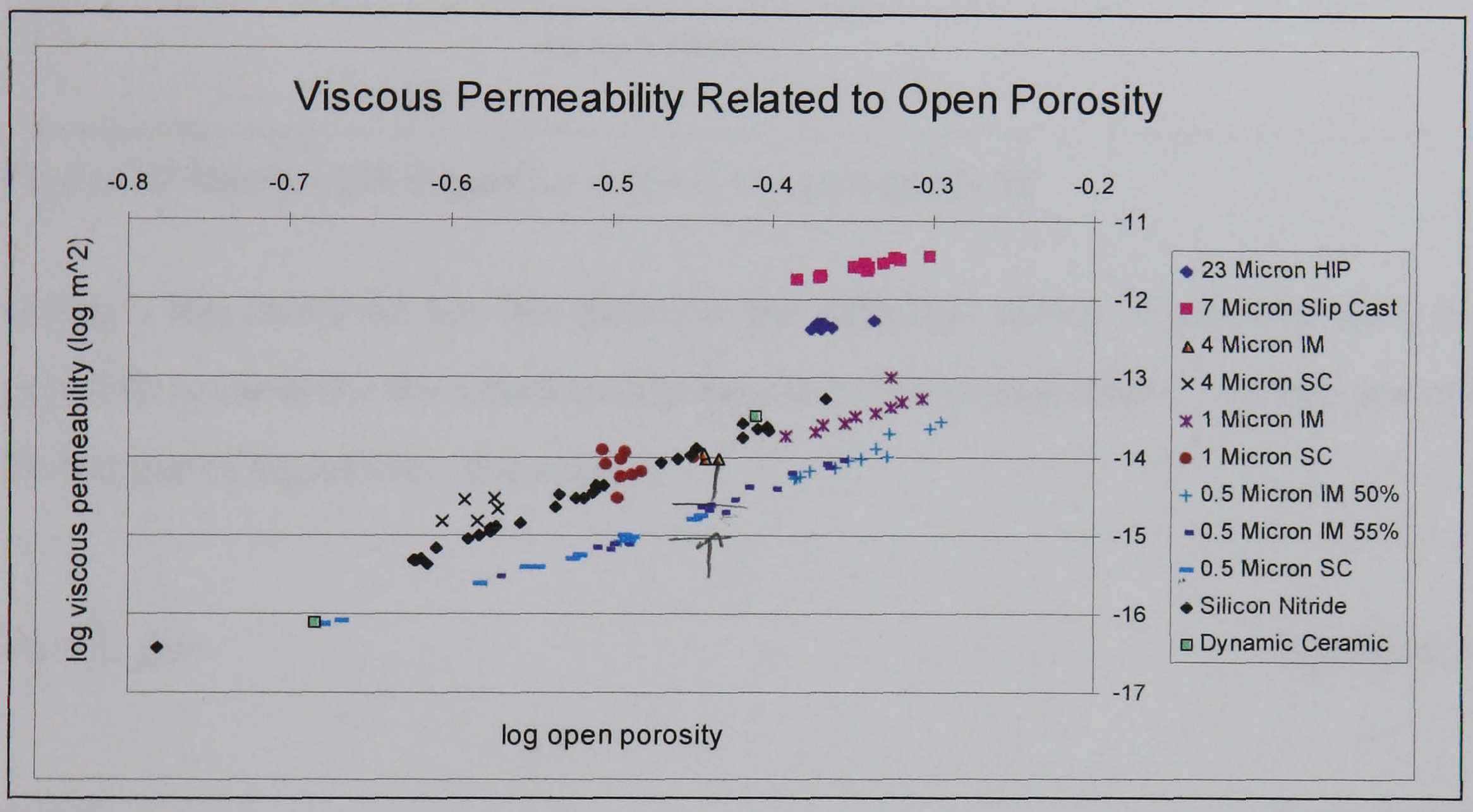

Figure 36 Viscous permeability related to open porosity

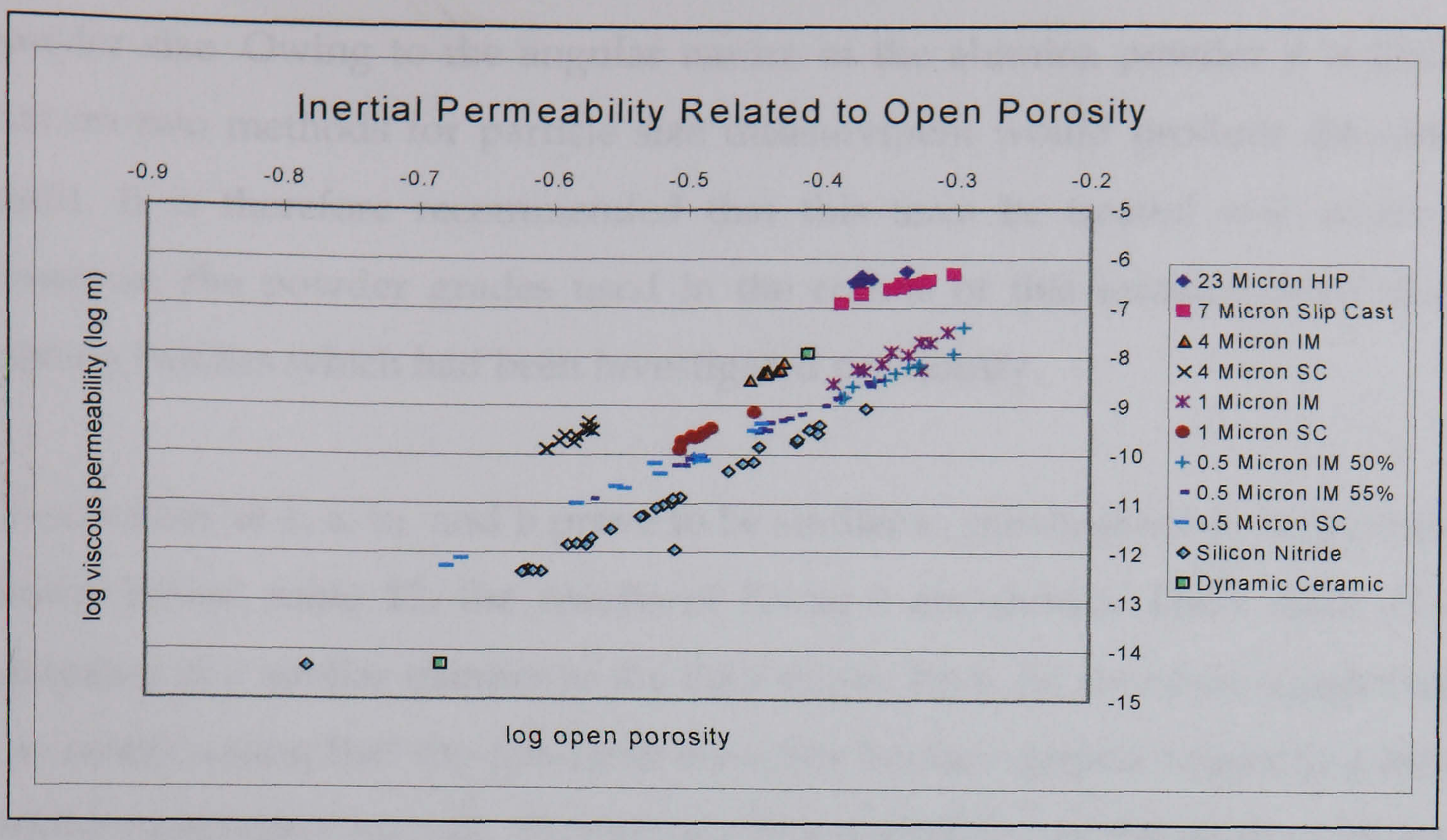

Figure 37 Inertial permeability related to open porosity

Using a log curve fit for the data for the different series of powder size, it is possible to describe the relationship between the permeability and the porosity by the use of equations of the form:

$$\Phi_v = k.\ \zeta_o^{a} \qquad \text{Equation 16}$$

$$\Phi_i = k_1.\ \zeta_o^{b} \qquad \text{Equation 17}$$

These results are tabulated below

Table 11 Relationship between permeability and porosity

Powder Size (microns)	k	a	k_1	b
23	2.31E-12	1.92	2.75E-05	5.04
7	5.87E-13	3.97	3.88E-05	6.33
4	1.99E-12	5.15	4.98E-05	9.10
1	1.63E-12	4.81	5.12E-05	10.85
0.5	1.06E-12	6.03	1.34E-05	10.25
Si_3N_4	3.54E-11	7.79	5.79E-05	13.14

The values quoted as powder size in the above table are nominal and are as designated by the manufacturer. No attempt was made to verify the actual

powder size. Owing to the angular nature of the alumina powder it is likely that no two methods for particle size measurement would produce the same result. It is therefore recommended that this term be treated with caution. However, the powder grades used in the course of this research were from existing batches which had been investigated previously.

These values of k, a, k_1, and b prove to be similar to previous work. In the table shown below, table 12, the results of Kwan [5] are shown. These data were generated in a similar manner to the data shown here, on the same equipment. It is worth noting that the constants are quite similar, despite originating from different experimental sets. This gives some confidence in the equipment and procedure. The powder size values given are as measured by a sedigraph, while the values in brackets are the nominal values quoted by the manufacturer.

No obvious fit exists between the powder size d_w and k, although using a power law correlation yields the following relationship:

$$k = 1.24E\text{-}12.d_w^{7.74E\text{-}2} \qquad \text{Equation 18}$$

For a, the following fit proved the most accurate:

$$a = 3.68E\text{-}3.d_w^2 - 2.50E\text{-}1.d_w + 5.71 \qquad \text{Equation 19}$$

Table 12 Relationship between permeability and porosity - comparison

Powder Size (microns)	k	a	k_1	b
42	3.20E-12	0.948	6.8E-5	4.44
22.6 (23)	3.02E-12	1.82	1.6E-5	3.50
12.2 (13)	5.47E-12	3.46	4.29E-05	5.06
6.25 (7)	1.09E-11	4.94	3.17E-05	6.99

By way of comparison, the relationships found by Kwan for k and a with d_w are listed below:

$$k = 2.74E\text{-}15.d_w^{-0.68}$$ Equation 20

$$a = -5.41E13.d_w^3 + 7.94E9.d_w^2 - 3.83E5.d_w + 7.05$$ Equation 21

At first glance it is surprising that there exists such a difference in the value of the power law component for k between these two works (equation 18 and equation 20). This appears largely due to the difference between the value of k for the 7 micron powder. Owing to the relatively low number of points with which to curve fit, any point that deviates has a strong effect on the curve, and the difference in value for k is two orders of magnitude. Combining the two sets of data we obtain the following relationships for k and a.

$$k = 1.53E\text{-}12.d_w^{0.243}$$ Equation 22

$$a = 2.72E3.d_w^2 - 2.29E1.d_w + 5.75$$ Equation 23

Whilst the best fit relationships equations vary, these two sets of figures illustrate that both viscous and inertial permeability vary strongly with the level of open porosity. Powder size in comparison also has an effect, in general the larger the powder particles the larger the permeability, but the magnitude is secondary compared to the porosity effect.

Other authors also found a similar effect previously. Tabulated below in table 13 are data for other analyses carried out by other authors using a slightly different power law model:

$$\Phi = k.\zeta^a.d_w^b$$ Equation 24

Table 13 Compilation of Previous Work

Reference	Equation	k	a	b
Robinson [65]	$\Phi = k.\zeta^a.d_w^b$	--	4.38	2.18
Cliffel [66]	$\Phi = k.\zeta^a.d_w^b$	--	1.871	1.871
German [67]	$\Phi = k.\zeta^a.d_w^b$	4.6E-11	6.8	0.73
German [67] (data from Smith [68])	$\Phi = k.\zeta^a.d_w^b$	4.8E-13	4.8	1.3
Smith [68]	$\Phi = k.\zeta^a.s_v^b$	190	2.42	-2.42

The above data results from the analysis of generally much larger particle sizes than are of use in the development of a single layer porous aerostatic bearing as is the aim here. The data covers a range in particle sizes from 5 to 715µm, and the materials consisted of nickel and stainless steel. What they illustrate that is of interest is the variability of the constants found. These data sets represent powders of more than two magnitudes difference in size, which doubtless encompass an equally wide variety of flow conditions and particle aspect ratios. This then overall shows that a certain amount of circumspect is required when evaluating potential powder types due to the variability in their nature.

4.2 Processing Conditions and Open Porosity

4.2.1 Alumina Bearings

The investigation into the relationship between the effect of temperature and the resulting open porosity is illustrated in Figure 38. This graphically illustrates the relationship between the open porosity and the sintering/low pressure HIPing temperature for a range of alumina powder sizes. It shows, as

expected, that the higher temperatures result in more dense structures. All the data were for a one hour sinter/HIP.

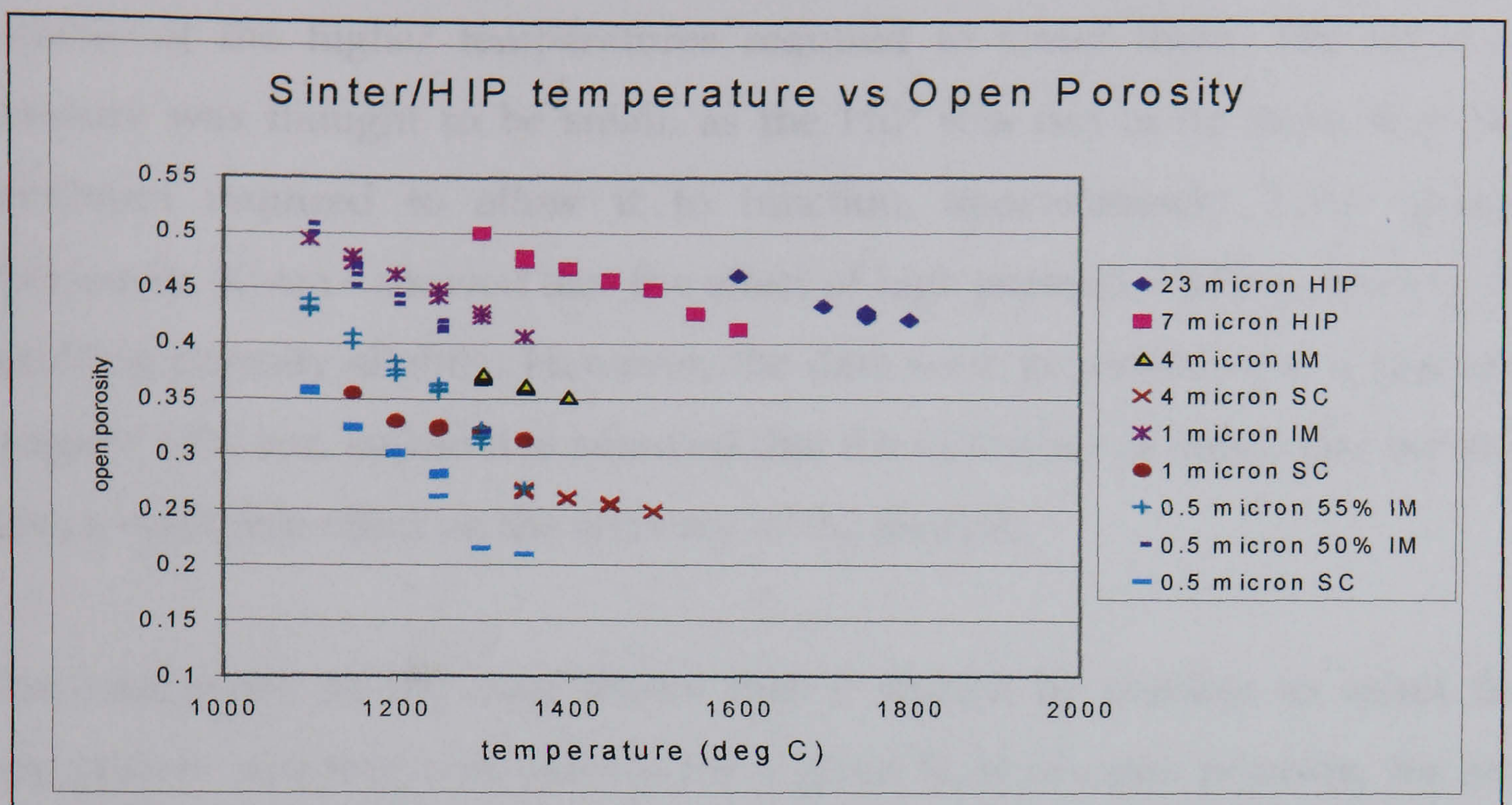

Figure 38 Open porosity as a function of processing temperature

These appear to vary in a largely linear manner, though due to the limited range of data it is expected that if expanded they would describe an exponential curve, as predicted by the Arrhenius equation, and they also show that the smaller powder sizes produce denser bodies for the same temperature. For example, taking a temperature of 1300°C, we can see that the 0.5 micron slip cast material has a level of open porosity of approximately 23%, while for the 4 micron slip cast material the open porosity rises to around 43%.

It also serves to illustrate the effect of green density on the final body. Taking the 0.5 micron injection moulded data as an example, it can be seen that the 55% green density data results in approximately 5% greater fired density than the 50% green density for the same sintering temperature. Another trend of note is that the slip cast samples reach a higher density for a given sintering temperature, indicating that they possessed a higher green density than the injection moulded samples.

It is worth noting that the data for the 7 micron and 23 micron were HIPed at a low pressure. This was due to the unavailability of an atmospheric furnace capable of the higher temperatures required to sinter them. The effect of pressure was thought to be small, as the HIP was run at no more than the minimum required to allow it to function, approximately 2 bar gauge. Previously, Kwan [5] showed that the effect of high pressure HIPing affected the resulting porosity slightly. However, the data were generated over a pressure range of 1500 bar, and so it is assumed that the difference of only a few bar will have a negligible effect on the accuracy of the analysis.

The consistency in the data shows that it should be possible to select the appropriate sintering temperature for a given level of open porosity, for any given powder size. This could be modelled through the use of the Arrhenius equation:

$$k_a = A_A.\exp^{(-E_a/RT)} \qquad \text{Equation 25}$$

Given a greater range of data it would be possible to determine values for the above variables.

The rate of densification was also examined as a function of temperature. Densification was defined as the change in density during the sintering period. Knowing the initial density from the green body data, and the final density from measurements made to the fired bodies, the amount of densification could be calculated. This data is plotted in figure 39.

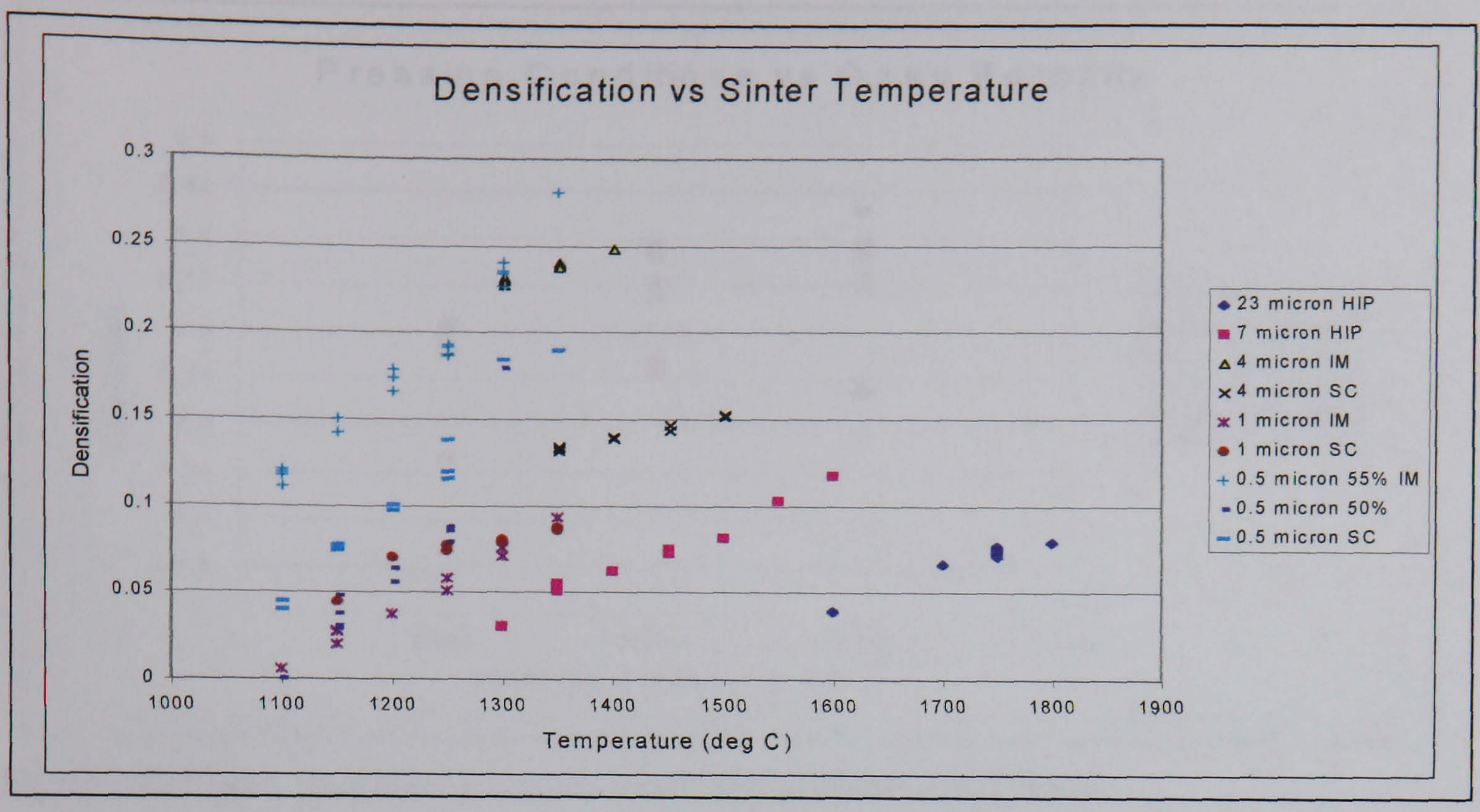

Figure 39 Densification as a function of temperature

It can be seen that the densification increases with temperature. Also, the smaller the powder size, the greater the densification.

The amount of closed porosity was measured for several samples to evaluate whether it was significant. This was done by utilizing the method developed by Kwan [5], described in the Experimental Procedure chapter. It was concluded that for the sample set measured, the amount of closed porosity was very small, less than 1%, which was considered to be small enough to be neglected.

4.2.2 Silicon Nitride Bearings

For the silicon nitride, figure 40 shows the trends in the final open porosity with pressing conditions. Unfortunately the full range of processing data for these materials was not made available. However, what is clear from the data is that for the powder that consisted of a close particle size distribution (the SPSD data set), the open porosity dropped as pressing pressure increased. This is perhaps to be expected, as the greater green density will normally result in a greater final density.

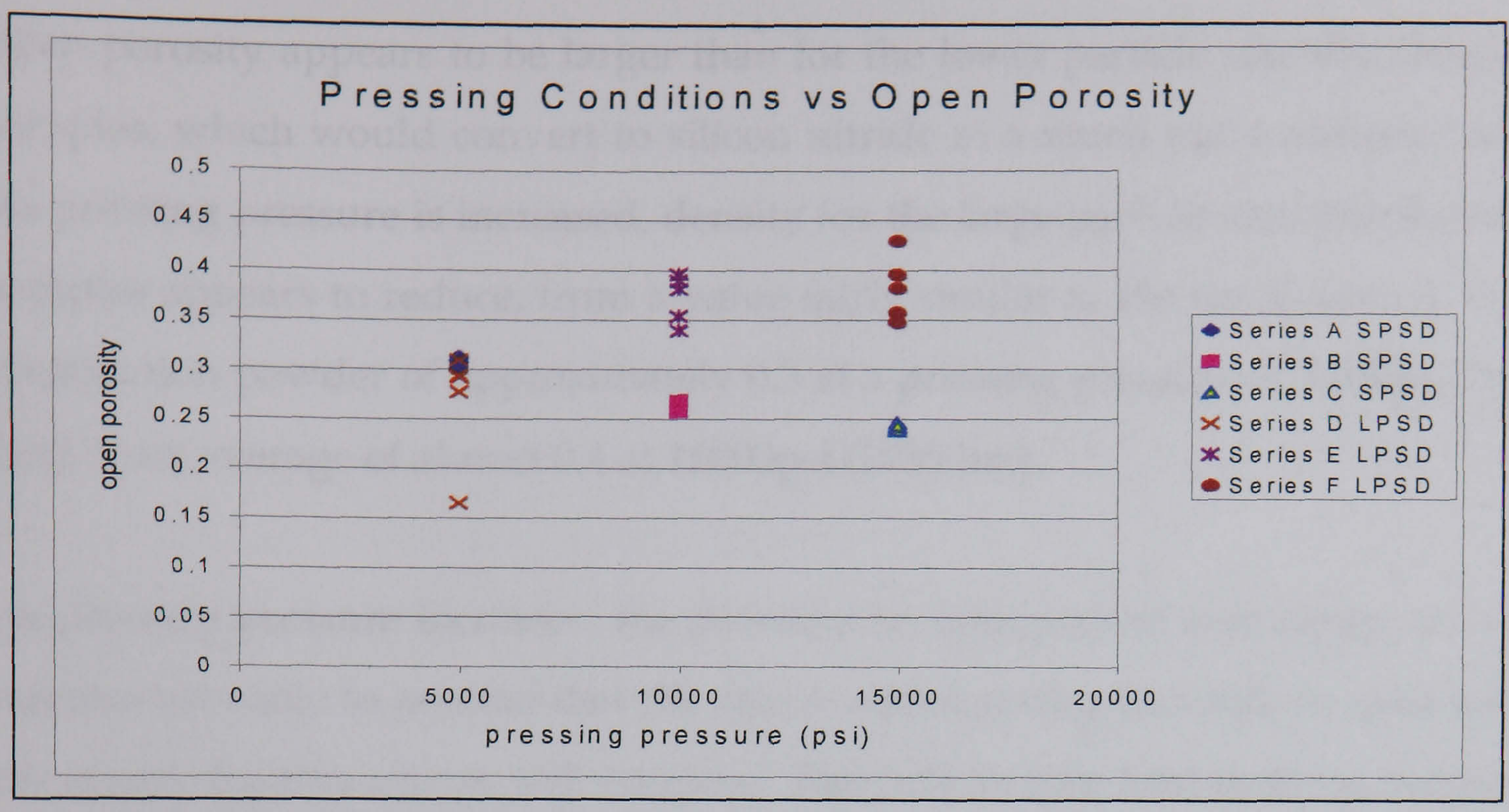

Figure 40 Open porosity as a function of pressing conditions

The opposite is the case with the large particle size distribution powders (the LPSD data set). Here we see that as the pressing pressure is increased the final open porosity decreases, contrary to the previous case. This can be explained by the change in powder size distribution and an understanding of the process used to fabricate the bearings. Owing to the lack of data for the actual manufacturing process, it is impossible to categorically state a reason, but the following hypothesis gives a likely scenario. The process used to produce the ceramic was a reaction bonding mechanism where silicon powder is pressed at temperature in a nitrogen atmosphere. The nitrogen reacts with the solid silicon powder to form silicon nitride. Given enough time, temperature, and sufficient quantities of nitrogen, the ceramic so produced tends to Si_3N_4, but it is possible that at the end of a pressing run that not all of the silicon has converted to silicon nitride. This means that for the larger powder particles, whose volume to surface area ratio is larger, that an appreciable quantity of free silicon would remain. This quantity could be estimated by sectioning samples and undertaking an EDX examination on an SEM.

The above open porosity graphs were calculated using density data for Si_3N_4, which of course may not be applicable for the samples using the larger range in powder size. As silicon has a lower density than silicon nitride, the level of

open porosity appears to be larger than for the lower particle size distribution samples, which would convert to silicon nitride at a much more uniform rate. As pressing pressure is increased, density for the large particle size distribution samples appears to reduce, from a value fairly similar to the small particle size distribution powder of approximately 0.3 at a pressing pressure of 5000psi (345 bar), to an average of almost 0.4 at 15000psi (1035 bar).

As pressing pressure increases, the powders become packed ever closer, so it is not unreasonable to assume that the rate at which nitrogen is able to react with the remaining free silicon will decrease. This will in turn lead to those samples processed at the highest pressures having the highest levels of free silicon remaining, which has the effect of appearing to increase the level of open porosity as the true density of the samples is not used for the calculations here.

This argument is backed up by figure 41.

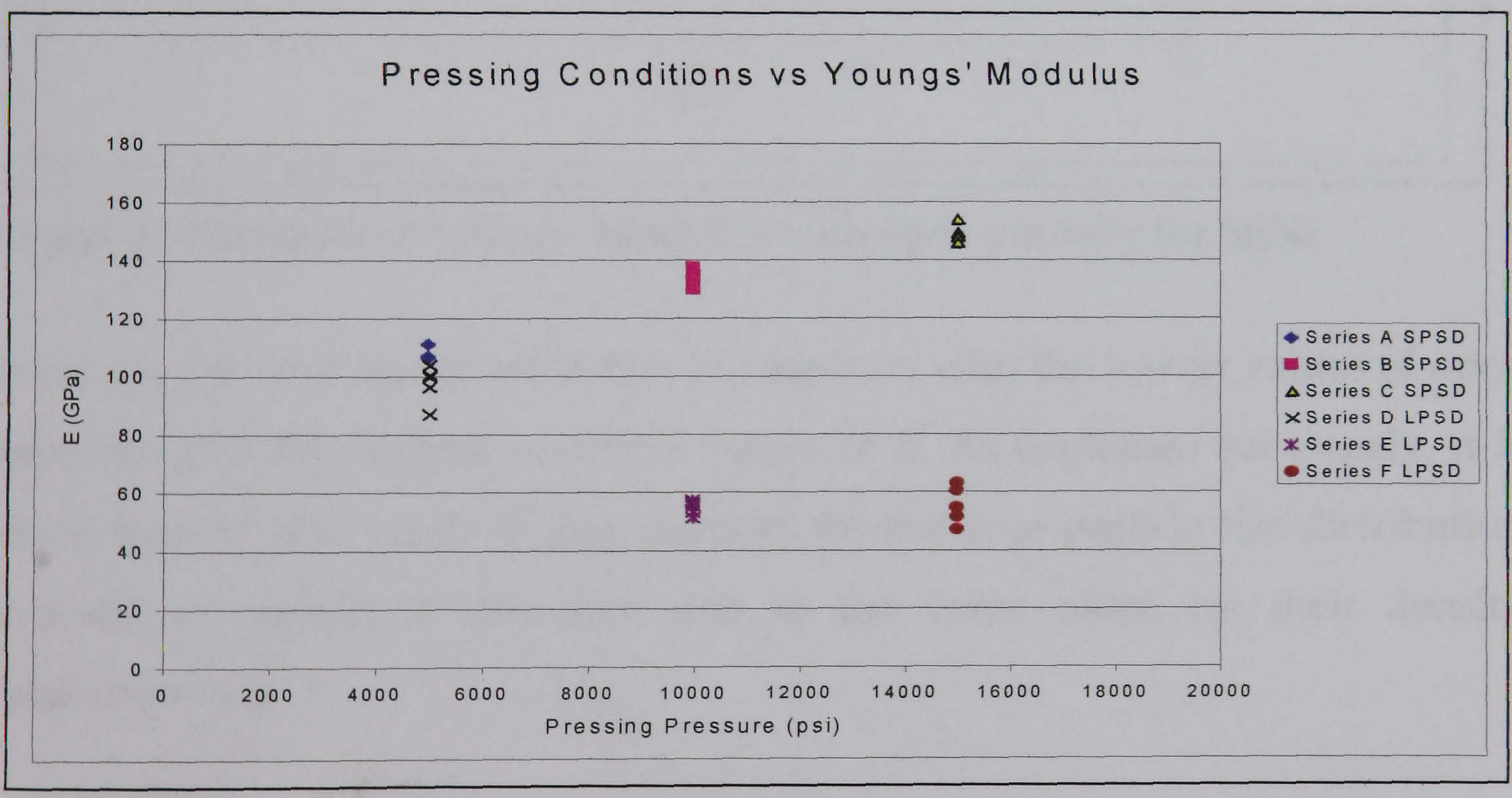

Figure 41 Variation in E with powder size distribution and pressing conditions

This shows the variation in Youngs' Modulus as a function of the pressing pressure and the powder size distribution. As the pressing pressure is increased for the sample set consisting of the small powder size distribution we see clearly that the trend is to increase the resulting value of E. The opposite is true

of the large powder size distribution data sets. Here we see increasing the pressing pressure leads to a reduction in Youngs' Modulus. As the modulus of silicon is much lower than silicon nitride (131GPa vs 304GPa) [132], any remaining silicon will reduce the overall measured E value.

The relationship between the open porosity and the value of Youngs' Modulus for each data set is also shown in figure 42.

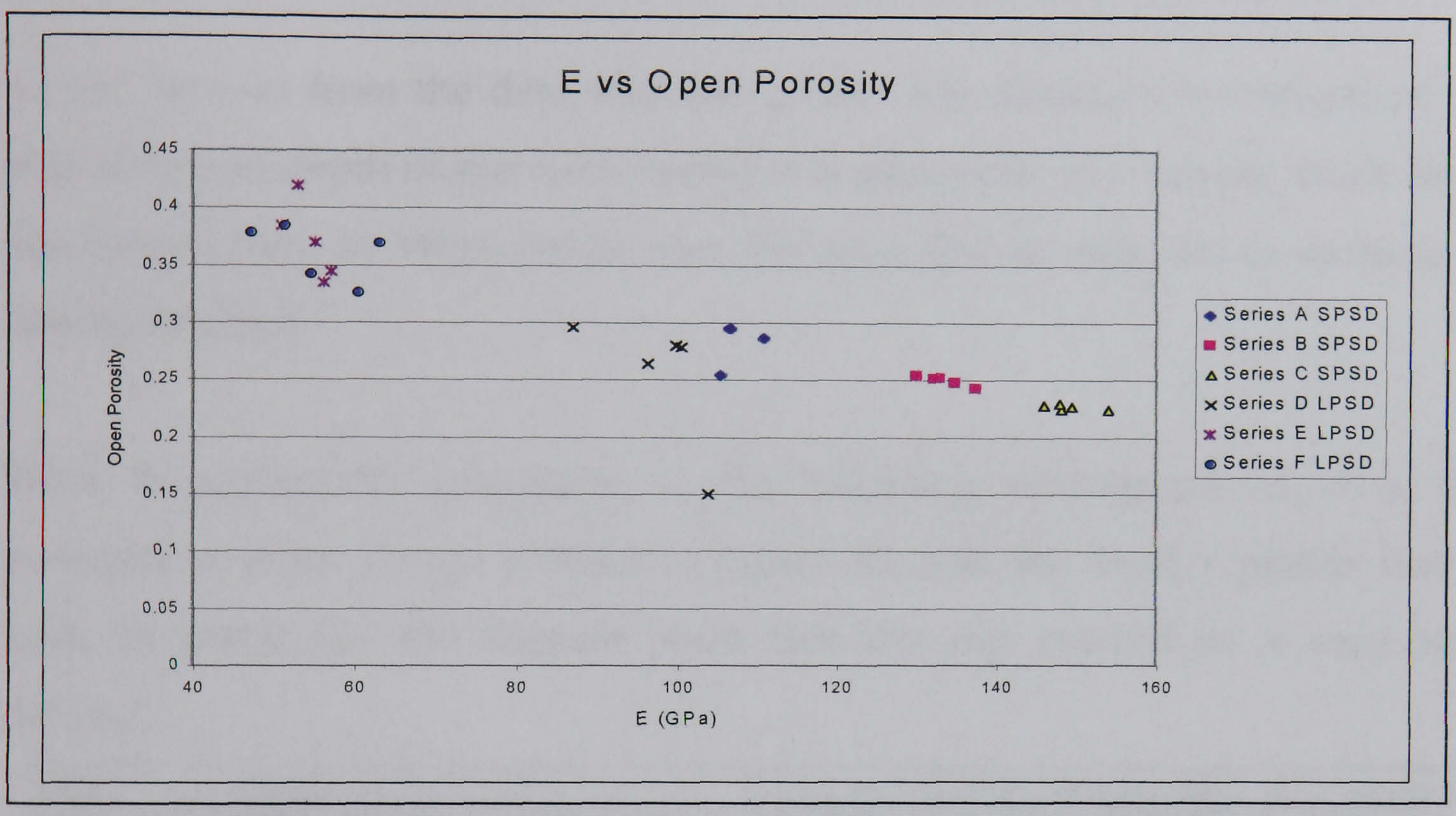

Figure 42 Variation of Youngs' Modulus with open porosity for Si_3N_4

It can be seen that the trend is that the samples with the lowest values of open porosity give the highest recorded values of E. As explained previously, it is likely that the true value of open porosity for the large particle size distribution sets are erroneous in this case due to the value taken for their density measurements.

4.2.3 Dip in Slip

The data tabulated below shows the increase in density recorded with this process after sintering.

Table 14 DIS Parameters

Time (s)	Depth of Slip (mm)	% Increase in Density
15	4	5.90
30	3.5	6.22
45	2	3.13
60	5	2.90
75	4	4.27
90	3	4.36

As can be seen from the data, this was purely a preliminary investigation. As both time and depth of slip were varied it is impossible to conclude much from this limited data set. What can be seen though is that in each case an increase in density resulted.

What is particularly interesting is the following micrograph showing the penetration of the 0.5µm powder in figure 43, and the density profile that it took. In particular, the deepest point that the slip entered to is very well defined.

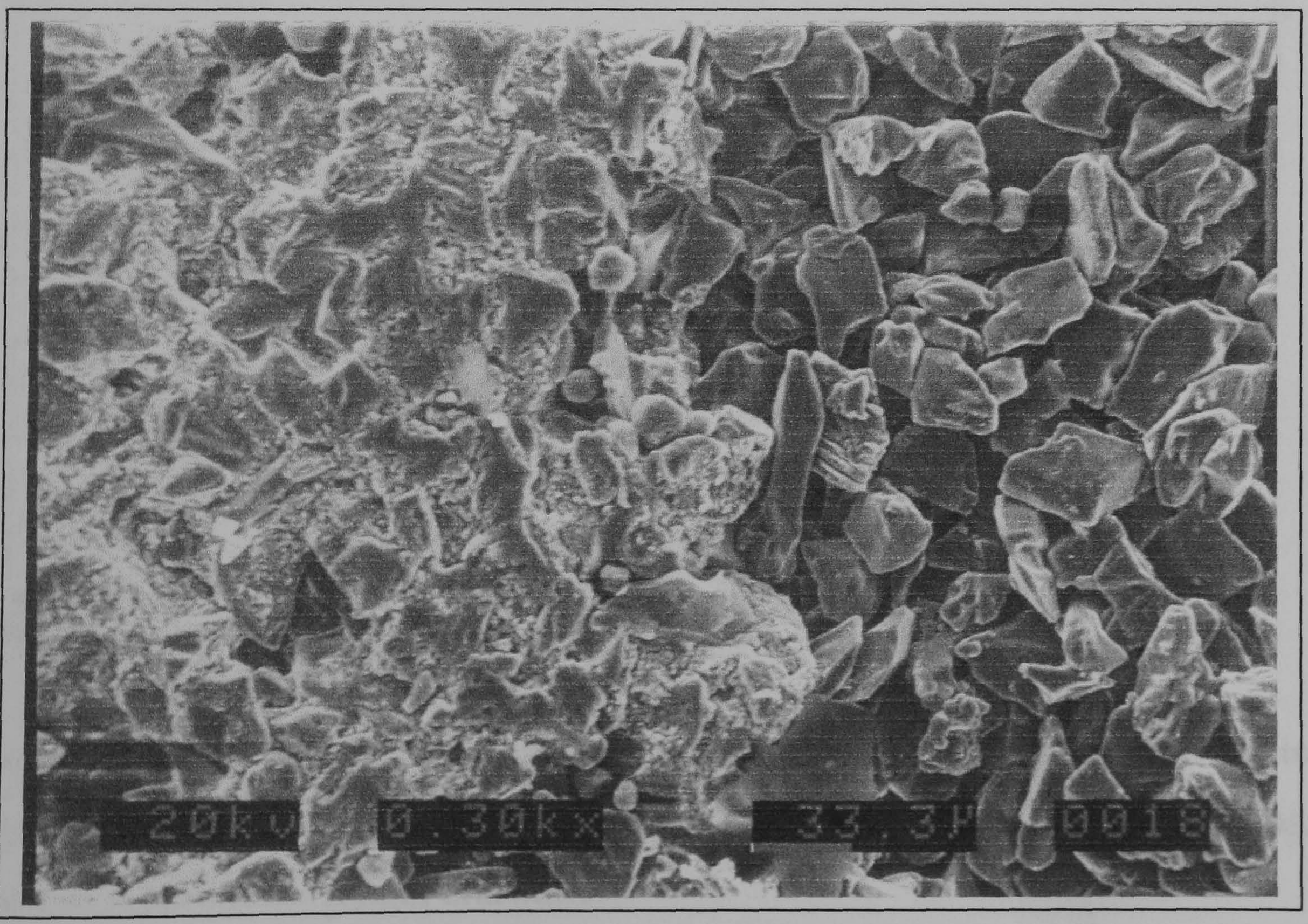

Figure 43 DIS penetration micrograph

This pronounced cut off line, along with the surface loading of the 0.5µm in the 23µm matrix, shows that this method carries potential as a substitute manufacturing route. Unfortunately, insufficient 0.5µm alumina was deposited to overcome instability problems as was shown when ground for stiffness testing. An alternative way forward with this technique would be to abandon the 23µm powder and instead use a smaller grade, such as the 7µm. This would reduce the sintering temperature, negate the use of a HIP, and lower the amount of 0.5µm alumina that would need to be deposited to overcome instability as the resulting pores would be much finer.

4.3 Mechanical Properties

Looking at figure 44, Young's Modulus is plotted as a function of density. Here we can see the effect that the porosity has on the resulting mechanical properties for all the alumina discs tested.

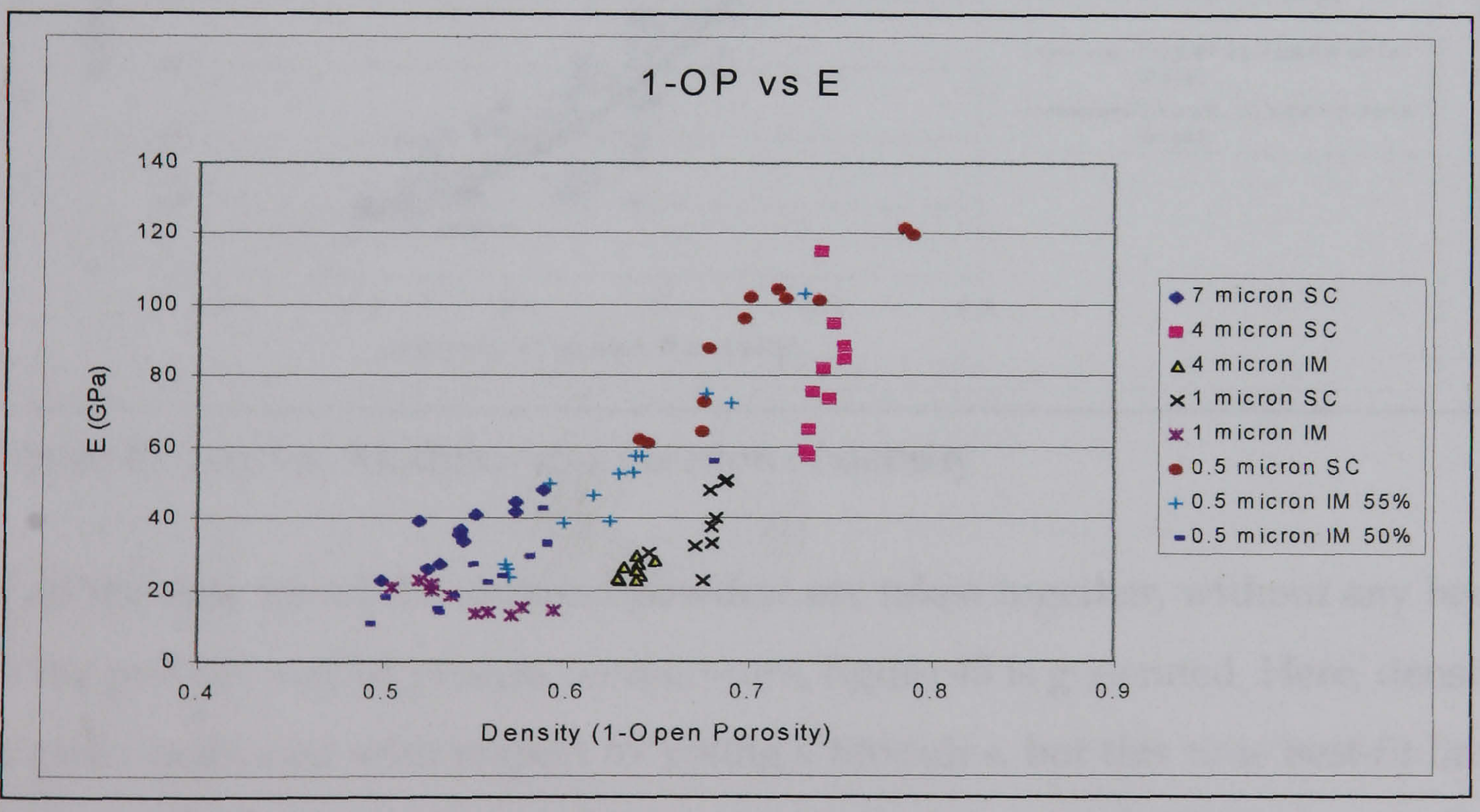

Figure 44 Modulus data for each bearing type

In general the trend is an increase in Young's Modulus with an increase in density. This is as expected, as the denser a body is, the fewer faults it contains, and so it becomes stronger and stiffer.

A notable exception is the 4 micron slip cast data. Here the data show a great range of values of Young's Modulus for a reasonably consistent density. The reason for this lies with the surface finish of the discs used for the tests. As the technique used for the evaluation of the mechanical properties was highly sensitive to surface flaws it was sometimes difficult to obtain accurate data from samples whose surface was machined less than satisfactorily, or contained small defects. Unfortunately this was the case for the 4-micron discs tested here. Several contained surface flaws due to porosity, thus giving the appearance of a large spread of data. It is highly likely that the range should be much lower, but due to the limitations of the testing equipment and the method by which these results are calculated, the appearance is that of a large degree of scatter.

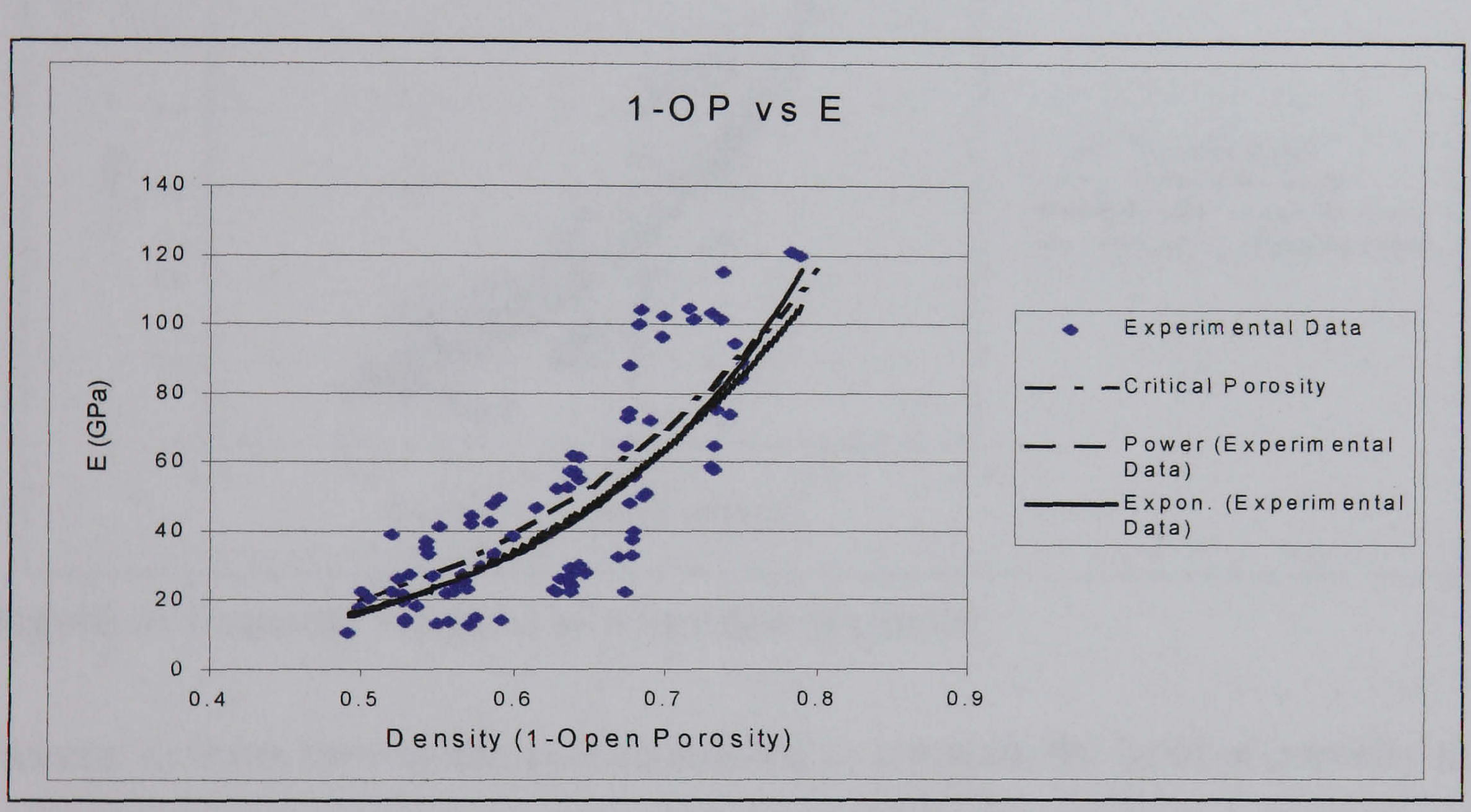

Figure 45 Youngs' Modulus as a function of density

If all the data for all the alumina powders are taken together, without any heed to the powder size or process temperature, figure 45 is generated. Here, density is again examined with respect to Young's Modulus, but this time best-fit lines are added using a combination of power law and exponential functions. The critical porosity best fit an exponential form and is explained below. Lumping all the data together in this manner also serves to circumnavigate limitations with the software package used to present the data. It was found to be impossible to trend data from more than one set, so in order to allow a

comparison to be made with previously published work, it was necessary to forego the ability to display the different groups of data individually.

For the power law, this gives a best-fit equation of the form $y = ax^b$, where the constants a and b are found to be 276 and 4.11 respectively. Continuing this analysis for Torsional Modulus, G, and Poisson's Ratio, figures 46 and 47 are generated as shown below. Again, best-fit lines are added to the results and the equations describing these lines are tabulated below.

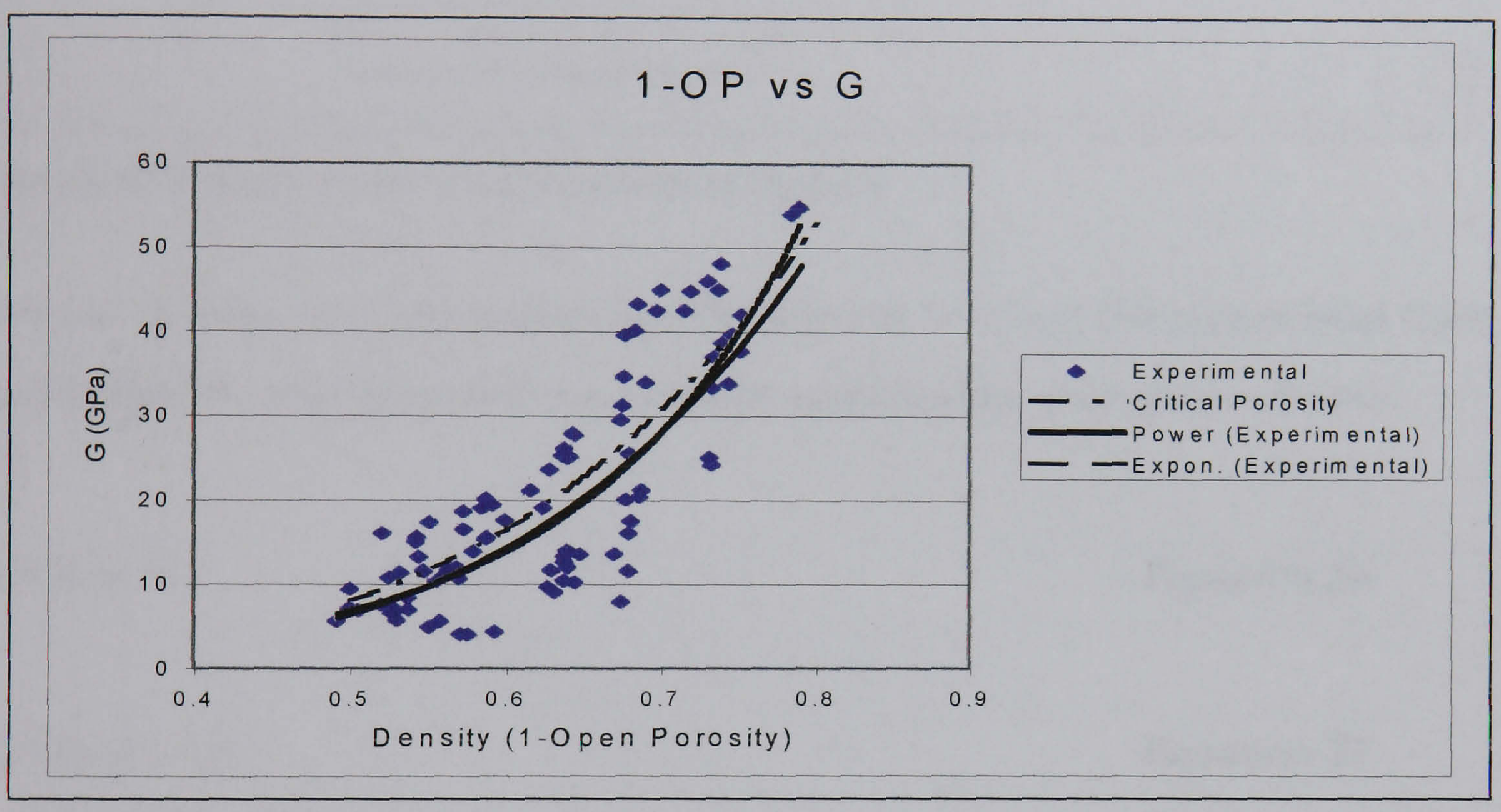

Figure 46 Torsional Modulus as a function of density

Several authors have in the past attempted to correlate the level of porosity in a body with the resulting modulus. Two of the more common methods used describe the relationship using exponential or power law functions.

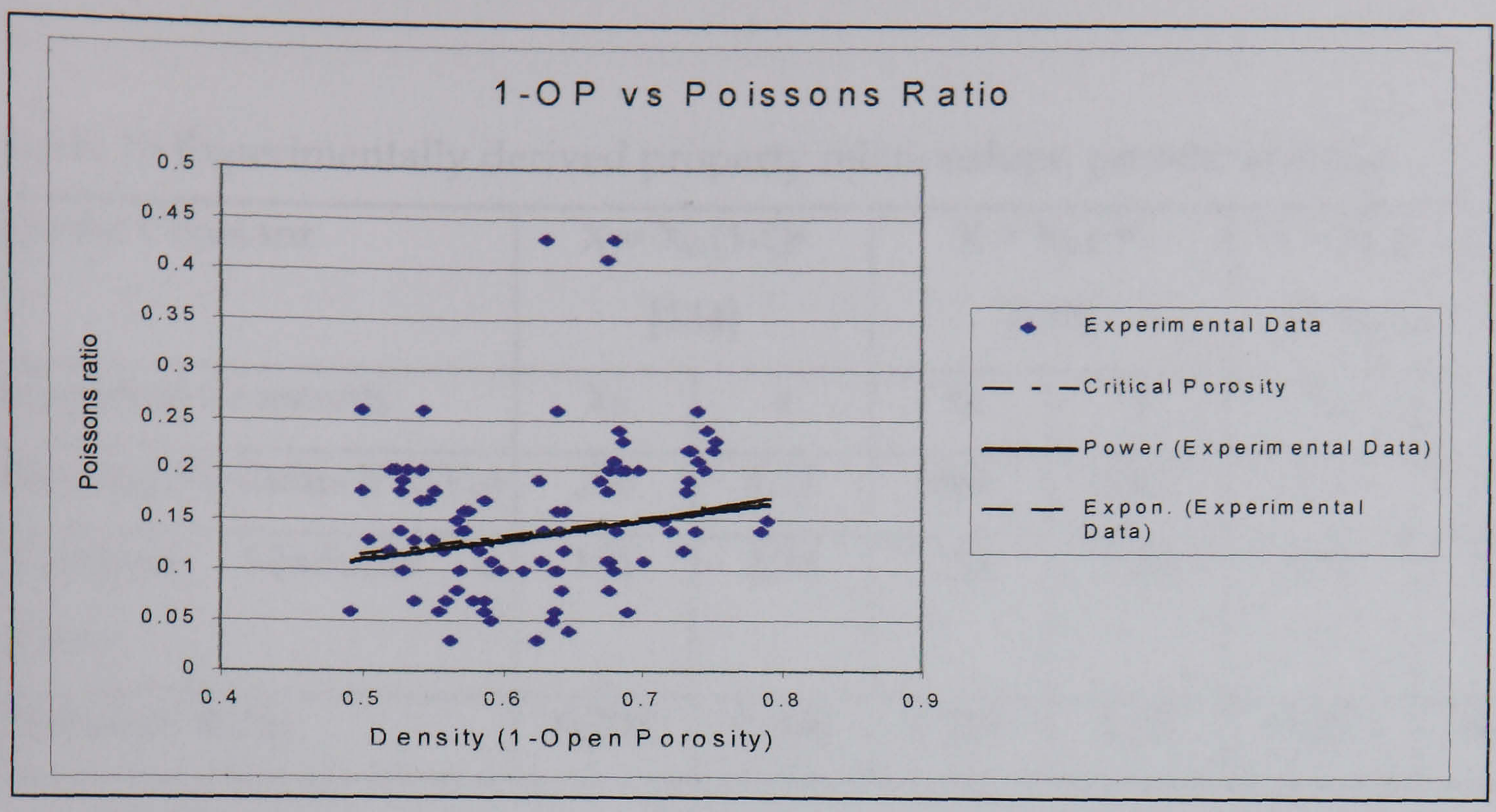

Figure 47 Poissons ratio as a function of density

Typical of these two approaches are Duckworth [133] using the exponential form, and Wagh [134], who proposed a power law relationship, both shown below.

$$E = E_0.e^{-b\zeta} \qquad \text{Equation 26}$$

$$E = E_0.(1 - \zeta)^a \qquad \text{Equation 27}$$

The power law form was earlier proposed by Phani [135], albeit in a slightly modified form. This contains the critical porosity term ζ_{cr}. at which the elastic modulus becomes zero.

$$E = E_0.(1 - \zeta / \zeta_{cr})^a \qquad \text{Equation 28}$$

This critical porosity was curve fitted by Wagh to be = 1, hence the simplified relationship in equation 24.

Using the experimental data generated in this present investigation, curve fitting revealed the following set of constants, which are tabulated in table 15 below.

Table 15 Experimentally derived property relationships, present analysis

Elastic Constant	$X = X_0.(1-\zeta)^a$ [134]		$X = X_0.e^{-b\zeta}$ [133]		$X = X_0.(1-\zeta/\ \zeta_{cr})^a$ [135] $\zeta_{cr} = 0.95$	
Empirical Constants	X_0	a	X_0	b	X_0	a
Flexural Modulus E (GPa)	276	4.11	464	6.62	267	3.77
Torsional Modulus G (GPa)	135	4.38	234	7.05	130	4.03
Poisson's Ratio	0.205	0.900	0.239	1.55	0.203	0.821

Taking the flexural modulus of fully dense alumina to be 410GPa [136], it can be seen that the constants generally fall some way short. In part this can be attributed to the data presented here for analysis. As can be seen from figures 46 to 48, the data are subject to a fair degree of scatter. As mentioned previously, the method used here to evaluate the mechanical properties was very sensitive to the surface finish of the test piece. Unfortunately, the quality of machining was not always as high as was desired with poor surface finishes in general, leading to values of modulus lower than those previously reported.

As an example of the importance of surface defect on the measured modulus for these 4μm alumina bearings, an injection-moulded sample of density 2.297g/cm^3 gave values of flexural and torsional moduli of 42.73 and 19.08 GPa respectively. A slip cast bearing of density 2.479g/cm^3 gave values for these moduli of only 26.10 and 9.112 GPa respectively. The slip cast sample was noted as having a hole visible on the upper surface, doubtless due to trapped air from the moulding process, so despite being denser, it still recorded lower values of E and G.

The value of ζ_{cr} was determined by trial and error in fitting the curve to the data to provide a reasonable fit. It is interesting to note that for the relationship

involving the critical porosity term proposed by Phani that the constant was experimentally derived to be 0.95, very close to the value of 1 found by Wagh.

Software allowing, the goodness of fit for the best fit lines shown above could be determined. One can evaluate the statistical significance of the goodness-of-fit of a particular model via a Chi-square test. There exist two types of Chi-squares, the traditional Pearson Chi-square statistic and the maximum likelihood ratio Chi-square statistic. In practice, the interpretation and magnitude of those two Chi-square statistics are essentially identical

In addition to the results found in the present analysis, those found previously by Kwan [5] are added in the following table.

Table 16 Experimentally derived property relationships, previous analysis [5]

Elastic Constant	$X = X_0.(1-\zeta)^a$ [134]		$X = X_0.e^{-b\zeta}$ [133]		$X = X_0.(1-\zeta/\ \zeta_{cr})^a$ [135] $\zeta_{cr} = 0.625$	
Empirical Constants	X_0	a	X_0	b	X_0	a
Flexural Modulus E (GPa)	479.7	3.91	576.1	5.38	409.5	1.82
Torsional Modulus G (GPa)	193	3.82	230.8	5.26	165.4	1.78
Poisson's Ratio	0.244	0.508	0.25	0.71	0.239	0.234

In contrast to the results reported here, the work by Kwan [5] suggested that a better fit was through the use of the power law fits. The higher values for X_0 found in the course of this particular research program, resulted from the utilisation of a larger range of porosity from a series of samples that were machined more exactingly.

4.4 Permeability Ratio

A criterion that can be used to determine the fluid flow characteristics through a porous bearing is the ratio between the viscous and inertial permeabilities.

It can be stated that the effects of inertial flow can be neglected when the inertial term as defined by Forchheimer is much smaller that the viscous one, i.e.:

$$\frac{z_p.\eta.(Q/A_p)}{\Phi_v} >> \frac{z_p.\rho.(Q/A_p)^2}{\Phi_i} \qquad \text{Equation 29}$$

or

$$\frac{\Phi_v}{\Phi_i} << \frac{\eta.A_p}{\rho.Q} \qquad \text{Equation 30}$$

Assuming a perfect gas,

$$\rho = \frac{p_{ref}}{R.T} \qquad \text{Equation 31}$$

Also, from the derivation in Appendix A,

$$\frac{p_1^2 - p_2^2}{2.p_{ref}} = \frac{z_p.\eta.(Q/A_p)}{\Phi_e} \qquad \text{Equation 32}$$

Substituting for (Q / A_p) and ρ,

$$\frac{\Phi_v}{\Phi_i} << \frac{2.\eta^2.R.T}{p_1^2 - p_2^2} \cdot \frac{z_p}{\Phi_e} \qquad \text{Equation 33}$$

For a given bearing design, however, the term Φ_e / z_p should be constant. This is because a larger thickness would be required for a more permeable material in order to achieve the same degree of pressure restriction. Taking the measured data from a typical bearing as an example, (a 0.5 micron injection moulded bearing), Φ_e / z_p = 6.16E-13 for a bearing number of 23.7 and a working gap of 2.5 μm.

Knowing the operating conditions of the bearing, the right hand side of equation 30 can be determined. The average exit pressure of the porous pad is approximately 0.67 of that of the gauge supply pressure according to Gerke [137] i.e.,

$$p_2 - p_a = \frac{2}{3} \cdot (p_1 - p_a) \qquad \text{Equation 34}$$

Substituting,

$$p_1^2 - p_2^2 = p_1^2 \cdot \left[1 - \frac{1}{9} \cdot \left(4 + 4.\bar{p}_a + \bar{p}_a^2 \right) \right] \qquad \text{Equation 35}$$

Using standard properties of air at 20 °C, and assuming a supply pressure of 5 bar,

$$\frac{\Phi_v}{\Phi_i} << 1.52E\text{-}5 \qquad \text{Equation 36}$$

if deviation from Darcy's law due to inertia effects is to be neglected.

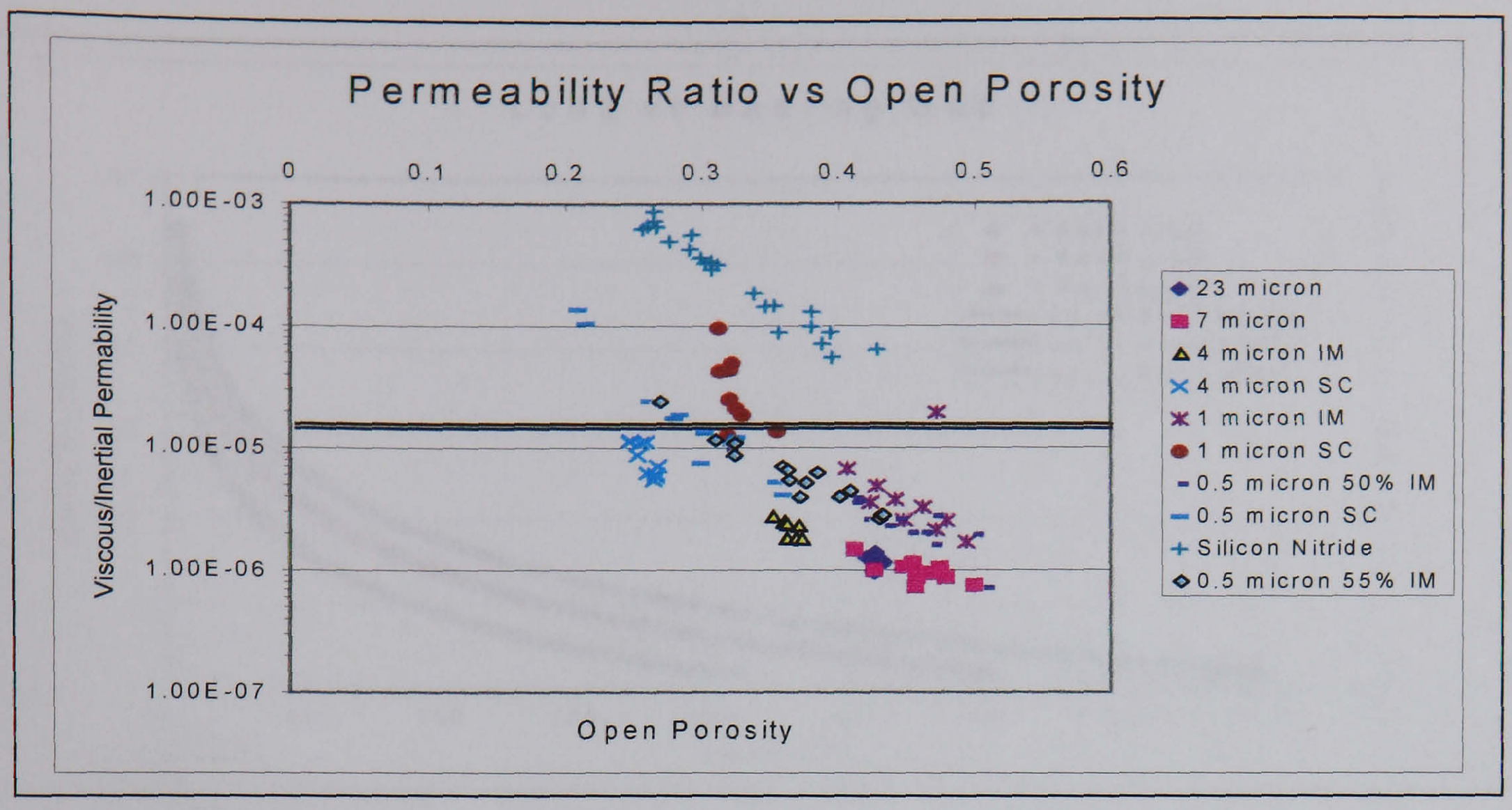

Figure 48 Permeability ratio

As can be seen from the above graph in figure 48, a large part of the data generated here is non-Darcian in nature (that above the line), and so for those, inertial terms could well be significant. It is worth noting that in general the finer powder size bearings tend to the non-Darcian regime. The exceptions are the 1 micron slip cast alumina and the 0.5 micron 50% initial density injection moulded samples. These are important observations as these two sets of bearings proved to be among the better performing bearings. It also gives the advantage of simplifying the design and parameter specification of these bearings.

4.5 Bearing Performance

Several aspects of bearing performance are fundamental to their operation, such as load carrying capacity and stiffness, and require to be measured.

Both of these parameters were measured for a number of bearings on the rig as detailed in the Experimental Chapter. An example graph of the response of a 0.5-micron alumina bearing is shown below.

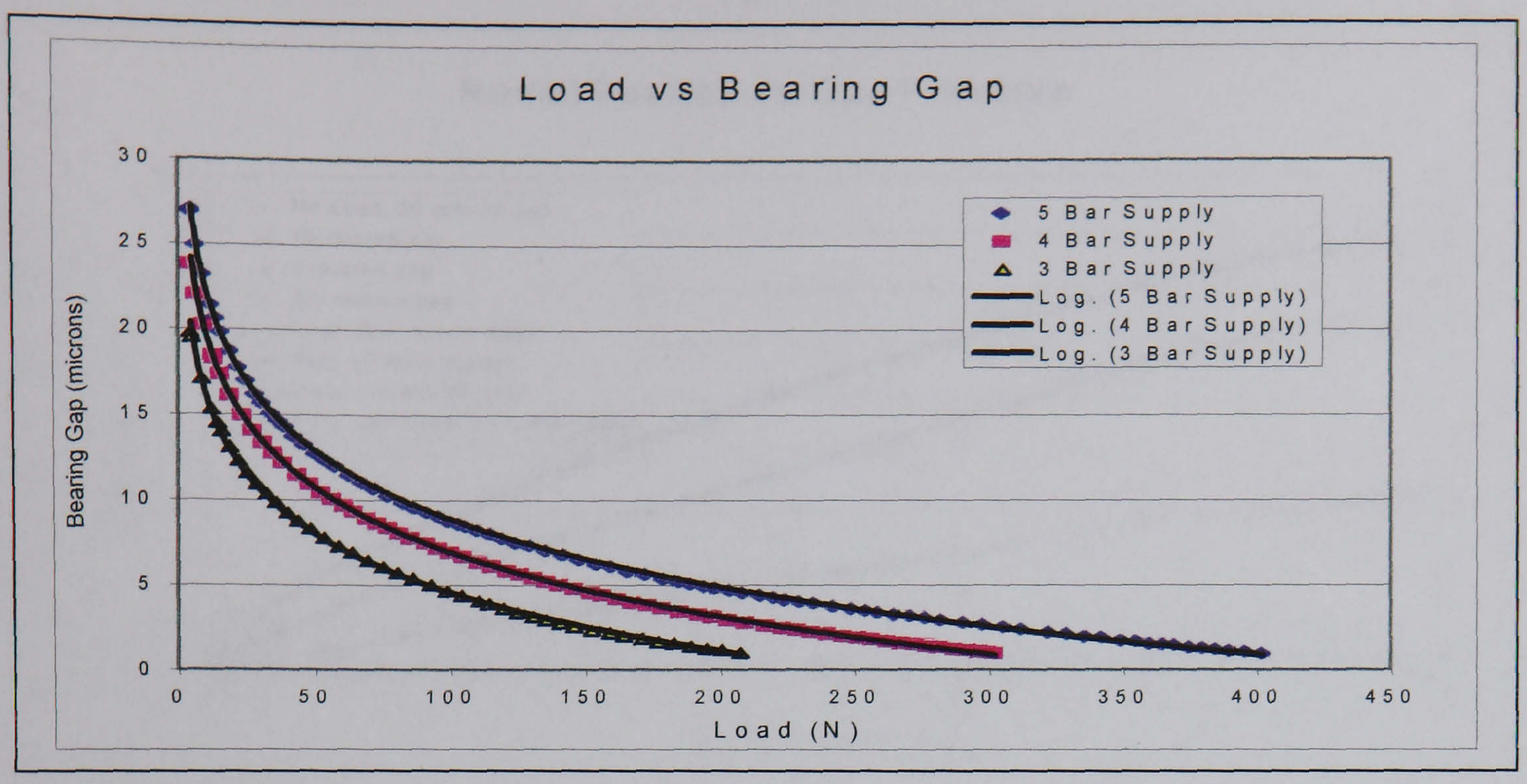

Figure 49 Bearing gap as a function of load

The first graph, Figure 49, shows the bearing response to an increasing load with three different bearing supply pressures. In every case it can be seen that the bearing gap changes rapidly with increasing load initially, but the slope of the line becomes less steep gradually with increasing load.

Curve fitting to these lines showed that logarithm relationship curves universally gave the best approximation to the real data. These best-fit lines can then easily be differentiated to provide the slope at any point, and hence the stiffness at any bearing gap.

Figure 50 shows an illustration of the pressure profile under the same bearing as shown above in figure 49. Here we see the change in gap pressure across the radius for four different bearing gaps, all at a supply pressure of 5-bar gauge. As can be seen, decreasing the bearing gap by increasing the load leads to an increase in gap pressure.

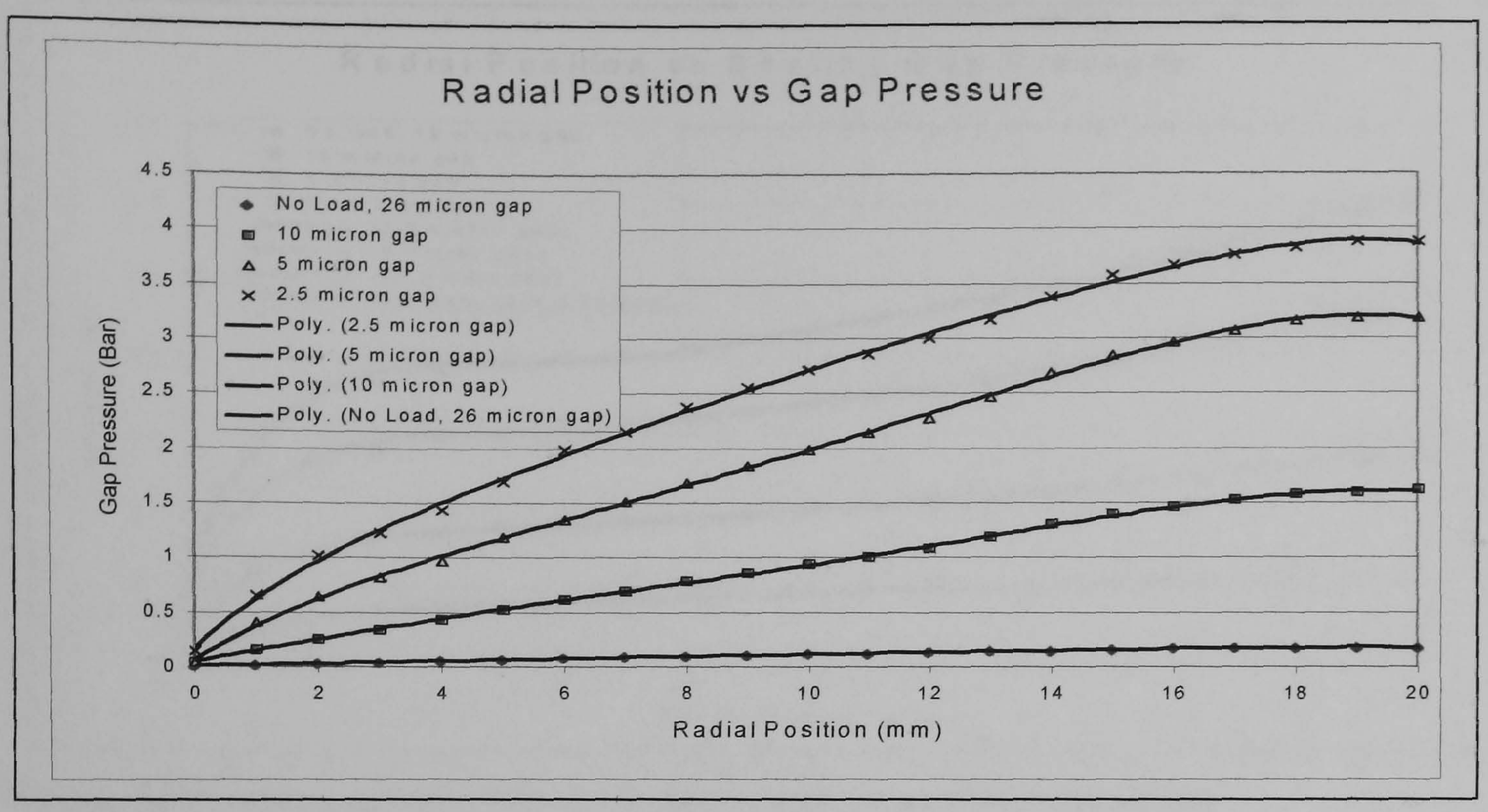

Figure 50 Pressure distribution under well machined bearing

This technique also proved valuable in helping to identify poorly manufactured bearings. A parabola approximates the ideal pressure profile under the bearing, similar to that seen above, while the actual data for another 0.5 micron bearing is illustrated below in figure 51.

Here we see the profile is anything but smooth, and the subsequent stiffness tests confirmed that the bearing was indeed defective. Another good indicator is the load required to give a specified bearing gap. For example, the above good bearing required a load of 345N to reduce the gap to 2.5 microns, whilst for the poor one, it needed less than 75N. Further, it can be clearly seen that the gap pressure in the defective bearing is a fraction of the better one, which has a peak value closer to that predicted by Gerke [137] of 2/3 supply pressure.

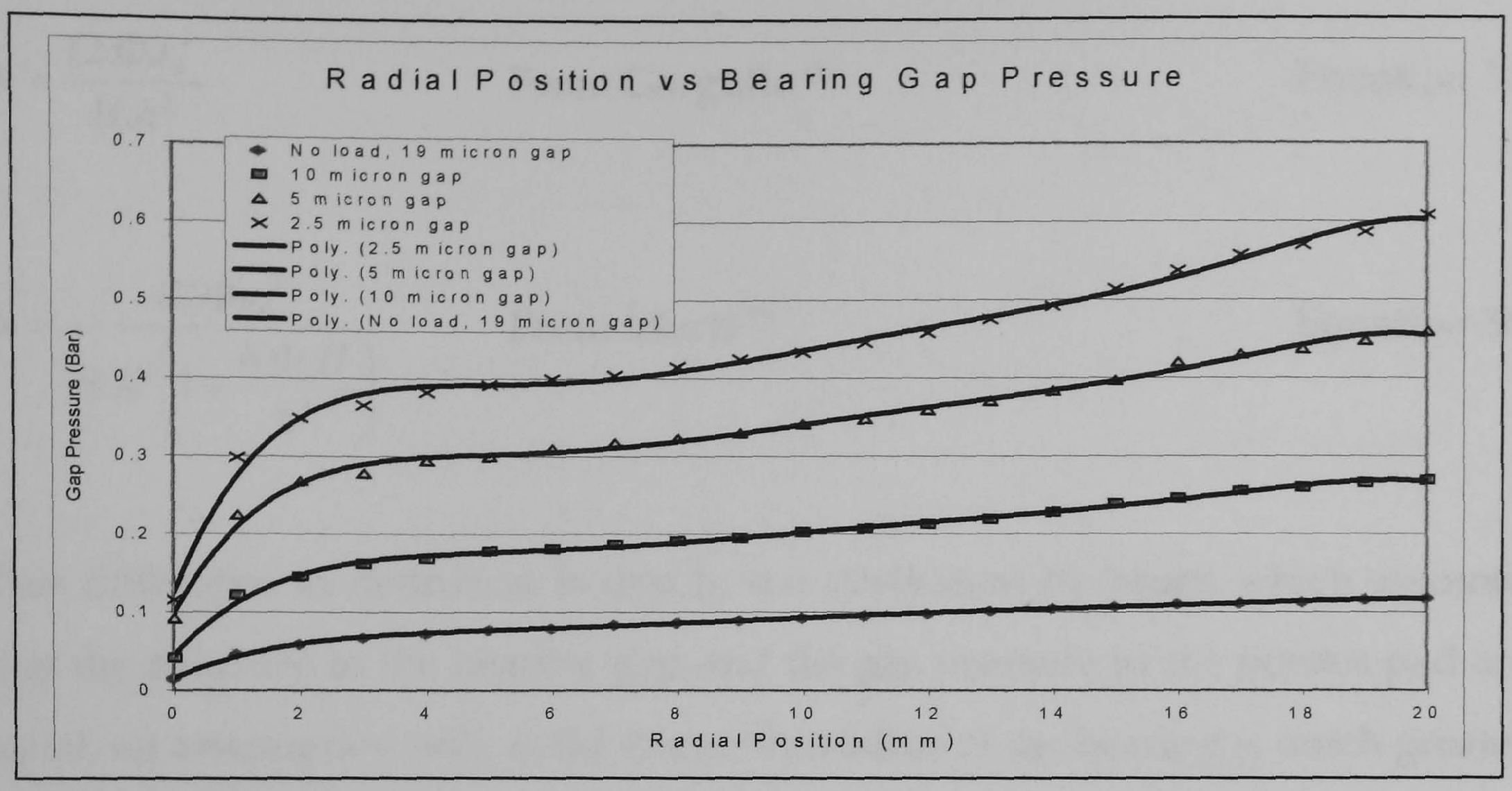

Figure 51 Pressure distribution under poorly machined bearing

4.5.1 Comparison of Bearing Performance Data

The data generated from the stiffness rig testing proved suitable for a number of comparisons with published works. Previously notable theoretical analyses were undertaken by Gargulio & Gilmour [70], and Murti [73]. However, there seems to be a lack of experimental verification of their work in the subsequent years. The great number of bearings tested here provides a good opportunity to examine their work in the light of real experimental data.

4.5.1.1 Load Carrying Capacity

Both Gargulio & Gilmour and Murti papers examine the relationship between the load carrying capacity of porous air bearings and the bearing number. The bearing number is a convenient dimensionless number that characterises a bearing and takes into account the geometry, permeability, and bearing gap. It is a useful tool in examining the state of operation of a bearing at any one time, as well as giving guidance in the design stage.

These authors each define the term bearing number in a slightly different way:

$$\Lambda = \frac{12.\Phi.r_0^2}{H.h^3}$$ From Gargulio [70] Equation 37

$$\Lambda = \frac{12.\Phi.r_0^2}{H.h^3\left(1+\frac{6.\Phi.H}{h^3}\right)}$$ From Murti [73] Equation 38

This difference in definition is due to the derivation by Murti which assumes that the pressure in the bearing gap and the gas pressure in the porous pad are equal, an assumption only valid where the radius of the bearing is much greater than the thickness, i.e., $r_0 >> H$.

Both assume viscous, laminar flow through the bearing, where inertial terms are neglected. Also there is no relative motion between the surfaces of the bearing and the counterface, the gas is Newtonian, has constant viscosity, is isothermal, and obeys the equation of state:

$$P = \rho \, . \, R \, . \, T$$ Equation 39

The bearing material is rigid, meaning that no deflection occurs due to the supply pressure and so the gap is constant, it is isotropic, has uniform permeability, and a constant thickness. Also, Darcy's law governs the flow in the bearing material.

In a similar manner, the load carrying capacity of a bearing may be examined in a non-dimensionalised way. Both sets of authors use a common format:

$$\frac{W}{W_0} = \frac{W}{\pi \, R_0^2\left(P_s - P_a\right)}$$ Equation 40

This equation relates the actual load on the bearing to the theoretical maximum load that the bearing could support. This maximum load supposition is only valid assuming a perfectly flat bearing surface, small pores, a perfectly conformable surface upon which the bearing acts, and no radial flow through the periphery of the bearing. This would then allow the pressure in the bearing gap to rise to the supply pressure, as the bearing gap becomes increasingly smaller. The validity of this will be discussed subsequently.

Figures 52 and 53 below illustrate surface roughness in the direction of grinding and perpendicular to the grinding direction for the better of the two bearings illustrated above, and figures 54 and 55 show the poorer bearing. What is immediately obvious is that neither of the two bearings is particularly flat, indeed pick up from the counterface could clearly be seen on the better bearing as seen in figure 56, and it is across these marks that the roughness measurements have been made. The scales on all of the four following graphs were kept the same, the gap between each horizontal line represents 2µm, and the gap between each thick vertical line was 0.5mm.

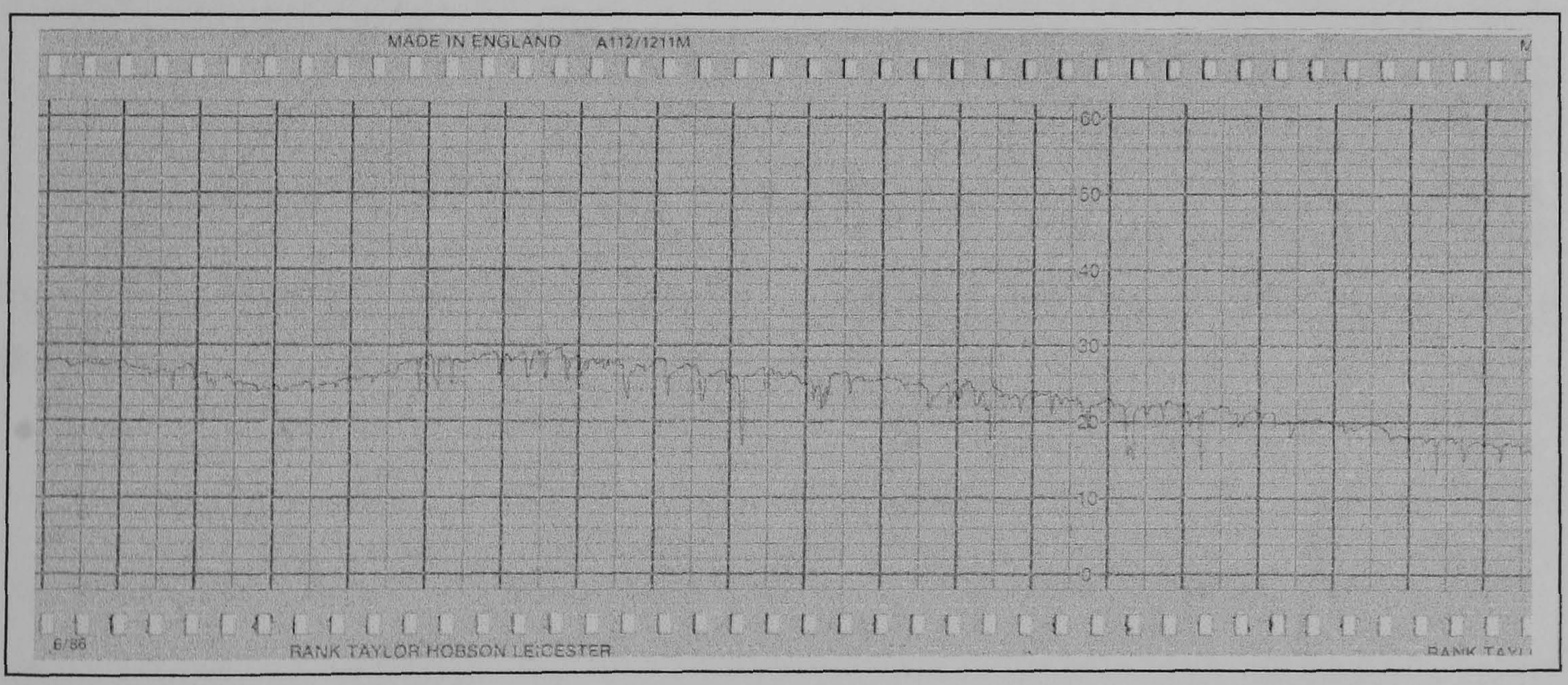

Figure 52 Surface profile of well-machined bearing in the direction of grinding

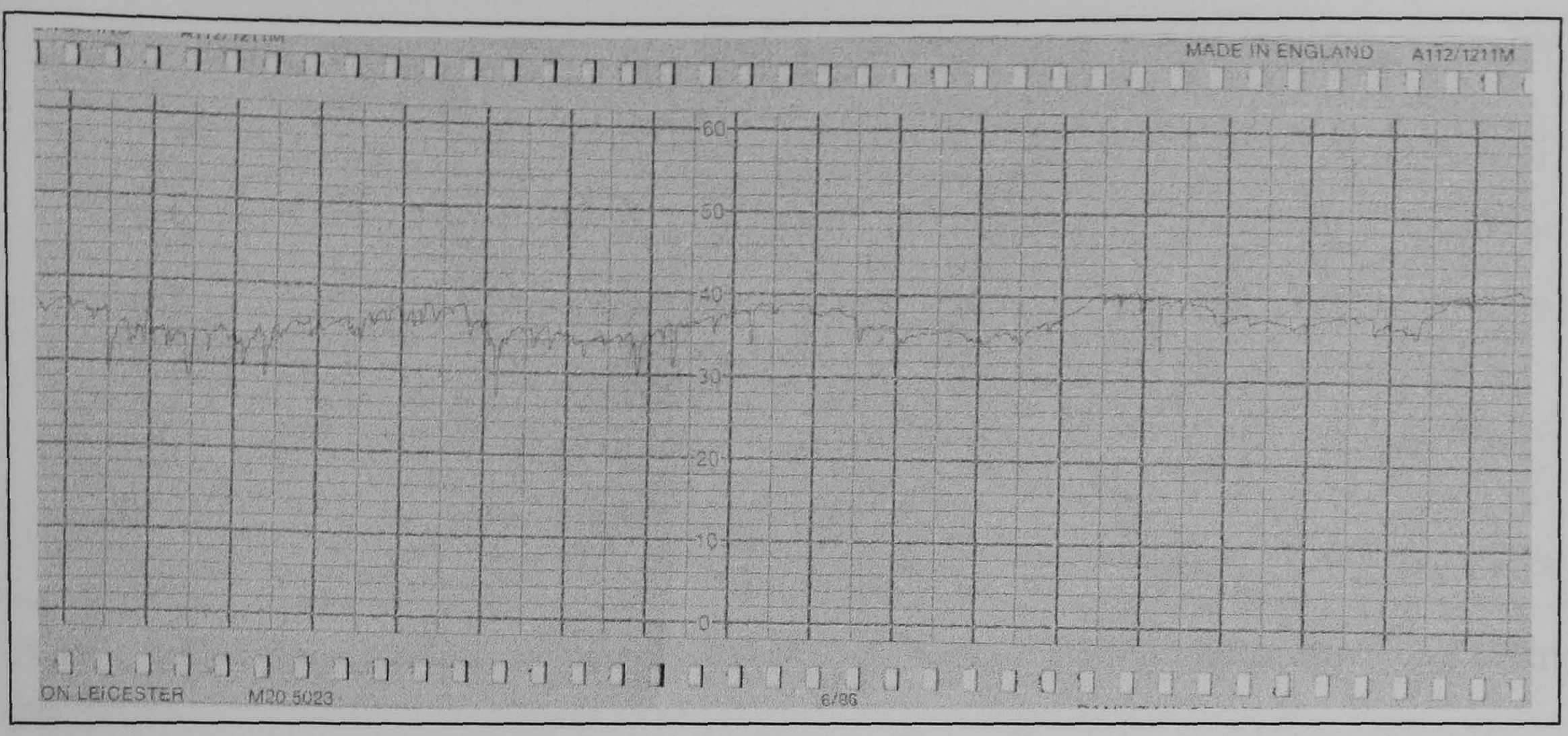

Figure 53 Surface profile of well-machined bearing perpendicular to grinding direction

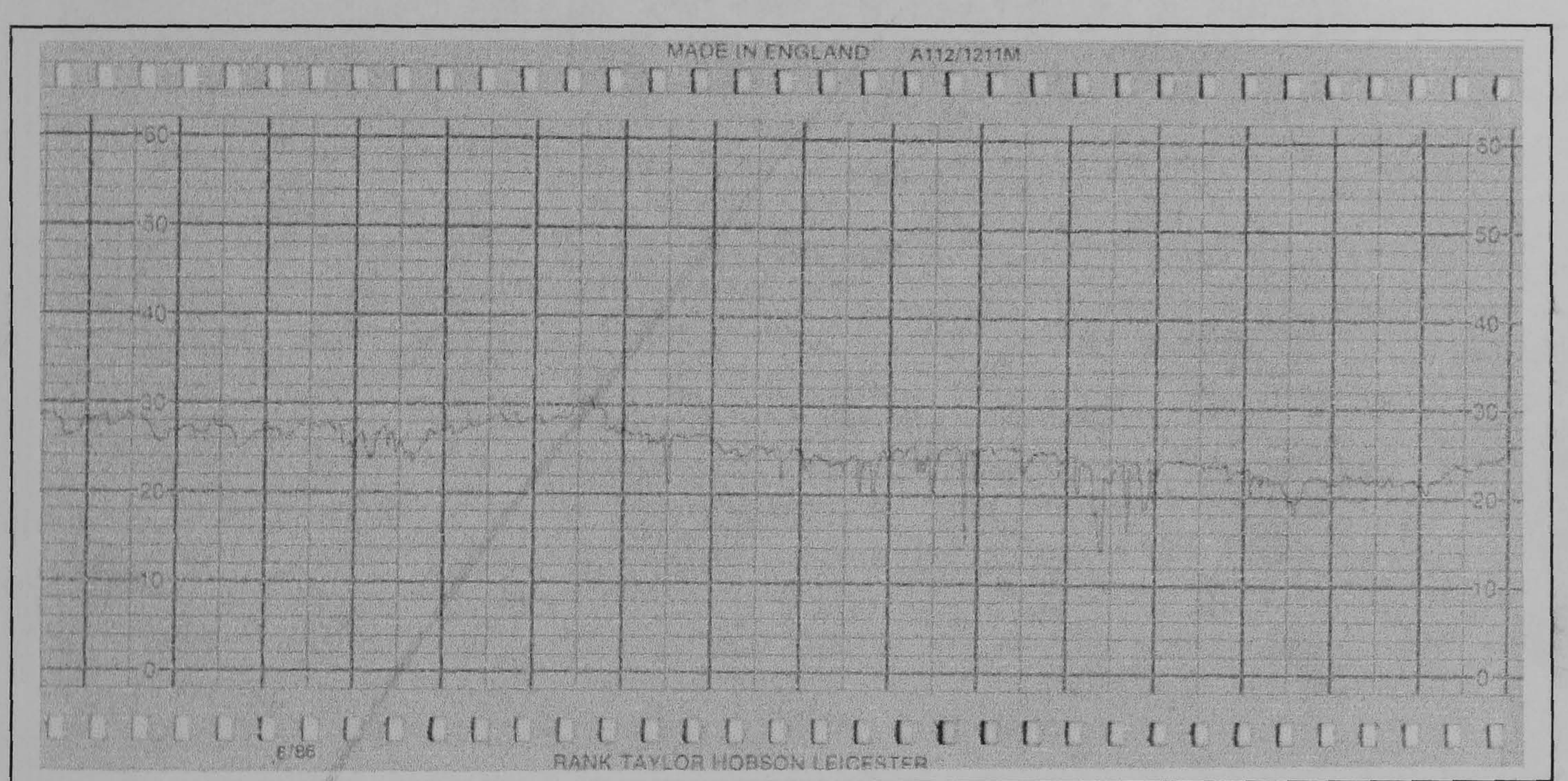

Figure 54 Surface profile of poorly machined bearing in the direction of grinding

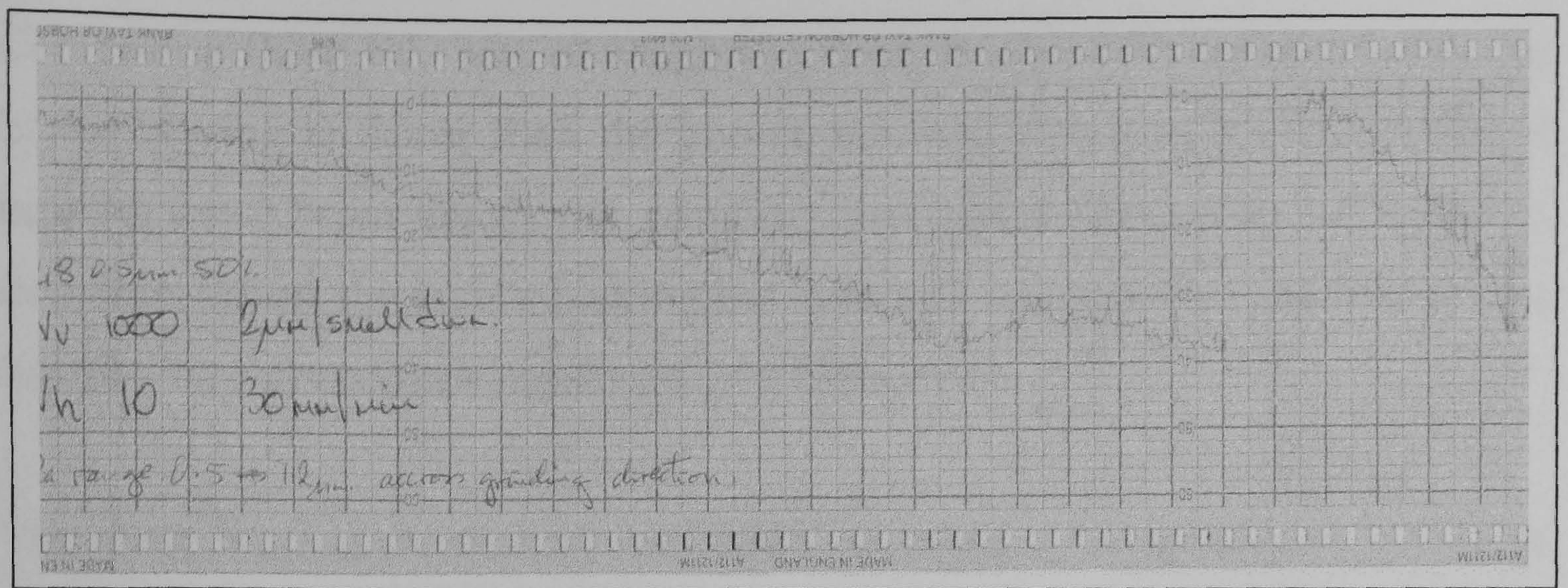

Figure 55 Surface profile of poorly machined bearing perpendicular to grinding direction

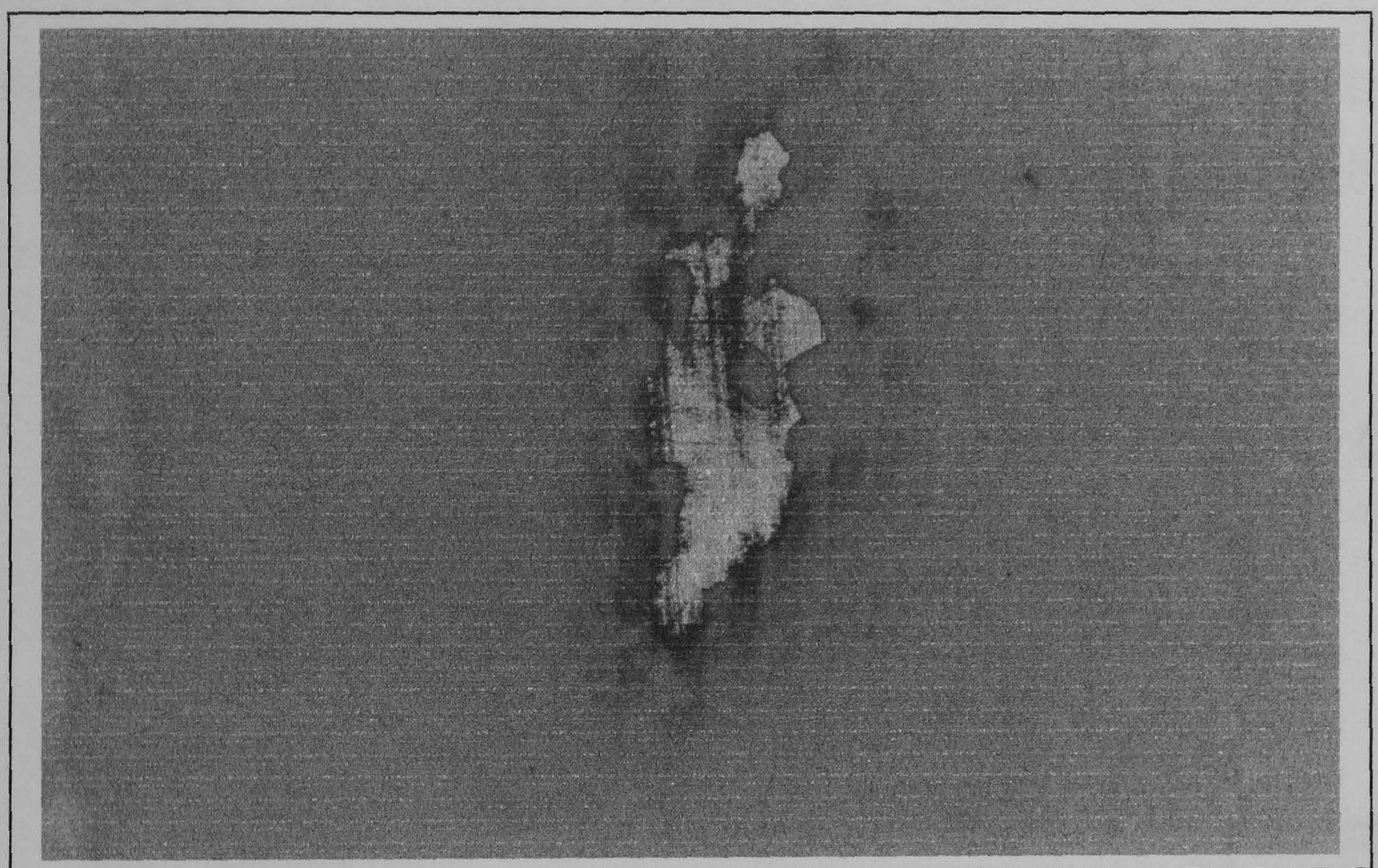

Figure 56 Metallic pick-up on surface of bearing

Both of these sets of data were taken with the bearing sitting clamped into the holder. The holder was then levelled so the shoulder of the bearing holder was horizontal. This was achieved by observing the trace needle as the stylus was passed over the surface. The holder was progressively shimmed until the error was removed. The out of flatness appears to be due to poor grinding, as grinding marks are still clearly visible on the surface, and the occurrence of metallic pickup on one bearing backs up this assumption.

Comparing these two sets of roughness data, it is visually apparent that the better bearing is flatter than the poorer bearing. Values of Ra for the better bearing are 0.74µm across the grinding direction, 0.72µm with the grinding direction, whilst the poorer bearing has values of 1.2µm across and 0.9µm with the grinding direction as measured on a Talysurf 10.

The same bearings were examined for form using a Form Talysurf 120L. The bearings were again examined in the grinding direction and across it. This produced four figures, figures 57 and 58 refer to the higher-performance component in the direction of grinding and perpendicular to the direction of grinding respectively. Figures 59 and 60 show the bearing that did not perform as well in terms of measured stiffness and load carrying capacity in the direction of grinding and across the direction of grinding.

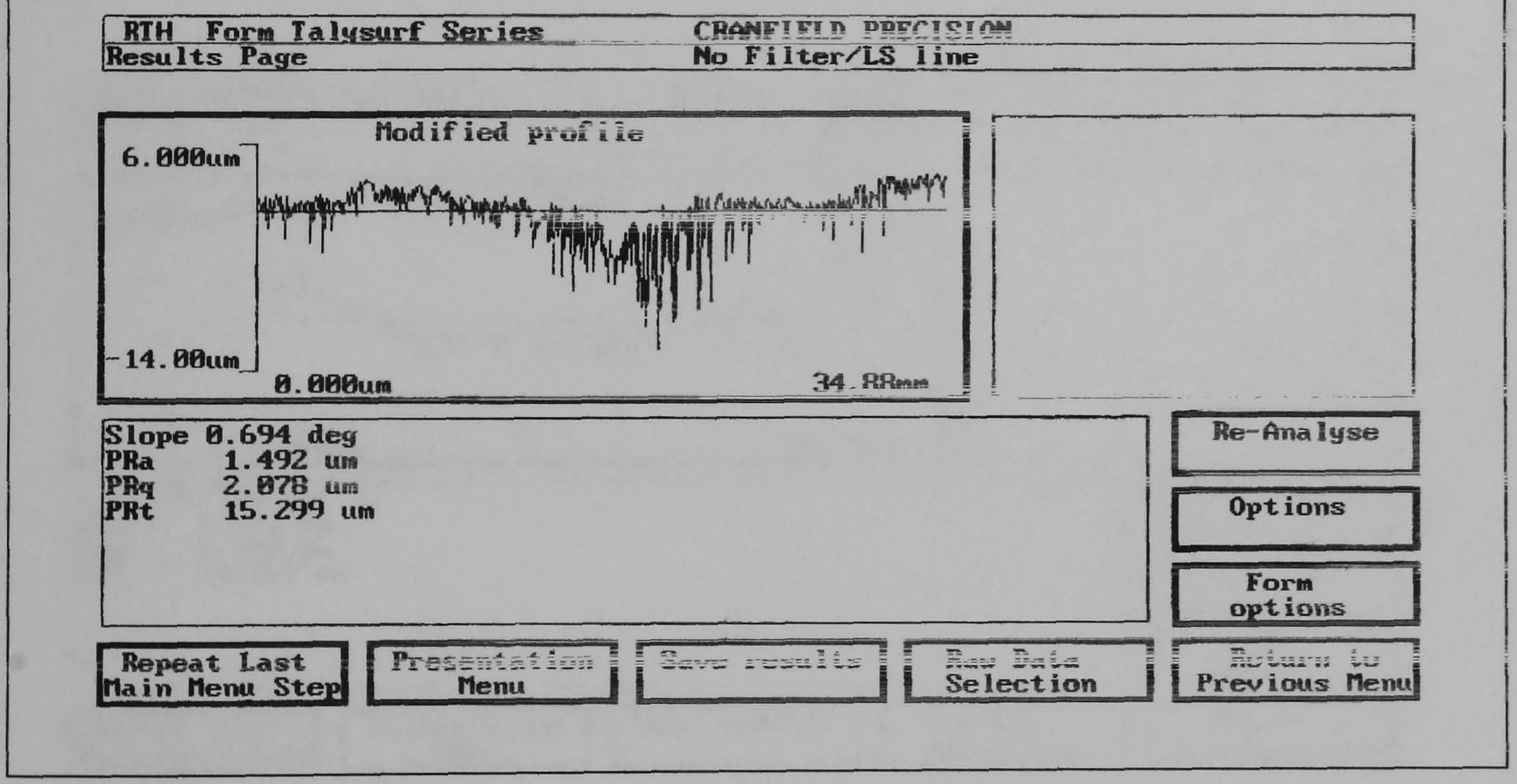

Figure 57 Surface form of better bearing in grinding direction

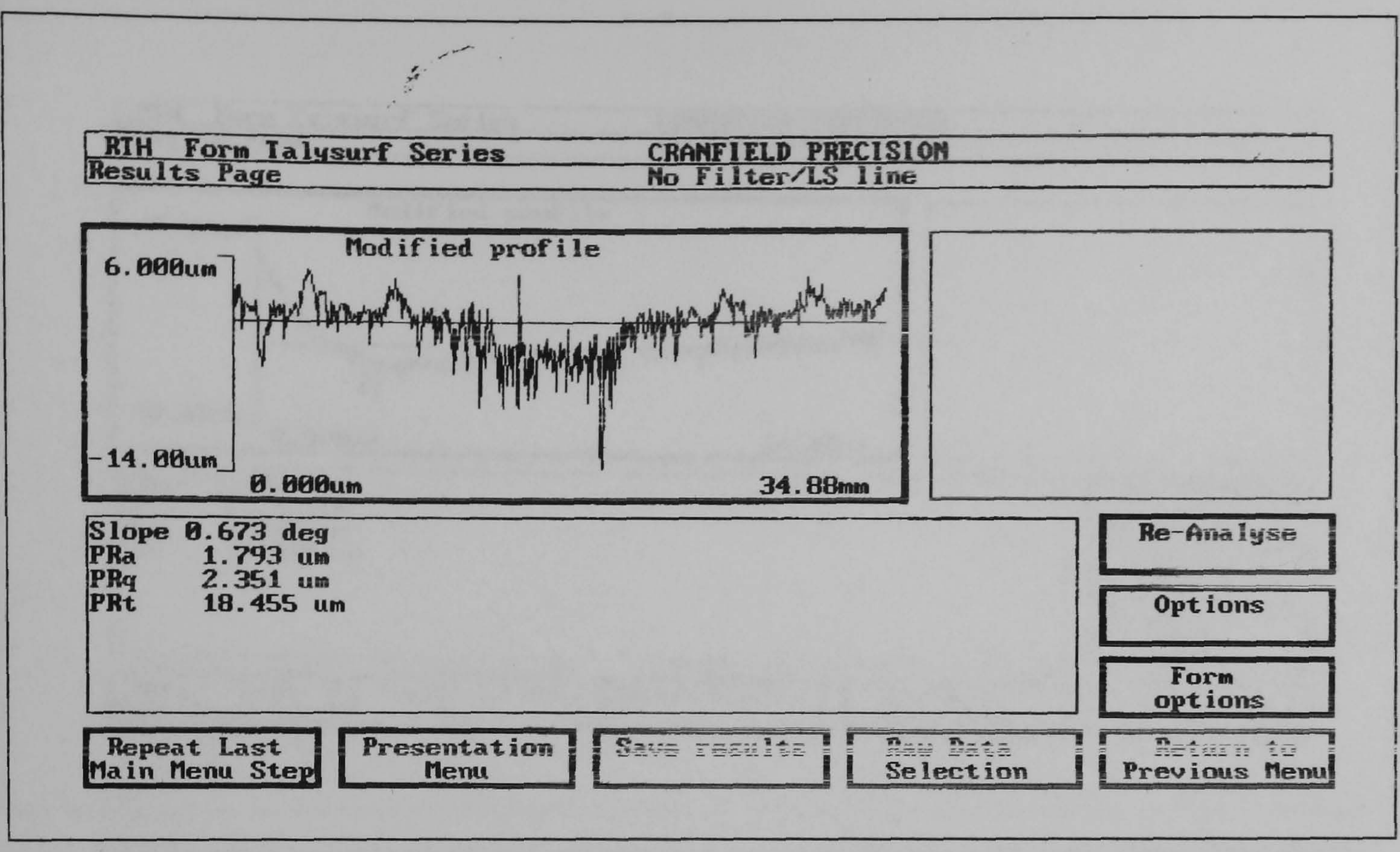

Figure 58 Surface form of better bearing perpendicular to grinding direction

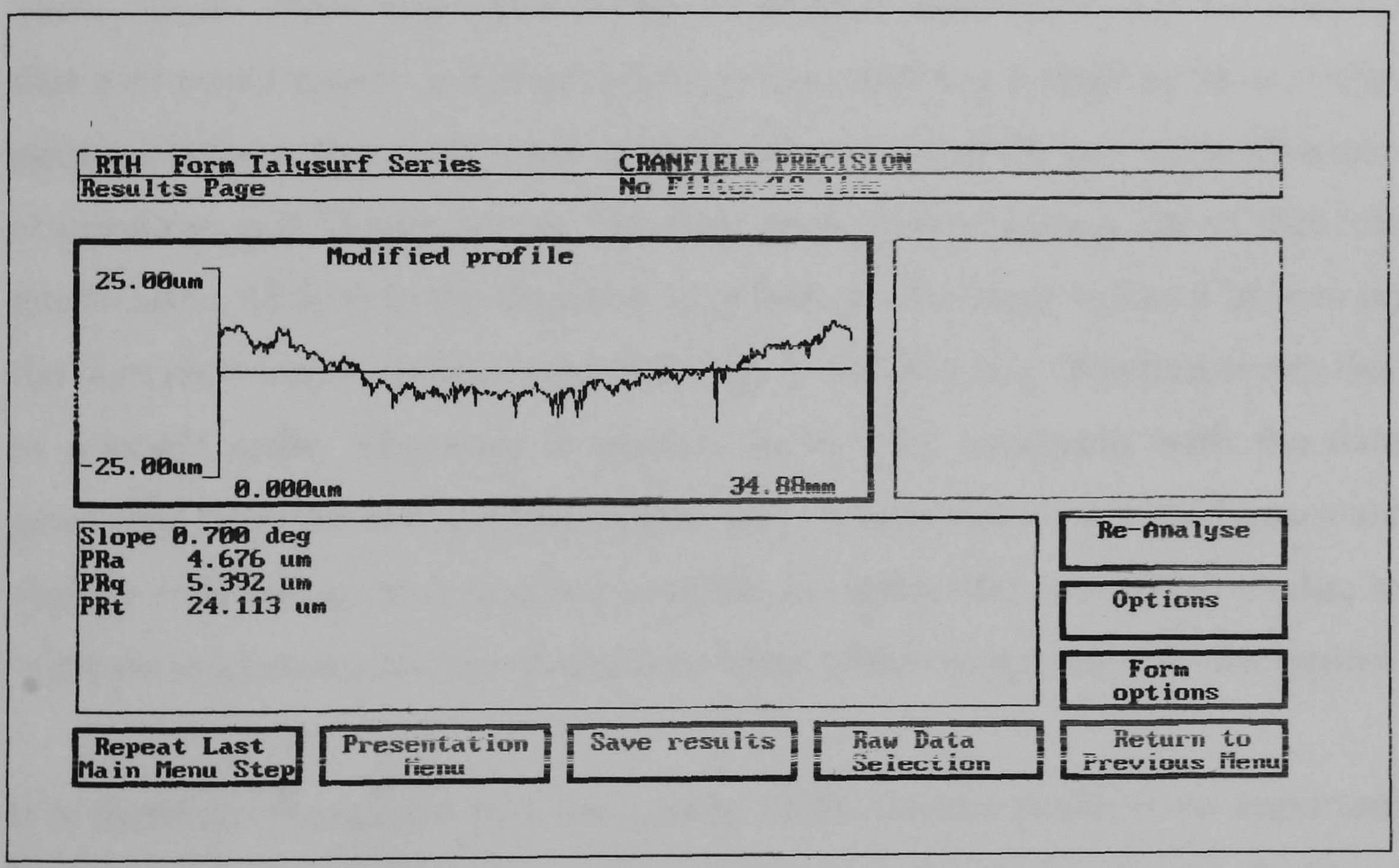

Figure 59 Surface form of poorer bearing in grinding direction

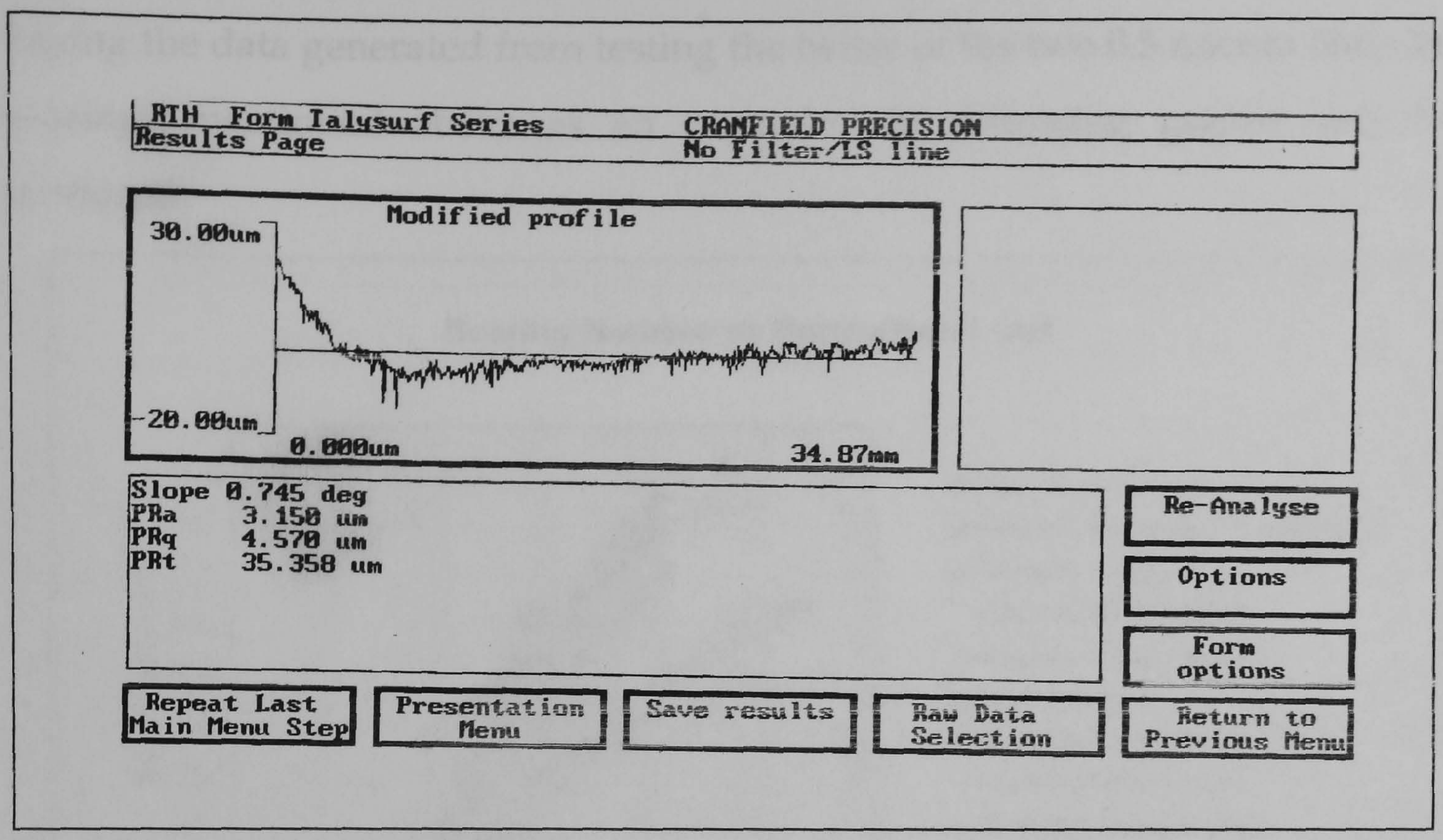

Figure 60 Surface form of poorer bearing perpendicular to grinding direction

These figures show that while neither bearing is particularly flat, the bearing that performed poorly is dished in one profile, and has a large lip at one edge perpendicular to that. This leads to large values of R_t of 24.1μm in the direction of grinding, and 35.4μm across. The scan of the better bearing shows that it is much flatter, 15.3μm in the direction of grinding. The larger value of 18.5μm on the scan showing the profile perpendicular to the grinding direction seems due to a single spike, otherwise it appears to be very consistent with the data generated from the run at right angles. The vertical scales on these figures are slightly misleading, as it was not possible to choose the cut off values due to software limitations, so care needs to be taken when comparing the four figures.

It is therefore postulated that the quality of the surface finish is an important parameter in the performance of the bearing, as the flatter, better machined component performed in a superior manner to the rougher one. A rougher, less flat, surface gives rise to a larger volume of dead air volume beneath the bearing, effectively aiding the losses by making it easier for the gas to escape. This correlates with the pressure profiles shown earlier.

Taking the data generated from testing the better of the two 0.5 micron alumina bearings mentioned above as an example, the following graphs may be produced.

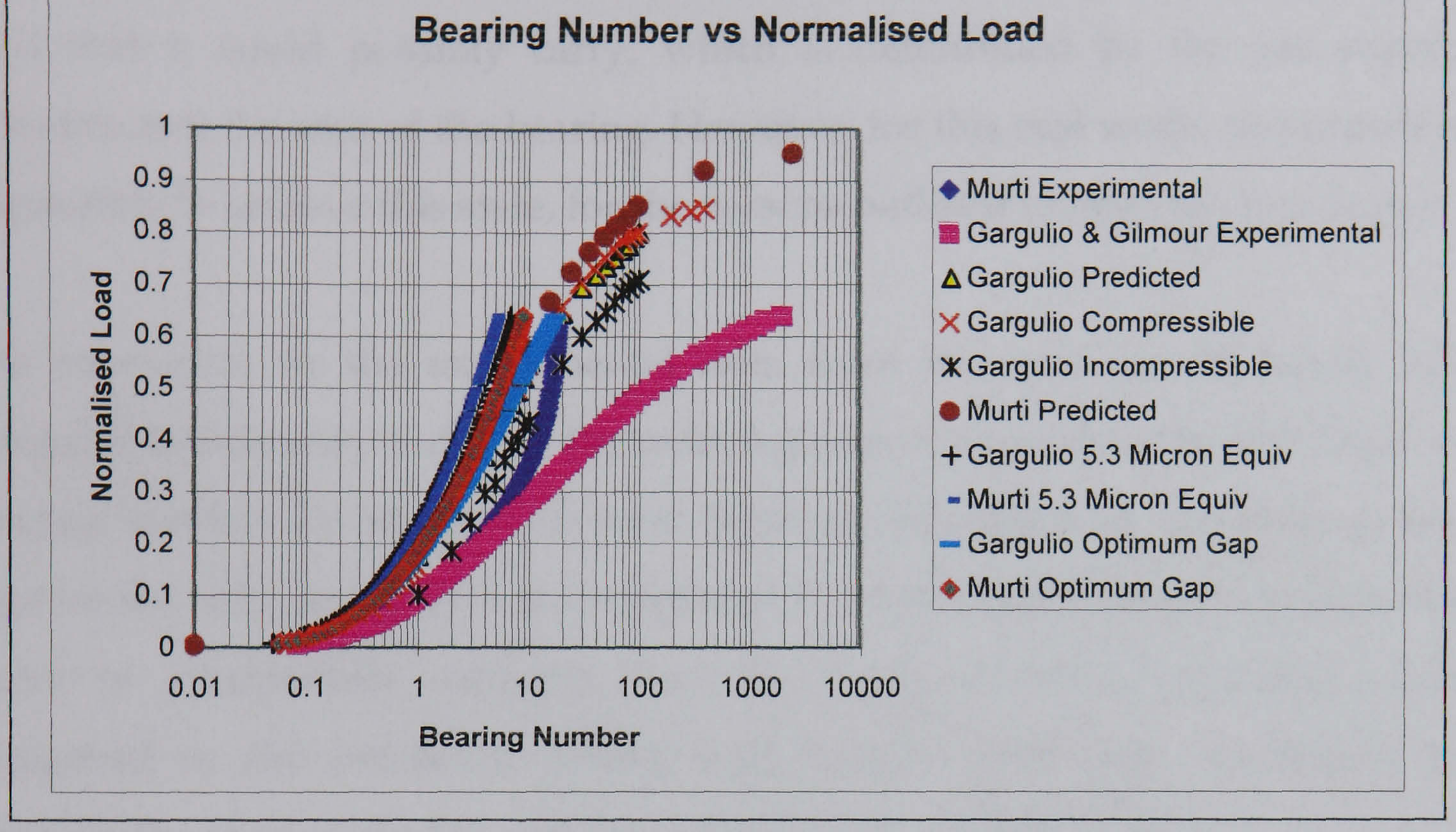

Figure 61 Normalised load as a function of bearing number

This graph, figure 61, shows real experimental data analysed using the theories postulated by both Murti and Gargulio & Gilmour, compared to their predicted responses.

The data shown above for Gargulio & Gilmour, labelled Predicted, Compressible, and Incompressible, are redrawn after carefully measuring the data presented in their paper [70], whilst the curve predicted by Murti is reproduced by interpolating the information in table 1 of his paper [73]. The curves designated Experimental represent the data generated during testing in the present work which have been subject to the equations defined previously (equations 37 and 38). The remaining four curves designated Equiv and Optimum are discussed later.

What is immediately noticeable is that the experimental curve as defined by the Gargulio & Gilmour analysis is of a very similar shape to that predicted, while

the Murti experimental curve is of a very different nature. Both fall below the predicted line. This is due to the lower than predicted response to the increasing load. According to the predicted behaviour the bearing should approach a state where the load it is carrying equals the maximum theoretical load that it could possibly carry, which is determined by the gas supply pressure and the area of the bearing. However, for this real world situation it is impossible to achieve this state, for the reasons outlined on the previous pages.

The separation in the experimental data from the analyses by Murti and Gargulio & Gilmour, is due to the extra term incorporated in the definition of bearing number by Murti. This term becomes significant as the bearing gap approaches zero, as the h^3 term dominates. The form of the Murti Experimental curve is substantially different over the range of data presented when compared to the predicted values, and further work was undertaken to evaluate the form of the curve beyond the real data as shown here.

For this imaginary bearing, the full range of data for all of the 0.5 micron alumina bearings, for all processing routes and conditions, were combined to form an "average" bearing. This technique produced a composite bearing that it was felt could evolve useful data. The reasoning behind using those bearings that did not perform as well as expected along with those that did was to attempt to generate a genuine baseline of performance that could realistically be achieved.

The procedure to produce this bearing was to curve fit log curves to the experimental stiffness data as was shown previously (figure 49), for every bearing tested and calculate the average constant and exponential values from all these tests to produce a log response that could be considered a mean response. Similarly, average data were taken for thickness and permeability values. Arithmetically then:

$$\frac{\Sigma Y}{n} = \frac{\Sigma A}{n}\ln(x) + \frac{\Sigma B}{n} \qquad \text{Equation 41}$$

The resulting curves showing the response of this bearing to an increasing load is shown in figure 62 below

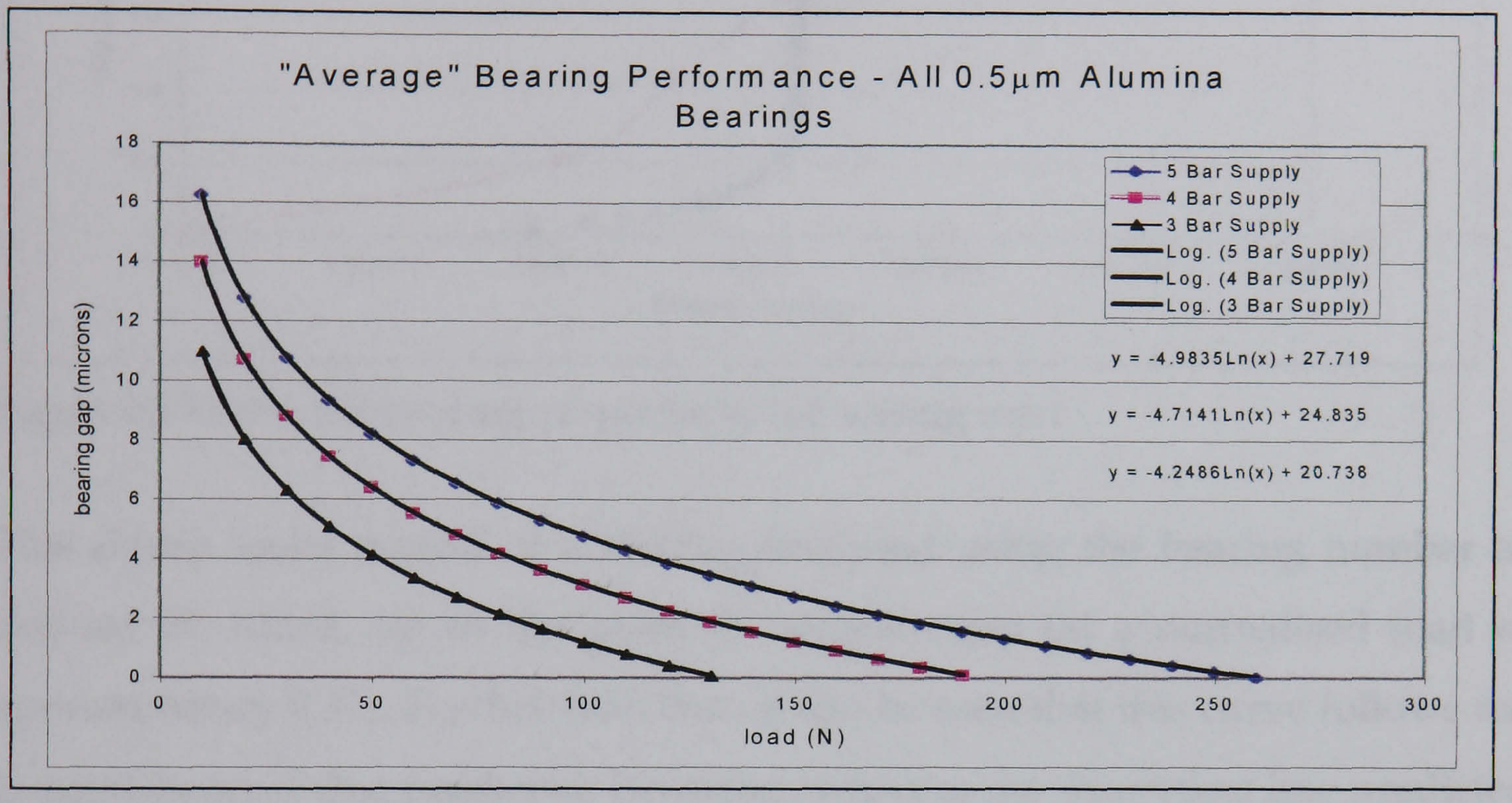

Figure 62 Deflection as a function of load for "average" bearing

The advantage of this bearing for the purpose of analysis was to allow an investigation of the relationship between bearing number and normalised load and stiffness at a range outside of that captured in real experimental data.

For example, it was possible to analyse the relationship of bearing number, as defined by Murti, with the normalised load as shown in figure 63 which shows the data for a 5 bar supply pressure. The upper half of the average bearing curve was generated using data that were produced by extending the data range illustrated in figure 62 above into negative gap, which will be discussed further later. This was easily achieved mathematically, as the log curve representing the response of the bearing to an increasing load was allowed to go below the x-axis. The resulting bearing number was always positive over the range of interest, as the equation describing it contains a product of two h^3 terms (equation 38).

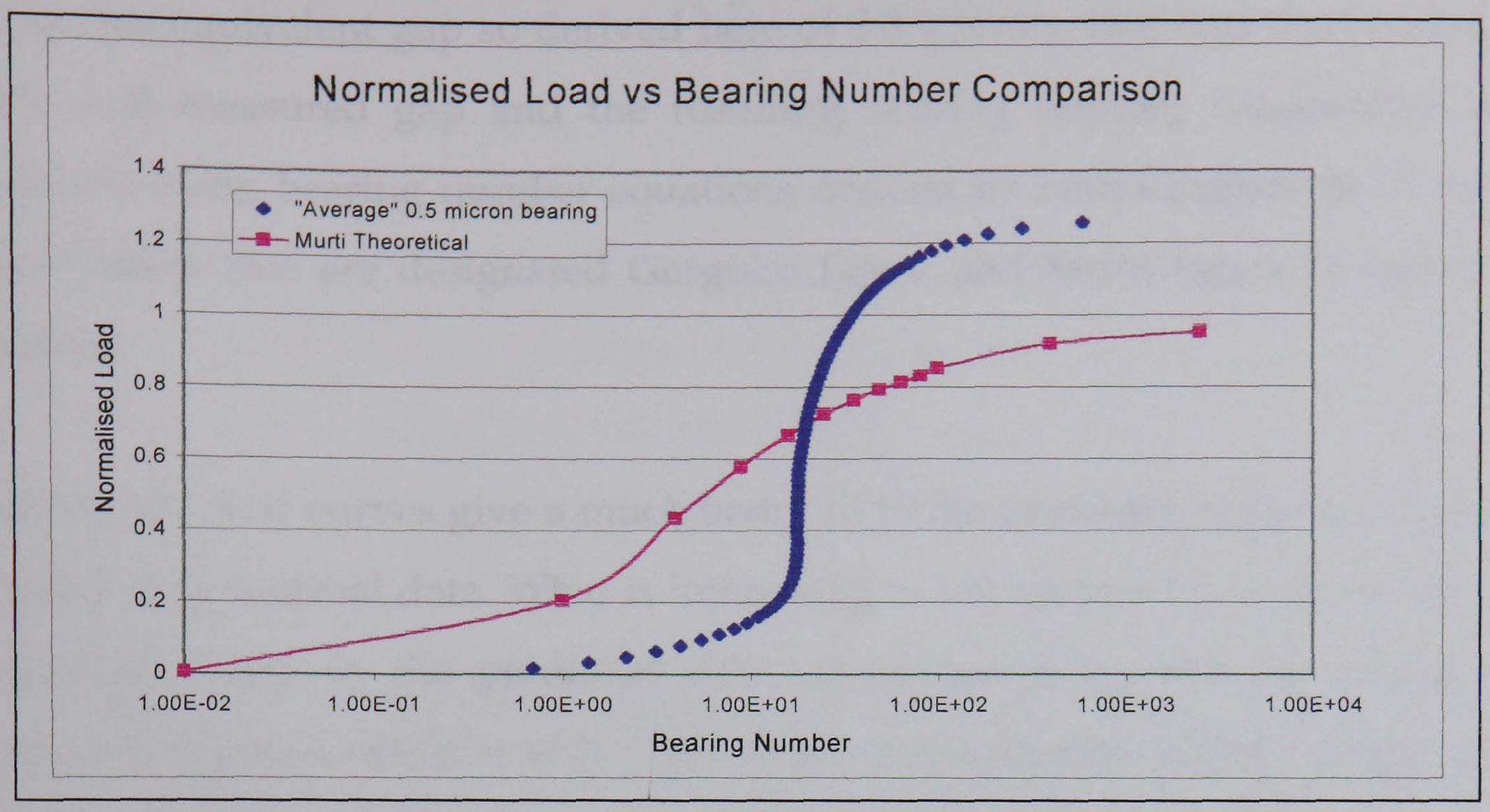

Figure 63 Extended bearing response to increasing load

This figure looks typical of a bearing analysed using the bearing number as defined by Murti, up to the point of negative gap (at a normalised load of approximately 0.41). Further than that, it can be seen that this curve follows the general trend of that predicted. However, whereas the theoretical line predicted by Murti asymptotically approaches 1 due to the way it is defined, it can be seen that this average bearing response is to approach a number in the region of 1.3. One can then feed this data back through the equations to give a value of bearing gap at which the curve flattens out. The value so generated gives a negative gap of 5.3μm. This value was then added to the stiffness data of several bearings and their response evaluated with this equivalent gap.

The idea of an equivalent gap has been used previously by researchers [81, 138, 139] to correct for shortcomings in the experimental data relative to the performance predicted by the bearing theories. The idea is to allow for phenomena such as slip flow and gas loss through the bearing edge in a simple manner. For example, the equivalent gap proposed by using a slip flow model [5] was 3.8μm, similar to that found in the present analysis.

It is this equivalent gap so derived here of 5.3 microns that was then added to the real measured gap and the resulting bearing number recalculated and plotted using bearing number equations defined by both Gargulio & Gilmour and Murti that are designated Gargulio Equiv and Murti Equiv in figure 61 above.

These two new curves give a much better fit to the predicted response than the actual experimental data. What is interesting to note is that by curve fitting the equivalent gap to the predicted data, an optimum number of around 3.6 microns appears which is very close to that predicted by Kwan [5] using a slip flow approach of 3.8 microns, and of 3 microns found by curve fitting his experimental data to the predicted line.

4.5.1.2 Bearing Stiffness

In addition to load carrying capacity, stiffness is of vital importance in air bearing applications. As mentioned previously, the stiffness is determined by the rate of change of bearing gap with change of load. As illustrated in figure 49, log curves fitting yields an excellent approximation to the true response of the bearing, allowing easy differentiation of the curve, and hence the stiffness at any bearing gap.

Murti [73] carried out a predictive analysis of stiffness but lacked any data to validate the theory. What is presented here is a comparison of the experimental data generated during the course of this research with that predicted by Murti.

The data for stiffness as predicted by Murti results from the solution of a derivation containing integrals that cannot be conveniently expressed in closed form, and so a numerical integration approach was adopted utilising Simpson's rule, which resulted in the following relationship:

$$K = \frac{k.h.(1+6.\Phi.H/h^3)}{\pi\, r_0^2.(p_s - p_a)}$$ Equation 42

The stiffness testing was undertaken as outlined previously, and highlighted a significant problem with one aspect of the rig design. The bearing under test is clamped securely against a shoulder and a cap is placed at the rear of the holder to provide a gas seal and supply the gas to the bearing. This holder is illustrated in figure 64.

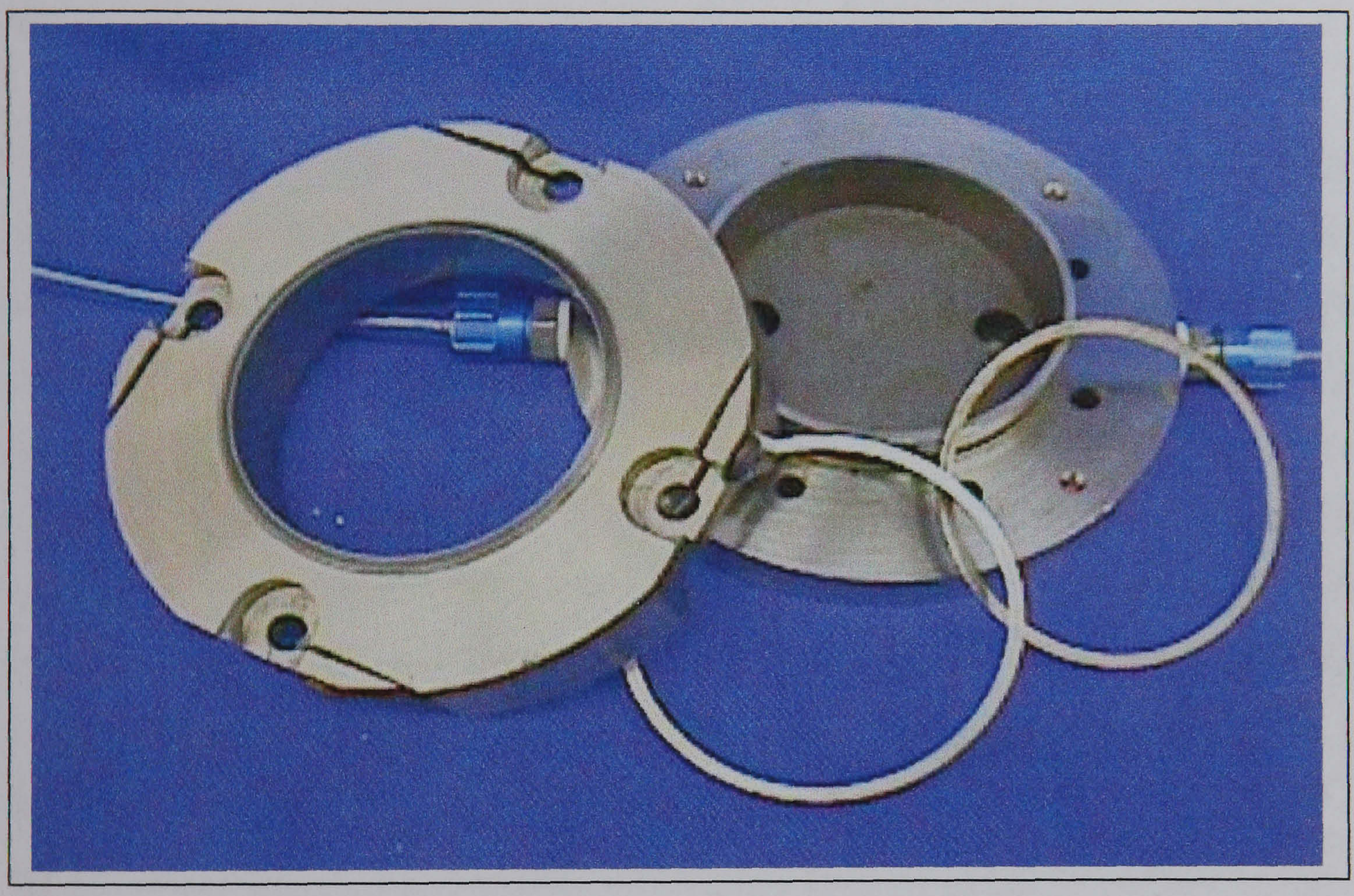

Figure 64 Bearing holder

Whilst this idea works perfectly well in theory, in practice it reveals a few shortcomings. Firstly, as the bearing is porous on every surface, the interface between the sealing edges and the bearing provide a useful gas path for leakage of supply gas around the side of the bearing. Attempts were made to eliminate, or at the very least, minimise this effect.

Sealing the edge provided problems of its own. For porous graphite applications lacquer has been used to selectively block pores, but due to the fine porous network present in the ceramic bearings, the extent of penetration of

the lacquer into the bearing was of some concern. The uncertainly regarding the effects this would have on the effective bearing area and permeability meant that this idea was disregarded. Instead, initially silicone sealant was applied to the edge of the bearing before insertion into the holder, the idea being to fill the gaps between the bearing and the housing and hence produce a gas seal. This very thick gel would not penetrate far into the ceramic matrix, thus ensuring the flow properties were not effected. In practice it proved very difficult to insert the bearing into the holder without the sealant smearing onto the bearing face.

Even if immediately wiped the silicone sealant tended to enter the pores slightly, reducing the effective area of the bearing. It was also found to be very difficult to remove this excess sealant in such a way that it no longer protruded beyond the bearing surface. As the measurements here typically measure to bearing gaps of less than 2μm, any protrusion inevitably lead to the bearing touching down prematurely at one point, skewing the resulting data. In addition it was found that is was very difficult to remove the sealant from the pores once it has entered. Even heating for 24 hours at 500°C was not sufficient as a char remained. This naturally leads to questions as to the reproducibility of the results for any particular bearing thus treated.

Another attempt was made to seal the bearing in place through the use of a gap filling cyanoacrylate adhesive (Loctite part number 411) [140]. This was an adhesive specifically developed for gap filling applications, and whose nature made for an excellent bonding agent of ceramic and metal. It also has the major advantage of being easily removed as cyanoacrylate adhesives dissolve readily in acetone, thus giving greater confidence in the likelihood of complete removal of the adhesive, and hence more chance of a reproducible experimental procedure.

This too suffered from a major disadvantage. Owing to the very fast acting nature of cyanoacrylate adhesives, it proved impossible to insert the bearing cleanly into the holder before the adhesive acted. This was due to the two closely fitting diameters between the bearing edge and holder and the relatively thin profile of the bearing. This led to bearings jamming at a slight angle during insertion and the adhesive gluing it firmly in place.

Eventually this approach was abandoned due to these complications, and a standard procedure adopted. This was to place the bearing in the holder and run a tack of the cyanoacrylate adhesive around the back of the bearing, at the junction of the bearing and the holder, in an attempt to produce some semblance of a seal. In all likeliness this effect would be small as the supply gas was still free to leak into the gap between the bearing and the holder past this adhesive layer, but it was felt better to attempt to seal the bearing.

It was also noted during some tests that some bearings inserted into the holder easier than others. It was decided to investigate this further, and a roundness profile of the inside diameter was taken with a Talyrond machine. This is seen in figure 65 below.

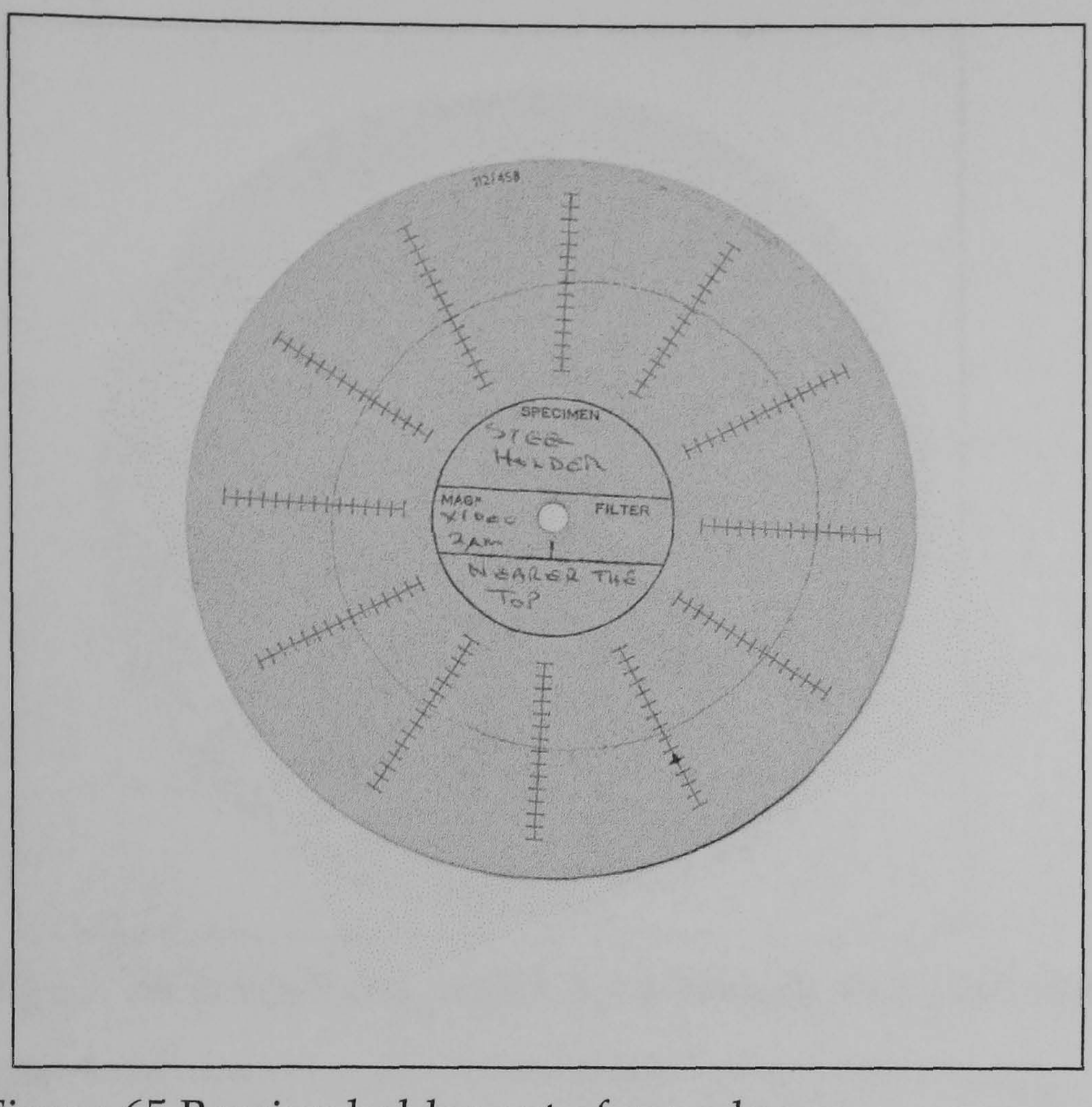

Figure 65 Bearing holder out of roundness

As can be seen from this figure, the holder is slightly elliptical, each tick mark on the radial lines represents 2µm. In addition to this error, it was noted that some bearings performed considerably better than others, despite being produced by identical routes. The key to the reason why, appears to lie with the ease of fit mentioned earlier. If we are to compare two bearings which are nominally identical but whose performance was very different, and subject them to the same roundness measurement as the holder, we begin to see a likely reason. Figures 66 and 67 below compare the roundness of a good bearing (Figure 66), with one that performed poorly (Figure 67).

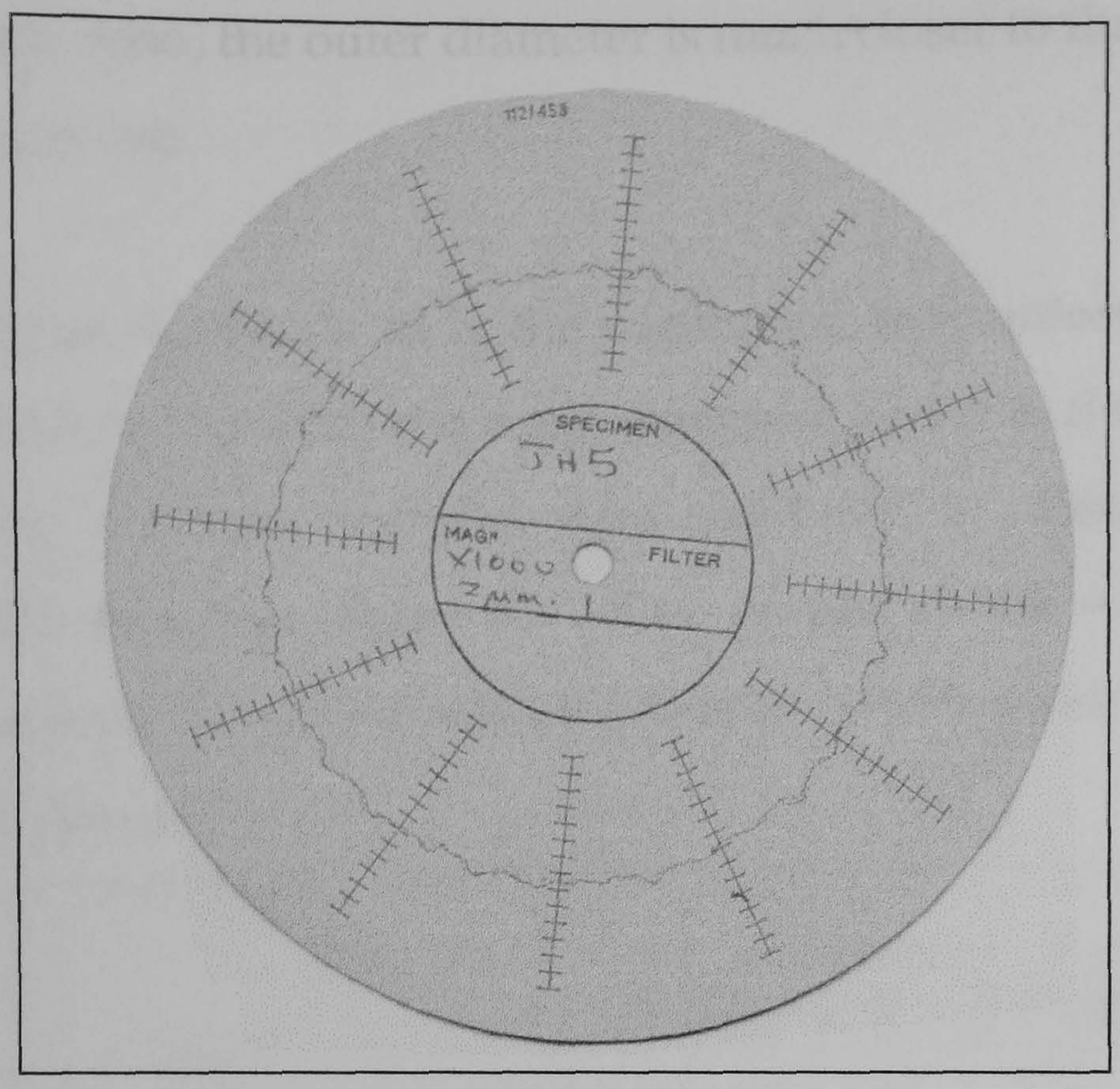

Figure 66 Roundness profile for a bearing that performed well

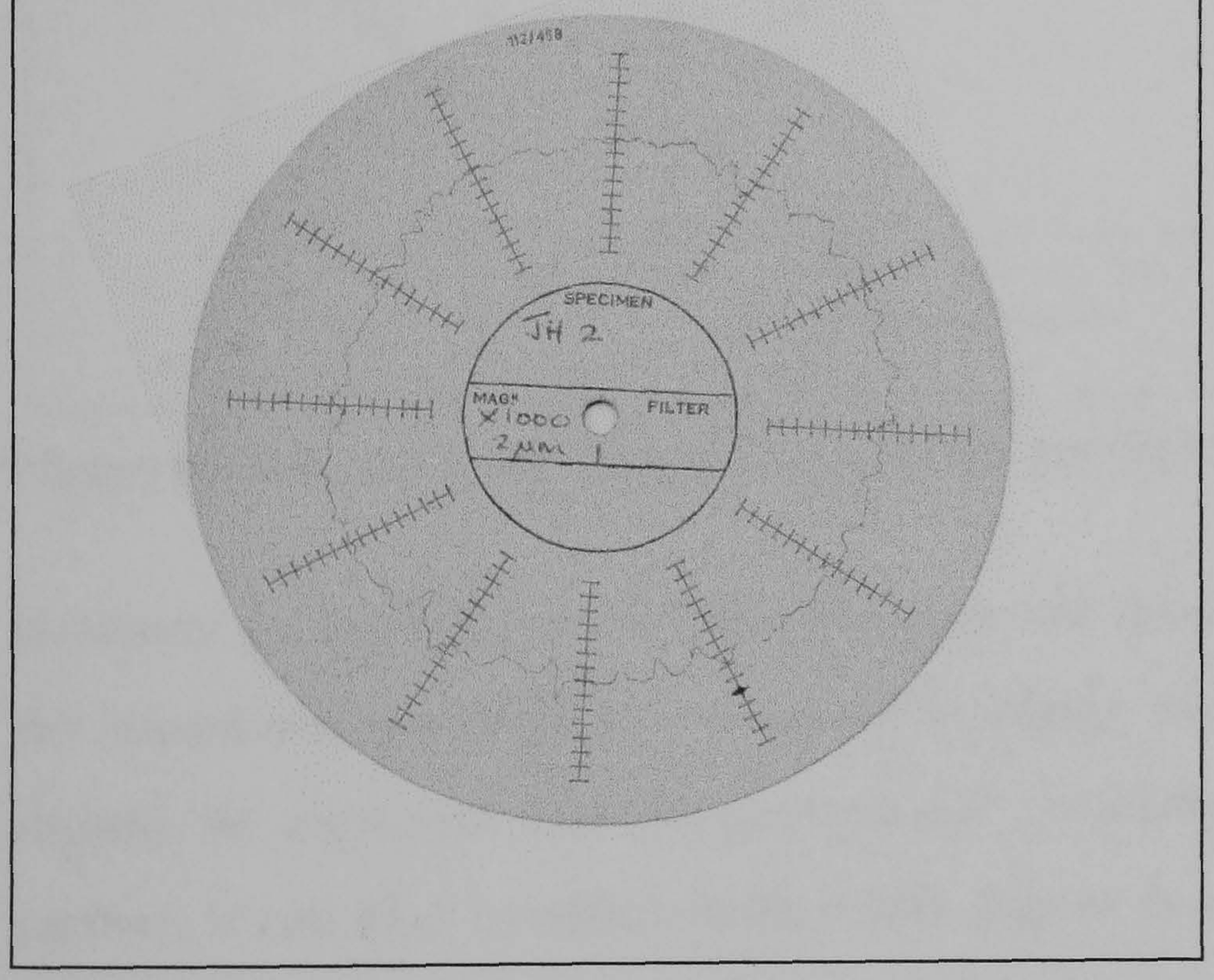

Figure 67 Roundness profile for a bearing that performed poorly

An imaginary circle drawn around the inner and outermost peaks and troughs illustrates the difference in finish between the two bearings. It is clearly seen that the bearing that performed better has a much smaller gap between the diameters of the two circles, while the bearing that was poor, has a much larger

one. Also, the outer diameter is much closer to that of the holder than that of the poor one.

What this leads to is the conclusion that unfortunately not all bearings were manufactured to the same standard, and it is therefore no surprise to find that the resulting stiffness data exhibited a substantial scatter. To graphically illustrate this, figure 68 below graphs all the stiffness data taken at a bearing gap of 2.5 microns with the bearing number calculated according to Gargulio & Gilmour.

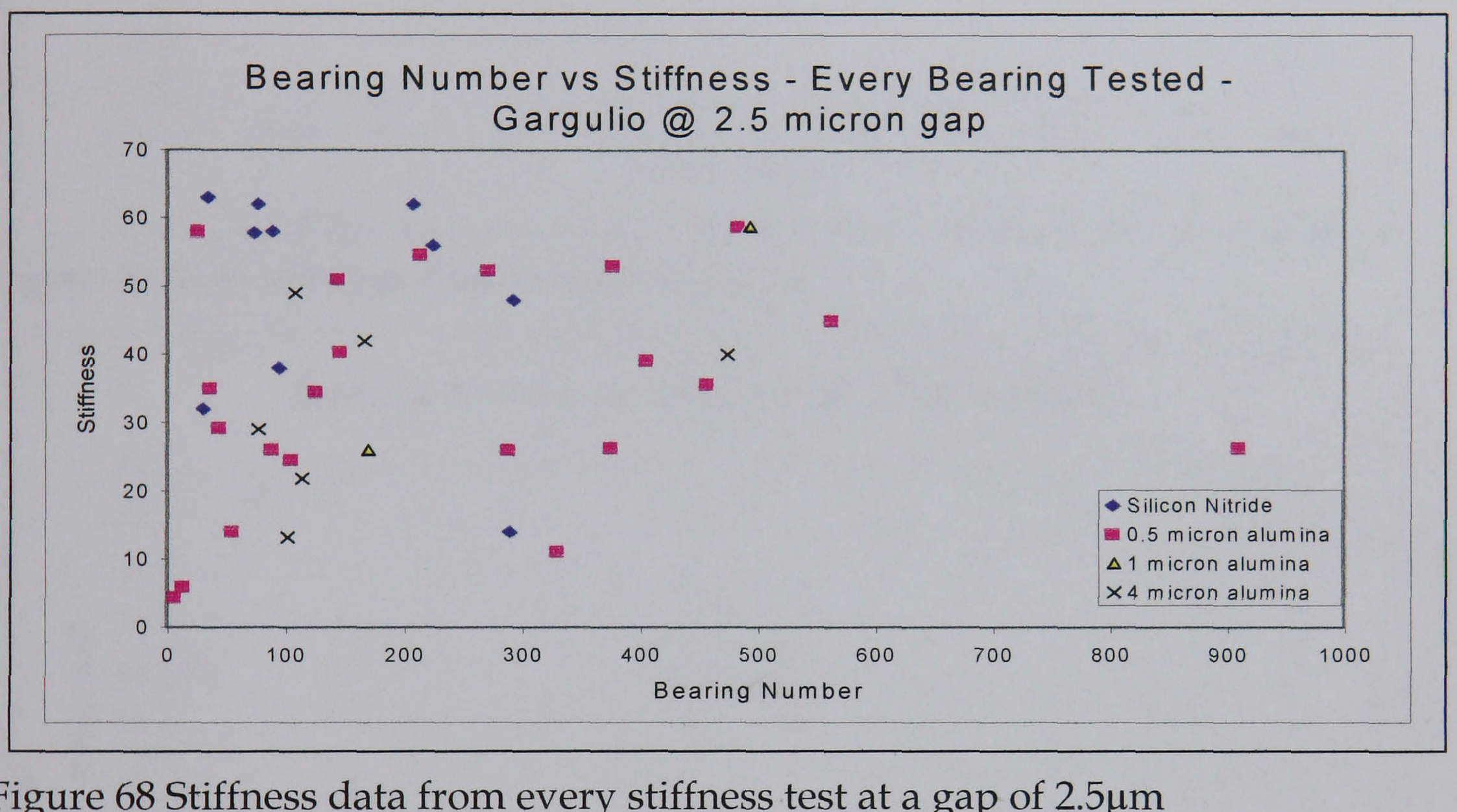

Figure 68 Stiffness data from every stiffness test at a gap of 2.5µm

However, in the light of the Talyrond analysis, it can be reasonably argued that the measured performance of many bearings are considerably below what should be expected due to geometrical deficiencies. Taking this argument further, it can also be stated with a fair degree of certainty, that no bearing so made will ever be able to out perform its expected envelope, only ever approach it.

With this in mind we can safely neglect the majority of the data here, and instead concentrate on those bearings that gave a better-measured performance.

If we then take only the stiffest bearings over a range of bearing numbers and bearing gaps from 2.5 to 10 microns, the following graphs are generated:

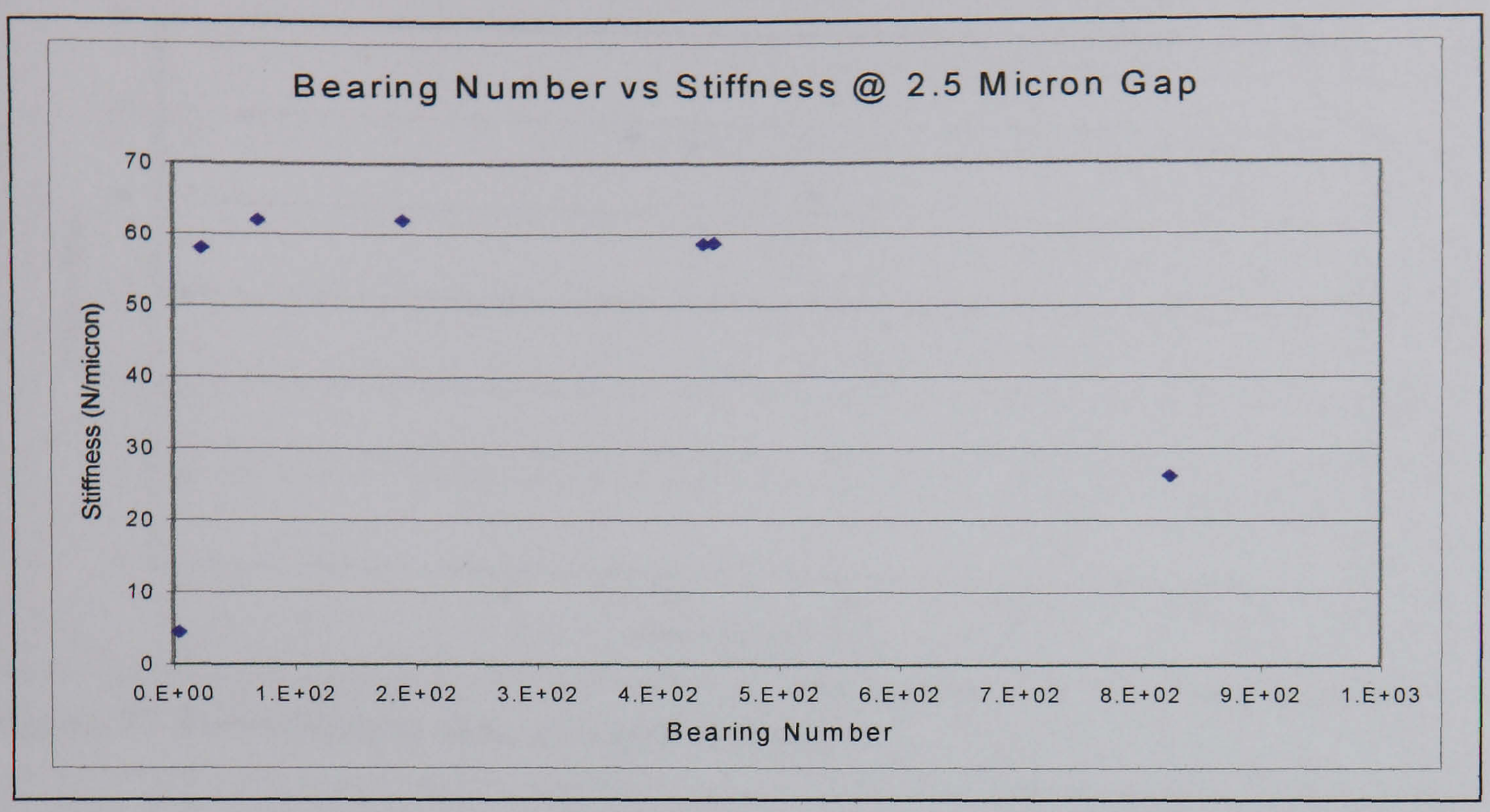

Figure 69 Best stiffness data at a gap of 2.5µm

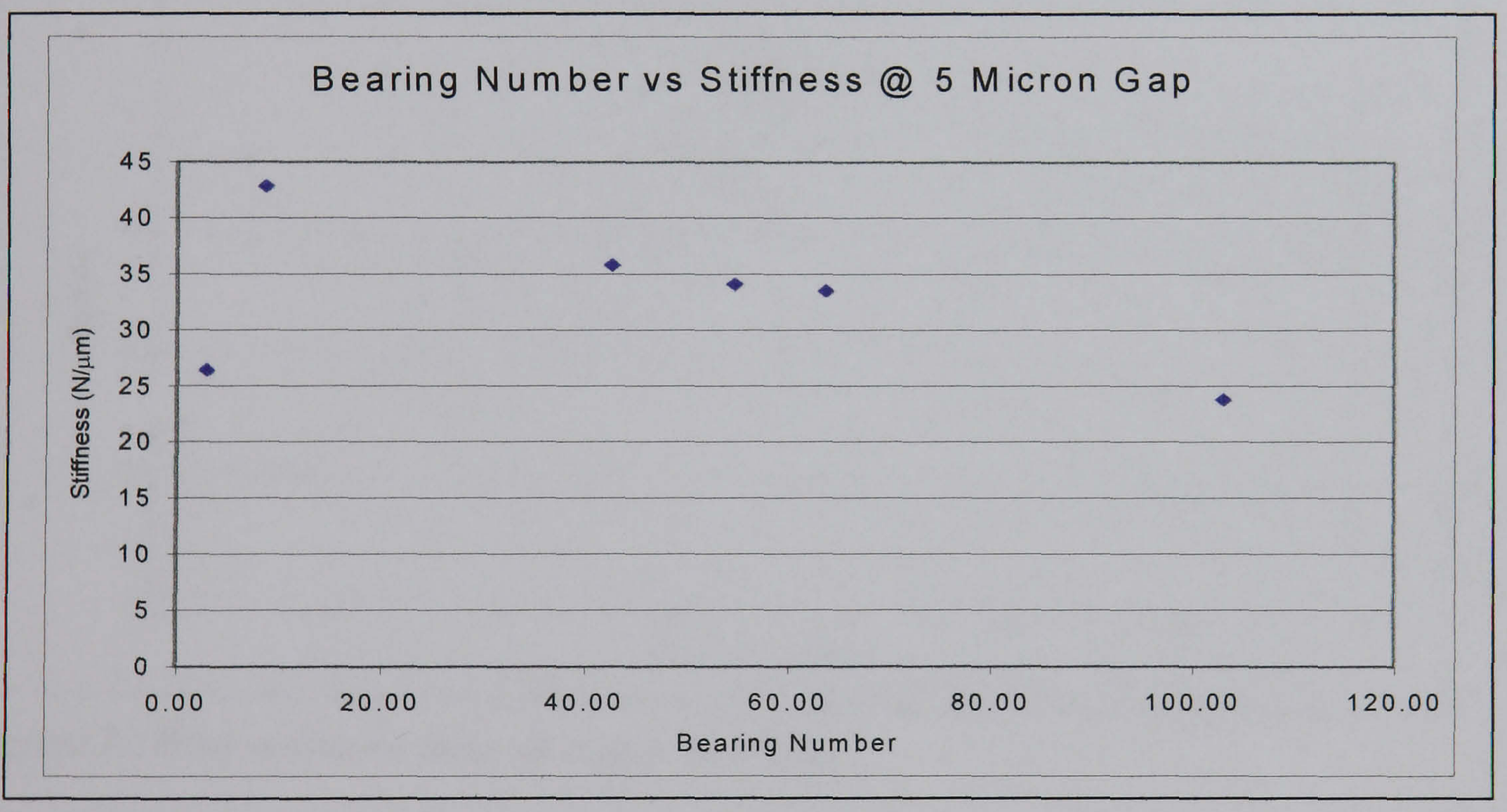

Figure 70 Best stiffness data at a gap of 5µm

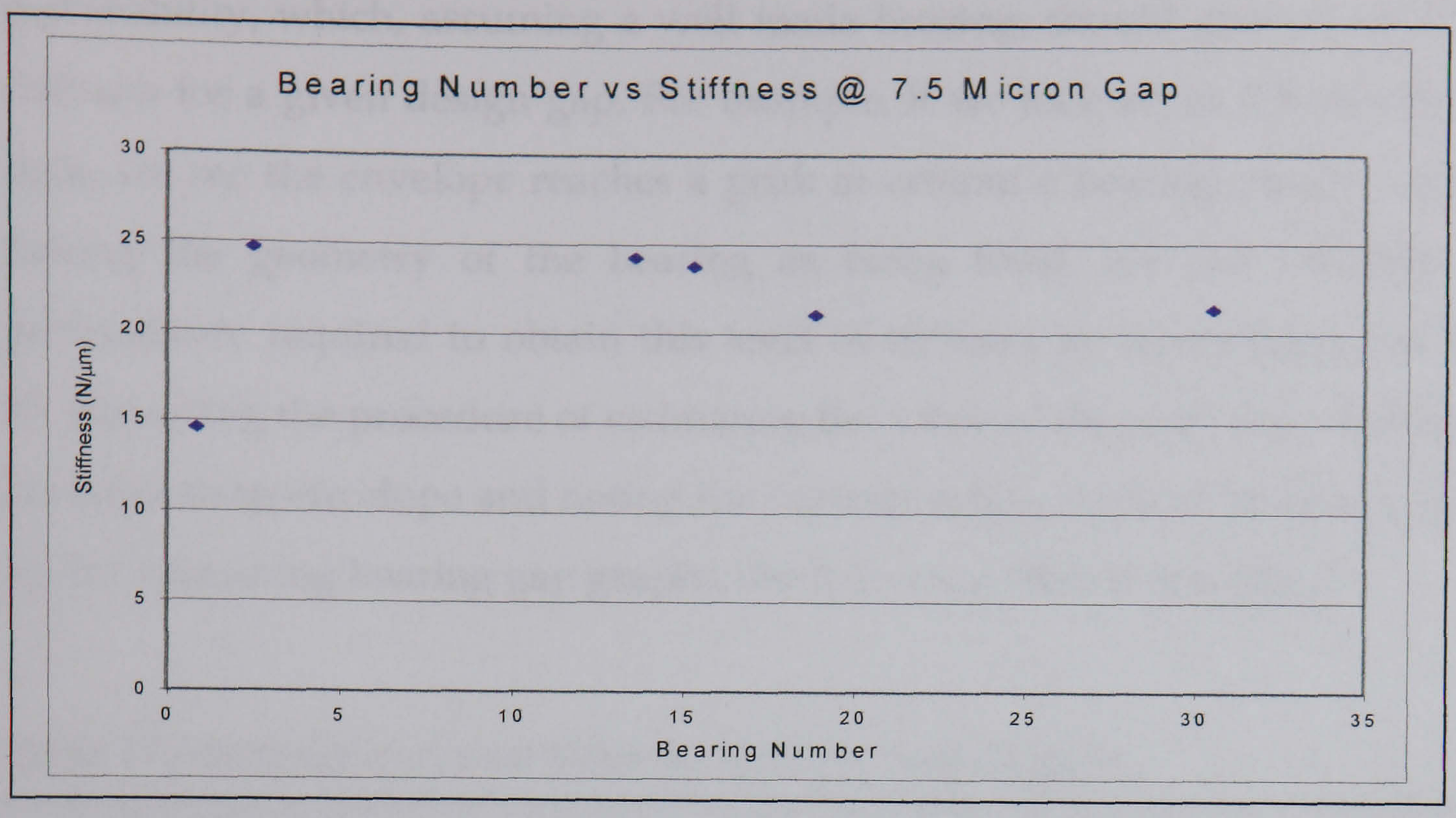

Figure 71 Best stiffness data at a gap of 7.5µm

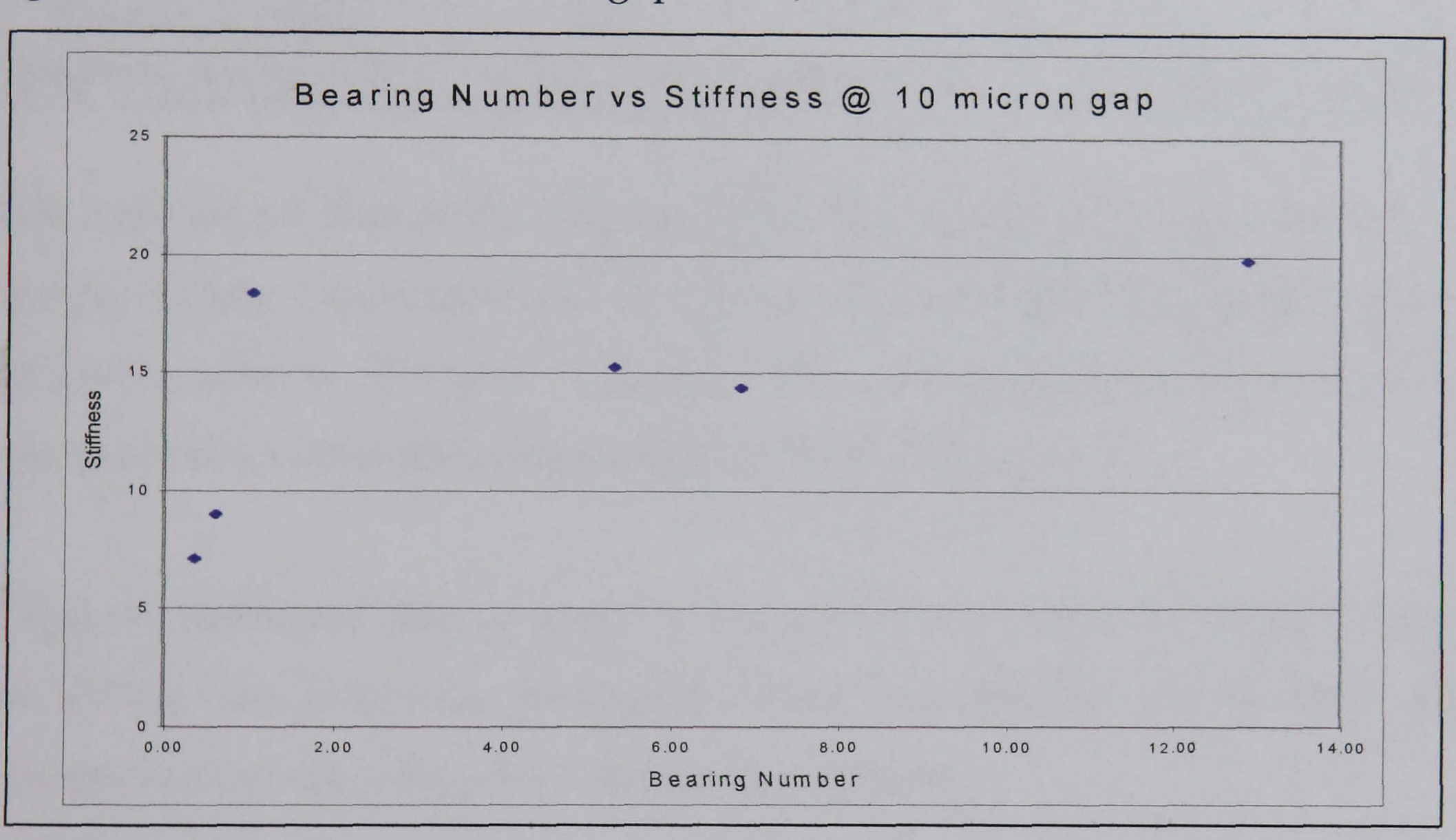

Figure 72 Best stiffness data at a gap of 10µm

What we are left with is an envelope that describes the optimum performance found by experimental means. It should be remembered that this envelope must pass through the origin, as the definition of bearing number contains a permeability term. As this term tends towards zero, less gas is able to pass through the bearing. At its extreme where permeability is zero, i.e., the bearing is now solid, no gas is able to penetrate the bearing at all which means the bearing will not operate, and so stiffness must also be zero. This gives an opportunity to reverse the bearing number calculations and estimate a value of

permeability, which, assuming a well made bearing, should give an optimum stiffness for a given design gap. For example, if we look at the 2.5 micron gap data, we see the envelope reaches a peak at around a bearing number of 200. Taking the geometry of the bearing as being fixed, we can calculate the permeability required to obtain this level of stiffness by rearranging equation 37. Repeating the procedure of estimating the value of the peak described by an encompassing envelope and noting the corresponding value of bearing number for the remaining bearing gap graphs, the following table is generated:

Table 17 Optimum permeabilities for varying bearing gaps

Bearing Gap	2.5μm	5μm	7.5μm	10μm
Bearing Number	200	30	13	6
Optimum Permeability	4.23E-15m²	5.59E-15m²	7.43E-15m²	8.12E-15m²

This table shows that as the bearing gap is increased for a fixed geometry, the bearing number decreases, and the value of permeability required to provide optimum stiffness increases. It appears that increasing the gap by a factor of four leads to an increase in the permeability by a factor of two.

Using the tabulated data as given at the back of the paper by Mutri [73], we can interpolate the following predicted values for stiffness performance for a porous bearing operating at a 5 bar supply pressure.

Table 18 Optimum stiffness from Murti[73]

Λ	0.01	1	2	9	16	25	36
K	0.0109	0.4029	0.5566	0.4987	0.4208	0.3608	0.3111
Λ	49	64	81	100	400	2500	
K	0.2725	0.2419	0.2772	0.1968	0.0978	0.0327	

Graphically, this is as shown below in figure 73.

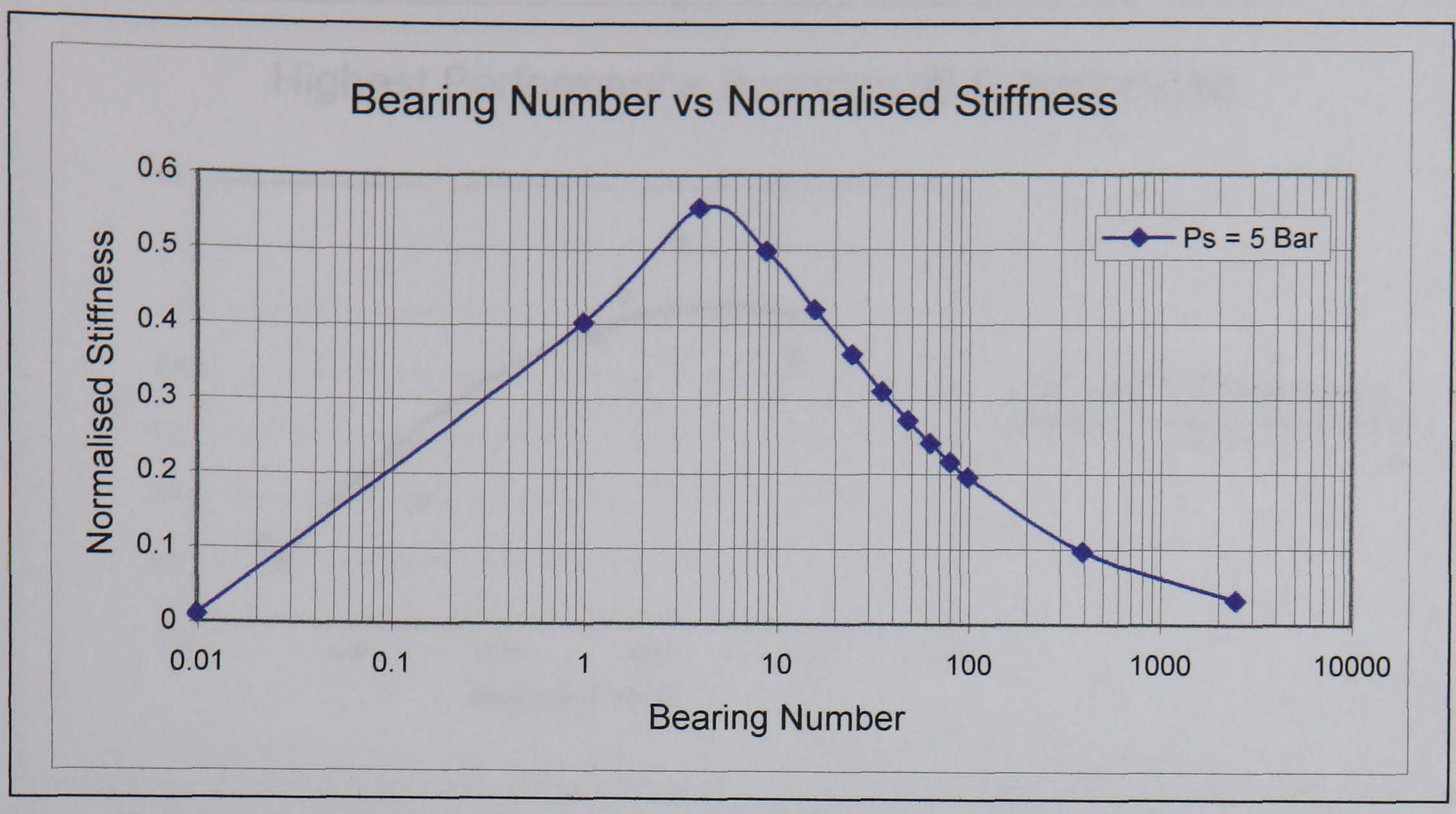

Figure 73 Theoretical optimum bearing stiffness, (from [73])

If we take the bearings that were identified above as defining the envelope for performance, and examine them using the definition for specific stiffness, K, as defined by Murti, (equation 38) for the same bearing gaps as were illustrated above, we obtain the following graphs:

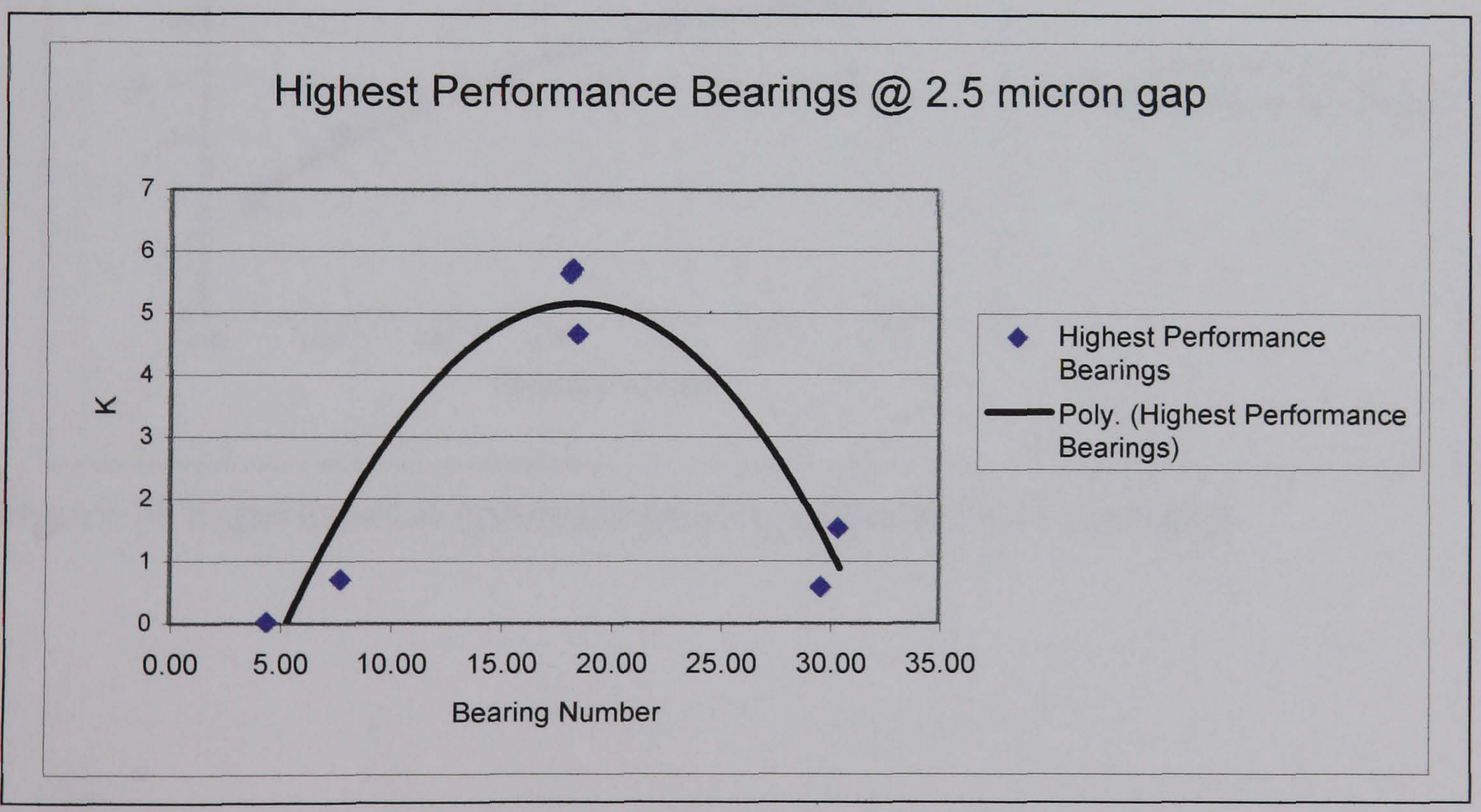

Figure 74 Experimental optimum bearing stiffness at a 2.5μm gap

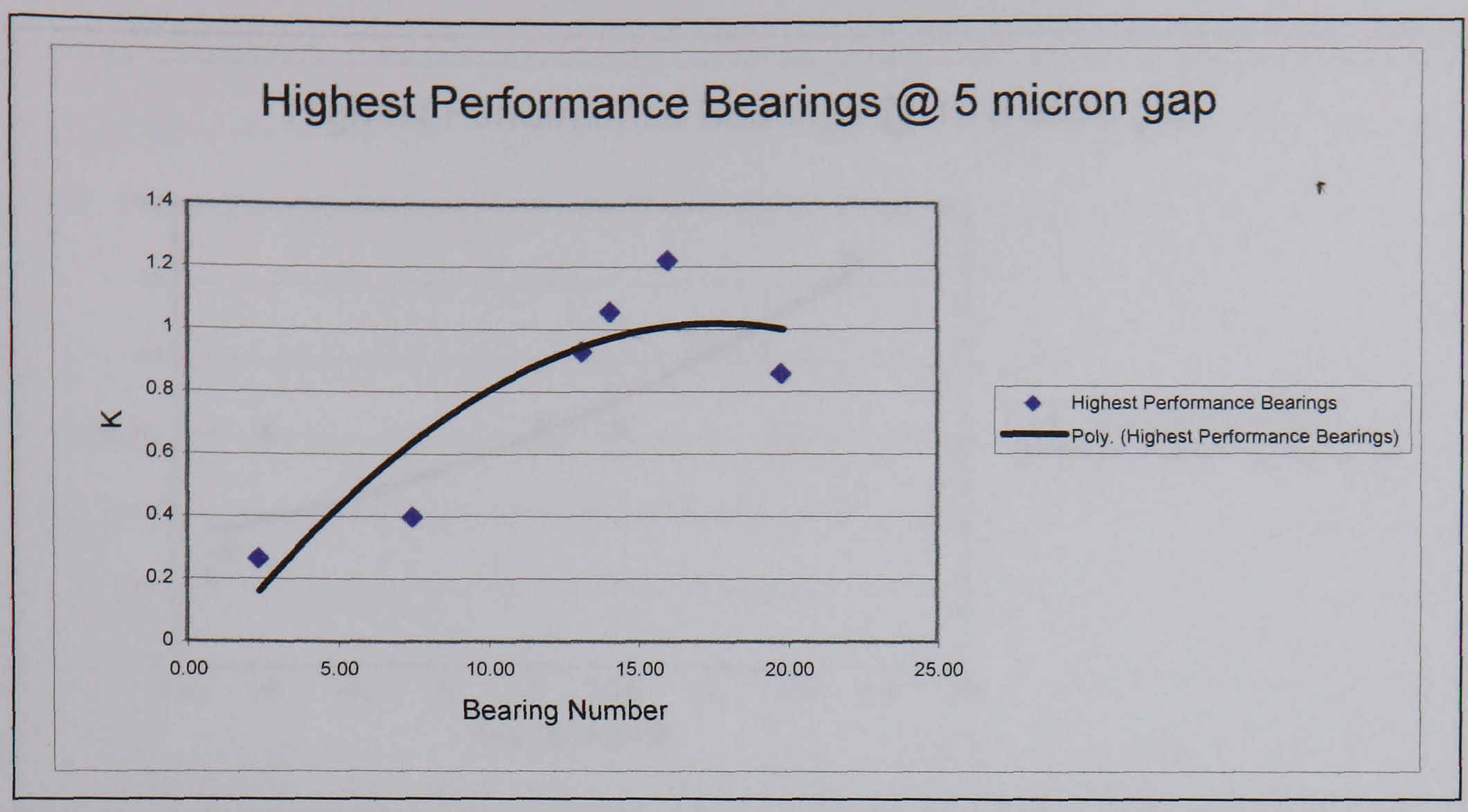

Figure 75 Experimental optimum bearing stiffness at a 5μm gap

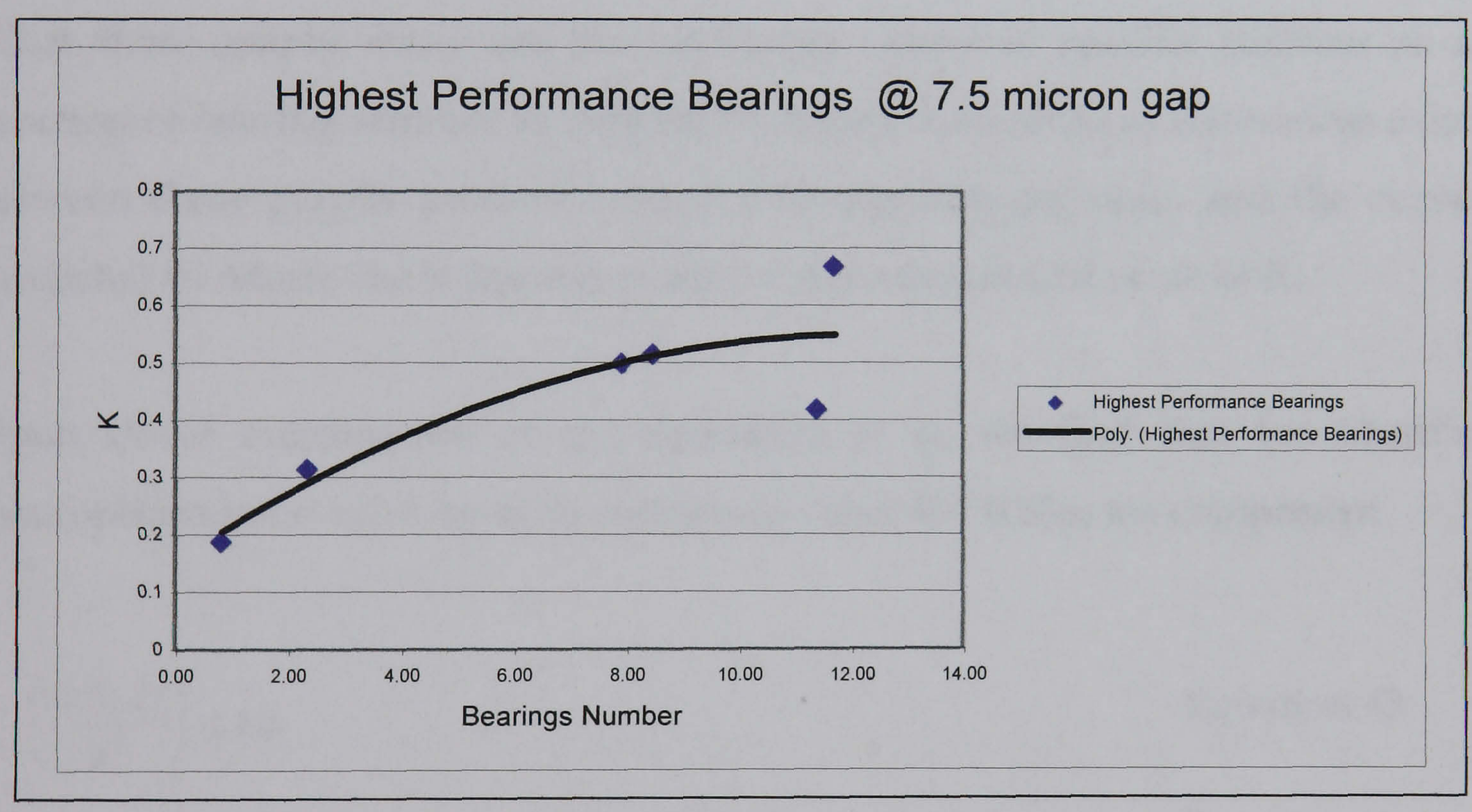

Figure 76 Experimental optimum bearing stiffness at a 7.5μm gap

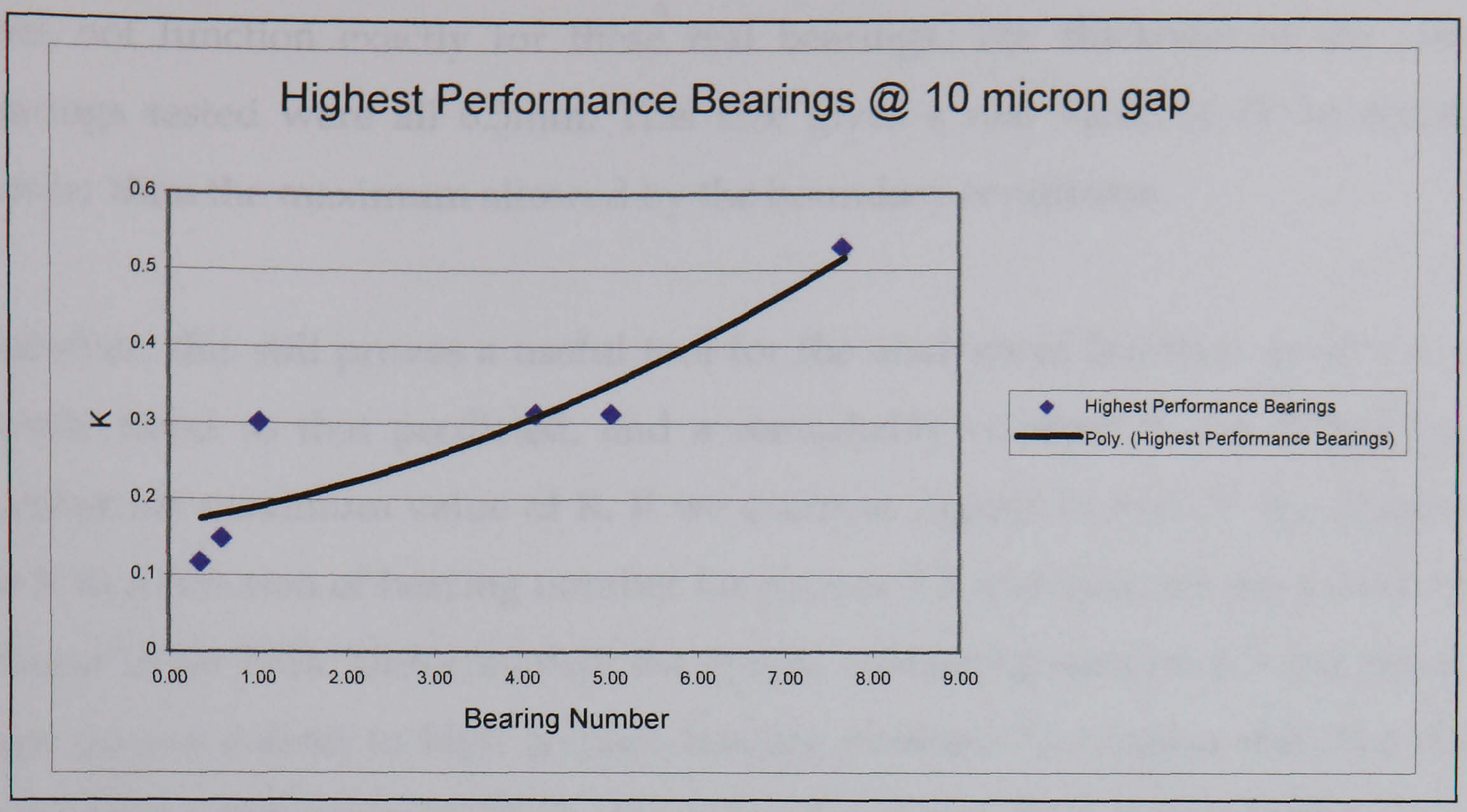

Figure 77 Experimental optimum bearing stiffness at a 10μm gap

What these graphs show are the calculated values of specific stiffness as a function of bearing number as defined by Murti. Two obvious differences exist between these graphs produced using real experimental data, and the curve predicted by Murti; the value and position of the maximum value of K.

Upon closer examination of the definition of K, we find that for Murti's assumptions to be valid, so at its maximum value $K \approx 0.566$, the component

$$\left(\frac{6.\Phi.H}{h^3}\right) \leq 1.4 \qquad \text{Equation 43}$$

This is approximate, and is arrived at by rearranging equation 38, with typical values taken for permeability, stiffness, gap, radius and pressure drop of 2E-15m^2, 60N/μm, 2.5μm, 0.02m, and 5E5N/m^2 respectively.

From this calculation, we can see that for this to be valid, the final value of H must be less than 1.8mm. During the derivation of the governing equation for K, Murti does assume that the radius is very much greater than the thickness of the bearing, i.e., r ≥≥ H, and it is therefore no real surprise that this analysis

does not function exactly for these real bearings. The thickness of the real bearings tested were all 6.5mm. This size gives a real value of H 3.6 times greater than the maximum allowed by the boundary conditions.

However, this still proves a useful tool for the analysis of bearings. It shows a similar trend to that predicted, and a remarkably constant value of bearing number for maximum value of K. If we examine figures 74 and 75, the graphs for K as a function of bearing number for gaps of 2.5 and 5μm, we see a peak at around 18 for both. Unfortunately the graphs containing data for 7.5 and 10μm gaps do not extend to high enough bearing numbers to confirm this, but do show that a maximum is likely to occur at higher values than plotted. In a similar manner to that adopted earlier, rearranging the definition of the bearing number, (equation 35), to obtain a value of permeability, we find that the value is found as 7.71E-15m^2 for the 2.5μm gap and 6.17E-14m^2 for a gap of 5μm. The value for the smaller gap is reasonably close to that predicted previously by Gargulio, but due to the closeness in the values of bearing number that the peaks occur at as seen in figures 70 and 71, the effect is to greatly increase the resulting value of permeability for the larger gap. However, this does clearly show an agreement with Gargulio in that as the gap increases, so does the optimum value of permeability.

Another important trend clearly seen from the data is that as the bearing gap is increased, the value of K is decreased. This is due largely to the effect of the term h. For every doubling of this value, the term

$$\left(\frac{6\Phi H}{h^3}\right)$$ Equation 44

is reduced by an order of magnitude.

The fact that K exceeds 1 as shown by the experimental data for the smaller gaps is also not necessarily problematic. As long as the limitations of the original derivation are accepted and understood, the relationship between the various geometrical parameters, permeability and stiffness still hold well. It is therefore still a useful analysis. Ideally, for maximum accuracy, this relationship should be rederived from first principles to take into account the true operating conditions.

4.5.1.3 Slip Cast and Injection Moulding Comparison

The performance of the alumina ceramic bearings did not appear to be significantly influenced by the processing route. It was found to be possible to reproduce the performance of one type with the other, by changing the processing conditions appropriately. Figures 78 to 80 illustrate this point with a comparison of a 1μm slip cast sample with a 0.5μm sample. These figures compare load/bearing gap, pressure distribution profiles, and normalised load carrying capacities respectively.

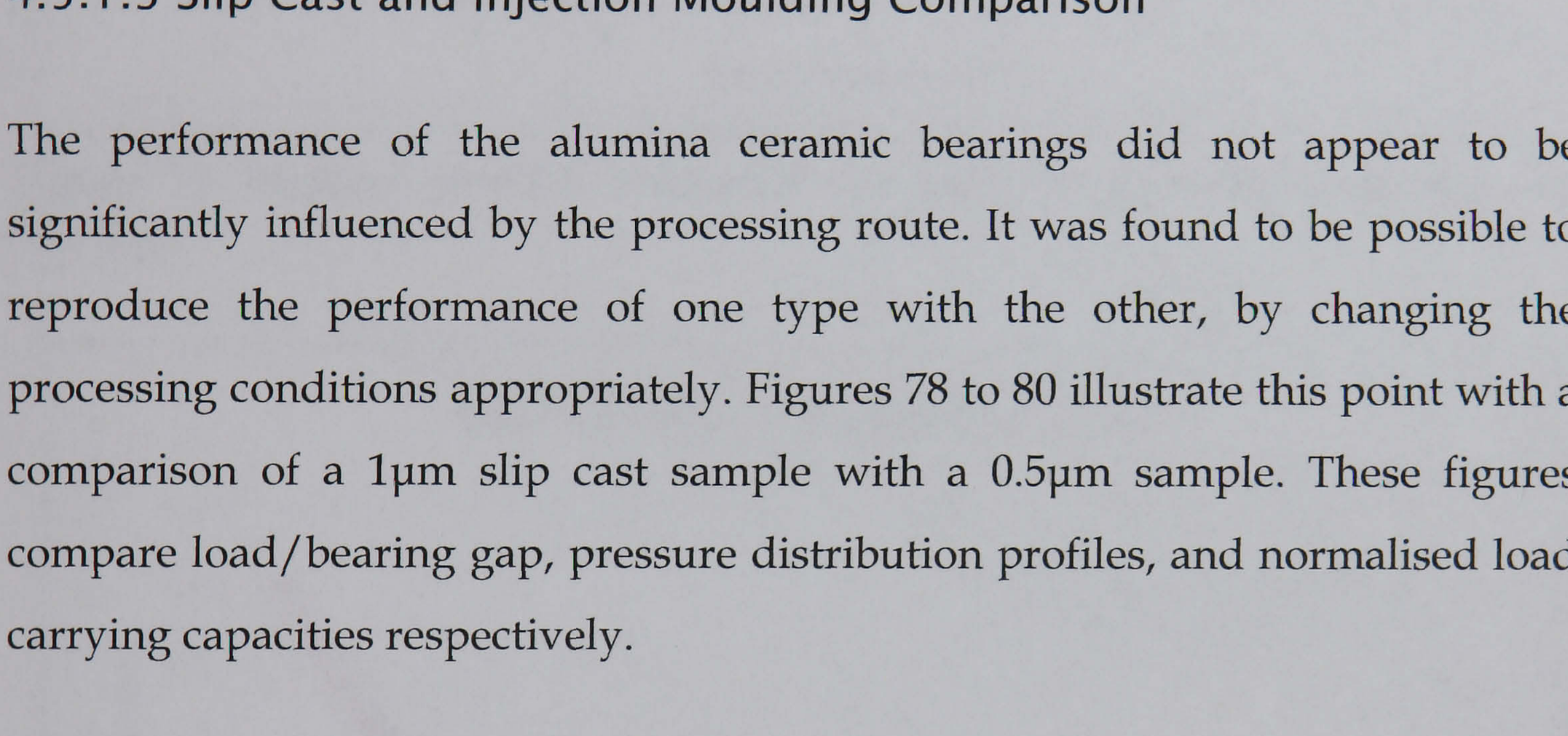

Figure 78 Deflection as a function of load for injection moulded and slip cast bearings

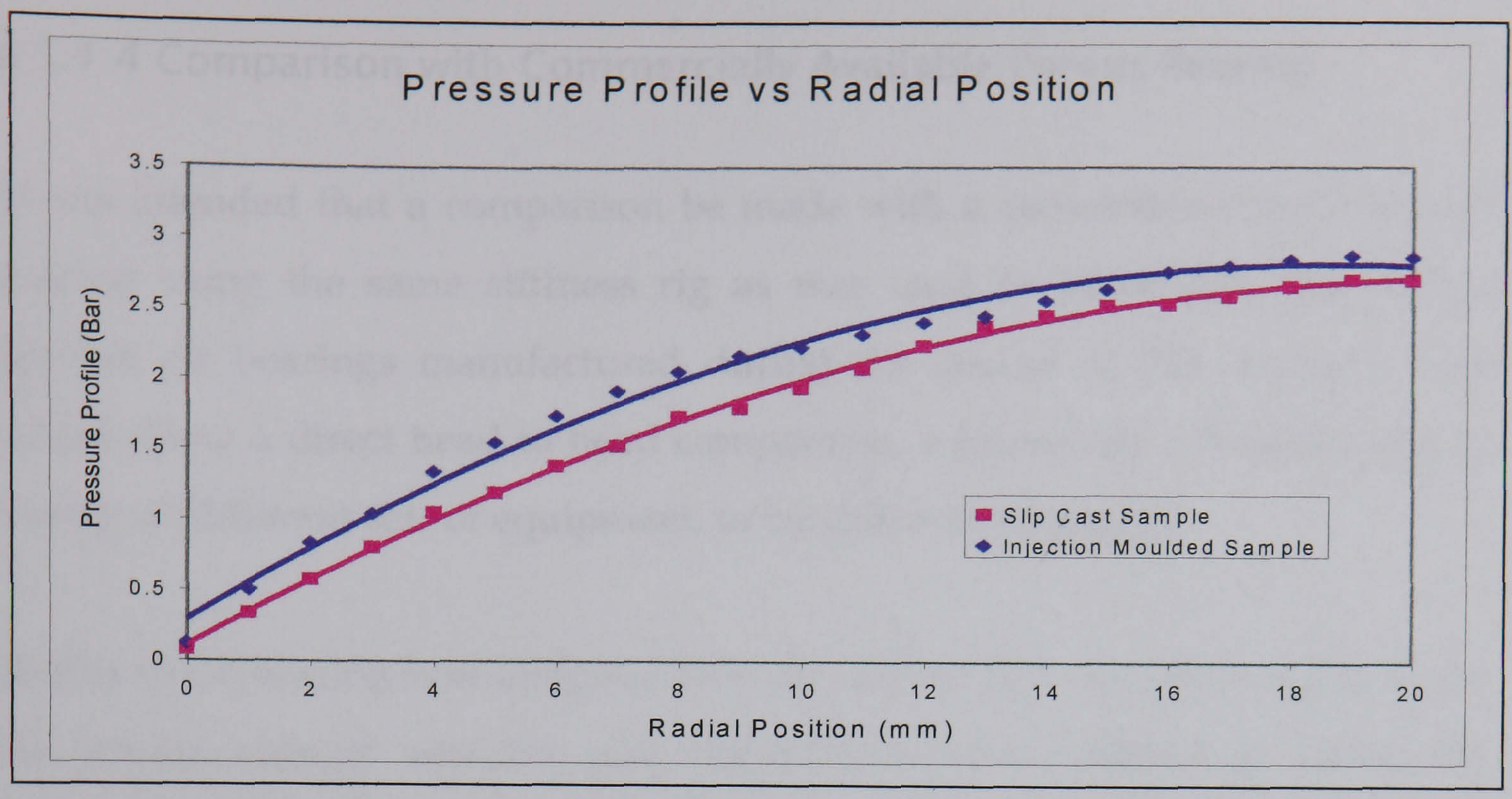

Figure 79 Pressure profiles measured for injection moulded and slip cast bearings

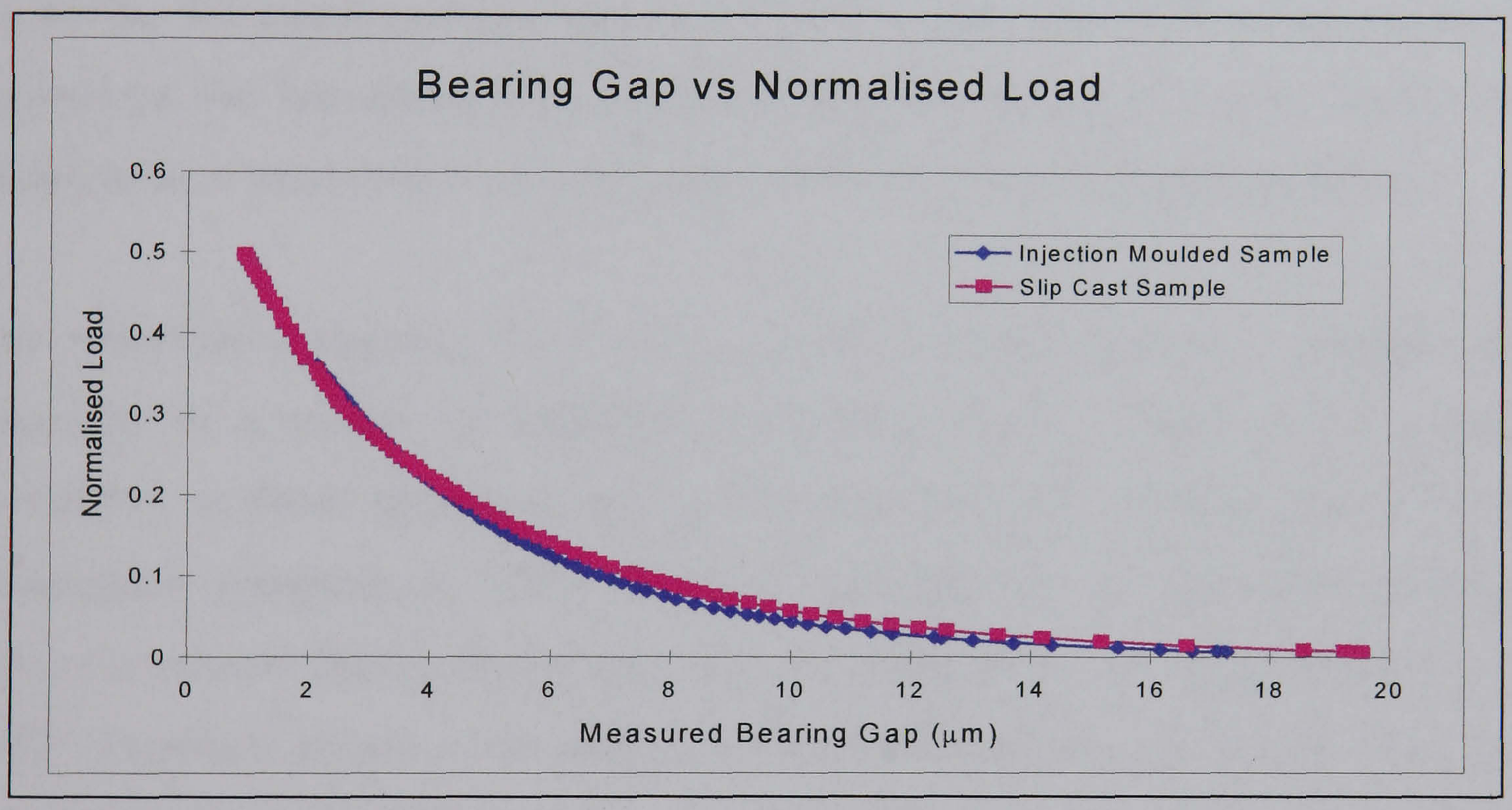

Figure 80 Deflection as a function of normalised load for injection moulded and slip cast bearings

These graphs clearly show the similarity between two different powder size bearings despite being fabricated by very different methods. This is quite important as it shows that bearing performance can be tailored to an individual application irrespective of the method chosen for its fabrication.

4.5.1.4 Comparison with Commercially Available Porous Bearing

It was intended that a comparison be made with a conventional pocketed air bearing using the same stiffness rig as was used to investigate the porous ceramic air bearings manufactured during the course of this research. This would allow a direct head to head comparison, without any ambiguity due to testing on different sets of equipment, or by different operators.

To this end a bearing was designed to fit the holder that was used on the rig for the porous ceramic samples, and manufacture was undertaken within the University. However, as with many of the porous ceramic bearings it was found to be out with the tolerances specified, and correctional work was planned using the Tetraform grinding machine. Unfortunately due to the work demands placed on the Tetraform, it was not possible to carry out this work within the timeframe of this project. An alternative comparison is therefore presented.

An American company, New Way, currently produces porous graphite air bearings in a variety of different geometries. Two of these are of similar geometry to those produced during the course of this research, and allow a reasonable comparison. These are 1.5" diameter and 2" diameter bearings. Those produced during the current research programme are 40mm diameter, or 1.57". Figure 81 shows a reproduction of the information supplied regarding the performance of the 1.5" bearing, and figure 82 shows the response of the 2" bearing.

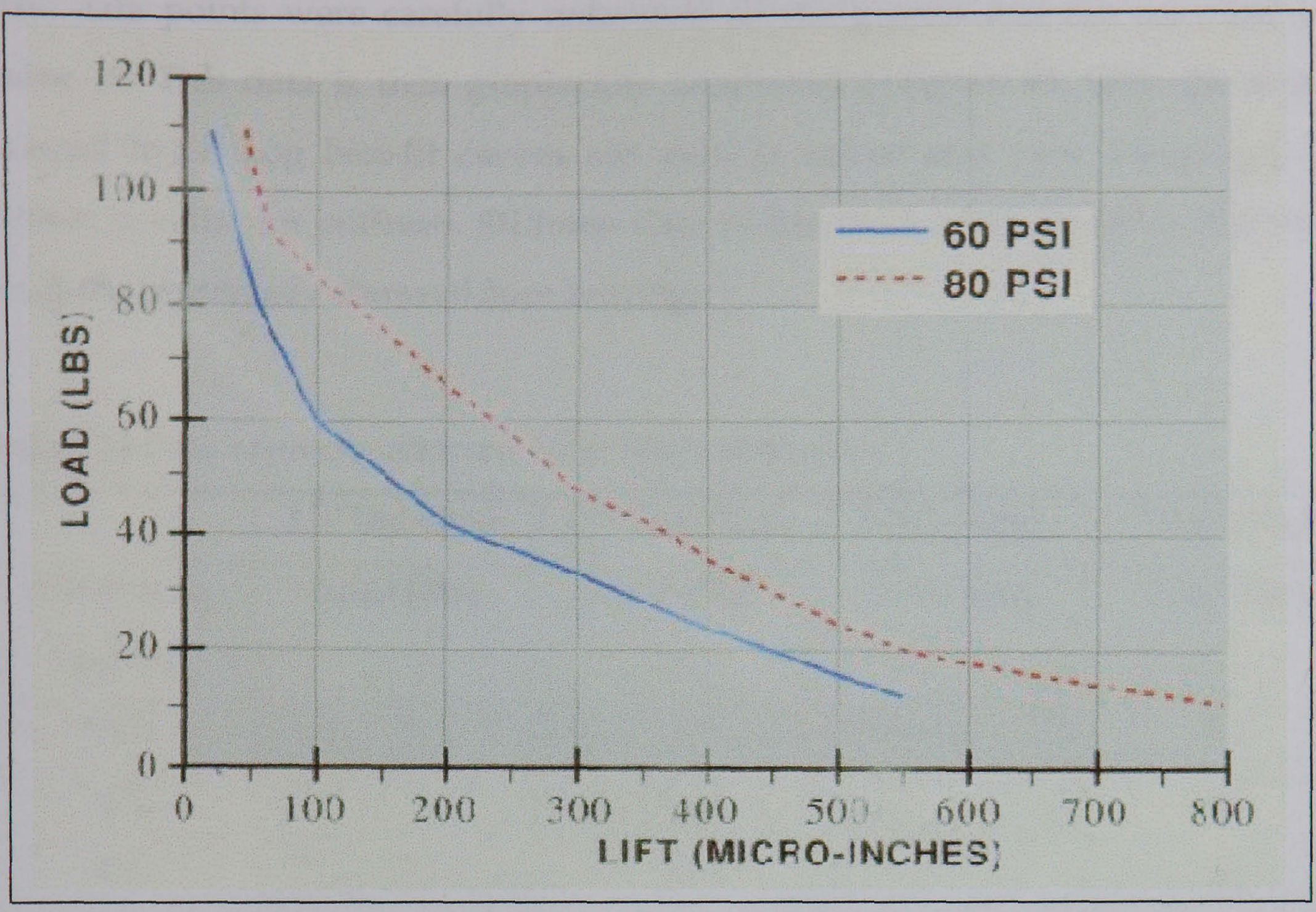

Figure 81 Deflection as a function of load for commercial 1.5" diameter bearing, (from [141])

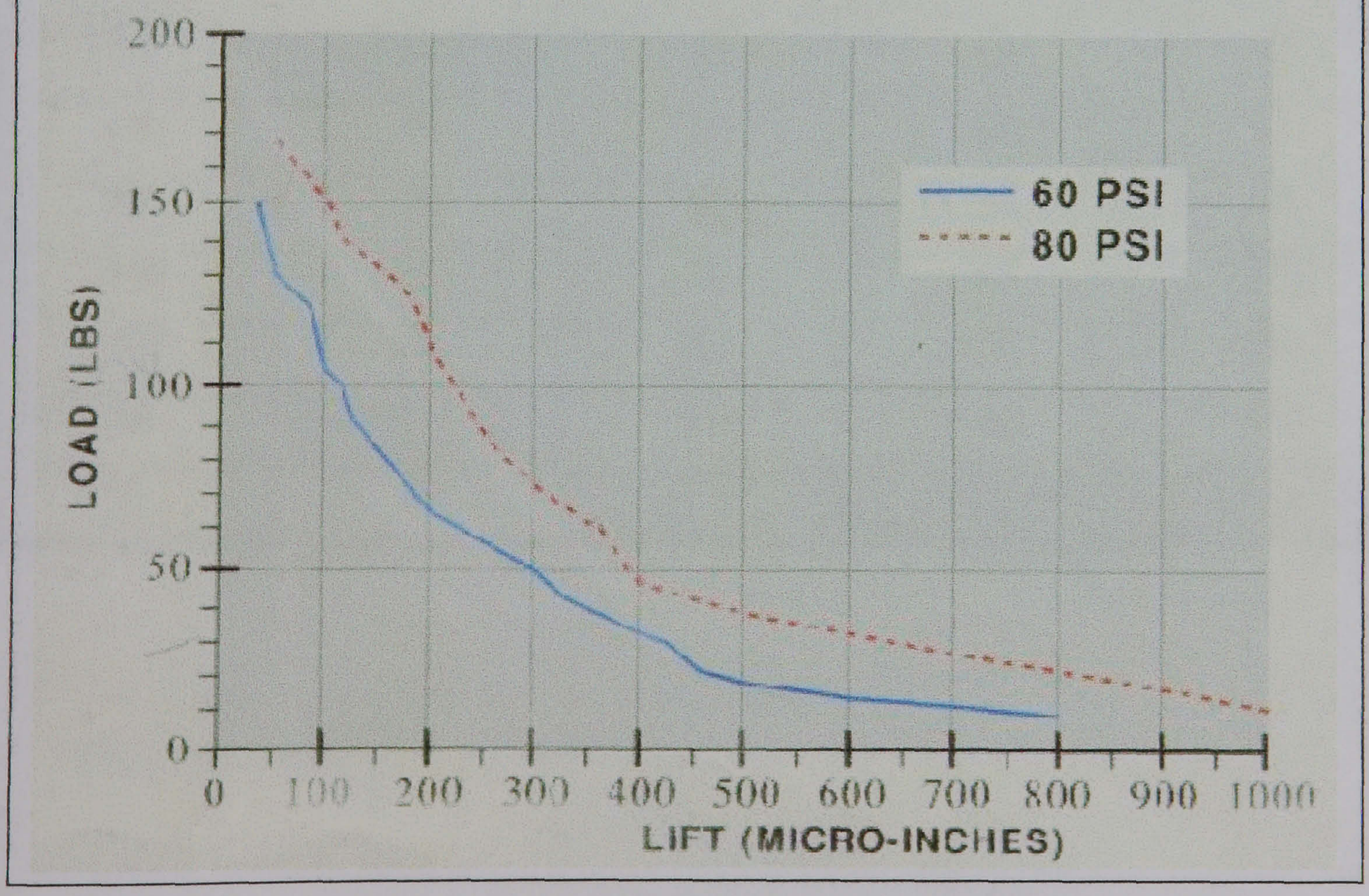

Figure 82 Deflection as a function of load for commercial 2" diameter bearing, (from [141])

The data points were carefully measured off the graphs and are recorded in table 19. This data is then graphically illustrated in figure 83, with the units altered to SI. Log best-fit curves are used as before and were integrated to obtain a value for stiffness. Stiffness data is shown in table 20 and compared with the previously shown 0.5µm bearing.

Table 19 Data reproduced from New Way catalogue

	1.5″Dia 60psi	1.5″Dia 80psi	2″Dia 60psi	2″Dia 80psi
Lift (micro inches)	Load (lbs)	Load (lbs)	Load (lbs)	Load (lbs)
1000				12
900				15
800		10	7	20
700		14	10	28
600		18	13	32
550	11			
500		25	18	39
400	23	35	42	45
300	34	47	50	72
200	42	65	63	108
100	60	84	105	150
50		110	150	170
25	25			

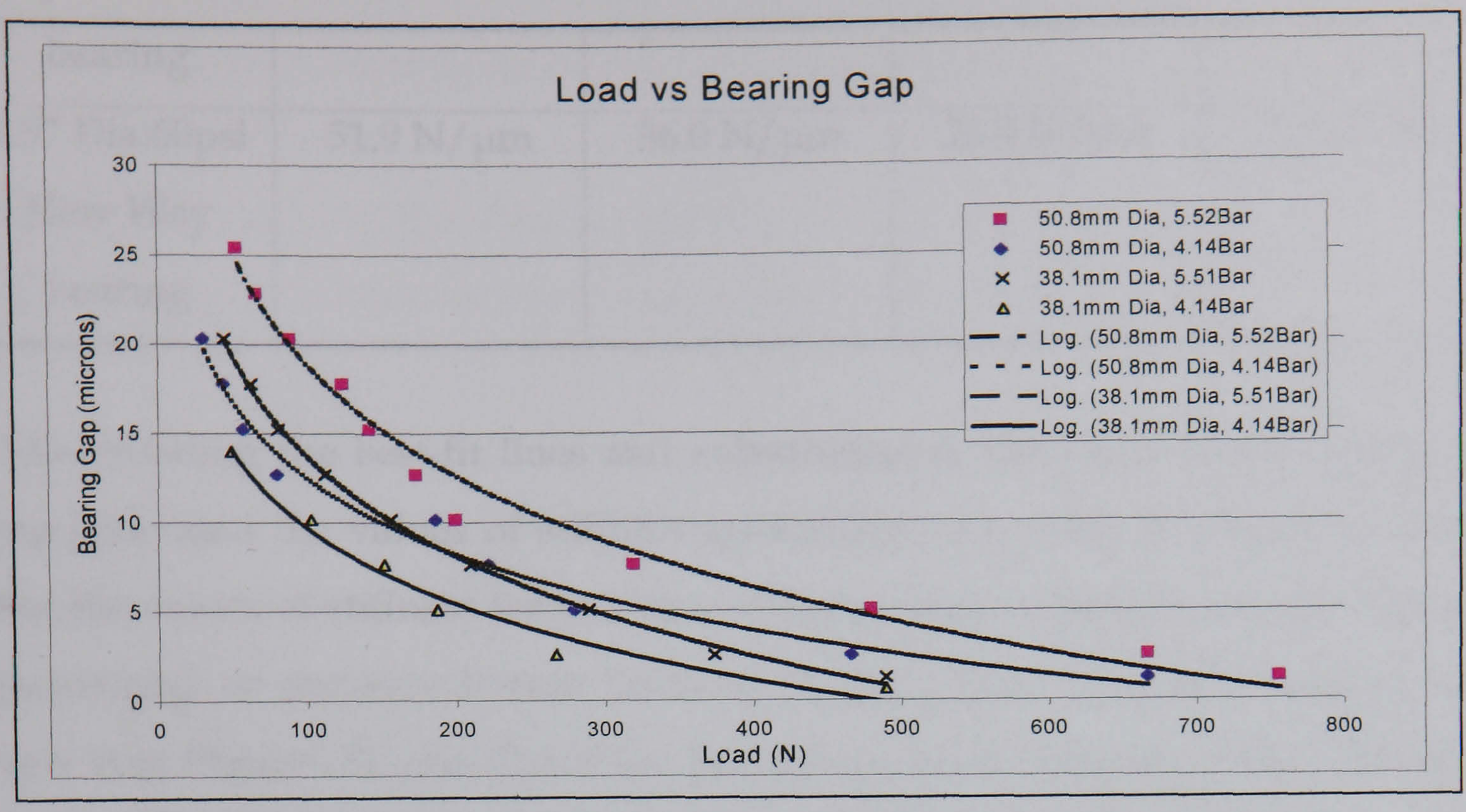

Figure 83 Re-plotted data from New Way

Table 20 Comparison of stiffness at different bearing gaps

Bearing ID	Gap(μm)			
	2.5	5	7.5	10
0.5μm bearing, 5 bar supply present work	52.2 N/μm	33.8 N/μm	21.8 N/μm	14.2 N/μm
0.5μm Bearing 4 bar supply present work	33.9 N/μm	21.5 N/μm	13.7 N/μm	8.6 N/μm
2" Dia 80psi New Way bearing	67.4 N/μm	54.2 N/μm	36.1 N/μm	24.1 N/μm
2" Dia 60psi New Way bearing	81.1 N/μm	51.1 N/μm	38.7 N/μm	29.4 N/μm
1.5" Dia 80psi New Way	49.0 N/μm	34.5 N/μm	23 N/μm	15.4 N/μm

bearing				
1.5″ Dia 60psi New Way bearing	51.9 N/µm	36.0 N/µm	26.4 N/µm	19.4 N/µm

Differentiating the best-fit lines and substituting in the value of the required gap generated the values of stiffness quoted above in table 20. It can be seen that the values of stiffness for the New Way bearings do not necessarily follow geometrical or pressure trends. Looking at the original graphs produced by New Way (figures 81 and 82) we see that the recorded response of the bearings is not a smooth curve, so it is not surprising that there is some variation in the calculated stiffness.

Comparing the values we see that the 0.5µm alumina bearing best compares to the 1.5″ porous graphite New Way bearing in terms of stiffness for a set gap. This is not surprising as the 1.5″ diameter represents a reduction of just 9% in area relative to the alumina sample. The 2″ bearing by comparison is a full 61% larger and so performance is expected to be greater. Comparing figure 82 with figure 49 previously, we see that the load carried by the New Way bearings are greater than the alumina bearing for a given gap. As the New Way units are properly bonded into their holders, and precision machined to achieve a high degree of flatness, this is unsurprising. The alumina bearing used for comparison here, although possessing a reasonable level of performance, has been demonstrated to have geometrical imperfections (section 4.5.1.1) that will ultimately reduce the degree of performance available. If these were to be overcome, it seems a realistic assumption that on the basis of this comparison, the performance of the porous ceramic bearing in terms of stiffness and load carrying capacity would match a porous graphite bearing of similar geometry.

It is interesting to note that from the data presented in table 20 the New Way bearings show no real change in stiffness with the change in supply pressure for

a given geometry, though the bearing gap for a given load does change, as seen in figure 83. Whether this is a real effect or an artefact is impossible to say. Given the quality of the data supplied it is perhaps prudent to be cautious regarding any definite conclusions regarding this comparison.

In addition, it is always difficult to accurately compare different sets of data (different geometries, supply pressures, finishes, etc.), made using different equipment by different operators, however similar they may appear.

5 Summary of Development Methodology

The procedure used for the investigation of the bearing manufacture was intended as a closed loop system, with each successive and iterative improvement being fed back into the loop to improve subsequent bearings. This is illustrated through figure 84.

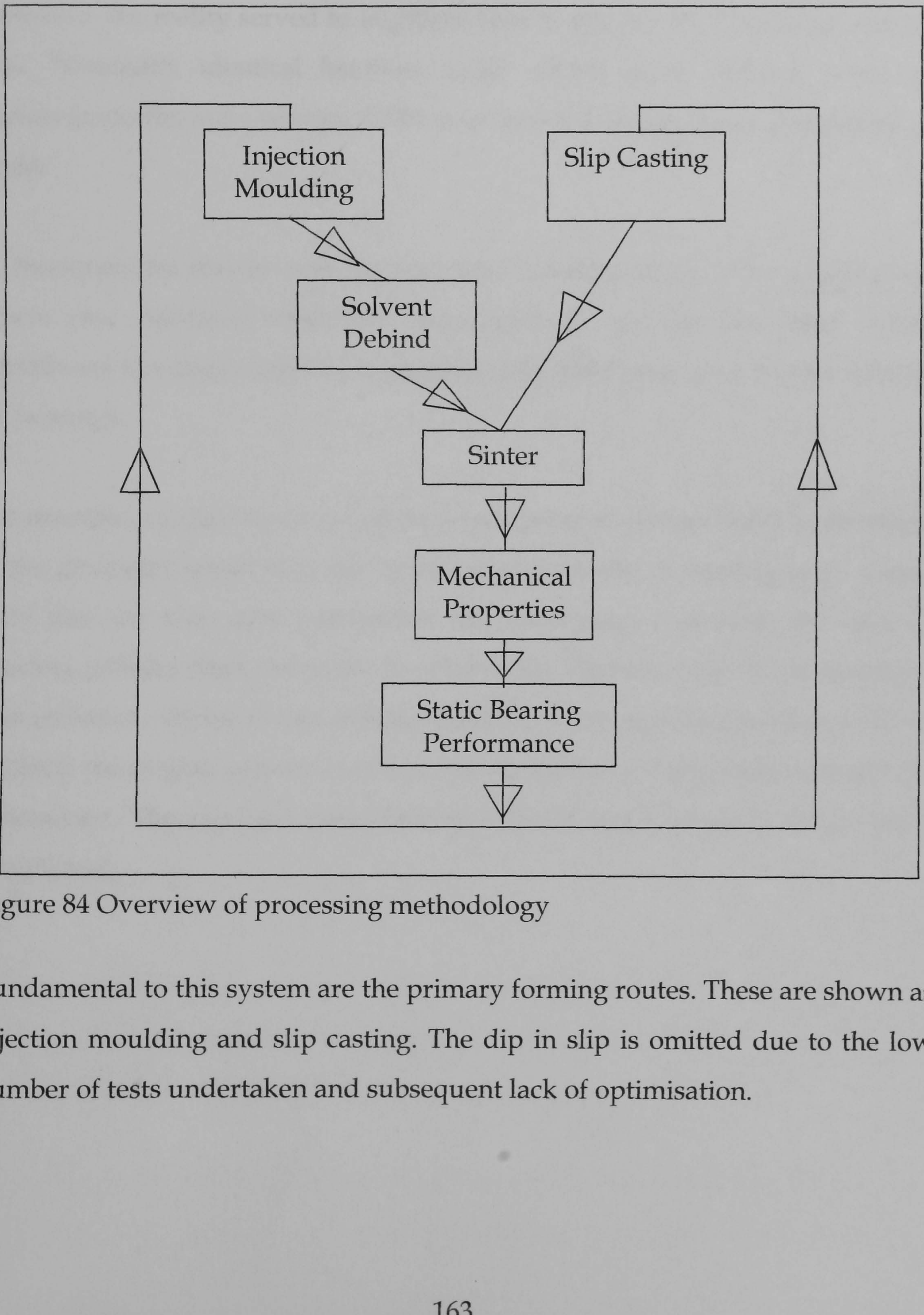

Figure 84 Overview of processing methodology

Fundamental to this system are the primary forming routes. These are shown as injection moulding and slip casting. The dip in slip is omitted due to the low number of tests undertaken and subsequent lack of optimisation.

With each iteration the knowledge base improves and so the final static bearing performance becomes more predictable. With this simple loop it was hoped to identify the main factors affecting the performance of the bearing. The main limitation to this simple model was that it assumed that the machining would be consistent and repeatable, and that the variation between different bearings could be traced to explicit differences in the process used to manufacture them. However, the reality served to highlight how important the machining process was. Nominally identical bearings could exhibit quite different levels of performance, the more obvious differences being in the geometry and quality of finish.

If, however, we restrict ourselves to data resulting solely from experiments where near optimum conditions were achieved, we see that what results contributes to a useful method of predicting the performance of porous ceramic air bearings.

For example, we have now established the optimum permeability for bearings of the geometry tested here for operation at a variety of bearing gaps. Along with this we also now understand the processing conditions for various alumina powder sizes necessary to achieve the desired value of permeability. This includes a choice of two primary forming routes and four powder sizes. In addition the largest powder size that can be used in a stable manner has been determined. The expected load carrying capacity and stiffness have also been established.

6 Conclusions

Several important conclusions can be drawn from this research programme.

- Both injection moulding and slip casting have been demonstrated as being appropriate methods for reproducible manufacture.

- Bearing performance is independent of manufacturing route. By choosing the correct processing conditions it is possible to achieve a bearing which will posses the same stiffness, load carrying capacity, and pressure distribution characteristics irrespective of the method used to fabricate it.

- The use of fine powder size in the manufacture of the bearings as tested here (4μm or smaller) produces bearings that are stable over the entire testing range, with no evidence of instability. Conversely, using powders larger than 4μm led to instabilities and air hammer over a wide range of operating conditions. It is thought that this is an effect of the reduced void volume at the surface of the bearings.

- Using the combination of fine powder sizes and single layer geometry has meant that sintering temperatures are sufficiently low to use atmospheric furnaces. Previous work using the two layered approach identified the HIP as having an uneven temperature distribution within it, leading to difficulties in controlling the resultant level of porosity and hence permeability. Being able to use lower temperatures in equipment that possesses better temperature distribution has greatly increased the level of reproducibility of manufacture.

- It was demonstrated that with single layer bearings it was possible to vary permeability over a wide range by alteration of the processing conditions.

These variables were powder size, green density (in the case of injection moulding), and sintering temperature.

- For a given set of production conditions, the worst case reproducibility in terms of measured permeability proved to be better than ±15%, with the best reproducibility of ±4%.

- It has been demonstrated that single layer porous ceramic bearings are suitable for use in air bearing applications and it is not necessary to resort to the complexity of a two-layer geometry.

- Single layer bearings fabricated from a variety of different powder sizes were demonstrated to posses sufficient mechanical strength to withstand a wide range of loadings.

- The quality of finish on the bearing had a serious impact on the performance. The load carrying capacity and stiffness appeared to be strongly related to the flatness of the bearing and the fit in the holder. It seems that a high degree of precision in the finish is still required.

- The static performance of many bearings was tested and compared to published theories. It was found that the load carrying capacity agreed well with that predicted but only after a correction for surface roughness was allowed for. Shortcomings in the predicted stiffness were highlighted due to differences in geometrical parameters between the real bearing and the idealised that the governing equations were derived for.

- Comparing the stiffness values with commercially available porous graphite bearings of similar geometry, the bearings produced in the course of this research programme were found to be of a similar performance for similar supply pressures.

7 Suggestions For Further Work

Although the work attempted within the scope of this programme proved quite comprehensive, covering several different manufacturing routes through to testing, there were several important aspects that were not attempted or require improving.

7.1 Improvements To Machining Process

The first aspect of this programme that requires further refinement regards the stiffness testing. It became increasingly obvious during the course of this phase that the machining that the bearings had undergone to produce the specified geometry was not up to standard. As was noted by the Talysurf readings previously, and the fact that metallic pickup from the counterface was apparent in specific areas, lead to the conclusion that the bearing faces were not ground to a high level of finish. Indeed, in the case of one bearing the finish was so poor that when placed upon the lapped counterface it was possible to rock it back and forth, showing the out of flatness in a very visual way. The Talyrond traces contained herein attest to the fact that the cylindrical grinding was similarly variable.

What is required is a repeatable machining process that eliminates the operator dependence on finish so far seen. For the horizontal grinding a machine such as the Tetraform should be employed. This machine has demonstrated that it is capable of producing very flat surfaces, and with little further work should be able to replicate this success with the porous ceramic bearings.

The cylindrical grinding stage ideally requires a machine capable of similar quality of work. However, this may not be as critical as an alternative concept may be preferable. If every bearing was bonded in place in the holder using a

good quality epoxy, as is done with commercially available porous bearings, the degree of fit between the holder and the edge of the bearing no longer becomes so exacting. Of course, a good fit is still paramount, but it may be that the variability so far witnessed may be acceptable due to the gap filling properties of the epoxy.

Unfortunately, it was not possible to implement these ideas during the course of this research. The Tetraform was only just becoming understood as this project came to an end, and a machine capable of similar finishes at a partner company was unavailable for the duration of the programme. An illustration of the potential improvement is shown below. Figure 85 shows a Talysurf trace over a typical 0.5µm 55% green density injection moulded bearing as ground using the standard horizontal grinder using the condition mentioned previously in sec

tion 3.5.2. The same bearing is again illustrated in figure 86 after being ground on the Tetraform.

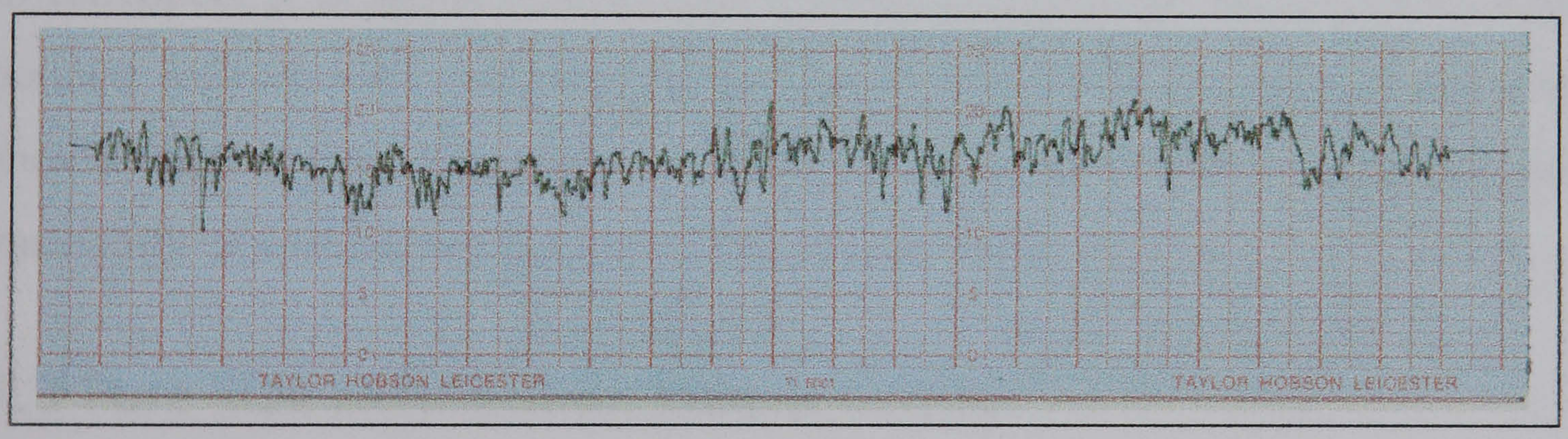

Figure 85 Talysurf measurement across conventionally ground bearing surface

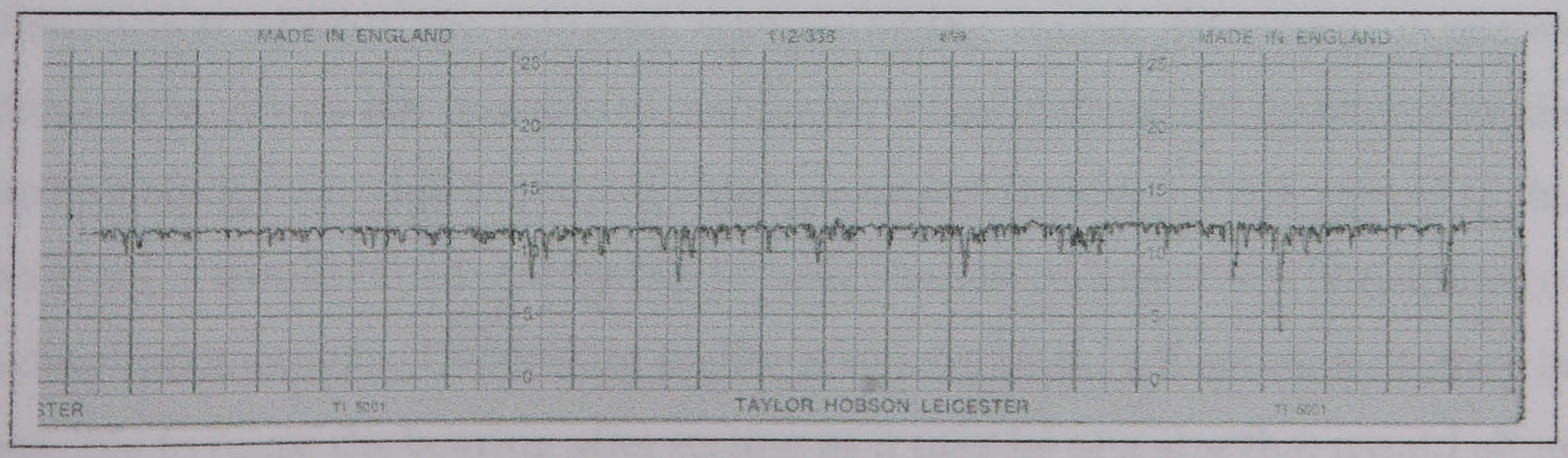

Figure 86 Talysurf measurement of Tetraform ground surface

What is immediately obvious is that the trace in figure 86 no longer shows peaks and troughs, only the troughs remain. As a result the R_a reduces from 1.2 in figure 84 to 0.3 in figure 86. Both of the traces were taken under the same conditions, each horizontal line represents a 1μm gap, and the distance between the thicker red vertical lines is 0.5mm.

7.2 Improvements To Stiffness Test Procedure

Due to the high number of bearings tested it was decided to reuse the same bearing holder for each test. Whilst this removed any variability regarding the effect of using different holders, it led to the compromised situation of attempting to seal each bearing into place in a reversible manner. As pointed out in the text, a poor fit between the holder and the bearing has a highly negative affect on the bearing performance. Pressurised gas will preferentially follow the path of least resistance to atmosphere; and in this case the relatively large gap between the bearing and the holder provides an ideal route.

In retrospect it is apparent that each bearing should have been permanently bonded into its own precision made holder before testing. Final machining should then have taken place on the bearing surface. However, given the variability of workmanship so far noted, this is at best wishful.

7.3 Pore Size Distribution Measurement

It would have been useful to be able investigate any dependence of pore size distribution against the different manufacturing routes. However, as shown previously, it was not possible to test this in a non-destructive manner with the current equipment due to the very high pressures involved. With regard to this problem it would be advantageous to have the use of a mercury porisimiter or helium pikanometer. Depending on the geometry of the pikanometer it may be possible to reuse the bearing after testing as it may be of a size that would allow the bearing to be tested whole. Failing this, additional sacrificial samples should

be made for pore size distribution testing. Given the level of reproducibility available from the manufacturing routes, this resulting data could then be used for the remaining batch samples with a high degree of confidence.

7.4 Dynamic Performance Testing

The dynamic performance of the bearings was not addressed. As any bearing operating under real conditions will be subject to various dynamic loads, this is an important consideration. Necessary modifications to the current equipment have been outlined previously in previous work at Cranfield University [5].

7.5 Improvements To Current Manufacturing Routes

Injection moulding improvements must involve a change in binder system. The presently used debinding system, although successful, requires the use of an organic solvent in order to remove the wax from the green body. This inherently contains potential health risks, and requires the use of specialised equipment for safe handling, such as fume cupboards, and generates a problem with disposal of waste. All this adds cost (as well as time) to the process, so the investigation into other binder systems which overcome these shortfalls must be a priority if the process it to meet with commercial success.

Further work is required to optimise the mould design of the bearings. Recent work has underlined the potential of computer based modelling in the mould design process [105], and this seems a perfect opportunity for its exploitation. Other moulding parameters such as heating of the mould cavity, length of sprue, etc., should also be investigated.

The slip casting route would benefit from an investigation into the rheology of the slip. This would allow a more quantitative approach to the optimisation of the slip make up for each powder size, rather than the more empirical approach adopted out of necessity here.

It would be of interest to continue the experimental work into the DIS bearings, as the present investigation has only really served to highlight the potential of a simple two-layer technique. This process could be further adapted to use a powder with a lower sintering temperature as the main body structure instead of the relatively large 23μm powder used so far. This would reduce costs and help make it a more feasible concept.

7.6 Other Manufacturing Routes

Despite the success of the methods investigated here, it would be foolish to consider that an optimum process had been developed. There still exist a number of other ceramic processing techniques that promise reproducible manufacture. Chief among these are the use of starch and proteins. These have been shown to be suitable for the suspension of alumina powder and consolidate upon the application of heat to form a green with sufficient mechanical strength to be handled [142].

Two other methods that show considerable potential for the fabrication of porous ceramic parts are direct coagulation casting (DCC) and hydrolysis assisted solidification (HAS). Unlike using starch or protein where the suspension is consolidated through the application of heat, DCC and HAS require an enzyme catalysed reaction to shift the pH of the suspension towards the isoelectric point of the ceramic. This causes coagulation to occur, and again a green body is formed [143, 144].

The great advantage of these routes is that they represent a simple approach to the forming process in which a great variety of different geometries may be fabricated. In addition they are remarkably environmentally friendly processes.

References

[1] Air bearing applications to machine tools and measuring instruments
Wunsch, H. L.
Journal of Lubrication Technology, pp 680 - 686, Oct 1968

[2] Application of gas lubricated bearings to instruments
Denhard, W. G., Pan, C. H. T.
Journal of Lubrication Technology, pp 731 - 740, Oct 1968

[3] Gas bearing turbomachinery
Sternlicht, B.
Journal of Lubrication Technology, pp 665 - 679, Oct 1968

[4] A study of high speed machines with rubber stabilised air bearings
Powell, J. W., Tempest, M. C.
Journal of Lubrication Technology, pp 701 - 708, Oct 1968

[5] Processing and fluid flow characteristics of hot isostatically pressed porous alumina for aerostatic bearing applications
Kwan, Y. P. B.
Ph.D. Thesis, Cranfield University, 1997

[6] Rolling bearings
Allan, R. K.
Sir Isaac Pitman & Sons Ltd., London, 1945

[7] Frottement des rouleaux
Coulomb, C. A.
Pp 278-280, 332, 1785

[8] On rolling friction
Reynolds, O.
Philosophical transactions of the Royal Society, London, Series A, Vol 166, pp 153-174, 1876.

[9] A practical treatise on railroads and carriages
Tredgold, T.
E. Bliss and E. White, New York, 1825

[10] A practical treatise on railroads
Wood, N.
Knight and Lacey, London, 1932

[11] Essais et expériences sur le tirage des voitures et sur le frettement de second espèce
Dupuit. A. J. E. J.
Paris, 1837

[12] Rolling friction, I-historical introduction
Hersey, M. D.
Journal of Lubrication Technology, pp 260-263, April 1967

[13] Rolling friction, II-cast iron car wheels
Hersey, M. D., Downes, M. S.
Journal of Lubrication Technology, pp 264-268, April 1967

[14] Rolling friction, III-review of later investigations
Hersey, M. D.
Journal of Lubrication Technology, pp 269-275, April 1967

[15] Rolling friction, IV-additional car wheel experiments
Hersey, M. D., Golden, P. L.
Journal of Lubrication Technology, pp 83-88, Jan 1970

[16] Rolling Bearing Analysis
Harris, T. A.
2nd Edition, John Wiley and Sons, 1984

[17] History of Tribology
Dowson, D.
Longman, 1979

[18] Properties and selection. Stainless steels, tool materials and special purpose metals
Metals Handbook, 9th Edition, Vol. 3

[19] The Reynolds Centennial: A Brief History of the Theory of Hydrodynamic Lubrication
Pinkus, O.
Transactions of the ASME, pp 2-20, Jan 1987

[20] Reflections
Hays, D.F.
Journal of Lubrication Technology, pp50-109, Jan 1987

[21] An outline history of the oil engine and its lubrication
Compiled from various authors
H. P. Dorey & Company Ltd., Essex, for Shell-Mex and B. P. Ltd., 1961

[22] The development of a porous ceramic water hydrostatic bearing for high precision applications
Almond, R. J.
PhD Thesis, Cranfield University, 2000

[23] Roundup of gas bearing technology
Unknown author
Conference Digest
Machine Design, pp 210-220, Sept. 12, 1968

[24] Design of aerostatic bearings
Stout, K. J.
The National Bureau of Standards - Washington D.C.

[25] Design of aerostatic bearings
Powell, J. W.
The Machinery Publishing Co. Ltd., 1970.

[26] An investigation of methods to improve the wear resistance of gas-bearing ceramic materials
Rowe, H. H. Jr.
Journal of Lubrication Technology, pp 829-840, Oct 1968

[27] Material combinations for hydrodynamic inert gas-lubricated bearings
Murray, S. F.
Journal of Lubrication Technology, pp 49 - 55, Jan 1968

[28] Precision Machine Design
Slocum, A. H.,
Prentice Hall, 1992

[29] A review of the state of the art for the design of self acting gas lubricated bearings
Fuller, D. D.
Journal of Lubrication Technology, pp 1-16, Jan, 1969.

[30] Analysis of a porous gas foil bearing
Baumann, G. W.
Journal of Lubrication Technology, pp 457-464, Oct 1971

[31] Flexible membrane hydrostatic air bearing
Levy, S. B., Cooghan, C. H. JR.
Journal of Lubrication Technology, pp184-190, Jan 1968

[32] Theoretical solution as a boundary-value problem for externally pressurised porous gas bearings
Mori, H., Yabe, H., Shibayama, T.
Journal of Basic Engineering, pp 622 - 630, Vol 87, No 3, Sept 1965

[33] Theory of externally pressurised circular thrust porous gas bearings
Mori, H., Yabe, H., Ono, T.
Journal of Basic Engineering, pp 613 - 621, Vol 87, No 3, Sept 1965

[34] The externally pressurised porous wall, gas lubricated gas journal bearing, I
Sneck, H. J., Yen, K. T.
ASLE Transactions, p 288, Vol 7, 1964

[35] A survey of gas-lubricated porous bearings
Sneck, H. J.
Journal of Lubrication Technology, pp 804 - 809, October 1968

[36] Gas-lubricated porous bearings: A bibliography
Majumdar, B. C.
Wear, pp 269 - 273, 36, 1976

[37] Porous aerostatic bearings - an updated review
Kwan, Y. B. P., Corbett, J.
Wear, pp 69 -73, 222, 1998

[38] Characterisation of porous materials
Holdsworth, S. D.
Chemical and Process Engineering, pp 184-191, April 1963

[39] ISO 4003: 1977
Permeable sintered metal materials - determination of bubble test pore size
EN 24003: European Committee for Standardisation, Brussels, 1993

[40] Ultra-precision airbearing workspindles for the economic micro-machining of optical quality components
McKeown, P. A., Wills-Moren, W. J., Carlisle, K., Chapman, P. D.
Proceedings of The International Society for Optical Engineering, pp 24 - 32, Vol. 1015, 1988

[41] Porous graphite air-bearing components as applied to machine tools
Rasnick, W. H., Arehart, T. A., Littleton, D. E., Steger, P. J.
Society of Manufacturing Engineers, Technical Report MRR74-02.

[42] Engineering at the limits
Cranfield Precision Ltd brochure

[43] Sintering crystalline solids. I. Intermediate and final state diffusion models
Coble, R. L.
Journal of Applied Physics, pp 787-792, Vol 32, No 5, May 1961

[44] The use of porous materials in externally pressurised porous gas bearings
Kilmister, G. T. F.
Powder Metallurgy, pp 400 – 409, 12 (24), 1969

[45] The use of porous materials in gas lubrication
Polome, J., Gorez, R.
Wear, pp 349 – 356, 60, 1980

[46] A new technique to manufacture high performance air bearings
Schultz, B., Muth, M.
Proceedings of the 8th International Precision Engineering Seminar, pp 533 – 536, May 1995

[47] Theoretical investigation of externally pressurised gas lubricated porous journal bearing with surface loading effect
Mori, H., Yabe, H,
Journal of Lubrication Technology, pp 195 - 20395 (2), 1973

[48] Creep of metals
Tapsell, H. J.
Oxford Universtity Press, 1931

[49] Experimental investigation of porous bronze bearings
Cusano, C., Phelan, R. M.
Journal of Lubrication Technology, pp 173-180, April 1973

[50] Theoretical investigation of externally pressurised gas-lubricated porous journal bearing with surface loading effect
Mori, H., Yabi, H.
Journal of Lubrication Technology, pp 195-203, April 1973

[51] Les fountains publiques de la ville de Dijon
Darcy, H.
1856

[52] The effect of fluid inertia on a porous thrust plate – an analytical solution
Hsing, F. C.
Journal of Lubrication Technology, pp 202 – 206, 93 (1), 1971

[53] The significance of fluid inertia and slip velocity in the steady-state analysis of externally pressurised gas lubricated porous thrust bearings
McRea, R. J., Donaldson, I. S.
Proceedings of the 7th International Gas Bearing Symposium, pp 1 - 20, 1976

[54] Flow of homogeneous fluids through porous media
Muskat, M.
J. W. Edwards Inc., 1937

[55] Flow of gasses and vapours in a porous medium and its bearing on adsorption problems
Barrer, R. M., Grove, D. M.
Transactions of the Faraday Society, pp 837 - 844, 47, 1951

[56] Fluid flow through porous metals
Green, L., Duwez, P.
Journal of Applied Mechanics, pp 39 - 45, March 1951

[57] A new approach to gas flow in capillary systems
Barrer, R. M.
Transactions of the Faraday Society, pp 35 - 40, 57, 1953

[58] Statistical hydrodynamics in porous media
Scheidegger, A. E.
Journal of Applied Physics, pp 994 - 1001, Vol. 25, No. 8, 1954

[59] Evidence for permeability minima in low-pressure gas flow through porous media
Grove, D. M., Ford, M. G.
Nature, pp 999 - 1000, Vol. 182, No. 4641, Oct 1958

[60] Wasserbewegung durch Boden
Forchheimer, P.
Zeitschrift des VDI, pp 1781 - 1788, 45 (50), 1901

[61] Experience relating to the steady performance of aerostatic porous thrust bearings
Taylor, R., Lewis, G. K.
Proceeding of the ImechE, pp 383 - 390, 189 (22), 1975

[62] Investigation of the effect of inertia in flow if air through porous bearing sleeves
Cieslicki, K.
Wear, pp 73 - 78, 172, 1994

[63] Steady-state solutions for an aerostatic thrust bearing with an elastic porous pad
Taylor, R., Lewis, G. K.
Proceedings of the 6th International Gas Bearing Symposium, pp 65 - 74, 1974

[64] An investigation of the viscous and inertial coefficients for the flow of gasses through porous sintered metals with high pressure gradients
Greenburg, D. B., Weger, E.
Chemical Engineering Science, pp 8 - 19, 12, 1960

[65] Permeability of tungsten matrices as a function of density, particle size, and shape
Robinson, A. T.
Transactions of the ASM, pp 650 - 657, 57, 1964

[66] Theory and applications of controlled permeability
Cliffel, E. M., Smith, W. E., Schwope, A. D.
Modern Developments in Powder Metallurgy, pp 114 - 128, 3, 1966

[67] Porosity and particle size effects on the gas flow characteristics of porous metal
German, R. M.
Powder Technology, pp 81 - 86, 30, 1981

[68] An examination of the effects of pore morphology on gas flow through sintered compacts
Smith, D. W., Marth, T.
Modern Developments in Powder Metallurgy, pp 825 - 854, 12, 1980

[69] Resistance to vibration of a hydrostatic thrust bearing
Sheinberg, S. A., Shuster, V.G.
Machine & Tooling, pp 24 - 29, 31 (11), 1960

[70] A numerical solution for the design of externally pressurised porous gas bearings: Thrust bearings
Gargulio, E. P., Gilmour, P.W.
Journal of Lubrication Technology, pp 810 - 817, Oct 1968.

[71] Theoretical and experimental analysis of externally pressurised porous gas thrust bearings
Andrisano, A., Maggiore, A.
Tribology International, pp 285 - 288, October 1978

[72] The flow of a viscous fluid through a porous wall into a narrow gap
Ishizawa, S., Hori, E.

Bulletin of JSME, pp 719 - 730, 9 (36) 1966

[73] Analysis of externally pressurised gas porous bearings
Murti, P. R. K.
Journal of Lubrication Technology, pp 354 - 360, 96 (3), 1974

[74] Effect of velocity slip in an externally pressurised porous thrust bearing working with an incompressible fluid
Murti, P. R. K.
Journal of Applied Mechanics, pp 404 - 408, 43 (3). 1976

[75] The steady state performance of an externally pressurised gas lubricated porous thrust bearing with a uniform film
Jones, O. K., Michalski, J., Lewis, G. K.
Joint ImechE/IprodE Comference on Externally Pressurised Bearings, pp 23 - 42, 1971

[76] Effect of velocity slip in an externally pressurised porous circular thrust bearing
Verma, R. L.
Wear, pp 239 - 244, 63, 1980

[77] Effect of velocity slip on the performance of aerostatic porous thrust bearings with uniform film thickness
Singh, K. C.
Wear, pp 323 - 333, 88 (3), 1983

[78] Static study of the porous bearings by the simplified finite element analysis
Tian, Y.
Wear, pp 203 - 209, 218, 1998

[79] Science data book
Tennent, R. M. Editor
Oliver & Boyd 1989

[80] Boundary conditions at a naturally permeable wall
Beavers, G. G., Joseph, D. D.
Journal of Fluid Mechanics, Trans ASME, pp 197-207, 30 (1), 1967

[81] On the boundary conditions of a porous medium
Staffman, P. G.
Studies in Applied Mathematics, pp 93 - 101, 50, 1971

[82] A model for the boundary condition of a porous material. Part 1
Taylor, G. I.

Journal of Fluid Mechanics, pp 319 - 326, 49 (2), 1971

[83] A model for the boundary condition of a porous material. Part 2
Richardson, S.
Journal of Fluid Mechanics, pp 327 - 336, 49 (2), 1971

[84] Roark's Formulas for Stress and Strain
6th Edition, McGraw-Hill, 1989

[85] Ionizable surface group models of aqueous interfaces
Healy, T. W., White, L. R.
Advances in Colloid and Interface Science, pp 303 - 345, 9, 1978

[86] Principles of physical chemistry
Mansfield, D. H.
Heinmann Educational Books, 1979

[87] Temperature dependence on point of zero charge of alumina and magnetite
Tewari, P. H., McLean, A. W.
Journal of Colloid Interface Science, pp 267 - 272, 40, Aug 1972

[88] Manufacture of porous ceramic bearings
MSc Group Project
Academic Year 1997 - 1998

[89] Influence of Acidity on the Electrostatic Stability of Alumina Suspensions in Ethanol
Wang, G., Sarkar, P., Nicholson, P
Journal of the American Ceramic Society, pp965-972, 80 [4], 1997

[90] Rheological Properties of Concentrated, Nonaqueous Silicon Nitride Suspensions
Bergström, L.
Journal of the American Ceramic Society, pp 2385-2396, 79 [9], 1996

[91] Experimental Evaluation of a New Flocculation-Filtration Model for Ceramic Shape Forming Processes
Haerle, A. G., Haber, R. A.,
Journal of the American Ceramic Society, pp 3033-3040, 79 [12], 1996

[92] Microwave enhanced slip casting of advanced ceramics
Vernon, A., Binner, J.
Industrial Ceramics, pp 27 - 30, Vol. 16, No. 1, 1996

[93] Powder injection moulding

German, R. M.
Metal Powder Industries Federation, 1990

[94] Injection moulding of ceramic materials
Schwartzwalder, K.
Ceramic Bulletin, pp 459 – 461, vol 28, 1949

[95] Direct expansion of ceramic foams
Guy, R. C. E., Evans, J. R. G.
British Ceramics Transactions, pp 165 – 169, No. 4, Vol. 96, 1997

[96] Sintering crystalline soids. I. Intermediate and final state diffusion models
Coble, R. L.
Journal of Applied Physics, pp 787 – 792, vol 32, no 5, May 1961

[97] Kinetics of high temperature processes
Coble, R. L., Kingery, W. D. Editor
Technology Press, Cambridge, Massachusetts, 1959

[98] Smith, C. S.
Transactions of the AIME, p175, 15, 1948

[99] Yttria Doping and Sintering of Submicrometer Grained α-Alumina
Sato, E., Carry, C.
Journal of the American Ceramic Society, pp 2156-2160, 79 [8], 1996

[100] Effect of yttrium and lanthanum on the final-stage sintering behaviour of ultra high purity alumina
Fang, J., Thompson, M. A., Harmer, M. P., Chan, H. M.
Journal of the American Ceramic Society, pp2005 – 2012, 80 [8], 1997

[101] Data sheet 570
Calcined alumina alcan reactive grades for ceramics
Alcan Chemicals Europe

[102] Data sheet 650UK
Alcan aluminas C-70 grade
Alcan Chemicals Europe

[103] http://rhodium.lycaeum.org/chemistry/isomerize.safrole.txt

[104] Data sheet 461
Alcan milled alumina grade RMA325
Alcan Chemicals Europe

[105] Powder co-injection moulding
Hanson, S.
PhD Thesis, Cranfield University, 2001

[106] Predictive process control of crowded particulate suspensions
Funk, J. E., Dinger, D. R.
Kluwer Academic Publishers 1993

[107] Particle packing characteristics
German, R. M.
Metal Powder Industries Federation, 1989

[108] Citric acid – A dispersant for aqueous alumina suspensions
Hidber, P. C., Graule, T. J., Gaucklet, L. J.
Journal of the American Ceramic Society, pp 1857 – 1867, 79 [7], 1996

[109] Mr Terry Marsh,
16 Dalston Drive, Moss Bank, St Helens, Merseyside WA11 7BE.

[110] Principles of ceramic processing
Reed, J. S.
John Wiley & Sons, 2nd Edition, 1995

[111] Ceramic injection moulding
Mutsuddy, B. C., Ford, R. G.
Chapman & Hall, 1st Edition, 1995

[112] Injection mould design
Pye, R. G. W.
George Godwin Ltd., 2nd Edition, 1978

[113] Powder injection molding
German, R. M.
Metal Powder Industries, 1990

[114] Injection moulding of elastomers
Penn, W. S. Editor
MacLaren & Sons, 1969

[115] Plastics mold engineering handbook
DuBois, J. H., Pribble, W. I., Editors
Van Nostrand Reinhold Company, 4th Edition, 1987

[116] Data Sheet 576
Baco RA 107 LS Grade

Alcan Chemicals Europe

[117] Determination of fluid permeability
BS 5600: Part 3: Section 3.6: 1988
ISO 4022: 1987

[118] Pressure sensors, transducers and transmitters
Sensortechnics manual, Volume 8

[119] Airflow sensors. High flow mass airflow/amplified
AWM 2000 Series and AWM 5000 Series data sheets
Honeywell Micro Switch Division

[120] SMC Electro-pneumatic regulator Series ITV2000
Data sheet
SMC Pneumatics (UK) Ltd

[121] Physical Properties of Air
Convective Heat and Mass Transfer
Kays and Crawford, McGraw Hill

[122] Ermittlung der Grössenverteilung von Poren in feuerfesten Baustoffen - Teil I
Žagar, L.
Archv fur das Eisenhuttenwessen, pp 561 - 562, 26 (9), 1955

[123] Ermittlung der Grössenverteilung von Poren in feuerfesten Baustoffen und Glasnutschen- Teil II
Žagar, L.
Archv fur das Eisenhuttenwessen, pp 657 - 662, 27 (10), 1956

[124] Uber die Textur von feuerfesten Baustoffen
Žagar, L.
Silicates Industriels, pp 306 - 312, 24, 1959

[125] Porengrössenverteilung nach dem Luft-Wasser-Verdrängungsverfahren
Berichte der Deutschen Keramik Gesellshaft, pp 13 - 17, 55 (1), 1978

[126] Improvement of the dynamic water-expulsion method for pore size distribution measurements
Gélinas, C., Angers, R.
Ceramic Bulletin, pp 1297 - 1300, 65 (9), 1986

[127] The most probable pore size distribution in fluid filter media I. Evidence of such a distribution from the results of extended bubble-point measurements.

Johnston, P. R.
Journal of Testing and Evaluation, pp 117 - 121, 11 (2), 1983

[128] On the stiffness and damping properties on an externally pressurised, gas-lubricated porous thrust bearing
Sun, D. C.
Proceedings of the 7th International Gas Bearing Symposium, pp 5 - 6, 1976

[129] Data Sheet, Kozake Laboratories Ltd
Supplied by Metrology International,
Harrogate

[130] EMOD version 9.17
Program for Elasticity Modulus Calculation
Users Guide

[131] Rupture fragile et résistance aux chocs thermiques de céramiques à usages mécaniques
Glandus, J. C.
Thèse présentée à l'université de Limoges

[132] Modern ceramic engineering
Richerson, D. W.
Marcel Dekker Inc, 2nd Ed., 1992

[133] Discussion of the Ryshkewitch paper
Duckworth, W.
Journal of the American Ceramic Society, p 68, 36(2), 1953

[134] Open pore description of mechanical properties of ceramics
Wagh, A. S., Poeppel, R. B., Singh, J. P.
Journal of Material Science, pp 3826-3868, 26, 1991

[135] Elastic modulus porosity relationship for Si_3N_4
Phani, K. K., Niyogi, S. K.
Journal of Material Science Letters, pp 511-515, 6, 1987

[136] Handbook of properties of technical and engineering ceramics
Morrel, R.
HMSO, London, 1st Edition, 1987

[137] Auslegung von ebenen und zylindrischen aeorstatischen Lagern bei stationärem Betreib
Gerke, M.

Lehrstuhl für Feingerätebau und Getreibelehre, Dr Ing Thesis, T. U. München, 1991

[138] A model for the boundary condition of a porous material Part I
Taylor, G. I.
Journal of Fluid Mechanics, pp 319 - 326, 49 (2), 1971

[139] A model for the boundary condition of a porous material Part II
Richardson, S.
Journal of Fluid Mechanics, pp 327 - 336, 49 (2), 1971

[140] Worldwide design handbook
Loctite European Group, 2nd Edition, 1998

[141] Air bearings for industry
New Way Machine Components, Inc.,
4009 I Market Street, Aston, PA 19014

[142] Novel water-based shaping of ceramic components
Lyckfeldt, O.
Conference and Exhibition of the European Ceramic Society, pp 219-220, Extended Abstracts, Vol.2, 1999

[143] Ceramic forming by gel bonding
Bowden, M. E., Machen, K., Brown, I. W. M.
Conference and Exhibition of the European Ceramic Society, pp 217-218, Extended Abstracts, Vol.2, 1999

[144] Direct coagulation casting - a new green shaping technique part I: Processing principles
Graule, T. J., Gauckler, L. J., Baader, F. H.
Industrial Ceramics, pp 31 - 35, Vol 16, No. 1, 1996

Appendix A Derivation of the Equivalent Permeability Coefficient from Forchheimer's Equation

Forchheimer's equation for compressible flow has been stated as:

$$\frac{p_1^{\,2} - p_2^{\,2}}{2.p_{ref}} = \frac{z_p.\eta.(Q/A_p)}{\Phi_v} + \frac{z_p.\rho.(Q/A_p)^2}{\Phi_i}$$

$$= \frac{z_p.\eta.(Q/A_p)}{\Phi_e}$$

Therfore $$\frac{1}{\Phi_e} = \frac{1}{\Phi_v} + \frac{\rho.Q}{\eta.A_p}.\frac{1}{\Phi_i}$$

Substituting for Q/A_p ,

$$\frac{Q}{A_p} = \frac{p_1^{\,2} - p_2^{\,2}}{2.p_{ref}} \cdot \frac{\Phi_e}{z_p.\eta}$$

$$\frac{1}{\Phi_e} = \frac{1}{\Phi_v} + \frac{\rho}{z_p.\eta^2} \cdot \frac{p_1^{\,2} - p_2^{\,2}}{2.p_{ref}} \cdot \frac{\Phi_e}{\Phi_i}$$

$$\frac{1}{\Phi_v} = \frac{1}{\Phi_e} - \frac{\rho}{z_p.\eta^2} \cdot \frac{p_1^{\,2} - p_2^{\,2}}{2.p_{ref}} \cdot \frac{\Phi_e}{\Phi_i}$$

$$= \frac{1}{\Phi_e.\Phi_i} \times \left[\Phi_i - \frac{\rho}{z_p.\eta^2} \cdot \frac{p_1^{\,2} - p_2^{\,2}}{2.p_{ref}} . \Phi_e^{\,2} \right]$$

$$\frac{\rho}{z_p.\eta^2} \cdot \frac{p_1^{\,2} - p_2^{\,2}}{2.p_{ref}} . \Phi_e^{\,2} + \frac{\Phi_i}{\Phi_v} . \Phi_e - \Phi_i = 0$$

Which can be rewritten as:

$$\Phi_e = \frac{-\frac{\Phi_i}{\Phi_v} + \left\{ \frac{\Phi_i^{\,2}}{\Phi_v^{\,2}} + 4.\frac{\rho}{z_p.\eta^2} . \frac{p_1^{\,2} - p_2^{\,2}}{2.p_{ref}} . \Phi_i \right\}^{1/2}}{2.\frac{\rho}{z_p.\eta^2} . \frac{p_1^{\,2} - p_2^{\,2}}{2.p_{ref}}}$$

Appendix B Injection Moulding Conditions

Dassett 30-tonne co-injection moulding machine: moulding conditions

1 Barrel	Mould: 10MM DISC	Run no.: DA	Date: 29/5/98	
Material: 55% ALUMINA · 5μ	C-no.:		CHRIS ROACH	
CF / kN: 300	COS / mm: 130	SMP / mm: 54		
MPP / bar: 10	CT / s: 35	COT / s: 1·5	TOL+ / °C:	
FZ B / °C: OFF	MZ B / °C: OFF	RZ B / °C: OFF	TOL- / °C:	
SB:	on / off	Autopurge: / off	IUS / %: 50	SBD / s: 2·0
Mould / °C: NO HEATING OR COOLING				

Specimen nos.:	1 - 26
FZ A / °C	165
MZ A / °C	165
RZ A / °C	120
NZ / °C	165
SS / mm	62
IHT / s	10
IHP / bar	200
EFI / mm	0
TP / mm	10
TPr / bar	150
ILT / s	20
SS / rpm	220
SD / mm	62
PP A Z5 / bar	5
PP A Z4 / bar	5
PP A Z3 / bar	5
PP A Z2 / bar	5
PP A Z1 / bar	5
SP A Z5 / %	70
SP A Z4 / %	70
SP A Z3 / %	70
SP A Z2 / %	70
SP A Z1 / %	70
Remarks:	LOWER PACKING PRESSURE STOPS SPRUE SINKING INTO MOULDING. SHRINKAGE IN MOULDING NOT VERY MUCH BY VISUAL.
Data saved: / n	Set no.:

jra/cinmo02.doc/20/5/96

Appendix C Permeability Rig Operation Instructions

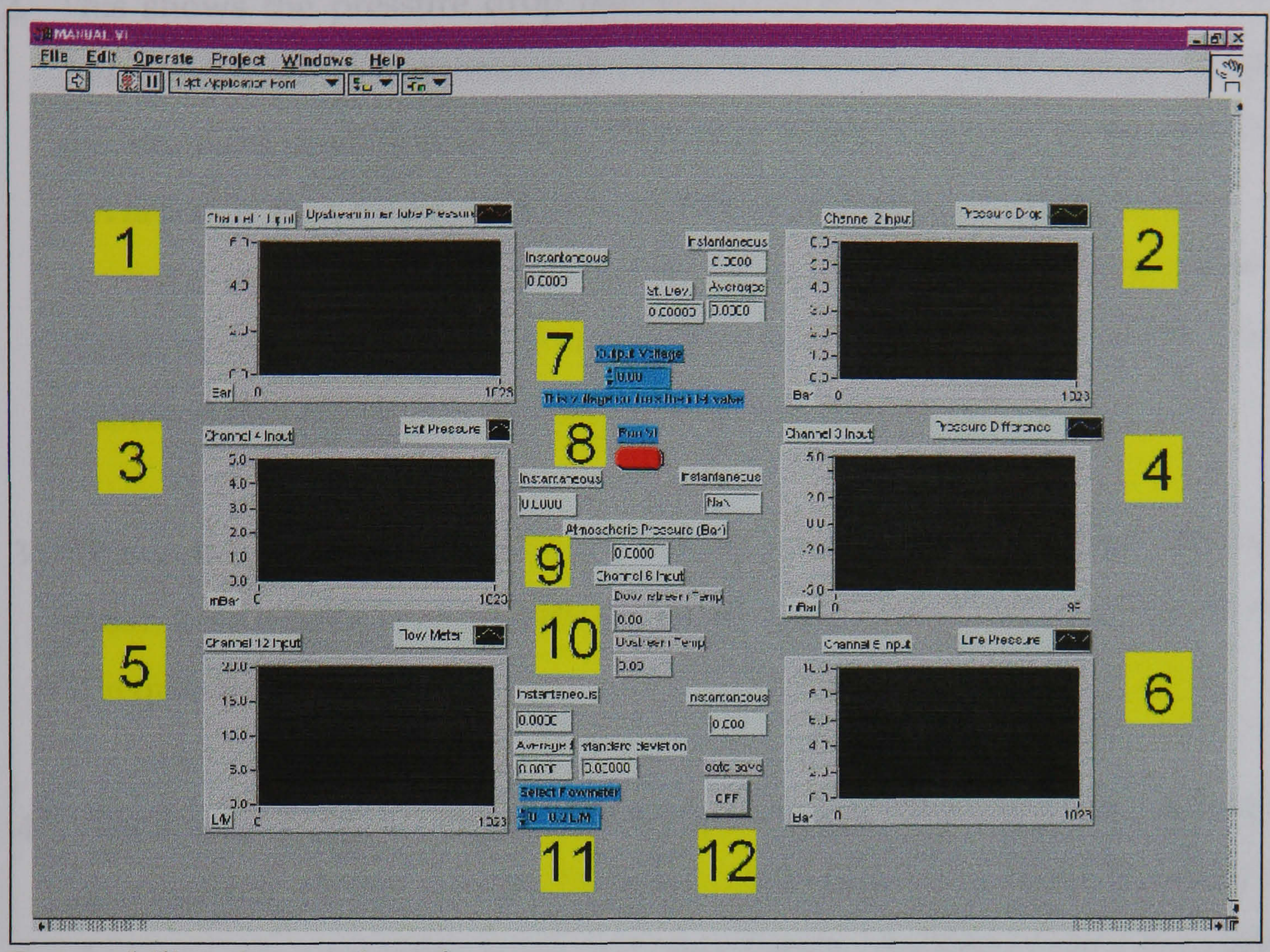

Permeability rig user interface

This brief user guide assumes the operator has a working knowledge of Windows and LabView.

- Launch LabView.
- Select Open from the File menu
- Navigate to LabView/User.lib/ and open manual.vi
- The above screen should open. This is the main screen and allows full control of the rig. In addition it gives the user a graphical illustration of the various parameters at any time. The areas highlighted with large numbers in the graphic are explained below:

1. This is the pressure in the supply tube upstream of the porous sample in bar. An instantaneous value of pressure is given in the small box to the right of the graph.

2. This shows the pressure drop measured across the porous sample in bar. Also shown are an instantaneous value, the average of 1000 data points, and the standard deviation of those 1000 data points. The use of the standard deviation is as a measure of the stability of the data. As this is one of the recorded data sets it is important that it is steady state. A high value of standard deviation shows that the data is not stable, whilst a low value indicated that the rig has reached steady state conditions.

3. This is the gauge pressure of the exit inner tube before the flow meter, in mbar. This is used to correct the pressure at which the flow rate is measured, if required.

4. This screen shows the pressure difference between the inner and outer tubes downstream of the sample, in mbar. This shows how well balanced the flows in the concentric tubes are, and ideally should be zero. A positive pressure shows that the outer tube is at a higher pressure, while a negative pressure shows that the inner tube is at the higher pressure. This is adjusted by using the manual valve at the top of the rig.

5. This shows the flow rate in l/minute. The flowmeter is user selectable (see 11) and the display shows the corrected flow for the selected meter. Also given are the instantaneous, average, and standard deviation in a manner similar to 2.

6. This is the supply line pressure supplied to the rig before the electro-pneumatic regulator used to control the flow in the rig. This has two functions. Firstly it confirms the presence of the supply air, and secondly shows how steady the supply pressure is. It was found that while other machines used the supply the pressure varied considerably. During permeability testing it is important to be able to balance the pressure

between the inner and outer tubes to as be as close as possible. In a good test this is possible to within ±0.003mbar. If this proves difficult it is usually due to a variation in supply pressure which can be qualified through the use of this graph. It is recommended that all testing be done under "quiet" conditions, i.e., with no other air users operating.

7. This is the control for the electro-pneumatic regulator. The output is shown in volts, and sets the pressure in the lower section of the rig before the porous test piece. The pressure in this section is given by dividing the output voltage by two, e.g. for an output of 2.5V, the resulting pressure is 1.25 bar.

   WARNING! DO NOT attempt to enter a value manually in the control box to rapidly increase the pressure. ONLY EVER RAMP THE PRESSURE UP USING THE SCROLL BAR. Failure to observe this may cause damage to the rig and be potentially dangerous. Values may ONLY be entered to decrease the pressure.

8. The control to operate the software. The user must first press this button (it will turn from red to green to indicate that it is ready to start), then the main run button (top left-hand corner).

9. This shows the atmospheric pressure recorded to correct the flowmeter readings (not currently functional).

10. These are the upstream and downstream gas temperatures taken just before and just after the porous sample. These are used to correct the conditions at which the readings are taken at.

11. This ring control selects the flowmeter to be used during the test. Continuously pressing up or down will bring the user back to the same

selection. It is necessary to set the correct flowmeter BEFORE button 8 is pressed.

12. This button initiates the save sequence. Upon pressing this a pop-up screen will appear allowing the user to select the number of data points to be averaged from each channel (the default is 100). This screen also contains an option to return to the main screen without saving, and a further button to continue the save process. If this is pressed the save as screen appears. This allows a filename to be specified, as well as a directory. The file format is comma-delimited text, as can be read by a spreadsheet. Once saved the user is returned to the first pop-up screen, and can return to the main screen by pressing the return to the main screen button. If cancel is pressed on the save as screen, LabView generates an error, and the user is prompted to abort or continue. Pressing continue returns the user to the initial pop-up screen. Aborting stops the programme in its present state, and is NOT recommended. The programme will stop running with high pressure still present in the lower half of the rig. If this is pressed, set the output voltage to zero (section 7), and restart the programme. This will then close the valve and dump the air to atmosphere.

All testing should then carried out with due regard to BS5600, Part 3.

Appendix D Stiffness Test Rig Operation Instructions

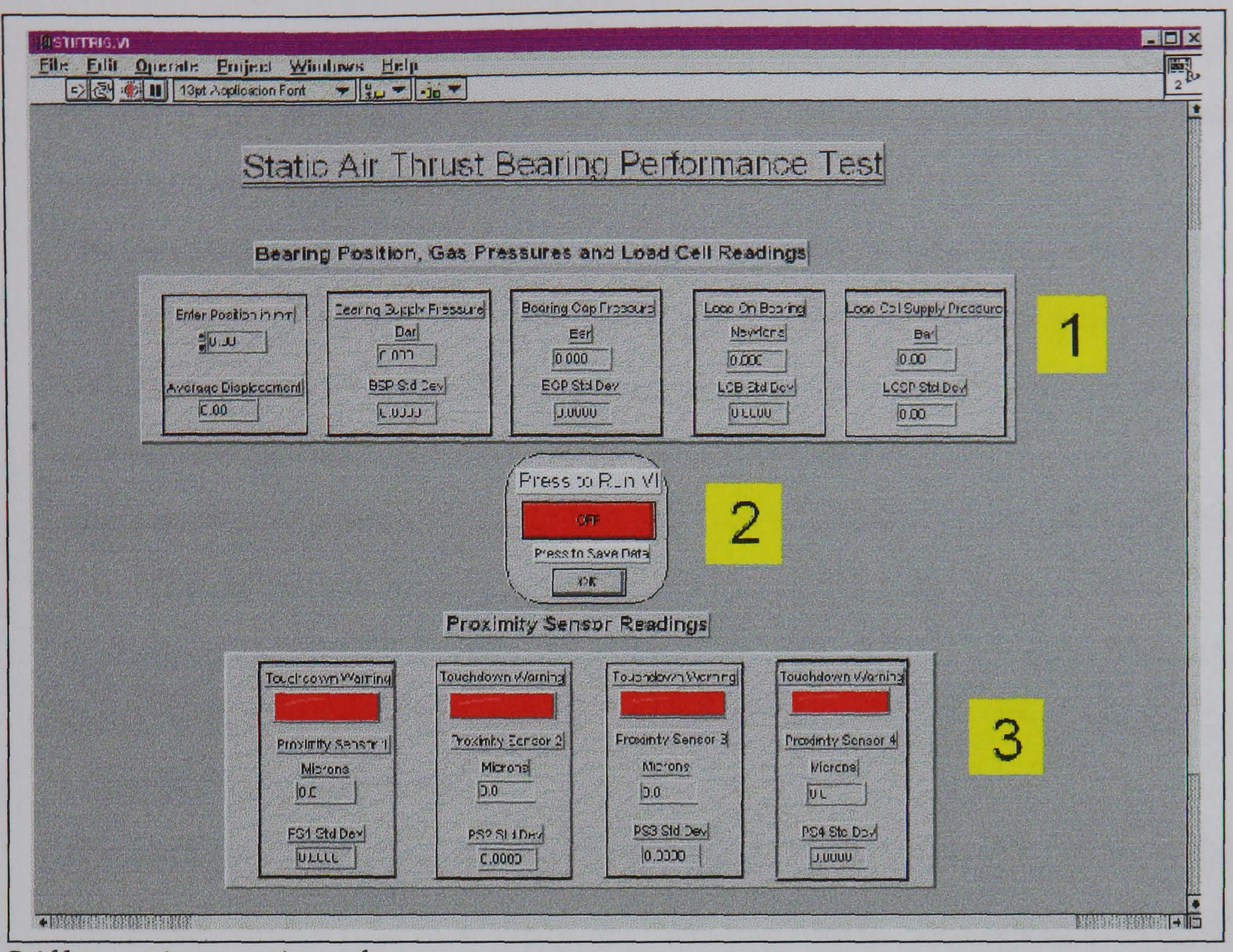

Stiffness rig user interface

This brief user guide assumes the operator has a working knowledge of Windows and LabView.

- Launch LabView.
- Select Open from the File menu
- Navigate to LabView/User.lib/ and open stiffrig.vi
- The above screen should open. This is the main screen and allows full control of the rig. In addition it gives the user a graphical illustration of the various parameters at any time. The areas highlighted with large numbers in the graphic are explained below:

1. This section gives the overall summary of the status of the test. The first box contains the position input, and the average bearing gap (calculated from

the average of the four reading given in 3). The position is entered manually, either through the scroll bars or by typing the number directly into the box. This position is used to keep track of the position of the bearing during pressure profile tests, and is read from the micrometer adjustment that is used to move the bearing.

The next box records the bearing supply pressure in bar. This is the pressure that feeds to the back of the bearing though the holder and is the mean of 100 data points. A value of the standard deviation is also quoted, allowing an assessment of the stability of the data to be made.

The bearing gap pressure and the standard deviation is shown in the next box. This is the pressure at a point under the bearing being tested. As the bearing is moved over the reference plate this value changes. This value, along with the position allows a map of the pressure profile under the bearing to be constructed.

The load on the bearing is calculated from the geometry of the load cylinder, the dead weight of the piston, and the pressure inside the cylinder. Also shown is the standard deviation.

The final box is redundant.

2. This section contains the control button to start the software. This button, when pressed, turns from red to green to indicate that the programme is ready. It is then started by pressing the run button on the main window (top left).

   The press to save button launches a pop-up window that allows the user to input a filename and select a directory.

3. The final section contains the data for each of the four position sensors. Each displays the gap reading and the standard deviation from the individual sensor. Also included is a touchdown-warning lamp. This turns red automatically once the reading falls below 1μm to warn the user.

Appendix E Bubble Test Instructions

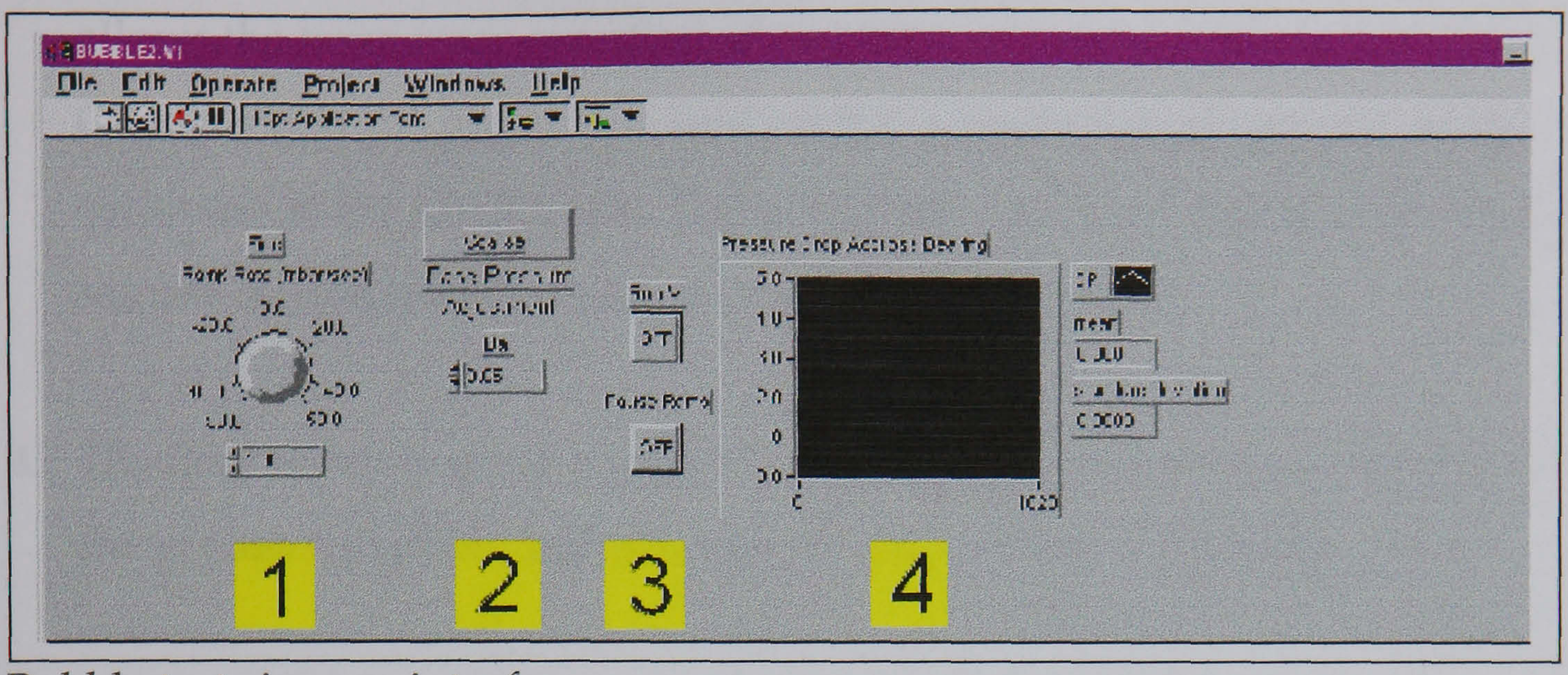

Bubble test rig user interface

This brief user guide assumes the operator has a working knowledge of Windows and LabView.

- Launch LabView.
- Select Open from the File menu
- Navigate to LabView/User.lib/ and open bubble2.vi
- The above screen should open. This is the main screen and allows full control of the rig. In addition it gives the user a graphical illustration of the various parameters at any time. The areas highlighted with large numbers in the graphic are explained below:

1. This rotary control sets the ramp rate at which the pressure is increased or decreased. It can be input by dragging the control around to the desired value, by using the scroll arrows, or by directly inputting the desired value.

2. The course base pressure adjustment allows the user to quickly arrive at the start pressure for the test. It ramps much more quickly than the control described in 1, and is intended for macro pressure adjustments only.

3. The run button starts the programme. Once it is pressed the main run button is pressed (top left), and the experiment started. The pause ramp button allows the temporary cessation of the increase (or decrease) in pressure. Once pressed the pressure is held until it is pressed again and the ramp continues at the pre-set rate. This is to allow time for visual inspection of the sample during testing under steady state conditions.

4. The final window gives a graphical illustration of the pressure drop across the porous test piece, and also includes the standard deviation.

Appendix F Flowmeter Calibration Curves

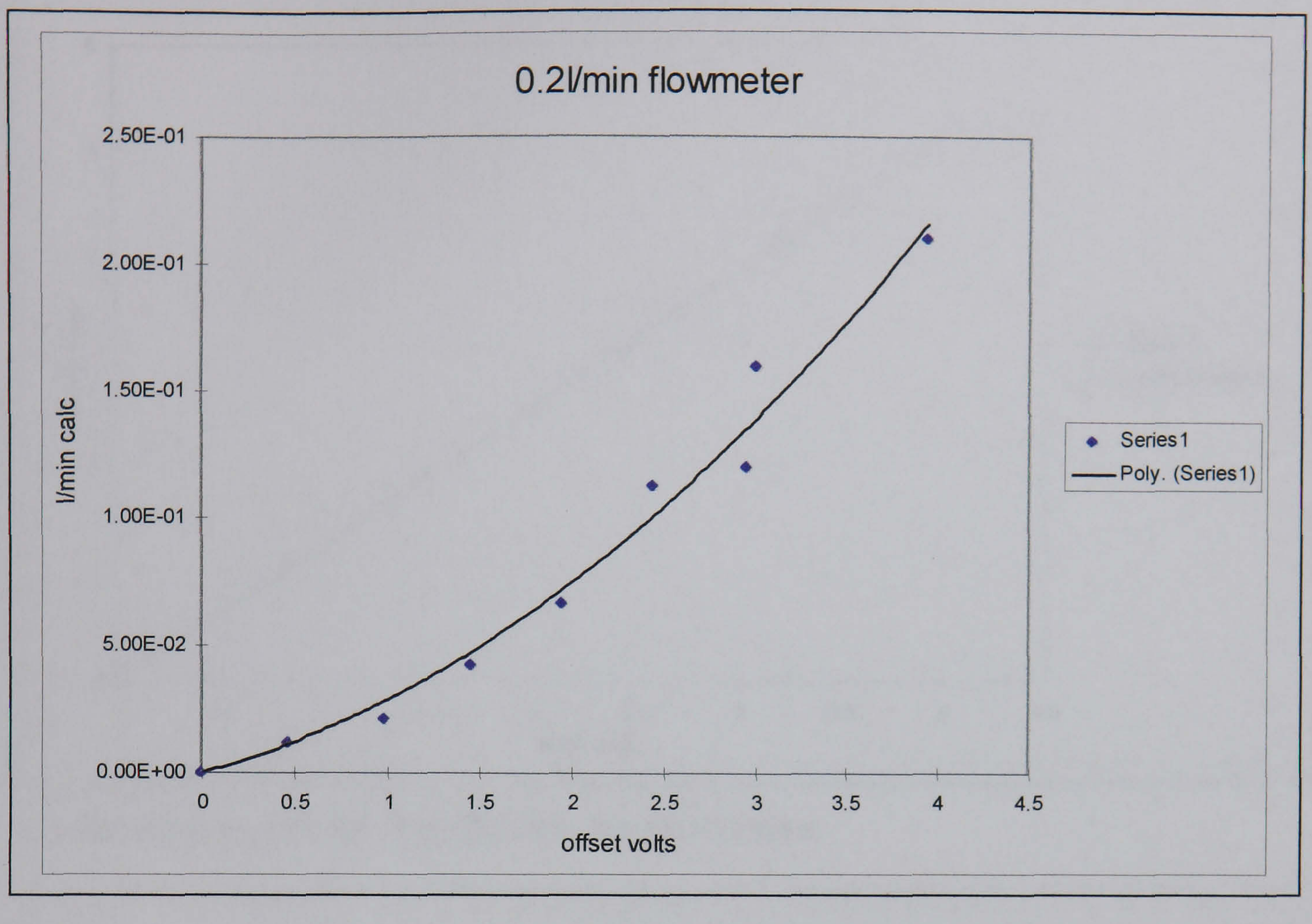

Calibration curve for 0 to 0.2l/minute flowmeter

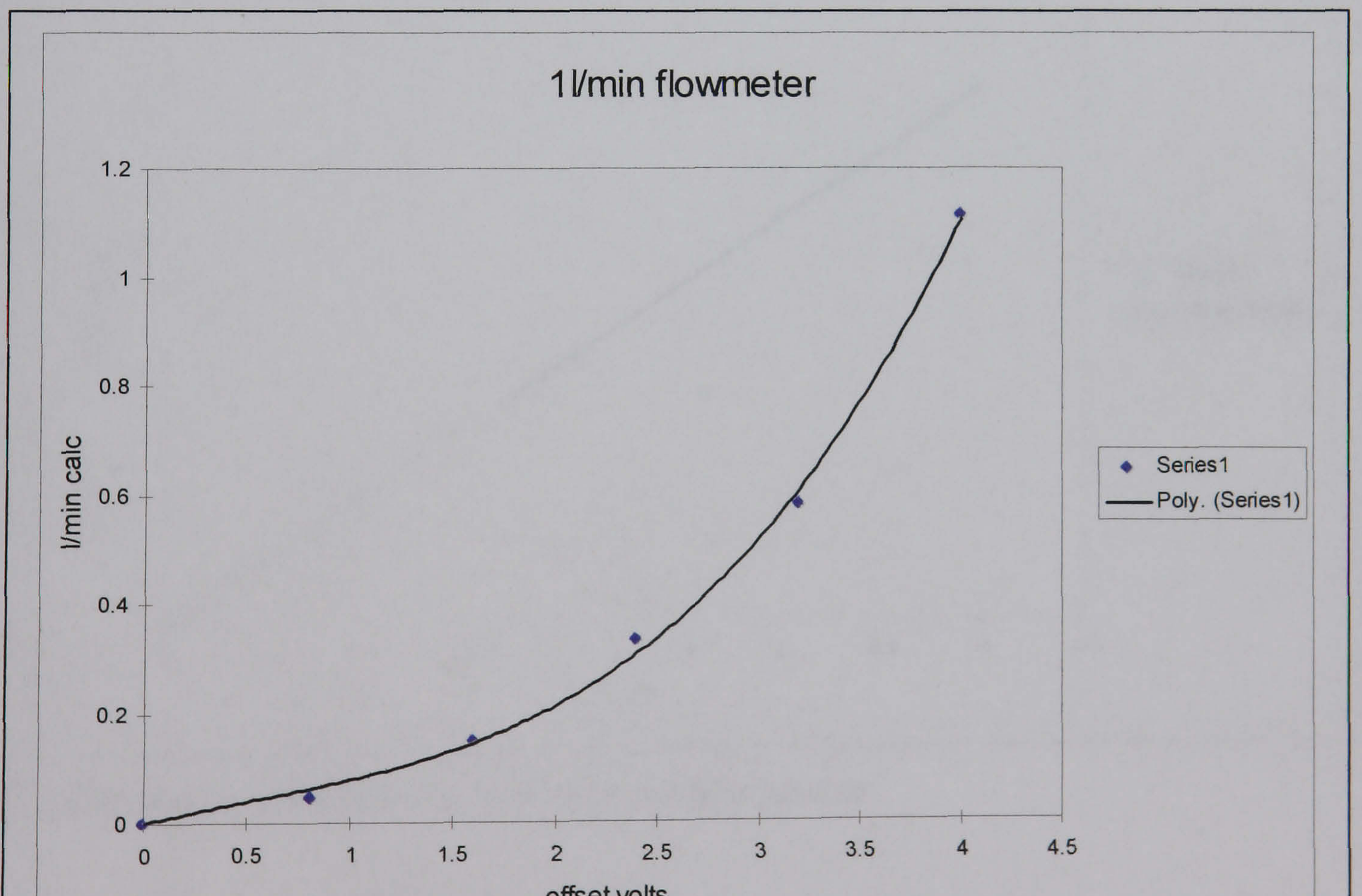

Calibration curve for 0 to 1l/minute flowmeter

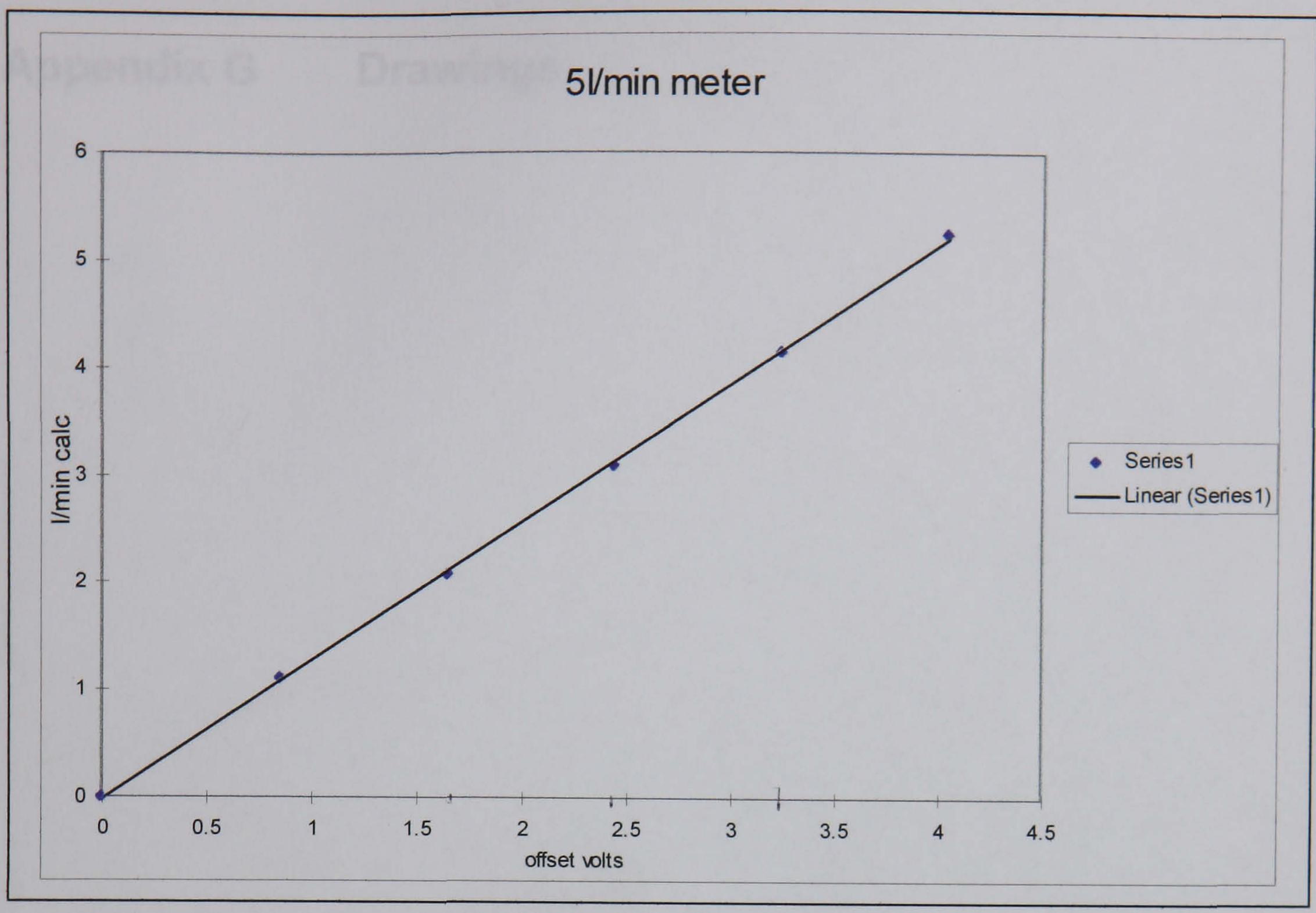

Calibration curve for 0 to 5l/minute flowmeter

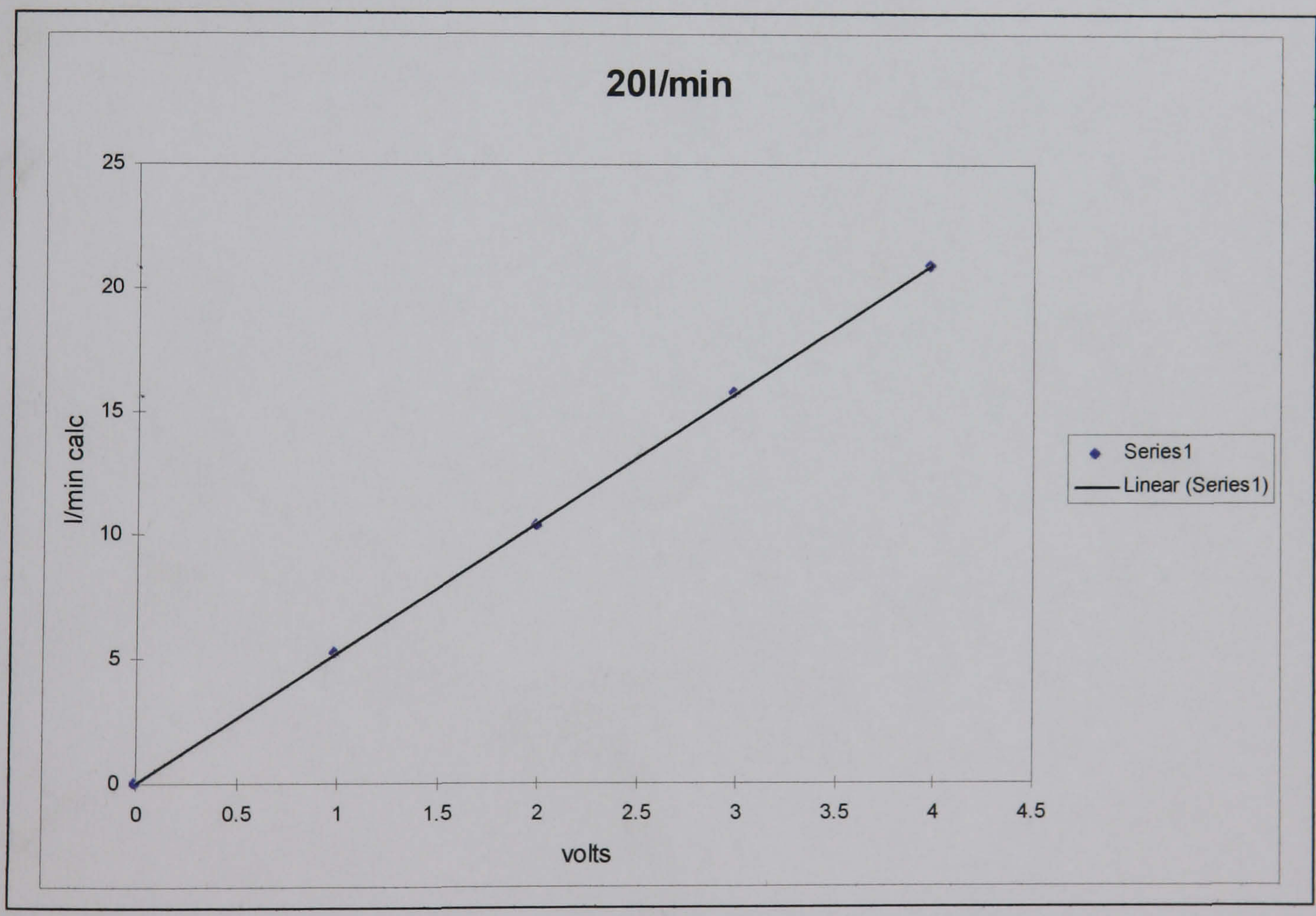

Calibration curve for 0 to 20l/minute flowmeter

Appendix G Drawings

SKETCH A.

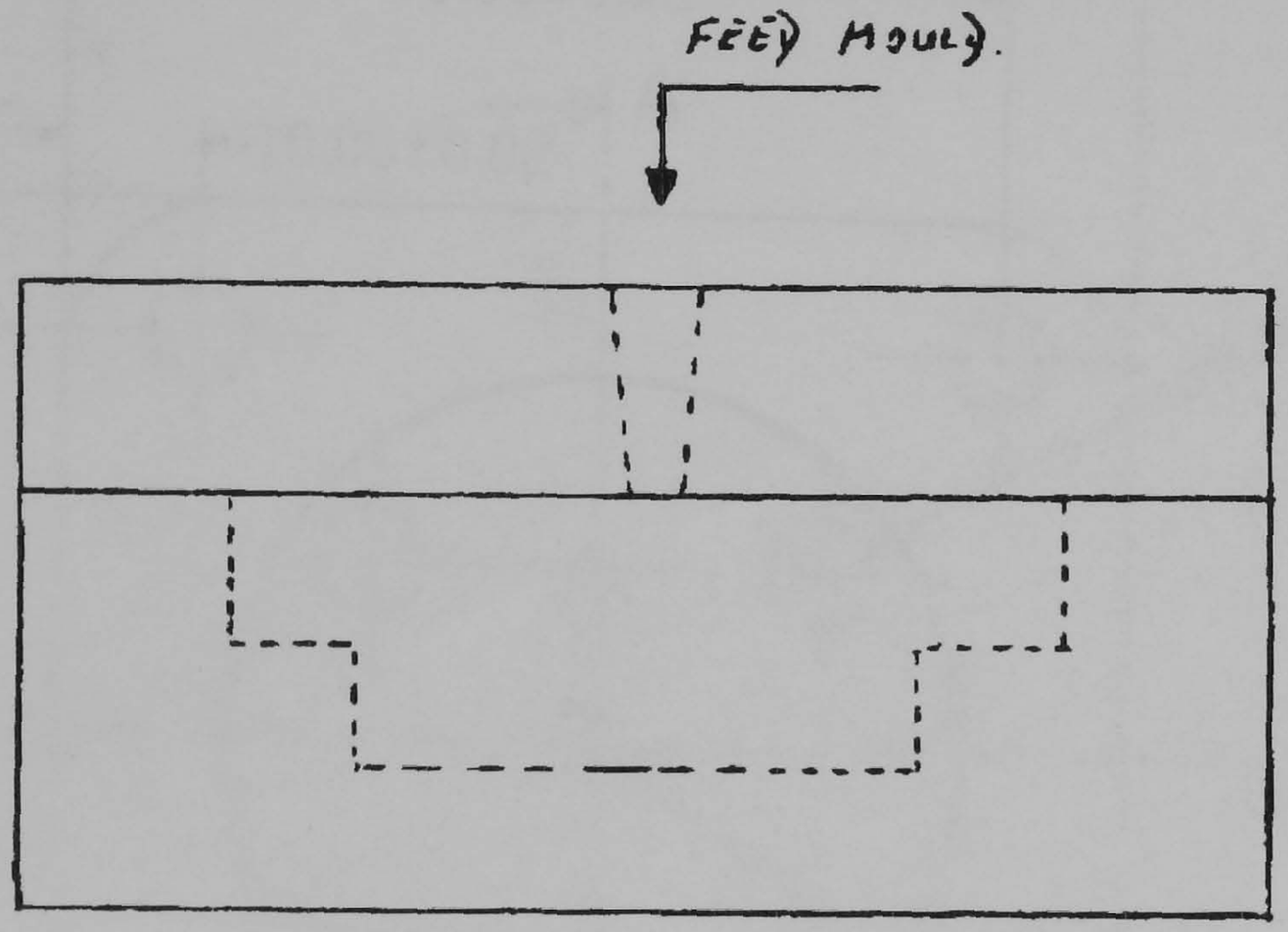

SIDE VIEW

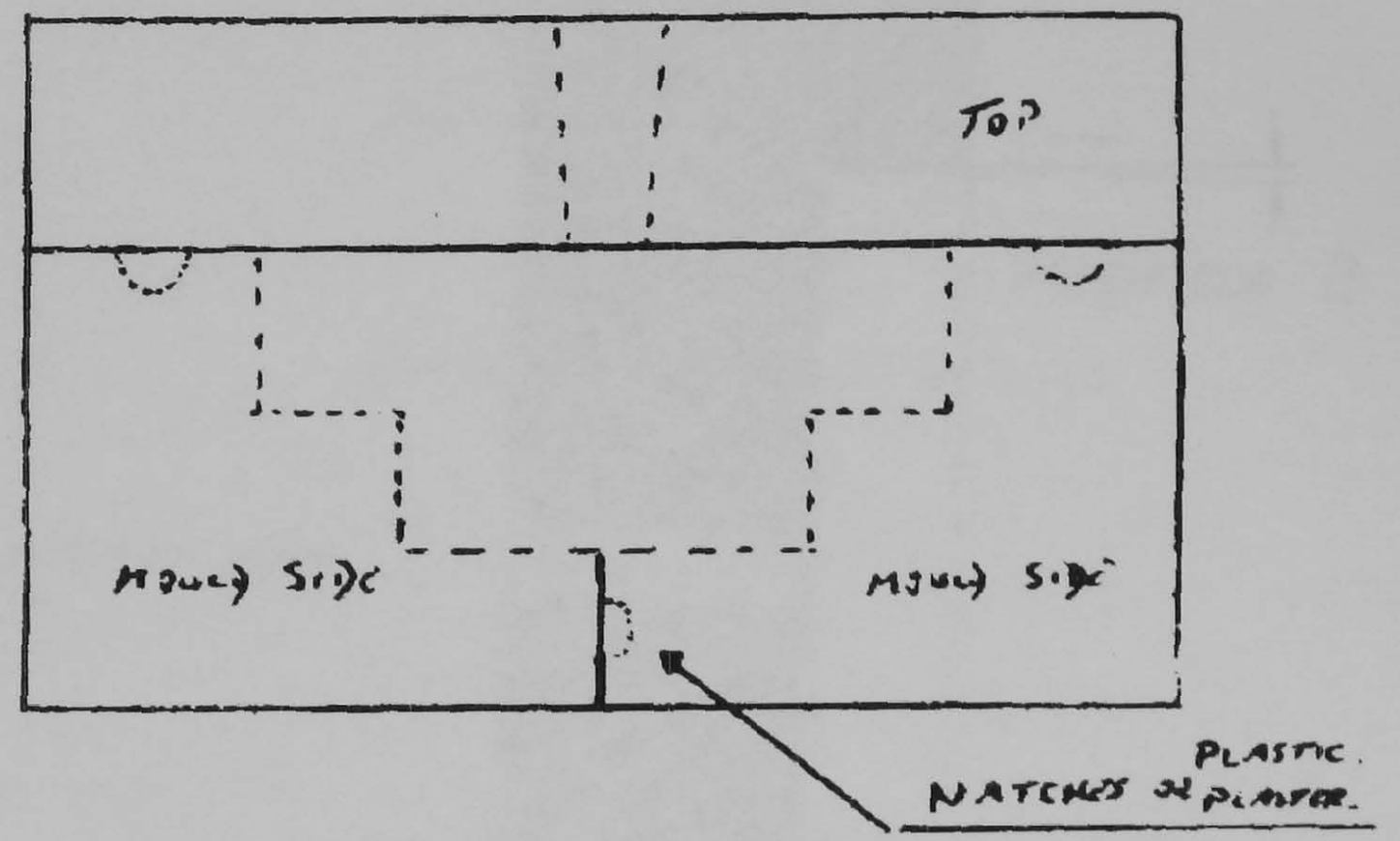

END VIEW

SINGLE THREE PART WORKING MOULD.

PLASTER

199

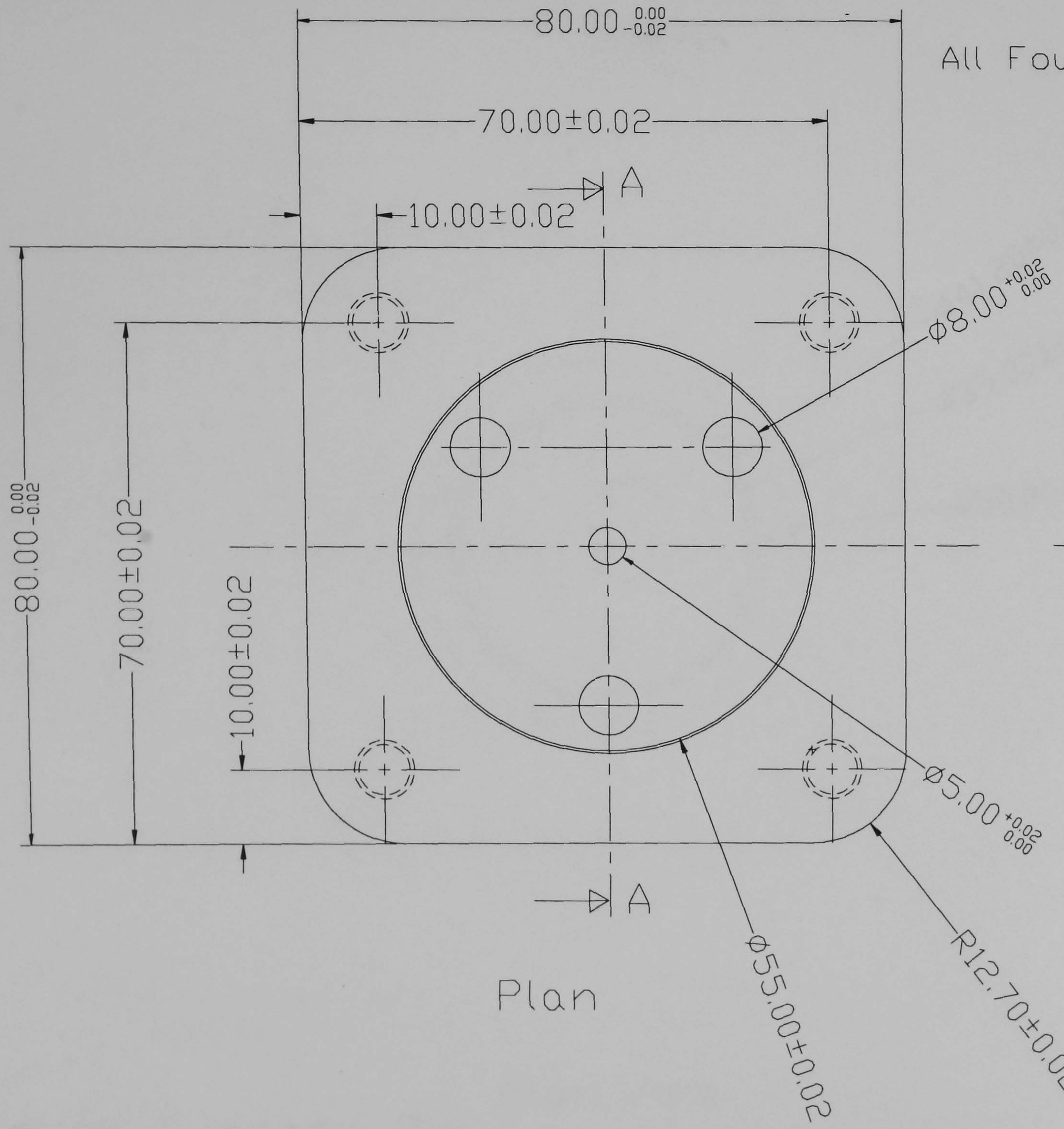

Plan

All Four Holes Drilled and Tapped M8

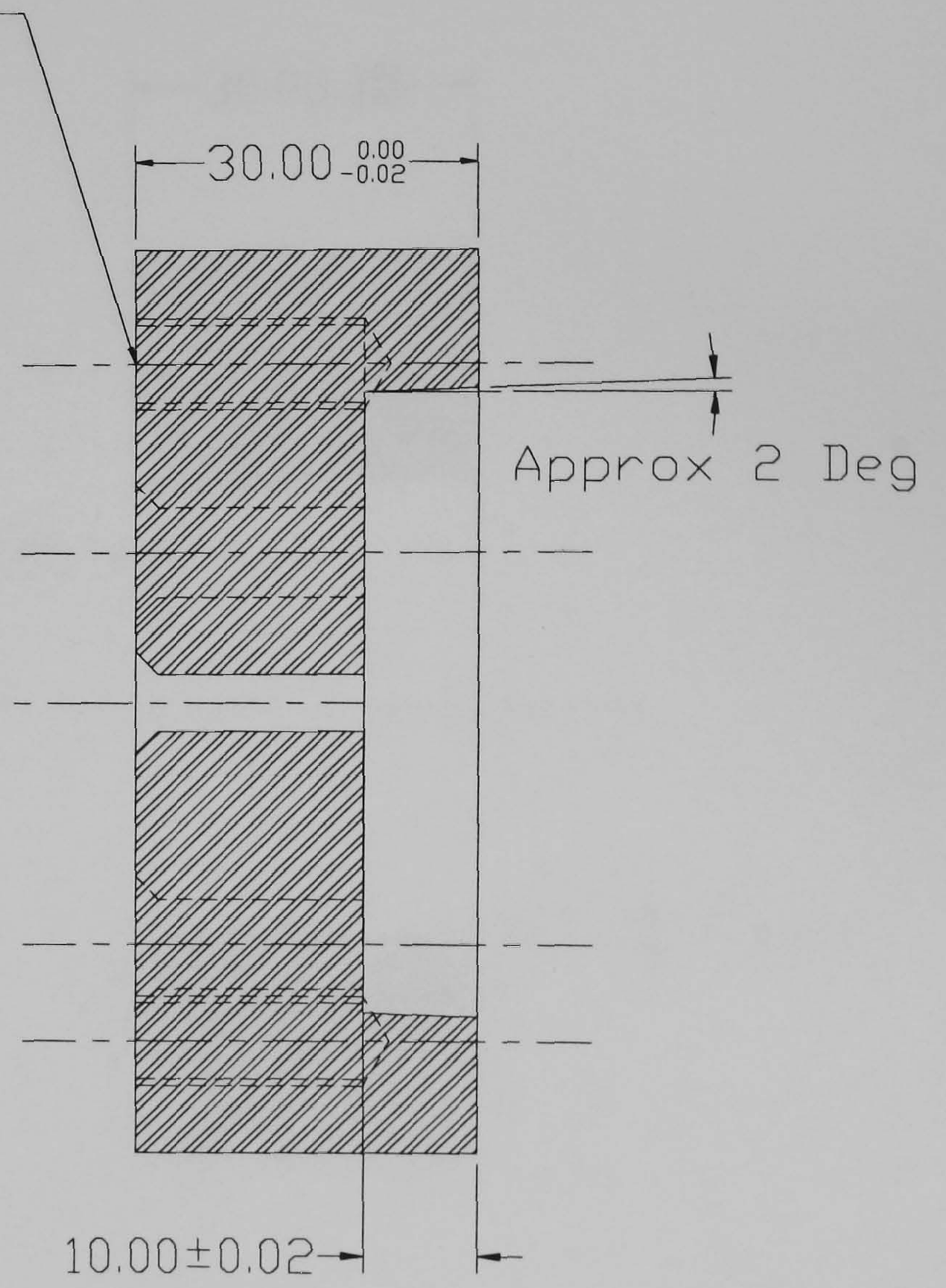

Section on A-A

*Note: 2mm Chamfer all Holes

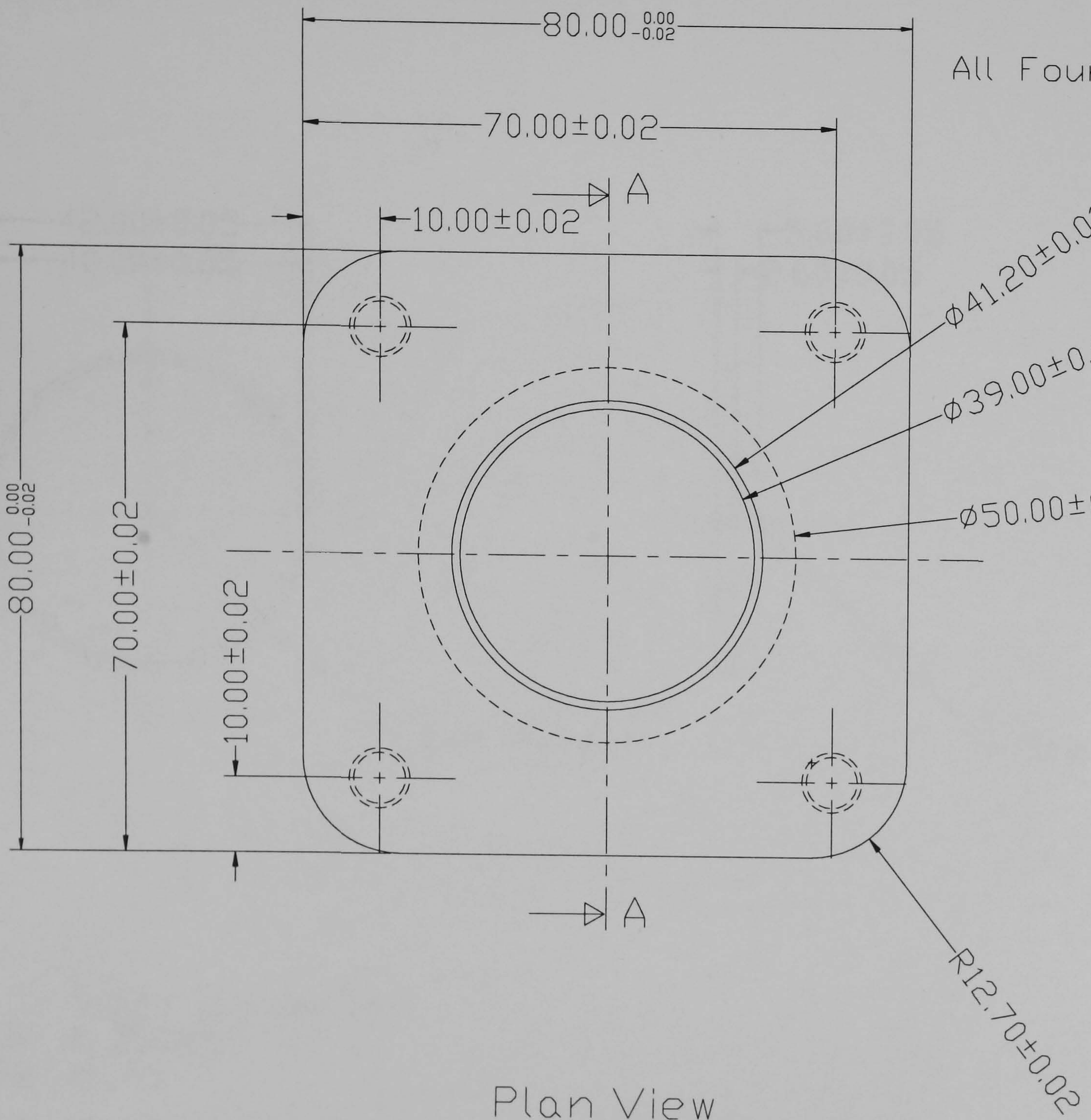

Plan View

All Four Holes Drilled and Tapped M8

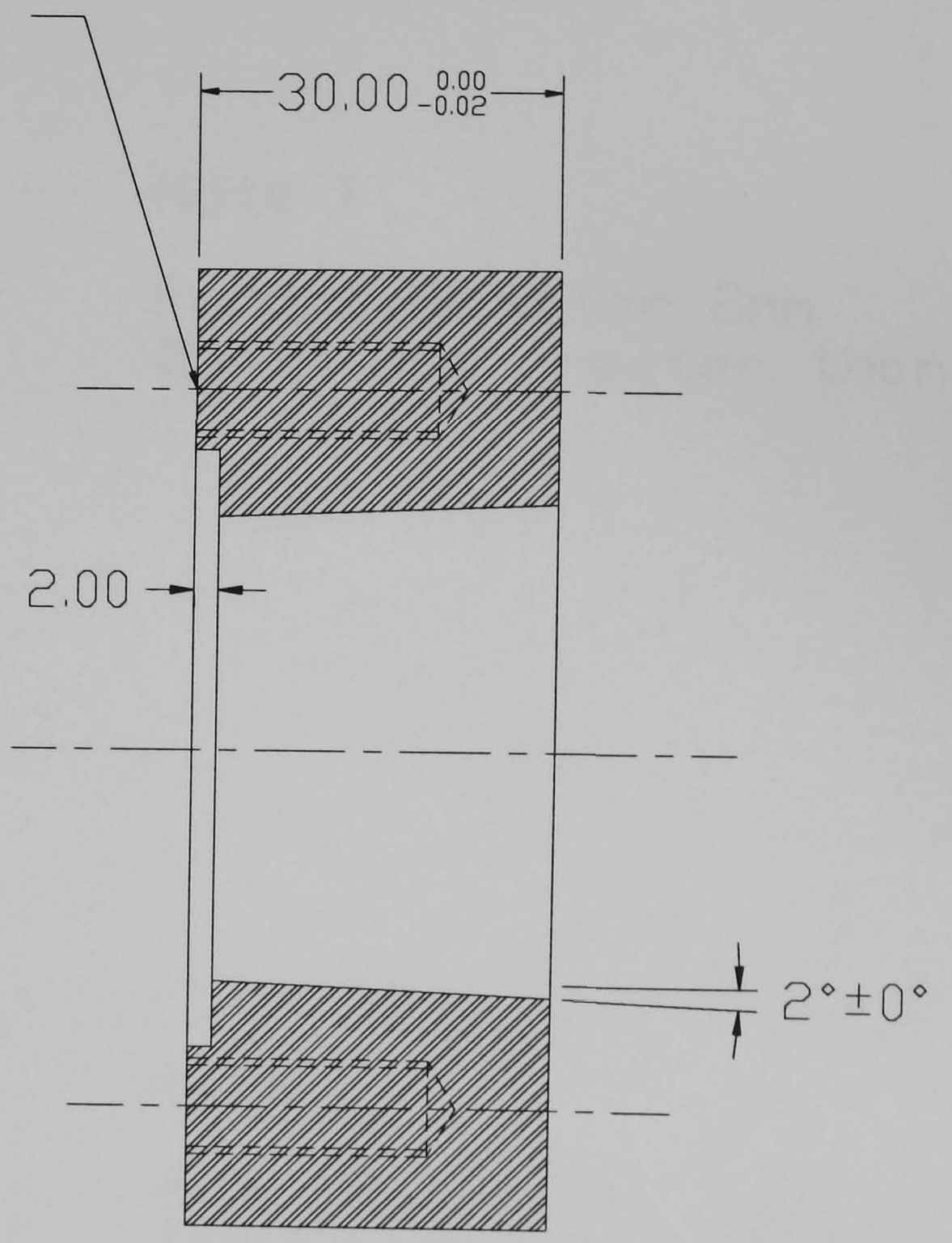

Section on A-A

Note* 1mm Chamfer on
Ejector Pin Holes as Shown

Note* All Ejector Pin
Holes Dia 4mm on
ø 31mm PCD

Bearing Mould Insert Scale 1:1 Mat'l: Steel

201

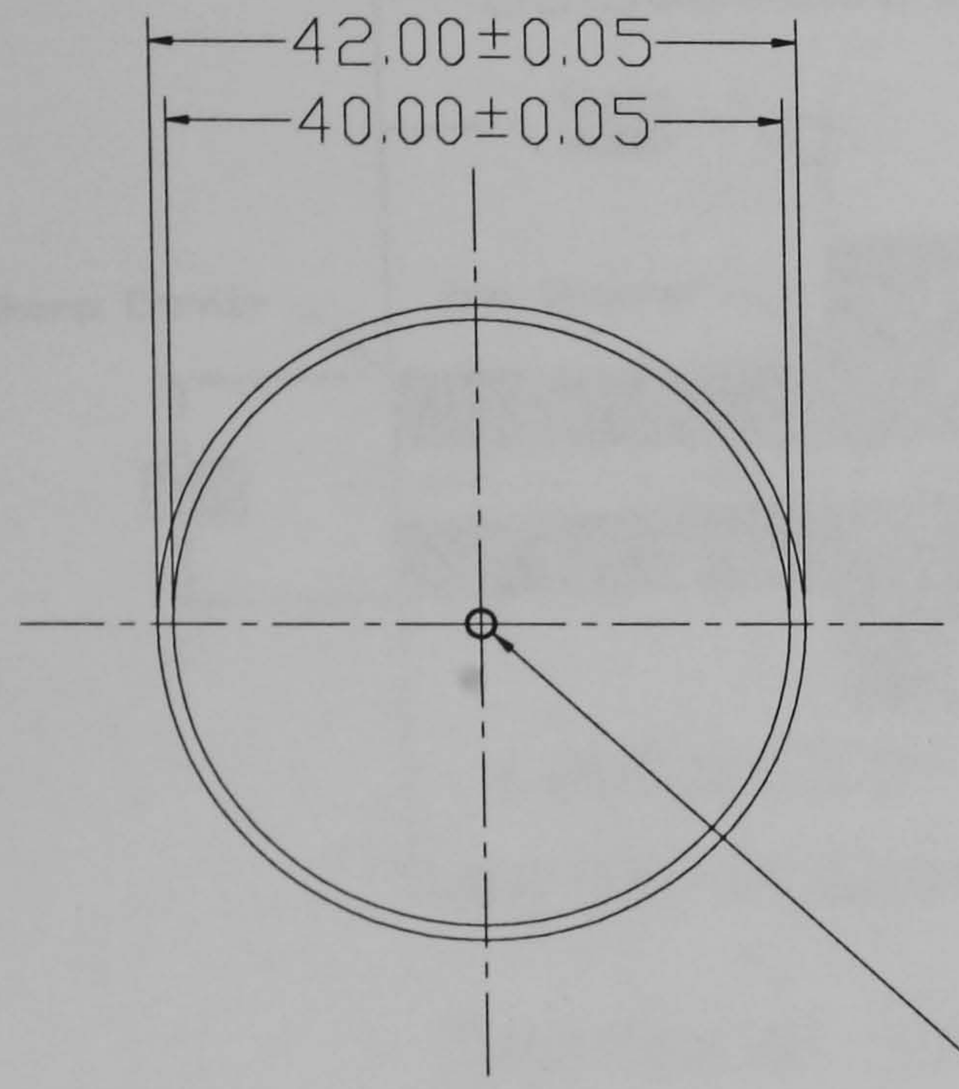

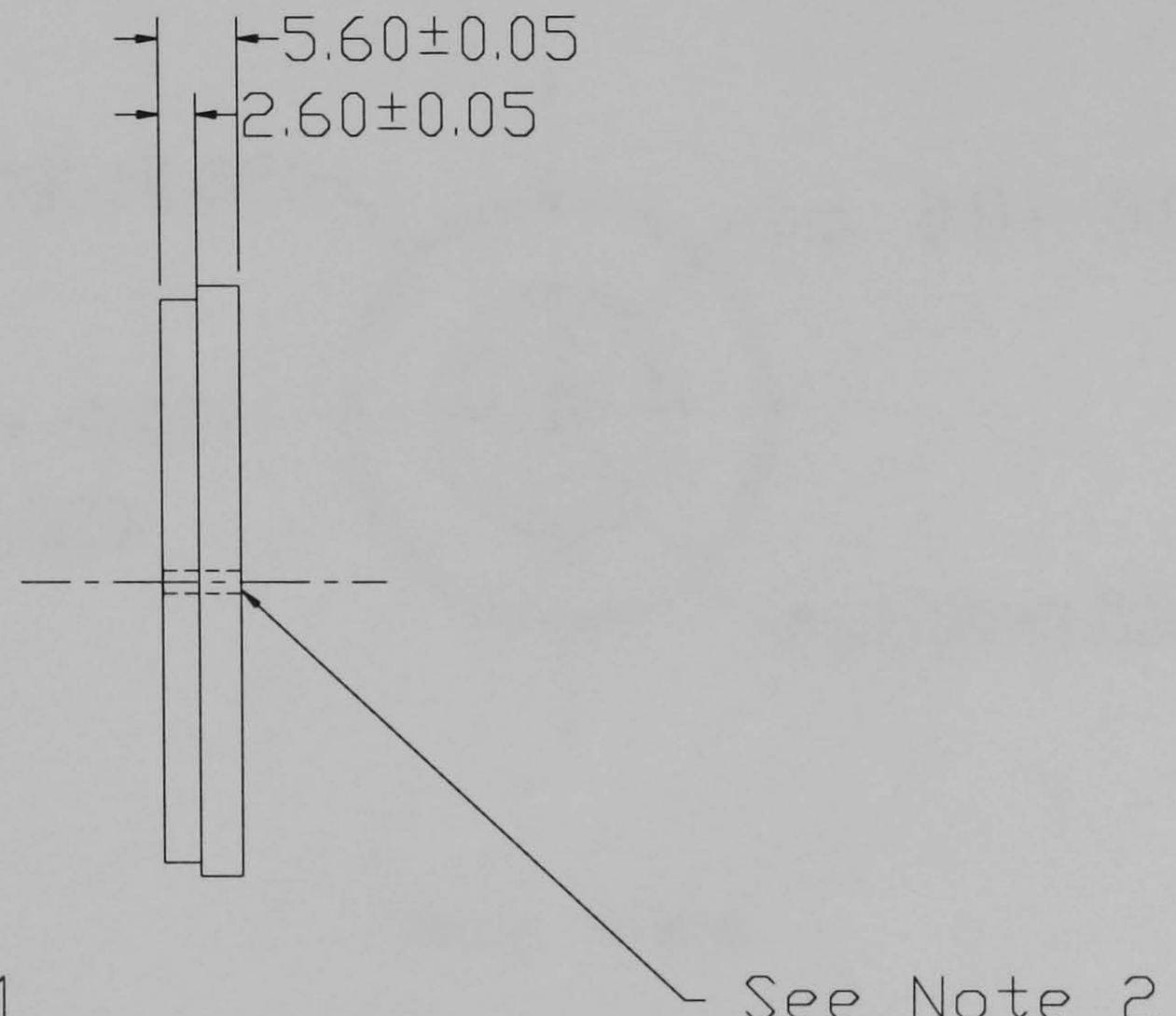

Note 1

Pocket diameter 2mm
Depth not greater than 0.05mm

Note 2

Hole drilled for insert
Insert diameter 0.0635"
Tolerance +/- 0.005"

1st angle projection
Chris Roach
22/06/99

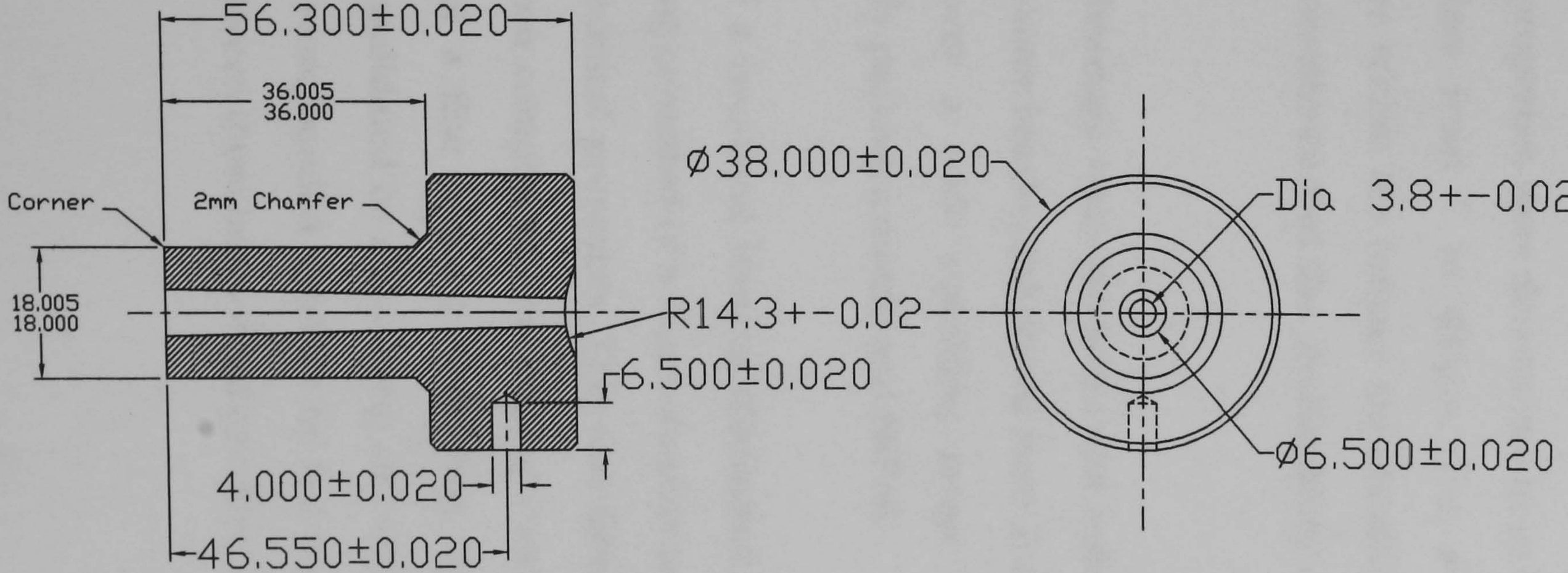

Sectional View

Plan View

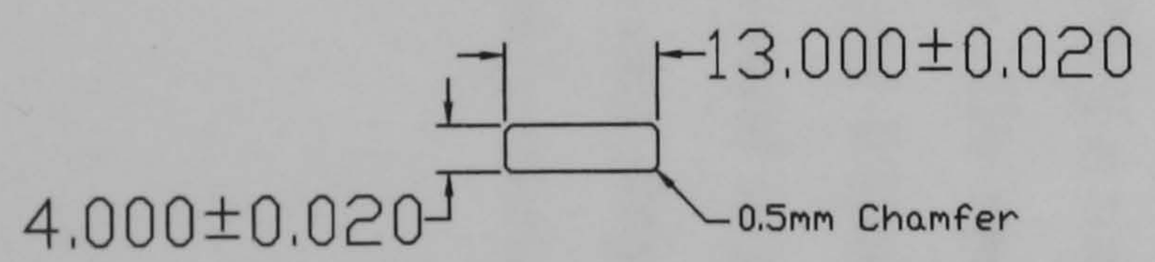

Locator Pin

Sprue Gate
Chris Roach 18/6.98
All Chamfers 1mm unless specified
Matl: Tool Steel or similar

Appendix H Summary of Previous Work

As this research follows closely from work undertaken previously at Cranfield University a brief overview of the programme is included below.

Several single layer and one two layer porous ceramic structures for aerostatic bearing applications were investigated using a capsule free hot isostatic pressing process, and in conjunction with slip and tape castings. The influence of various process parameters on open porosity, and the empirical relationships between porosity, particle size and the resulting fluid flow and structural properties were determined from experimental data over a range of powder sizes from 7 to 400μm. The measurement and uniformity of temperature within the furnace are identified as the most important factors affecting consistence and the predictability of the permeability of the porous substrate.

Prototype bearings were produced and tested, based on the above materials. The single-layer bearing fabricated from 7μm alumina powder was found to unstable over a wide operating range. This bearing was formed by vibrationally packing a mould and HIPed.

The use of a two-layer bearing eliminated the stability problem. This two layer bearing consisted of a 23μm alumina substrate which provided the bulk of the mechanical properties. This was fabricated by HIPing a vibrationally formed green component, and then ground to final size. The second layer consisted of a fine pressure restricting layer made from 0.5μm alumina powder consolidated by slip casting and sintering, also ground to size. These two layers were bonded together by hot pressing a tape cast strip of 0.5μm alumina between them before final grinding to the required geometry.

Slip flow measurements of the porous material in air and at small gaps indicated significant deviation from Beavers theory. The effect of velocity slip was found to be most significant in both test bearings, and was allowed for by the addition of an equivalent clearance to the bearing gap. The value of the equivalent clearance was deducted from the experimental data. The static load characteristics and the pressure profile of both test bearings agreed well with published theories, once the above-mentioned correction for slip was applied.